Office of Naval Research
Science & Technology

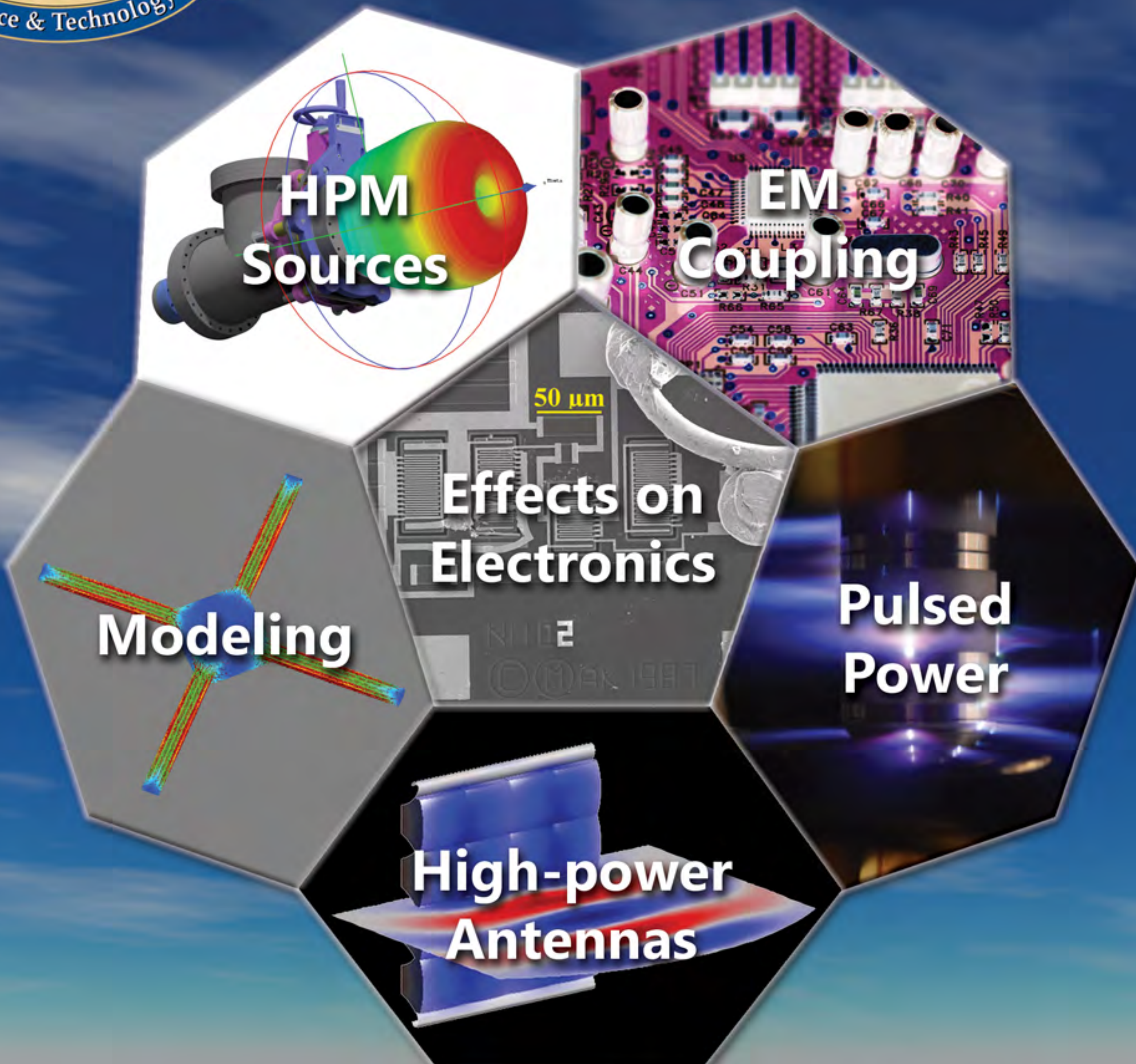

DIRECTED ENERGY WEAPONS (DEW) HIGH POWER MICROWAVE (HPM) 6.1, 6.2 AND SBIR PROGRAMS FY23 ANNUAL REPORT

Mr. Ryan Hoffman, Program Manager

Directed Energy Weapons (DEW) High Power Microwave (HPM) Program
Annual Report for FY23

Table of Contents

Directed Energy Weapons (DEW) High Power Microwave (HPM) Program
Annual Report for FY23

Table of Contents

Introduction

Ryan Hoffman
Program Officer, Office of Naval Research

The Directed Energy Weapons (DEW) Program of the Office of Naval Research (ONR) was initiated in response to the rapid development and growing threat of directed energy technologies by adversaries. Directed energy weapons are defined as electromagnetic systems capable of converting chemical or electrical energy to radiated energy and focusing it on a target, resulting in physical damage that degrades, neutralizes, defeats, or destroys an adversarial capability. The U.S. Navy uses HPM to gain and sustain tactical, operational, and strategic advantage in the arena of EM Maneuver Warfare and Integrated Defense for U.S. forces across the full range of military operations, including power projection and integrated defense missions. The ability to focus radiated energy reliably and repeatedly at range, with precision and controllable effects, while producing measured physical damage, is the measure of DEW system effectiveness. In anticipation of DEW advancements, the ONR HPM Program comprises a portfolio of initiatives and research projects which seek to provide the science and engineering basis for means and methodologies to provide the Navy advanced HPM technologies, systems, and techniques enabling a new class of weapons that will be highly effective in the battlespace. The goal is to be the most effective steward of DEW systems.

Asymmetric threats are proliferating worldwide and likely will continue to do so until such time as effective countermeasures are deployed. Often enough, Rules of Engagement will restrict kinetic engagement with asymmetric threats contingent on the particulars of the scenario. DEW systems – or more specifically for this report, HPM weapons – are expected to allow Naval commanders significantly more flexible responses to a number of asymmetric threats, including various small surface craft and unmanned aerial vehicle (UAV) threats. This flexibility is possible since the restrictions on engaging targets might be removed or reduced based on recognition of 1) the low collateral damage and 2) the non-lethal and reversible effects associated with HPM weapons.

HPM weapons create pulses of electromagnetic energy over a broad spectrum of known radio and microwave frequencies, causing either temporary or permanent results on electronics within targeted systems at scalable effects. HPM weapon systems can be used to disrupt, disable, or potentially destroy critical electronic circuitry in target systems, even in restricted scenarios, while also having the advantage of low cost per shot. HPM weapons deliver electromagnetic energy through coupling of the electromagnetic wave to target circuits through aperture or cable points of entry, thereby inducing currents in the circuitry capable of causing a variety of effects. Potential effects include erroneous signals, system lock-up, shutdown, loss of communications between systems, and physical damage.

As DEW falls within the Fundamental Research part of the broad ONR Science & Technology (S&T) investment portfolio, projects funded are long-term initiatives, covering basic research or applied science. These investigations can have a five to twenty year horizon. Across the HPM technology thrust areas, research projects within the program include performers from academia, industry, government laboratories, and small businesses. Moreover, the program includes performers whose research is financed through Navy SBIR/STTR funding. In addition, S&T solutions from an international technical community are afforded through ONR Global, which funds projects that foster cooperation in areas of mutual interest with global partners. The program encourages the cross-pollination of ideas and collaboration among performers worldwide, and offers an annual review where performers provide updates on the status of their research and present results to their DEW peers. Furthermore, data and facilities sharing are encouraged within the program. This approach contributes to increased success for the program and for the Navy.

Focus areas cover HPM sub-systems that optimize power and/or energy density at the electronic target for a variety of platform sizes and capabilities while minimizing size, weight, power and cost. Examples of related areas for S&T investment and research include supporting technologies such as power electronics, pulsed power drivers, power modulators, as well as frequency agile RF sources and antennas.

Additional research focus areas include research into electronic system coupling, interaction, and effects with the first goal of enabling development of predictive effects tools for current systems. A second goal of this work includes an exploration of in band and out of band coupling and interaction mechanisms. This exploration will exploit developing advances in frequency and bandwidth agility both to identify new potential weapon system possibilities as well as to achieve significant improvements in size, weight, power, and cost in new variants of existing systems.

Research Challenges and Opportunities

- RF coupling and modeling tools to capture complex EM wave interactions with electronics and associated enclosures, RF component disruption, along with novel techniques for experimental validation. Prediction of effects on electronics with improved techniques for HPM lethality testing and analysis. Analysis of HPM coupling mechanisms, electronic device interaction physics, and component level effects validated through experiment. Development of tools and techniques for more efficient identification and utilization of novel RF waveforms.
- Pulsed power/power electronics; including high energy density capacitors, power conditioning, high voltage switches, dielectric insulators, 3D printed/novel materials and power modulator pulse forming networks that enable higher duty cycle operation
- Solid state and vacuum electronic based HPM sources that provide frequency and waveform parameter tunability and are reconfigurable to adapt to changing requirements; computer codes for modelling HPM physics to enable the next generation of devices
- Wide bandwidth high power amplifiers that provide the ability of very rapid waveform adjustment.
- High power, low profile, or conformal antenna designs and capable radome materials, novel array concepts, high power beam steering techniques and distributed beam forming approaches.
- Novel HPM sensors, instrumentation and algorithms are of interest for measurement of waveforms and diagnosing system performance as well as applied to Electronic battle damage indication (eBDI).

ONR Grant Reports

Improving Performance of Crossed-Field Amplifiers Through Modulation Injection

Grant No. N00014-21-1-2024

Period of Performance: October 1, 2022 to September 30, 2023

Prepared by:

Dr. Allen L. Garner, Principal Investigator
Professor and Undergraduate Program Chair, School of Nuclear Engineering
Purdue University
363 N. Grant St.
West Lafayette, IN 47907
Tel: (765) 494-0618
Email: algarner@purdue.edu

This work was sponsored by the Office of Naval Research (ONR), under grant number N00014-21-1-2024. The views and conclusions contained herein are those of the authors only and should not be interpreted as representing those of ONR, the U.S. Navy or the U.S. Government.

Grant or Contract Number: N00014-21-1-2024
Date Prepared: 30JAN2024
Project Title: Improving Performance of Crossed-Field Amplifiers Through Modulation Injection
Annual Summary Report: FY23
Principal Investigator: Allen L. Garner, 765-494-0618, algarner@purdue.edu Purdue University

Section I: Project Summary

1. Overview of Project

Abstract: Crossed-field devices, such as crossed-field amplifiers (CFAs), offer high efficiency, high power density, and robust performance. Improved CFA gain-bandwidth product and reduced noise would contribute to greater use and operational capabilities. This report highlights our progress toward benchmarking the particle-in-cell (PIC) codes ICEPIC and VSim to assess a commercial CFA, our completion of theoretical models describing the maximum current in two-dimensional (2D) crossed-field devices, our assessment of the maximum current allowed in a collisional crossed-field diode, and our initial work on changes in 2D maximum current with ion emission from the anode.

Objective: This effort will study the effects of electron modulation on a high power (1 MW) L-Band CFA using theory (Purdue University) and simulation using the particle-in-cell codes ICEPIC (Confluent Sciences) and V-Sim (Boise State University and Tech-X). The first task entails developing and validating a CFA model using thermionic emission models. This result will next be combined with secondary emission models and theories and validated. This will subsequently permit the examination of the causes of drive saturation and gain-bandwidth limitations. This combined theory and simulation will then be used to characterize the effects of electron modulation with and without secondary emission on gain, bandwidth, saturation, and noise on CFA efficiency, pulse width, output power, bandwidth, and frequency timing. Finally, an assessment on the impact of noise in the CFA will be performed by examining how particle orbits are impacted based on the thermionic and secondary emission models and the impact of space-charge on the electromagnetic properties of the device. This will involve including sensitivity analysis into the theoretical studies of single electron orbits, including second emitter into the theory and studying the interaction between electrons emitted from each source, and using simulation to examine electromagnetic mechanism in more detail.

Introduction: The electromagnetic spectrum is becoming both congested and contested, requiring greater flexibility in electromagnetic sources. As platforms become much more loaded with electronics and technology, the compactness, efficiency, capability, and controllability of individual electromagnetic sources must increase. Therefore, this proposal strives to both maintain the high amplitude operation associated with DE technology and determine ways in which DE devices can provide information rich signals with choices in center band frequency, high bandwidth frequency modulation, and exquisite phase control. Traditional crossed-field DE devices, such as magnetrons, operate at high amplitude, but with only modest bandwidth or shot-to-shot frequency control. In contrast, the CFA provides bandwidth and phase control, but with orders-of-magnitude lower power. Thus, the CFA characterization proposed here will determine the limitations in gain-bandwidth product and enhance CFA tunability, which is critical for electromagnetic warfare.

Background: Crossed-field devices, such as crossed-field amplifiers (CFAs), offer high efficiency, high power density, and robust performance. Improved CFA gain-bandwidth product and reduced noise would contribute to greater use and operational capabilities. Currently, there are no high-power CFA models available for public research studies at universities. This gap is especially important as we try to realize the promise of higher power devices represented by Directed Energy High-Power RF (HPRF) devices. Almost every type of high-power radiofrequency (HPRF) device is an oscillator. While these sources produce very high-power pulses, the waveform control, typically measured in the bandwidth, is insufficient for radar or communications. This restricts these directed energy (DE) sources to jamming and counter-electronics missions, rather than the more information-intense full-fledged electronic warfare. This proposal goes to the heart of the question "what are the limits to high power amplifiers?" The university community currently lacks the well characterized, high power sources with intense space-charge that can mimic a HPRF device to address these questions. This problem becomes more acute for CFAs. CFAs are the highest power amplifiers widely used; however, they suffer from the limits of the gain-bandwidth product. The lack of a publicly available CFA model using first-principles, particle-in-cell simulations to serve as a benchmark for research hinders the examination of potential methods to improve design.

We use a model of the L3 Technologies L4953 CFA (discontinued) that was operated by the Federal Aviation Administration (FAA). Because this model is discontinued and unclassified, L3 Technologies is willing to allow our team to use the design to develop a high-power CFA model. This CFA model would become a benchmark for CFA research in universities, industry, and national laboratories to allow comparing future simulations and modifications to CFAs and other amplifiers. After developing the model, we would then study the effects of electron modulation on gain, bandwidth, and noise. We can study, via simulation, the saturation effects that occur in CFAs and determine whether techniques such as current modulation can improve the gain-bandwidth performance including performance at higher input powers. This would include studying the cause of saturation and techniques to maintain/increase gain-bandwidth product for HPRF production. Table 1 summarizes our team's overall research concept. We propose using VSim and ICEPIC and theoretical analysis to (1) develop and validate CFA models using emission-based cathodes, (2) extend the validated model using a combined thermionic emission and simple secondary emission model to approximate the secondary emitting component, (3) apply simulation and theory to analyze the saturation of gain-bandwidth in high power CFAs, (4) study the effects of a modulated cathode and electron back-bombardment on the gain-bandwidth product, and (5) analyze the effects of electron modulation and electron back-bombardment on noise generation and noise reduction with simulation and theory.

From this effort, studying the back-bombardment of field emission cathodes and out of band noise suppression will enhance the effectiveness of radar/communications/electronic warfare by removing spurious signals that degrade source performance for a given application and providing a signature to adversarial platforms. By providing high power, multi-frequency operation, this study could reduce SWAP-C (size, weight, power and cost) of the system.

2. Activities and Accomplishments

Modulated emission from the cathode itself offered improvements to efficiency but reduces the total emission current and power, so we shifted focus to end hat emission, as shown in Figure 1. The primary cathode operates in the space-charge limited (SCL) regime (blue electrons) and the end hats emit modulated current (green electrons) to follow the spokes. The combination of cathode and end hat emission allows for high powers unobtainable by modulated emission from the cathode itself. Control over the placement of modulated electrons in the spoke is shown in Figure 2, where modulated electrons are red, cathode electrons are blue, and the active regions on the end hats are outlined in black for optimal and non-optimal phases of emission. **Error! Reference source not found.** shows that the modulated end hat emitters stabilize operation at high voltages and magnetic fields, allowing for higher output power. We achieved <1 dB (1.5 MW) improvement. Note that all the additional 10 A from the end hat emitter collects on the anode and adds ~1 MW of power. Adding the end hat emitters pulls an additional 0.5 MW of power from the SCL cathode. While this improvement to power is only marginal, we have demonstrated control of the injected electrons and many different emission profiles may be tested.

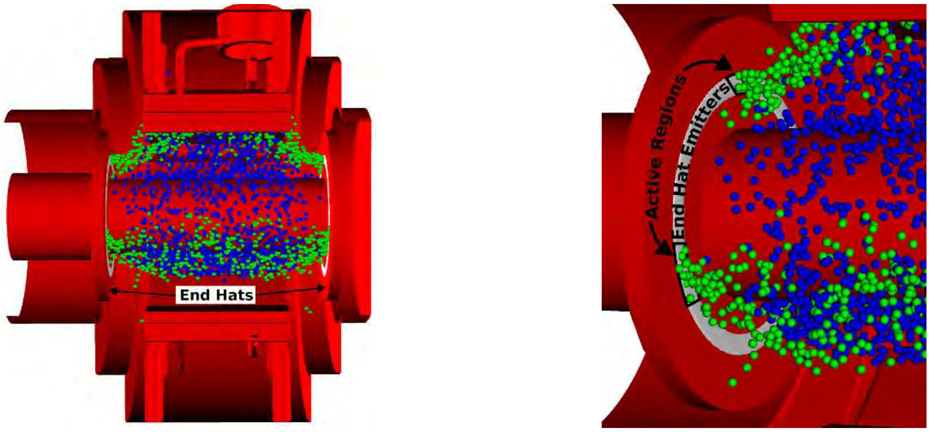

(a) (b)

Figure 1. Figure 1: CFA model showing electrons emitted from modulated end hat emitters in green and SCLC emission from the cathode in blue. (a) The full model clipped to see inside, and (b) a close-up view of the end hat emitters and the active emission regions which are modulated to follow the spokes.

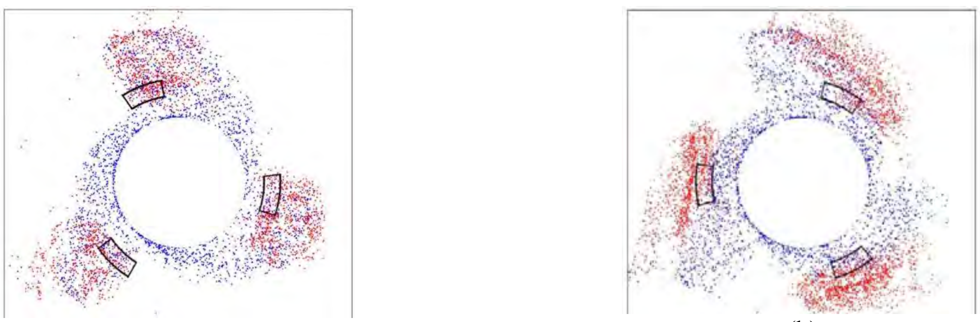

(a) (b)

Figure 2. Figure 2: Electron positions for end hat emitters in red and SCLC cathode emission in blue. The black outlines indicate the end hat emission area for different phases, (a) optimum phase slightly in front of the spoke, and (b) non-optimum phase slightly behind.

We also developed diagnostics to elucidate device physics to identify possible contributions to noise generation. Figure 4 shows the electron density as a function of angle and time with the corresponding amplitude of the fast Fourier transform (FFT) in the rotating frame of reference. The transit wobble at 0.43 GHz dominates the spoke frame of reference, but there is no transit wobble frequency component on the output signal shown in Figure 5. The phase of the first spoke in Figure 4(a) is a skewed sinusoid, as confirmed by the high amplitude harmonics in Figure 4(b). There is an additional component at 0.18 GHz in Figure 4(b), identified as $f_{sideband}$, at the front of the spoke. This frequency component corresponds to peaks 0 and 3 in Figure 5, where the 0.18 GHz signal at the front of the spokes inter-modulates to form sidebands at 1.11 and 1.48 GHz. These visualizations identify a direct connection of noise in the spoke and noise on the output. This paves the way for further research into methods to stabilize the spoke and reduce noise. Preliminary simulations using an off-axis cathode and modulated high voltage inputs can affect, and sometimes reduce, noise on the output. While previous studies have shown that off-axis cathodes can improve performance, these visualizations offer a way to explain the phenomenon and possible ways to improve it.

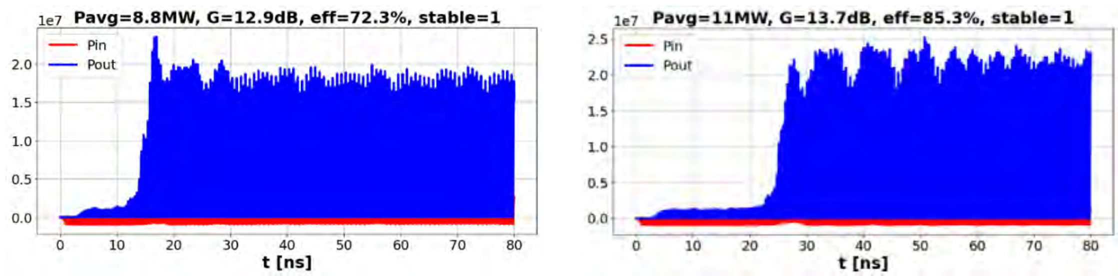

(a) (b)

Figure 3. Figure 3: The maximum output power (a) without end hat emitters and (b) with end hat emitters

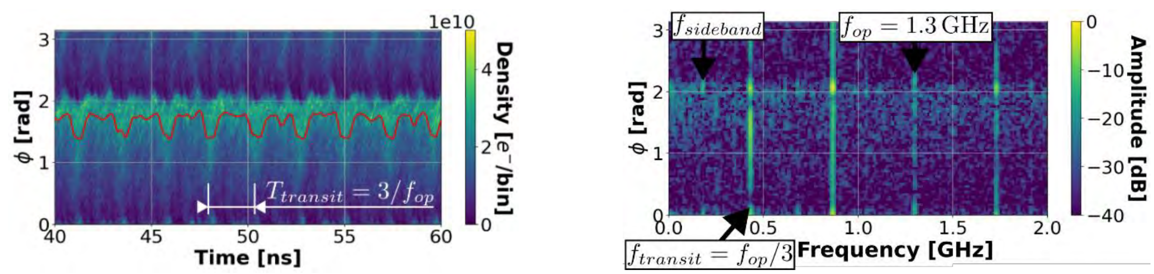

(a) (b)

Figure 4. Figure 4: (a) The charge density in ϕ and time and (b) the corresponding frequency amplitude in ϕ. The red line in (a) follows the phase of the spoke. The transit wobble period and frequency are identified in (a) and (b), respectively. The sideband frequency corresponds to the separation of the sidebands from the operation frequency on the output signal.

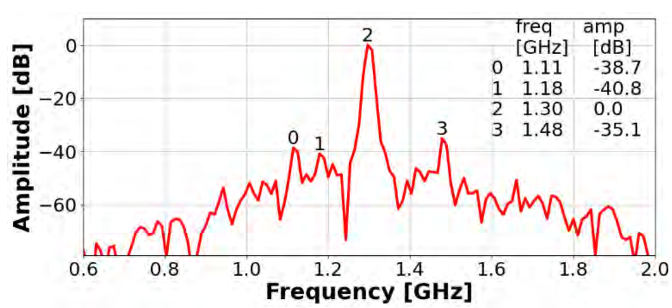

Figure 5. Figure 5: Amplitude of the FFT of the output voltage during steady state with the frequency and amplitude of peaks. Peaks labeled 0 and 3 correspond the intermodulation of the operation frequency and $f_{sideband}$.

Confluent Sciences has obtained agreement between ICEPIC and VSim calculations of the L-4953 crossed-field amplifier for the variation of input power, output power, and cavity quality factor (Q) with frequency in cold (no electron emission) calculations, and the variation in gain with AK voltage in hot (including electron emission) calculations. However, ICEPIC and VSim still differ significantly in the "tuning procedure" calculations. The difference suggests that the ICEPIC realization of the tube might be characterized by a dispersion relation that differed significantly from the actual tube, motivating ongoing efforts toward determining the dispersion relation of the L-4953 according to ICEPIC.

Early in the year, we obtained essential agreement between the ICEPIC and VSim L-4953 calculations for transmitted and received power, S_{12}, and gain vs AK voltage; however, ICEPIC and VSim differed when attempting to the tuning procedure calculations. While most of these differences most likely arose due to the cavity Q, as loss had not yet been introduced into the ICEPIC calculations, the differences motivated numerical determination of the device dispersion relation.

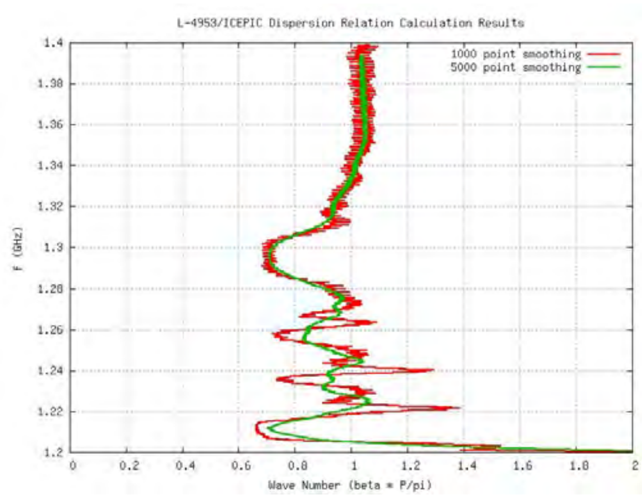

Figure 1. Figure 6. ICEPIC results for L-4953 in the vicinity of the operating band

Numerical tools were developed to assist the ICEPIC calculations of the L-4953 dispersion relation by following BSU's VSim assessment. While still underway, initial results using a swept-frequency method show forward-wave characteristics in the operating band, contrary to BSU results from VSim, which show backward-wave characteristic across these frequencies. Figure shows recent results for the dispersion relation – still a work in progress.

The dispersion relation curve from ICEPIC differed from the VSim results in some important details. The primary difficulty is the behavior across the operating band (1.28 GHz – 1.35 GHz). Here, the BSU result indicates that the dispersion relation is a backward wave. Our ICEPIC results show that the backward wave description is applicable at the low end of the operating band, but not across its full width. Efforts to refine these results are ongoing.

Purdue University is developing a new theoretical prediction of SCL current (SCLC) in a coaxial geometry, which would provide an important benchmark for PIC simulations. We used ICEPIC to calculate SCLC for several voltages, as summarized in Table 1.

Table 1: Calculated space-charge limited current for 2D cylindrical diodes in ICEPIC

Input Voltage (kV)	Resultant Voltage (kV)	Current (A)
120.9	23.25	2339.4
170.9	29.92	3373.2
220.9	35.69	4431.6
270.9	40.28	5520.8
320.9	45.12	6612.9
370.9	49.22	7117.3

We derived a closed-form solution and a semi-empirical solution for uniform SCLC for a 2D planar emitter with nonzero monoenergetic initial velocity. Figure 7 compares the theory, the empirical relationship, and the PIC (XOOPIC) results for various emission widths W and β which the ratio of the initial kinetic energy of the electron to the electric potential energy. The theoretical SCLCs for various emission widths and initial velocities agree well with the results obtained from PIC simulations using the over-injection method in XOOPIC. We compared a semi-empirical form that simply incorporates geometry and velocity as multiplicative corrections to the classical Child-Langmuir (CL) law J_{CL}. This semi-empirical form can be used for rapid solutions and insight for complicated scenarios, particularly for lower velocities. At higher velocities, the geometry and velocity corrections cannot be decoupled, and the full theoretical solution is necessary.

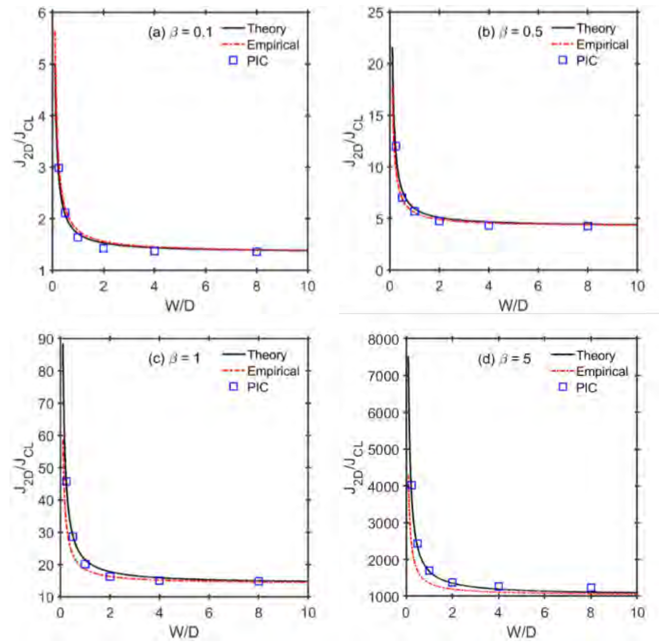

Figure 7. 2D over-injection limiting current J_{2D} normalized to the CL law J_{CL} from theory, semi-empirical form, and XOOPIC as a function of W/D for (a) $\beta = 0.1$, (b) $\beta = 0.5$, (c) $\beta = 1$, and (d) $\beta = 5$. The maximum discrepancy between the theory and PIC is ~11%.

We also derived an analytical solution and a semi-empirical form for the 2D uniform limiting current with a nonzero monoenergetic initial velocity in a crossed-field gap without magnetic insulation. Figure 8 shows the 2D limiting current from the analytical solution as a function of W/D for various initial velocities and magnetic fields in the y-direction B_y (normal to the infinite direction with electric field across the gap is in the x-direction). The analytical solution agrees with the XOOPIC results up to $\beta = 1$ for B_y similar to the nonmagnetic cases and provides closer estimates to PIC simulation compared to the semi-empirical solution (not plotted) for small W/D (e.g., $W/D \leq 1$). Note that it also matches with the PIC results for the magnetic field in the z-direction B_z (parallel to the infinite direction) with zero initial velocity ($\beta = 0$).

We next extended previous calculations of limiting current in a crossed-field gap to incorporate collisional effects. The collisional crossed-field limiting current recovers the vacuum case for no collisions and reduces to nonmagnetic SCLC with monoenergetic initial velocity for $B \to 0$, given by the general space-charge limiting current. Increasing the collision frequency makes the electron trajectory across the gap more linear, which decreases its dependence on the magnetic. The limiting current also is continuous as $B \to B_H$, where B_H is the Hull cutoff, differing from the discontinuity observed for the vacuum crossed-field case. Figure … shows that the limiting current normalized to general SCLC (GSCLC) with nonzero injection velocity as a function of magnetic field exhibits a similar trend to that observed for a misaligned crossed-field gap in vacuum, in which magnetic insulation is also eliminated. The ratio of the limiting current to GSCLC, $\bar{J}_c/\bar{J}_g$, decreases for some range of B/B_H, followed by a plateau. The trend implies that the ratio approaches a constant for $B/B_H \to \infty$, as observed for the misaligned gap. For higher collisionality, the magnetic field has less influence on electron trajectory, so $\bar{J}_c/\bar{J}_g$ approaches a larger constant.

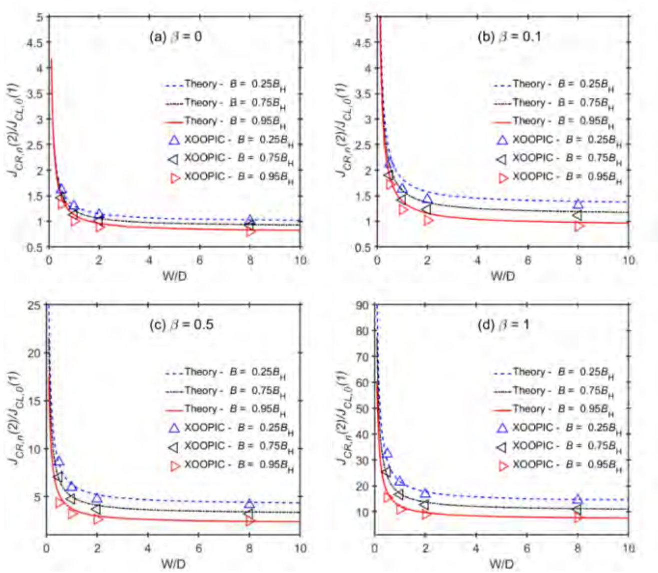

Figure 8. 2D limiting current density normalized by 1D CL current density from the analytical solution and XOOPIC as a function of W/D for crossed-magnetic fields $0 < B_y < B_H$ for (a) $\beta = 0$, (b) $\beta = 0.1$, (c) $\beta = 0.5$, and (d) $\beta = 1$. Note that with zero initial velocity ($\beta = 0$), the analytical solution also matches the XOOPIC results for the magnetic field in the z-direction.

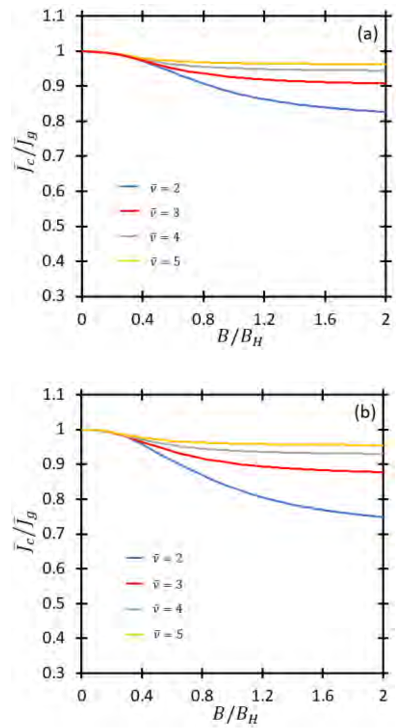

Figure 9. Nondimensional limiting current $\bar{J}_c$ normalized to GSCLC with injection velocity $\bar{J}_g$ as a function of magnetic field B normalized to the Hull cutoff B_H for various collision frequencies $\bar{\nu}$ and initial velocities (a) $\bar{v}_0 = 0$ and (b) $\bar{v}_0 = 0.3$.

3. Findings and Conclusions

Modulated end hat emitters stabilize operation at high voltages and magnetic fields, allowing for higher output power. While this improvement to power is only marginal, we have demonstrated control of the injected electrons and many different emission profiles may be tested. Many aspects of the L-4953 from ICEPIC agree with both VSim and laboratory/manufacturer measurements. Work characterizing the dispersion relation of the ICEPIC rendering of the tube is continuing with the goal to compare ICEPIC and VSim dispersion relation calculations. Purdue has successfully used 2D particle-in-cell and theory to characterize the limiting current in a 2D, magnetically insulated crossed-field diode, including assessing the relative contributions of Brillouin and cycloidal flows. They have also developed a theory that accounts for the limiting current in a collisional crossed-field diode.

4. Plans and Upcoming Events

BSU is working to write up a manuscript entitled “Spoke Characterization in Re-Entrant Crossed-Field Amplifiers via Simulation.” Visualizations of unstable operation better show the correlation between the transit wobble and the sidebands and may be the subject of another manuscript. These visualizations also provide an excellent way to explain why offset cathodes often perform better, another possible manuscript. Confluent's next focus will depend upon the comparison of the ICEPIC and VSim versions of the dispersion relation. If they agree well, we will complete the tuning procedure calculations and model the modulation injection. Disagreements between the dispersion relationship will necessitate troubleshooting to identify and rectify the cause. Purdue University will complete manuscripts on the limiting current in a 2D, non-magnetically insulated crossed-field diode and the limiting current in a collisional crossed-field diode. Next, Purdue will continue efforts on exploring the impact of bipolar flow on the limiting current in 2D crossed-field gaps using XOOPIC, extending the work described above. Several studies have explored the impact of bipolar flow on 1D diodes and recent work by Adam Darr at Sandia explored the impact of bipolar flow on electron trajectories, but none have assessed the implications on limiting current in 2D.

Separately, Purdue will finish work with Tech-X on using VSim, Leidos using MICHELLE, and Purdue's own simulations using XPDP1 to benchmark theories on 2D SCLC with nonzero injection velocity. Purdue will also finish work with Confluent on benchmarking its cylindrical SCLC theory.

Recommendations for Future Work: The efforts over the past few years have developed extensive knowledge in crossed-field systems from fundamental 1D and 2D theories and simulations to more detailed device physics using ICEPIC and VSim. A future program could work to extend these efforts to experimental benchmarks. One approach would be to experimentally validate CFA behavior based on different modifications, such as bipolar flow or endhat emitter modifications. A more fundamental study could explore benchmarking the emission simulations and theories developed here to experimental results. For instance, field emission plays a major role in Avalanche Energy's fusion devices, which used crossed-field geometries. A future study could involve performing experiments with Avalanche's systems, benchmarking to the simulations and theories developed in this effort, and then expanding the experiments, simulations, and theories.

5. Transitions and Impacts

None

6. Collaborations

John Luginsland, AFOSR, Ongoing discussions with Stellant Systems (formerly L3 Harris now). Purdue worked with Sandia National Laboratories on developing nexus theory for crossed-field physics with collisions and is incorporating part of that effort into extending the present effort. Purdue has also continued to explore collaborations with Avalanche Energy concerning crossed-field physics nexus theory for fusion applications. Purdue has also had conversations with John Petillo from Leidos concerning SCLC calculations that may become relevant for this grant.

7. Personnel

Principal investigator: Allen Garner, Purdue, 1 month, N
Co-PIs: Jack Watrous, Confluent, 5 months, N; Jim Browning, BSU, 1 month, N;
Business Contact: Brin Reed, Purdue, not paid from the grant
Team Members: Xiaojun Zhu (Grad), Purdue, 6 months; Jack Wright, Purdue, 2 person-months; Lorin Breen, Purdue, 1 month; Marcus Pearlman, BSU, 4 months; Nilesh Maker, BSU, 6 months
Subs: David Smithe, Tech-X, 1 month

8. Students

4 graduate students / 0 undergraduate students assisting during reporting period

9. Technology Transfer

Purdue worked with Sandia National Laboratories on applying crossed-field nexus theory to their efforts on magnetically insulated transmission lines (MITLs). TechX submitted an SBIR proposal using BSU's end-hat injection idea for magnetron phase control to the DoE for accelerators. BSU is working with its intellectual property department to file a patent on this concept.

10. Products, Publications, Patents, License Agreements, etc.

Publications resulting from this project:

<u>Archival Publications</u>

X. Zhu, N. R. Sree Harsha, and A. L. Garner, "Uniform space-charge-limited current for a two-dimensional planar emitter with nonzero monoenergetic initial velocity," Journal of Applied Physics **134**, 113301 (2023).

M. Pearlman, D. Smithe, C. Roark, M. Worthington, J. Watrous, A. Garner, and J. Browning, "Simulation of the pulsed 4.7 MW, L-band crossed-field amplifier," IEEE Transactions on Electron Devices **69**, 7053-7058 (2022).

<u>Conference Oral Presentations</u> (non-archived, presenter italicized)

M. Pearlman, J. Watrous, D. Smithe, A. Yue, A. L. Garner, M. Worthington, J. Browning, "Electron Spoke Characterization During Amplification in a Crossed-Field Amplifier via Simulation," 50th IEEE International Conference on Plasma Science, Basic Phenomena, O-7.5.1, 25MAY2023.

X. Zhu, J. W. Luginsland, J. Browning, A. L. Garner, "Electron Cycloidal and Brillouin Flows in a Two-Dimensional Planar Crossed-Field Gap," 50th IEEE International Conference on Plasma Science, Basic Phenomena, O-3.1.1, 23MAY2023.

<u>Conference Poster Presentations</u> (non-archived, presenter italicized)

N. K. Manker, M. Pearlman, J. Watrous, C. Roark, D. Smithe, A. L. Garner, M. Worthington, and J. Browning, "Secondary Electron Emission Study In L-4953 Crossed-Field Amplifier," 50th IEEE International Conference on Plasma Science, Santa Fe, NM, P.2.30, 23MAY2023.

M. Pearlman, J. Watrous, D. Smithe, A. Yue, A. L. Garner, M. Worthington, and J. Browning, "A Simulation Study of the Gain Limits of a Crossed-Field Amplifier," 50th IEEE International Conference on Plasma Science, Santa Fe, NM, P-2.29, 23MAY2023.

J. Watrous, M. Pearlman, J. Browning, and A. Garner, "Benchmark Calculations of a Well-Characterized Cross-Field Amplifier using ICEPIC," 50th IEEE International Conference on Plasma Science, Santa Fe, NM, P-2.28, 23MAY2023.

<u>Theses</u>

X. Zhu, "Modeling and Characterization of Solid-State and Vacuum High-Power Microwave Devices," Ph.D. Dissertation, Elmore Family School of Electrical and Computer Engineering, Purdue University, December 2023.

<u>Invited Seminars and Colloquia</u>

A. L. Garner, "Theoretical Analyses of Electron Physics in Crossed-Field Geometries," Avalanche Energy Designs, Tukwila, WA, 07 September 2023.

A. L. Garner, “Incorporating Geometry, Multiple Dimensions, and Collisions into the Child-Langmuir Law,” Air Force Research Laboratory, Albuquerque, NM, 30 August 2023.

A. L. Garner, “Extending Crossed-Field Device Physics to Collisional and Nonplanar Conditions,” Sandia National Laboratories, Albuquerque, NM, 29 August 2023.

A. L. Garner, “Electron Emission Theories for More Realistic Geometries and Conditions,” Center for Applied Optics, University of Alabama at Huntsville, Huntsville, AL, 01 August 2023.

A. L. Garner, “Vacuum and Collisional Crossed-Field Device Physics,” Naval Research Laboratory, Washington, DC, 26 July 2023.

11. Point of Contact in Navy

Zach Drikas, NRL

High Power, High Frequency, Repetitively Pulsed Oscillators

Grant No. N00014-23-1-2143

Annual Report for Fiscal Year 2023

Period of Performance: January 1, 2023 to September 30, 2023

Prepared by:

Professor Nicholas Jordan, Principal Investigator
Associate Research Professor
University of Michigan Plasma Physics, Pulsed Power, and Microwave Lab
112 NAME Building
2600 Draper Dr.
Ann Arbor, MI 48109
Work: (734) 763-0213
Email: jordann@umich.edu

This work was sponsored by the Office of Naval Research (ONR), under grant (or contract) number N00014-23-1-2143. The views and conclusions contained herein are those of the authors only and should not be interpreted as representing those of ONR, the U.S. Navy or the U.S. Government.

Grant or Contract Number: N00014-23-1-2143
Date Prepared: 1/18/2024
Project Title: High Power, High Frequency, Repetitively Pulsed Oscillators
Annual Summary Report: FY23
Principle Investigator: Nicholas Jordan, 734 763 0213, jordann@umich.edu
University of Michigan

Section I: Project Summary

1. Overview of Project

Abstract:
In this period, the first 9 months of the effort, we have designed (through PIC simulation) a scaled X-band MILO and a subsequent overmoded X-band MILO with larger feature sizes.

Objective:
Our goal is to address, via high power microwave (HPM) research, some of the critical problems facing Navy operations due to asymmetric electronic threats. We propose to develop an X-band (8-12 GHz) MILO driven by a 1.6 kJ, 25-30 Ohm, Marx generator capable of producing highly-repeatable 20-400 kV, 100-200 ns voltage pulses with a 50 ns rise-time and flat-top voltage stability of ±5% at repetition rates of 1 Hz (10 Hz in burst fire operation).

Introduction:
Abbreviations used in this report:
MILO – Magnetically Insulated Line Oscillator
SWS – slow wave structure
OXMILO – overmoded X-band MILO
CP – circular polarization
LP – linear polarization
REP – repetitive experimental platform
AK – anode-cathode
AFRL – Air Force Research Lab
ONR – Office of Naval Research

Background:
In a recent effort, funded by the Office of Naval Research, we successfully developed a dual-frequency harmonic magnetically insulated line oscillator (MILO) requiring only 10 kA for operation in L- and S-band, and a first-principles theory of MILO operation and insulation requirements. Building on this successful program, we will extend this design to X-band.

2. Activities and Accomplishments

X-band MILO

We designed an initial X-band MILO for operation at 10 GHz and ~10 kA at 300 kV. The dimensions of this initial design were small, and we were concerned it would suffer from severe plasma closure and arcing during the experiment. To increase the feature sizes, we focused on developing an Over-moded X-band MILO (OXMILO), which would operate around 8.5 GHz.

We initially developed a design targeting the HEM_{11} mode, which proved to operate in a circular polarization (CP). We have now tweaked that design so that the MILO runs in a linearly polarized mode (LP). The geometry for both models is shown in Figure 4, and the relevant design parameters and key performance characteristics are given in Table 1.

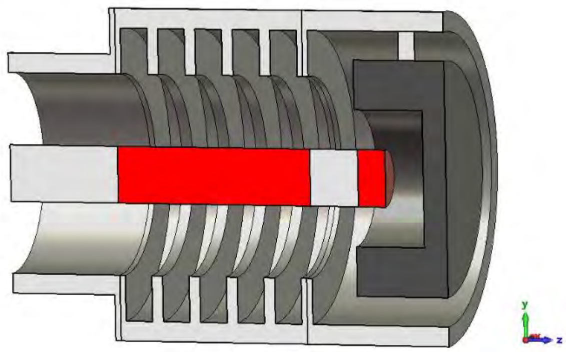

Figure 4: Over-moded X-band MILO design at nominally 6.5 GHz. Red areas are allowed emission zones on the cathode.

	CP	LP
Cathode Radius	5 mm	5 mm
TM_{01} Frequency	6.5 GHz	6.5 GHz
AK Gap	11.5 mm	12.7 mm
Pitch	6.9 mm	6.9 mm
Anode SWS Inner Radius	16.5 mm	17.7 mm
Anode SWS Outer Radius	24.6 mm	25.8 mm
Steady State Input Current	10.4 kA	10 kA
Power Output	33 MW	34 MW
Frequency	8.581 GHz	8.471 GHz

Table 1: Parameters of the OXMILO

In CST Particle Studio simulations at 300 kV, this MILO drew a steady state input current of ~10.4 kA and produced 34 MW at 8.471 GHz, successfully driving the HEM_{11} mode as shown in Figure 5a/b.

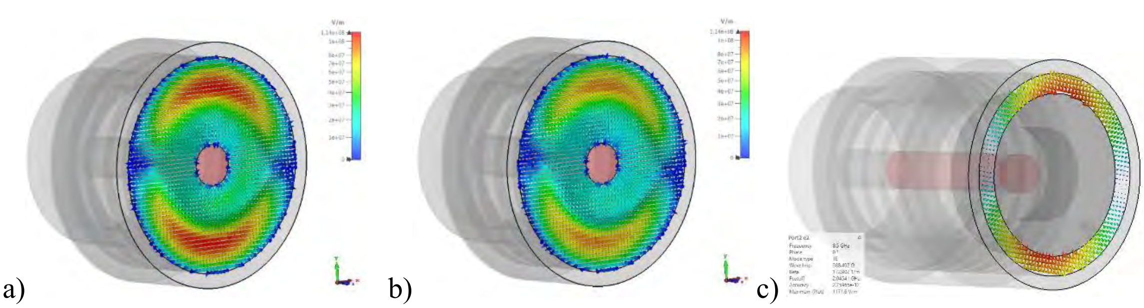

Figure 5: (a-b) Cross-section, taken at the 4th cavity, of the OXMILO-LP operating in the HEM_{11} mode. Part (b) is 2 ns after part (a), showing an oscillating linear mode polarization. (c) Cross-section, taken at the output port, of the OXMILO-LP operating in the HEM_{11} mode.

While the OXMILO oscillates in the HEM_{11} mode within the SWS, this becomes a TE_{11} mode at the output, as shown in Figure 5c. Unlike the previous design, it is consistently linearly polarized in a vertical orientation.

Unlike the CP design, all 34 MW of output power are present in the vertical polarization, as shown in Figure 6. The start-up time is similar.

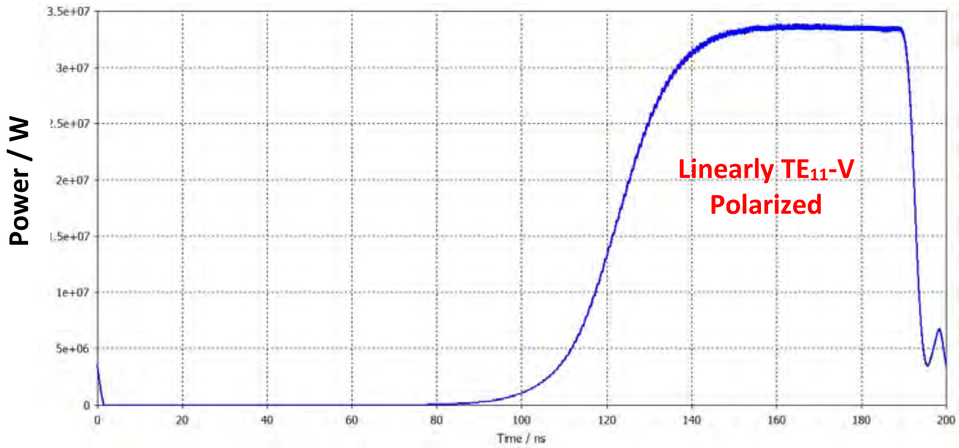

Figure 6: Power in the vertical field component at the output. No power was present in the horizontal component, unlike the previous design.

Subsequent simulations investigated the addition of choke cavities to ensure proper wave propagation into the extractor, and the effect of variable applied voltage. It was found that the linearly-polarized design (OXMILO-LP) with an applied voltage of 300 kV will operate in the TE_{21} mode at ~9.5 GHz and produce steady state combined output power of ~32 MW. Other configurations produced only TM_{01} and TE_{11} oscillations at lower frequencies. Example space charge density and output power plots are provided in Figure 7 and Figure 8, respectively. The TM_{01} mode is at 8.1 GHz, HEM_{11} is ~8.5 GHz, and the HEM_{21} is ~9.6 GHz.

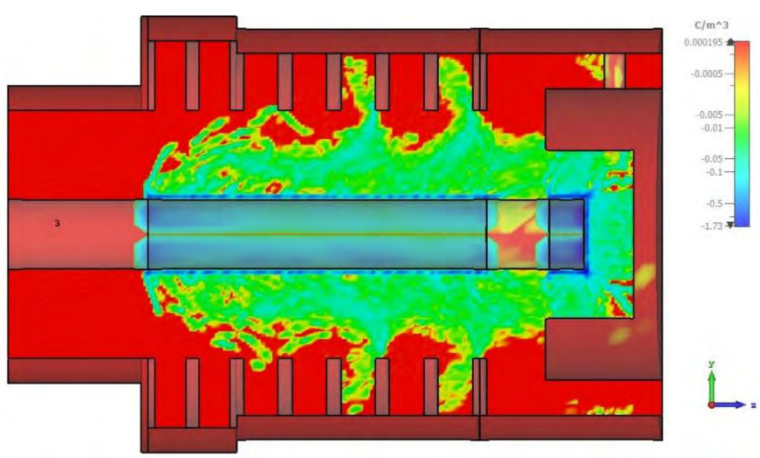

Figure 7: OXMILO-LP simulated space charge density cross-section at 141.5 ns simulation time (steady state operation), showing pi-mode spoke formation.

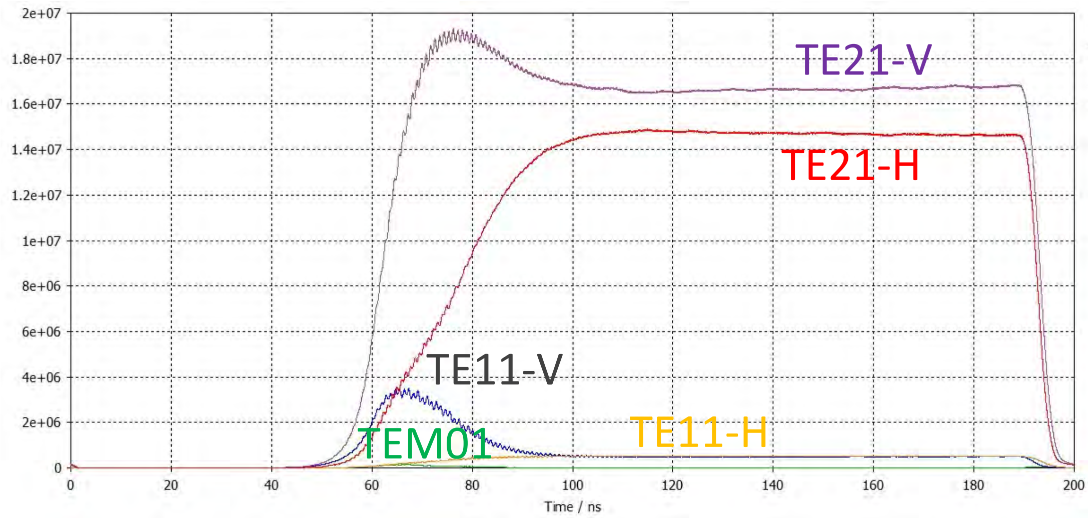

Figure 8: OXMILO-LP simulated output power in the various modes present within the device. At this voltage, the MILO primarily operates (at steady state) in the TE_{21} mode.

REP Pulser

The final components of the Repetitive Experimental Platform (REP) were delivered, and the system was been assembled (Figure 9) and tested. We developed a simple system to remotely control the power supplies, as well as an SF6 recapture system composed of an oil-free air compressor and a 60 gallon air receiver tank.

Figure 9: (left) ONR DURIP-funded Repetitive Experimental Platform (REP) assembled with protection circuit (silver cylinder on the right) and power supplies (below cart). (right) Newly machined insulating stack for REP.

We modified the small oil-free compressor to be able to run in reverse as a small vacuum pump. A 60 gallon air receiver tank holds the SF6 when it is pumped out of the REP pressure vessel. Some amount of mixing with air occurs, but the vendor has assured us that this is not an issue for the pulser, and can be compensated by a small increase in working pressure.

We have designed and machined parts for the insulating stack (Figure 9), as well as a trigger circuit to trigger REP. It was found that the trigger circuit has substantial (>1 us) delay and jitter.

MADCAP Source

The MADCAP recirculating planar magnetron source was shipped from AFRL, and has arrived at Michigan. We have uncrated it to verify that nothing was damaged in shipment. Though some of the internal structure of the shipping crate was not assembled correctly, the source seems to have survived the transfer.

We have measured the inductance and resistance of the custom electromagnet on MADCAP, and are modeling it in SPICE to evaluate the magnetic fields that will be achievable with our current capacitor bank.

Brillouin Flow Modeling

We conducted a range of fundamental simulations of Brillouin flow, using CST Particle Studio (CST-PS). In these simulations, a step discontinuity was introduced in the anode, and steady-state electron motion was observed. We found that when the electron flow was from a region of small anode radius to large anode radius (left to right in Figure 10), periodic bunching of the electron flow would occur. This effect was not observed when the direction of electron flow was reversed.

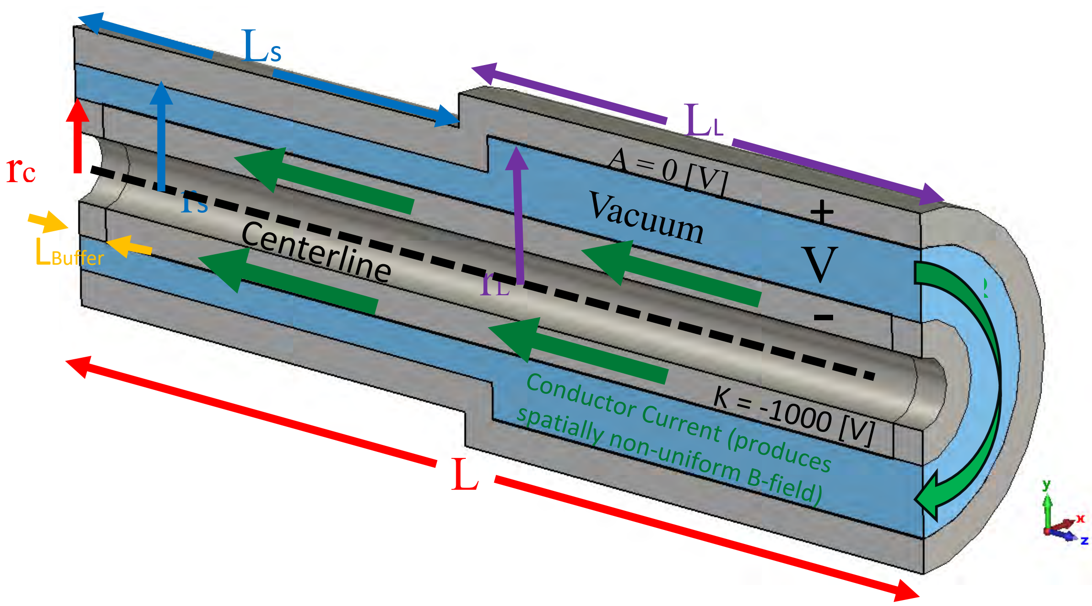

Figure 10: Model of the cylindrical step discontinuity simulation in CST-PS. Electrons are uniformly emitted across the cathode, and flow from left to right. A constant, spatially non-uniform magnetic field is applied.

The overall length of the cylinder, L, is 300 mm, with a cathode radius, r_c, of 20 mm, an anode radius, r_s, of 30 mm in the small gap region and 40 mm in the large gap region, r_L. The cathode explosively emits across its entire surface, with the exception of a 10 mm long buffer region on each end, at a threshold field of 100 V/m. Using the CST Magnetostatic solver and a 2.59 kA current drive on the cathode, a constant but spatially non-uniform magnetic field is calculated, and then applied to the CST-PS simulation. The length of the small and large anode radius sections, L_s and L_L, are identical and each equal to half the total length.

For the case shown in Figure 10, with electrons flowing left to right, the Brillouin flow current in the small AK gap region settles into a steady state current of ~0.28 A within 20 ns, as shown in Figure 11a. This represents the electron current passing through a 2D plane approximately half-way down the small anode radius section.

Using a similar monitor in the large AK gap region, however, measures a fairly stable current of 0.15 A after ~20 ns, but bunches begin to form at the anode radius step discontinuity and are detected at the 2D monitor at 80 ns. As Figure 11b shows, throughout the 200 ns simulation, the Brillouin flow current does not settle into a steady state value.

a) 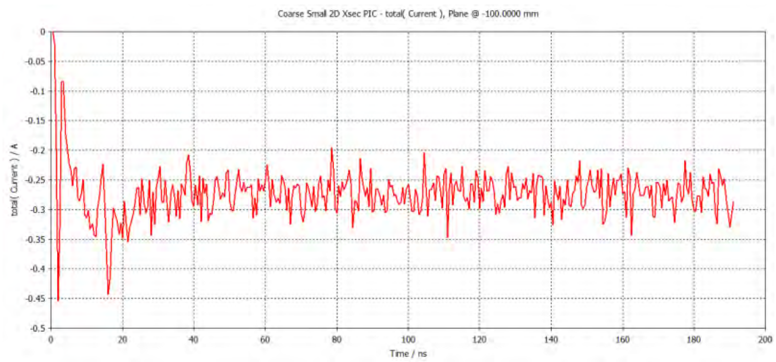

b) 

Figure 11: The electron current passing through a 2D cross section of the model, approximately midway along the **small** AK gap region (a) and the **large** AK gap region (b). The steady state hub current is ~0.28 A in the small gap. In the large gap, no steady state current is observed, and electron bunches form within the transmission line.

Using the cylinder geometry and magnetic flux ratio, we can calculate the Brillouin flow hub current from our recently developed analytic theory[1]. For the small and large anode radius regions, we find these currents to be 0.38 A and 0.099 A, respectively.

When the direction of current flow is reversed, such that electrons would flow right-to-left in Figure 10, no bunch formation is observed, and monitors in the small and large anode radius sections observe hub

[1] Y. Y. Lau, D. A. Packard, C. J. Swenson, J. W. Luginsland, D. Li, A. Jassem, N. M. Jordan, R. D. McBride, and R. M. Gilgenbach, "**Explicit Brillouin flow solutions in magnetrons,magnetically insulated line oscillators, and radial magnetically insulated transmission lines**", *IEEE Transactions on Plasma Science*, vol. 49, no. 11, pp. 3418–3437, Nov. 2021, doi: **10.1109/TPS.2021.3092606**.

currents of 0.4 A and 0.09 A, respectively. This more closely matches the hub currents predicted by our analytic Brillouin flow theory.

We have recently run convergence studies for these simulations and are currently writing up this work for publication.

3. Findings and Conclusions

Our initial MILO design was too small to be feasibly manufactured. Thermal management was also a concern. The OXMILO increases the feature sizes while maintaining high frequency operation. It was also designed for operation at only 10 kA and 300 kV, reducing the thermal concerns of higher current MILOs. When proven, these design features could benefit other MILO designs throughout the DoD.

4. Plans and Upcoming Events

In the next year, we will get our new Marx generator, REP, fully functioning and conduct resistive load tests. We will complete the design of the OXMILO and its extractor, and will fabricate and test it experimentally to compare to analytic and computational predictions of its performance. We will complete and publish the first phase of our analysis of Brillouin flow in a step-discontinuity, a problem relevant to the fundamentals of MILO operation (as well as many other magnetically insulated flows).

Two of the graduate students working on the project, Ryan Revolinsky and Emma Guerin, will attend the US Particle Accelerator School Microwave Sources course in Jan 2024.

5. Transitions and Impacts

We have discussed possible collaboration on a desired X-band source with 100’s MW output power and 20% bandwidth with David Robie, Dave Hidinger, and Braxton Bragg from Lockheed Martin. We discussed Phase II SBIR collaboration on an X-band antenna with Han Lin, Kiran Raj, and Michael Herndon from Epirus, and provided a letter of support to their Phase I effort. We have visited Collins Clark Technologies and had many discussions about pulsed power and HPM sources with its founder.

6. Collaborations

We have discussed visits to UM with Matt McQuage, Jack Chen, and Josh Pompeii at NSWCDD. We discussed the MADCAP source with Brad Hoff and David Simon at AFRL, confirming goals for the project and summarizing the work conducted at AFRL previously. Dr. Randy Curry and Dr. Greg Frye-Mason from Sandia National Lab visited our lab to discuss pulsed power collaboration and student employment opportunities.

7. Personnel

Principal investigator: Prof. Nicholas Jordan (3 months)
Co-investigator or Co-PI: Prof. Ryan McBride (0 months)

8. Students

Graduate Students: 3

Undergraduate Students: 2

9. Technology Transfer

We have discussed visits to UM with Matt McQuage, Jack Chen, and Josh Pompeii at NSWCDD. We discussed the MADCAP source with Brad Hoff and David Simon at AFRL, confirming goals for the project and summarizing the work conducted at AFRL previously.

10. Products, Publications, Patents, License Agreements, etc.

Publications resulting from this project:

Archival Publications

R. A. Revolinsky, E. N. Guerin, S. V. Langellotti, C. J. Swenson, L. I. Welch, D. A. Packard, N. M. Jordan, Y. Y. Lau, and R. M. Gilgenbach, "Dual-Frequency, Harmonic, Magnetically Insulated Line Oscillator," *IEEE Transactions on Plasma Science*, vol. 51, no. 7, pp. 1905–1916, Jul. 2023, doi: 10.1109/TPS.2023.3285509.

Conference Papers

N.M. Jordan, A.N. Brusstar, J. Chen, G.V. Dowhan, E.N. Guerin, S.V. Langellotti, D. Li, R.A. Revolinsky, A.P. Shah, R. Shapovalov, T.J. Smith, B.J. Sporer, C.J. Swenson, L. Tafoya, L.I. Welch, D.E. White, Y.Y. Lau, R.M. Gilgenbach, R.D. McBride, "HPM, Pulsed Power, and High Energy-Density Physics Research at the University of Michigan", Pulsed Power Conference, San Antonio, TX, June 2023.

R.A. Revolinsky, E.N. Guerin, S.V. Langellotti, C.J. Swenson, L.I. Welch, D.A. Packard, N.M. Jordan, Y.Y. Lau, and R.M. Gilgenbach, "Simulations and Experiments on the Dual-Frequency, Harmonic, Magnetically Insulated Line Oscillator", ICOPS, Santa Fe, NM, May 2023.

R.A. Revolinsky, E.N. Guerin, S.V. Langellotti, C.J. Swenson, L.I. Welch, D.A. Packard, N.M. Jordan, Y.Y. Lau, and R.M. Gilgenbach, "Magnetically Insulated Line Oscillators Designed with a Brillouin Flow Model ", Annual DE Science Technology Symposium (DEPS), San Antonio, TX, April 2023.

R.A. Revolinsky, E.N. Guerin, S.V. Langellotti, C.J. Swenson, L.I. Welch, D.A. Packard, N.M. Jordan, Y.Y. Lau, and R.M. Gilgenbach, "Experiments on a Dual-Frequency, Harmonic, Magnetically Insulated Line Oscillator", International Vacuum Electronics Conference, Chengdu, China, April 2023. [Keynote]

11. Point of Contact in Navy

Matt McQuage, NSWCDD, 10-2-2023

Fundamental Studies for Nanoscale Vacuum Electronic Emission Devices

Grant No. N00014-22-1-2483

Annual Report for Fiscal Year 2023

Period of Performance: October 1, 2022 to September 30, 2023

Prepared by:

Professor Ravi P Joshi, Principal Investigator
Texas Tech University
Department of Electrical and Computer Engineering
2500 Broadway MS 3102/Campus
Lubbock TX 79424
Tel: 806-834-7979
Email: ravi.joshi@ttu.edu

This work was sponsored by the Office of Naval Research (ONR), under grant number N00014 -22-1-2483. The views and conclusions contained herein are those of the authors only and should not be interpreted as representing those of ONR, the U.S. Navy or the U.S. Government.

Grant Number: N00014-22-1-2483
Date Prepared: January 30, 2024.
Project Title: New Anode Materials for High Lethality HPM Sources
Annual Summary Report: CY2022 – CY2023
Principle Investigator: Ravi P Joshi, 806-834-7979, Email: ravi.joshi@ttu.edu
Texas Tech University, Lubbock, TX 79424

Section I: Project Summary

1. Overview of Project

Abstract: The major goals and objectives of this research are to carry out fundamental research directly tied to the advancement of effective high lethality high power microwave (HPM) sources. It involves assessing and then developing anode materials that help reduce the number of adsorbates on the surface, as these can limit both the repetition rate of HPM sources and the pulse length.

This work is a joint collaborative effort between Texas Tech University (TTU) and the University of New Mexico (UNM). The work at TTU will involve Molecular Dynamics (MD), Monte Carlo and first principles Density Functional Theory (DFT) simulations to gauge incident electron penetration, the energy deposition, anode surface temperatures and the depth profile at the anode, quantification of the possible out-gassing, and desorption of surface adsorbates.

The overall goal is to reduce contaminants and surface desorption by using different anode materials, and especially including surface coatings.

Objectives: Texas Tech University in collaborative partnership with the University of New Mexico is working to explore new materials that reduce outgassing and desorption from the anode as it can ultimately lead to ion production in the interaction space of beam-driven high power microwave (HPM) devices. One of the central objectives is to understand and attempt to mitigate the nature of anode ion production due to stimulated and thermal desorption of neutrals. Appropriate collaborations with the University of New Mexico on a parallel effort would provide for meaningful comparisons between predictions and measured data for are a more comprehensive analysis. Careful modeling and simulation work (coupled with complementary experimental measurements at UNM for validation, model verification and fine-tuning) will enable progress towards this project objective.

Introduction: Simulations based on Molecular Dynamics have been carried out to specifically probe: (i) The possibility of a surface coating that is durable, resistant to degradation, and will resist surface adsorption. With much lower adsorption than the conventional anode materials, the scope for desorption will greatly diminish. (ii) The coating will also have the dual purpose of acting as a barrier to stop out-gassing from within the anode bulk region. (iii) A number of materials need to be compared for optimal performance. (iv) Since both outgassing and desorption are temperature dependent, it becomes important to use electrical parameters typical of an HPM system to model the surface heating at the anode. (v) Finally, it is relevant and useful to obtain the threshold temperatures for desorption for different species, such as carbon and related carbides, oxygen and related oxides, as well as nitrogen from surfaces.

Background: The dynamics of HPM devices during the radiation production phase are dominated by large electron currents periodically impinging on the anode surfaces, over relatively small areas. This leads to lead to energy deposition and heating of the anode, which then facilitates outgassing and desorption of surface contaminants. Here, our aim is evaluate appropriate material coating for suppressing outflow of neutrals by atomic simulations, by first understanding and quantifying the typical surface temperature under HPM operation. Then, possible desorption at the temperatures need to be evaluated.

2. Activities and Accomplishments

(A) Modeling Anode Heating for Electrical Parameters Characteristic of HPM Operation

Electron Penetration and Energy Deposition: In order to obtain the heating and temperature profiles, the energy deposition from an incoming electron swarm was simulated. Towards this goal, Monte Carlo techniques were used to track incident electrons upon their entry into copper, taken as a representative anode material. The electron scattering, interaction within the material, and energy losses based on energy-dependent mean free paths and stopping power were taken into account. Details of such Monte Carlo implementations was provided in previous monthly report, and is avoided for brevity.

A result showing the electron penetration range in copper as well as other metals such as gold and silver were obtained for purpose of verification. Our results were compared with data available in the open literature. Figure 1 shows a comparison of the electron range between the TTU results and available data in the literature [https://physics.nist.gov/PhysRefData/Star/Text/ESTAR.html]. Our predictions are seen to be in good agreement over different energies and also for various metals.

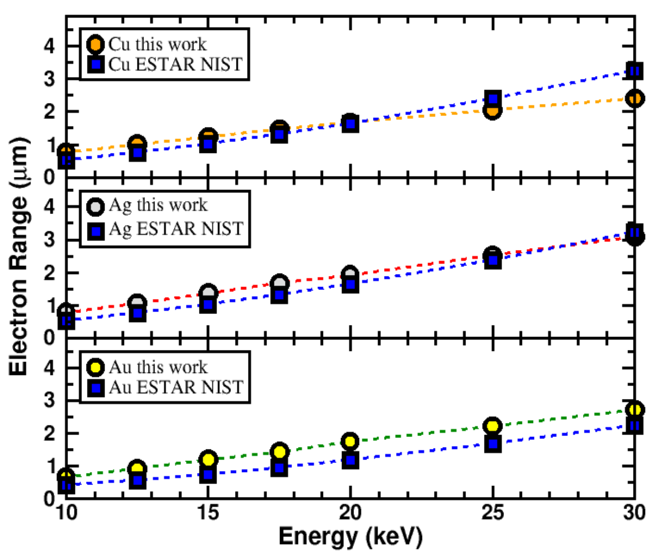

Figure 1. Simulation results obtained showing the electron range in different metals such as copper, gold and silver based on our Monte Carlo simulations as a function of incident electron energy. Our results were compared to available data in the literature [https://physics.nist.gov/PhysRefData/Star/Text/ESTAR.html] and seen to be in good agreement over different energies and also for various metals.

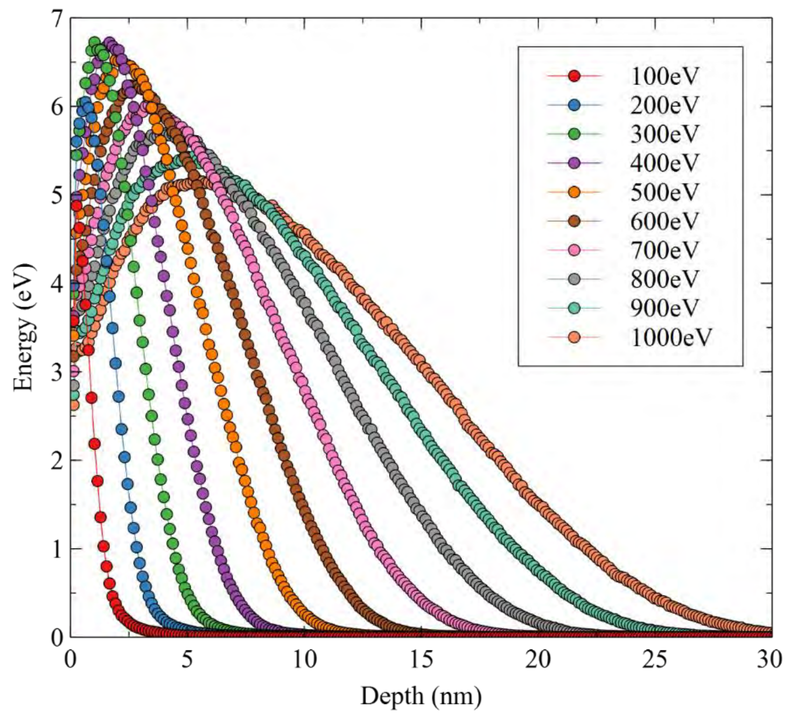

Figure 2. Simulation results obtained showing the energy deposition by an incident electron swarm. Different electron energies ranging from 100 eV to 1000 eV were simulated based on a kinetic Monte Carlo procedure in copper. Internal scattering, energy loss and stochastic mean-free paths were taken into account.

Next, a typical result of the energy dissipation within the copper anode due to incident monoenergetic electrons at various energies is given in Fig. 3. This is a representative result and shows that the TTU team developed the capability of calculating and predicting energy deposition in the target material as a function of depth.

Heating and Temperature Increases due to Energy Deposition: Next, the energy deposition was used as the input to time-dependent temperature calculations $T(z,t)$ as a function of depth (z). Based on the above energy dissipation, the power deposition density within the copper was obtained. This was the source term for material heating. The internal temperature profile was obtained through a solution of the one-dimensional time-dependent heat flow equation as

$$\rho \, C_p \, \partial T(z,t)/\partial t - k \, \partial^2 T(z,t)/\partial z^2 = S(z) \; . \qquad (1).$$

where ρ = material density, C_p = specific heat, k = thermal conductivity of the material, S = volumetric power dissipation in units of W/m^3, and T = temperature. Details of the numerical solution for the one-dimensional time-dependent heat flow equation were provided in a previous monthly report, and so are omitted here.

A simple textbook problem (example in the book by M. Necato Ozisik, Heat Conduction, Wiley and Son, New York, 1993, pp. 87-89) was used. In the problem, a 0.1 m long copper wire was assumed to have internal power density dissipation of 10^8 W/m^3 , with one end assumed to be insulating (i.e., $dT/dz = 0$) and the other end held at 0 K. The result shown in Figure 3 was obtained with $S = 10^8$ W/m^3, a 0.1 m long copper bar, $\rho = 8.96 \times 10^3$ Kg/m^3, C_p = 386 J/kg/K, k = 389 W/m/K. The analytic result is also given at different times, and the numerical predictions match the analytic solution very well. This validates our numerical implementation.

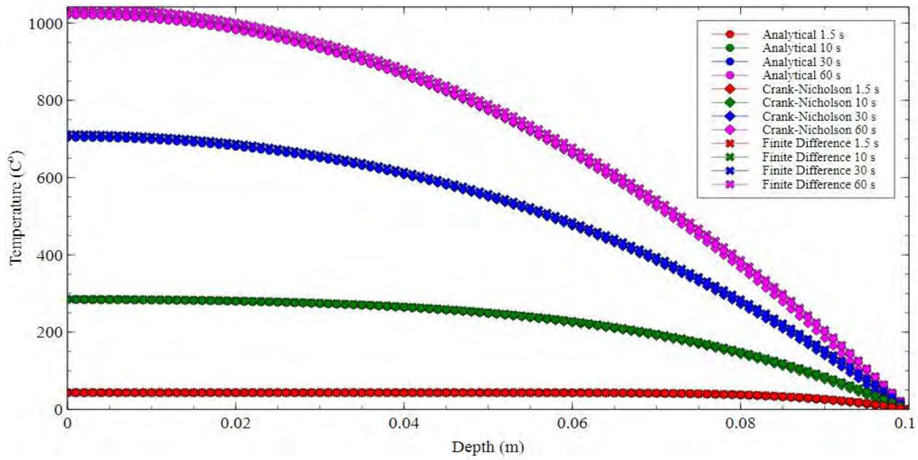

Figure 3. Simulation results obtained showing good agreement between numerical calculations and an analytic solution. This was aimed at validation of the numerical implementation.

Next, the temperature rise and internal heating were probed for situations of actual electron beam irradiation. The parameters for the heating simulation were modeled after the experimental setup at UNM. Thus, electrons accelerated by a 30 kV cathode-to-anode bias was chosen, with a current of 10^4 A incident on the anode. The anode diameter was taken to be 4 inches based on details furnished by Dr. Salvador Portillo at UNM. The length of the copper anode was taken to be 20 micrometers, at an initial temperature of 300K. The time-dependent current from the UNM experiment is given below in Figure 4. Though heating was not measured experimentally, at least the beam parameters (flux, energy, cross-sectional area, etc.) used in our simulations exactly reflected those of a real operational system. The time-dependent variations in incident electron flux were included in the simulations based on the temporal behavior of the beam current. The dissipated power density in copper for the above parameters was determined from Monte Carlo simulations, and the temperature profile versus depth into the copper anode is shown in Figure 5.

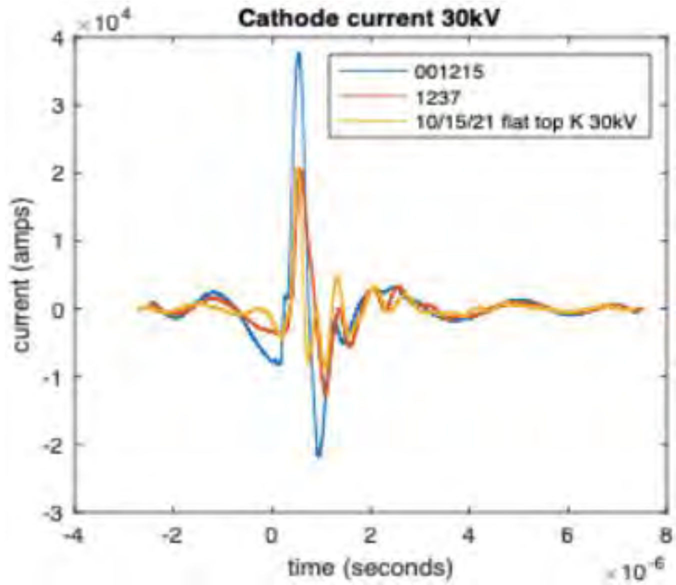

Figure 4. Data obtained from UNM for cathodes fired at 30 kV with 1 cm anode-cathode gap. The diameter of the cathode was 1 inch and the diameter of the anode was 4 inches, though not all of the anode was hit by electrons.

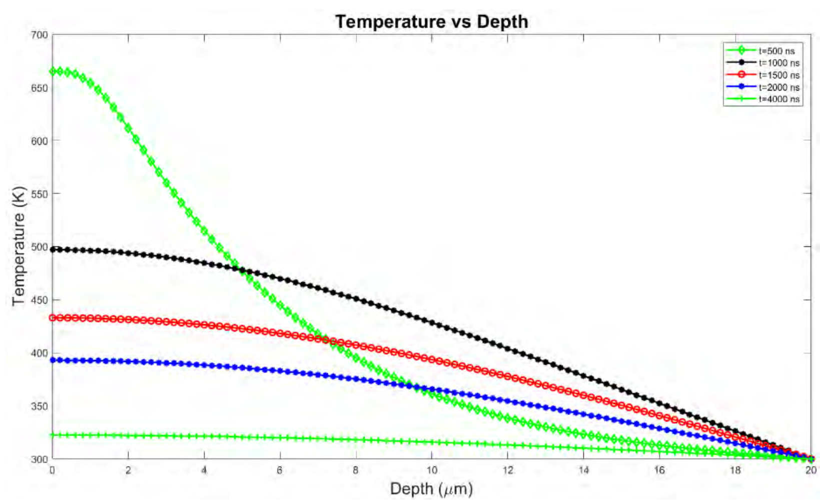

Figure 5. Temperature profiles in a copper anode up to a depth of 20 microns due to the power dissipation by the incident electron beam with temporal characteristics given in Figure 4. The beam was on for about 650 ns, and the highest temperature at the surface was predicted to be about 660K.

Results for the internal temperature rise caused by the incident swarm with characteristics shown in Figure 8 are presented in Fig. 9. Temperature profiles are shown for different times of 500 ns, 1000 ns, 1500 ns, 20000 ns, and 4000 ns. Since the incident electron flux was operative mainly over the first ~650 ns time interval, the heating was also active and on-going over this timeframe. Thus, the temperatures increased up to ~650 ns. Beyond this time, the copper material began to cool gradually as the incident flux was practically turned off. *The highest temperature of about 660K is predicted for this external electron beam pulse within the copper anode.*

(B) Molecular Dynamics Simulations for Surface Desorption in Copper

Simulations were performed for desorption of surface species from copper. For this purpose Molecular Dynamics simulations were carried out at various temperatures for copper with a few species at the surface. The goal was to predict the threshold temperature above which a particular species would not be able to remain at the surface and would be desorbed. However, as a separate and independent confirmation of the MD result, the cohesive energies (ΔE) for various species attached to a copper surface were obtained from Density Functional Theory (DFT) calculations. The requisite temperature (T) to break the attachment and release the species could simply be calculated as: $k_B T = \Delta E$. The values obtained from DFT are given in Table 1 below, with C_2/Cu having the most negative level and thus, implying a very strong bonding of carbon molecules to copper. The weakest bond (and hence easiest to break) is predicted to be for carbon dioxide on copper (CO_2/Cu system).

Table 1. Calculated cohesive energies of various molecules and adsorbates on copper host.

System	Cohesive Energy	Work Function
Clean Cu	-	4.40 (4.48)
C_2/Cu	-3.202	4.86
N_2/Cu	-0.316	5.59
CO_2/Cu	-0.044	4.57
NO_2/Cu	-2.694	6.55

Based on the above table, CO_2 molecules on Cu are expected to driven off first at an energy ("E") of 44 meV. This corresponds to an equivalent temperature ("T") of about 650K. The equivalent temperatures for the dissociation of the other adsorbates given in Table 1 work out to the values enumerated in Table 2

Table 2. Equivalent temperatures for the various species given in Table 1.

System Name	DFT Predicted Temperature Dissociation (°K)	Wavelength(nm)
C_2	37130	387.21
N_2	3481	3923.57
CO_2	650	Heating
NO_2	30741	460.225

The temperatures required for dissociation in all the species listed, except for CO_2, is excessive and well over the melting point of copper. This implies that perhaps very short duration laser pulses might need to be used for driving off the species.

Molecular Dynamics simulations were also carried out to probe the dissociation of CO_2 adsorbates this species is the easiest to dislodge based on the binding energies of Table 1. A copper slab was constructed with a smattering of CO_2 molecules at the surface. The top five layers were kept at 650 °K, and the bottom copper layers at the 300 °K ambient level. Heat exchanges were allowed between the top layers and the rest of the copper atoms at the lower depths. A snapshot of the system at 700 ps is shown in Figure 6. Though most of the CO_2 molecules are intact and lie at the top, some can be seen getting dislodged, and floating way from the copper surface. A later snapshot after about ~1 ns in Fig. 7 shows a lot of the molecules to have left the surface. *Thus, MD results are in agreement with the DFT simulation results at 650K*.

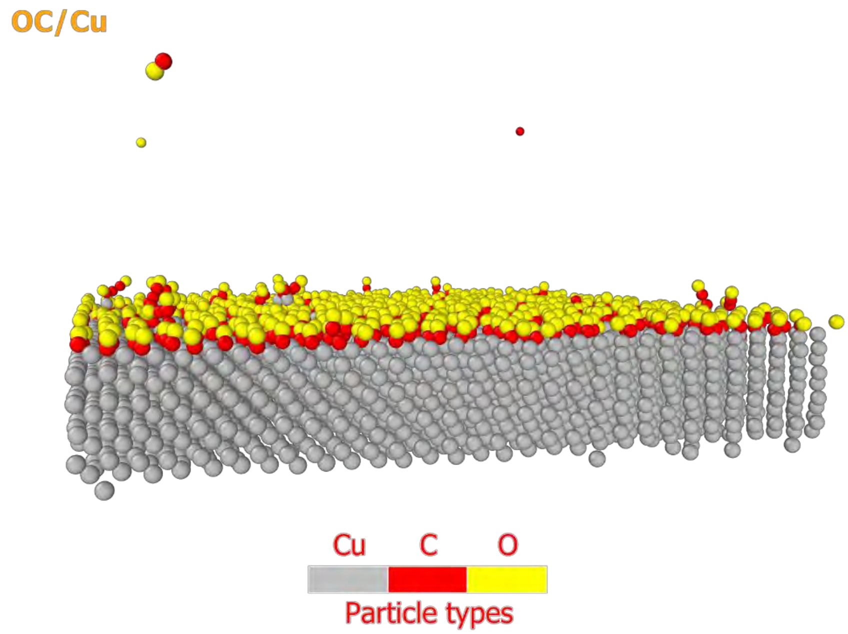

Figure 6. A 700 ps snapshot showing a copper slab covered with CO_2 molecules. Though most of the CO_2 molecules are intact and lie at the top, some can be seen getting dislodged, and floating way from the copper surface.

The surface smoothness was also probed as a potential role in influence out-gassing. A rectangular copper structure with six pillars and five voids was constructed as shown in Figs. 8 and Fig. 9 (alternate view). The red spheres in the two figures denote the copper atoms, while the blue spheres represent the hydrogen atoms included at random sites inside the copper structure. The structure was kept at a temperature of 700K and initial simulation runs performed to obtain a stable configurational set up. To begin with, a hundred hydrogen atoms were placed in the copper structure. Thus, mathematically their number was given as: $N_0(t=0)=100$. The population of hydrogen remaining in the copper material over time obtained from MD simulations is shown in Figure 10. As evident, the population reduces faster with the voids.

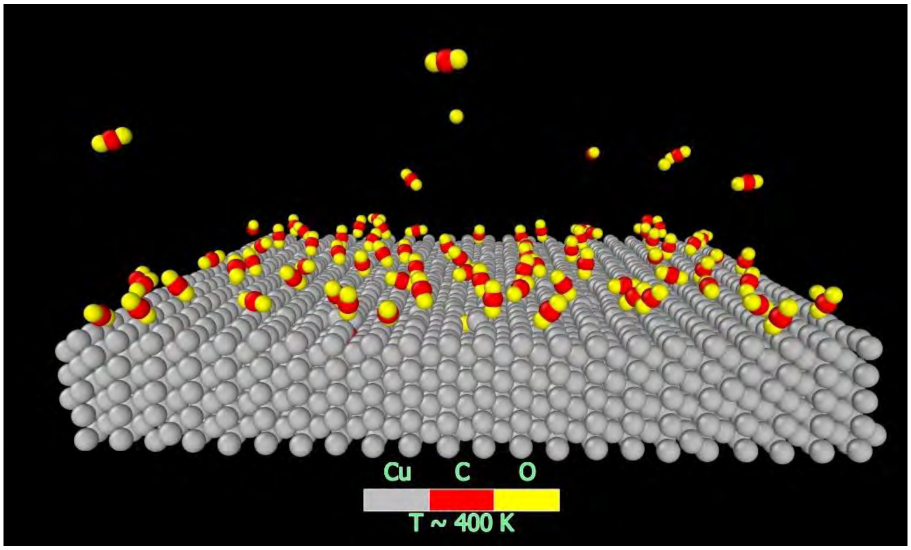

Figure 7. A ~1ns snapshot showing a copper slab with CO_2 molecules. The figure shows a lot of the CO_2 molecules to have left the surface.

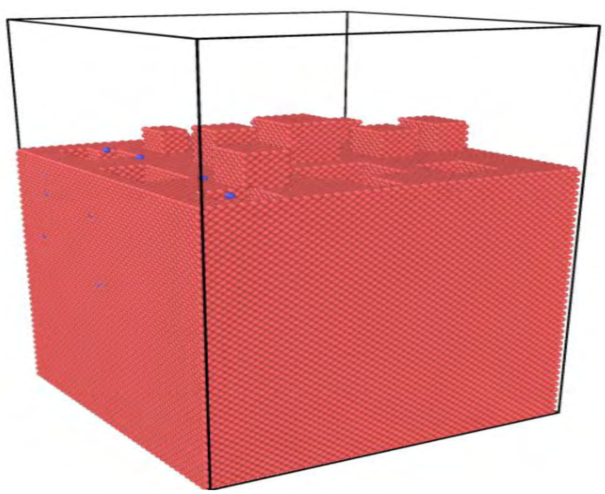

Figure 8. Three dimensional copper structure with hydrogen atoms chosen for outgassing simulations. The red spheres represent copper, and the blue spheres denote hydrogen atoms.

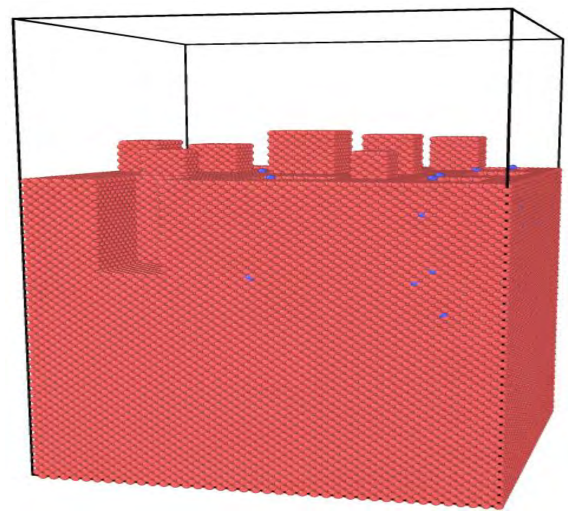

Figure 9. Alternate view of the simulated copper structure with a rough surface.

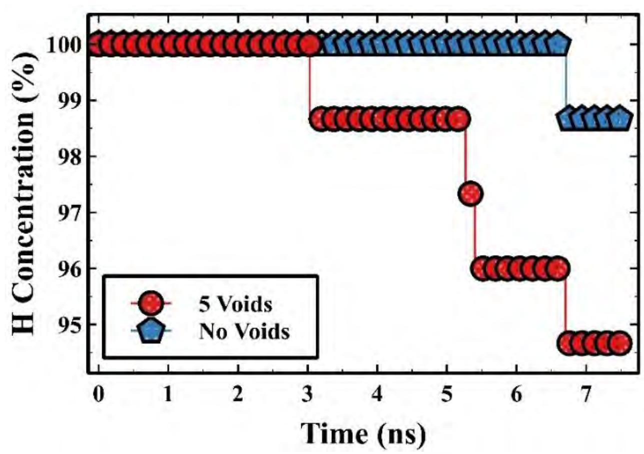

Figure 10. Time-dependent population of hydrogen atoms in the copper structure.

Thus, an ideal periodic material with a clean and smooth surface is not predicted to lead to as much outgassing. *The simulation results clearly underscore the importance of polishing the surface and obtaining as smooth a surface as possible.* Furthermore, our simulation results are in good agreement with the observed reductions in outgassing with smoothened surfaces, as reported by Luo et al. [Y. Luo, X. Wu, K. Wang, and Y. Wang, "Comparative study on surface influence to outgassing performance of aluminum alloy," Applied Surface Science **502**, 144166 (2020)].

(B) Simulations for Platinum Coating

Platinum Coating as a Barrier to Trap Outflow from Anode Bulk: A central goal of this project is to try and reduce outgassing from anodes in HPM devices. There can be two potential sources for outgassing: (i) various gaseous species (e.g., dissolved or trapped hydrogen atoms within the bulk anode) which would migrate and emerge upon anode heating during HPM device operation. (ii) Surface adsorbates which could disintegrate or desorb as hot electrons slam against the anode surface.

We have tried using a Platinum capping layer on top of the anode metal to stop the gas contained within the bulk host from coming out. For this, Molecular Dynamics simulation were performed to track the movement of trapped hydrogen atoms, to probe if a surface coating layer could effectively act as a barrier and stop the emergence of the gas.

Platinum was chosen as it is known to be an inert, noble metal, and not likely to form oxides easily. The latter would be beneficial since a potential source of oxygen is through oxide bond breakage at the surface from incident high energy electrons. Without much oxide formation, this source of oxygen in the HPM system would then be avoided, given the lack of oxides to begin with.

Furthermore, adsorption energies of oxides on various metals were computed based on Density Functional Theory (DFT), and the results obtained are given in Table 3 below. The values listed are for Aluminum, Nickel, Platinum, and Rhodium metals. It is, however, significant that the Pt-O adsorption energy is relatively weak. This suggests that if Platinum were to be used as a coating, it would be easy to get rid of the oxide and blow away the oxygen through laser surface treatment.

Table 3. Calculated adsorption energies of oxygen on different metals.

Bond	Adsorption Energy (eV)
Al-O	-2.740
Ni-O	-1.788
Pt-O	-0.502
Rh-O	-1.228

It is, however, significant that the Pt-O adsorption energy is relatively weak. This suggests that if Platinum were to be used as a coating, it would be easy to get rid of the oxide and blow away the oxygen through laser surface treatment.

First principles *ab-initio* MD calculations were carried out for aluminum (chosen as the anode host) with a coating of platinum. The Al atoms are shown in grey, while the hydrogen atoms are represented by the smaller red spheres. The Pt atoms are shown as blue spheres. The combined Al-H-Pt structure after running the MD simulations for a time interval of 4500 fs is given in Fig. 11. *The result shows that all of the hydrogen atoms remain within the host Al material and do not cross or escape the surface. Thus, a single*

Pt layer at the top of the aluminum (which would be a surface coating in practice) would also prevent the hydrogen atoms from leaving the aluminum host.

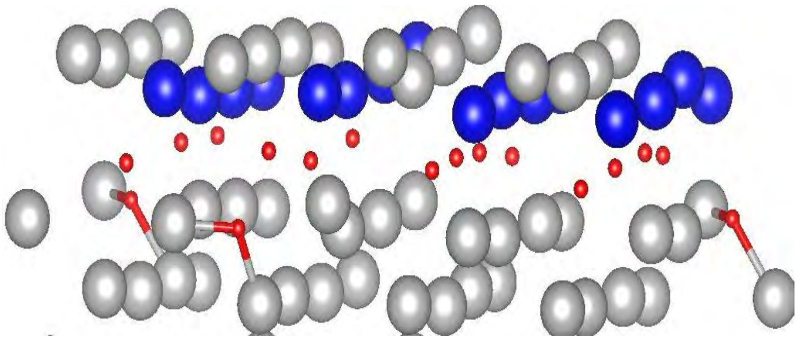

Fig. 11. First-Principles Molecular Dynamics simulations of Al (grey spheres), H (red spheres) mono-sublyer, and Pt (blue spheres) mono-sublayer system at 300 K. The structure after a duration of 4500 fs from the initial starting time is shown. No H atom outgassing or escape from the surface is predicted.

<u>Adsorption and Cleaning Platinum Surface</u>: Having shown the effectiveness of Pt coating as a barrier layer in trapping gas that may be in the anode volume, the next set of simulations were aimed at probing the surface Pt surface properties. This is important to determine whether the adsorbate (e.g., oxygen atoms) could be made to leave the surface upon a temperature increase, thus cleansing the surface of the oxygen contaminant.

The initial configuration and placement of oxygen is shown in Fig. 12(a) for copper and Fig. 12(b) for platinum. In each case the starting oxygen contaminant atoms were chosen to be at locations above the copper platinum surfaces. Results from a final set of snapshots taken after running the simulations for 40 ps are shown on Figs. 13(a) and 13(b) at the same 1100K temperature for comparing Cu with Pt. In Fig. 13(a) for copper, the oxygen atoms can be seen to penetrate up to 6 monolayers into the Cu material. *By comparison, some oxygen atoms still remain free, while the majorty, though attached to the surface, do not penetrate into the platinum.*

The above set of results clearly show the advanatge of Pt in resisting adsorption, and also in preventing deep penetrations into the host. Consequently, it is very likely that surface laser treatments could easily expunge any of the adsorbed oxygen from Pt. However, for copper, the oxygen may remain, especially if the oxygen has penetrated deeper into the host. Such residual oxygen in copper would then lead to strong outgassing during HPM device operation.

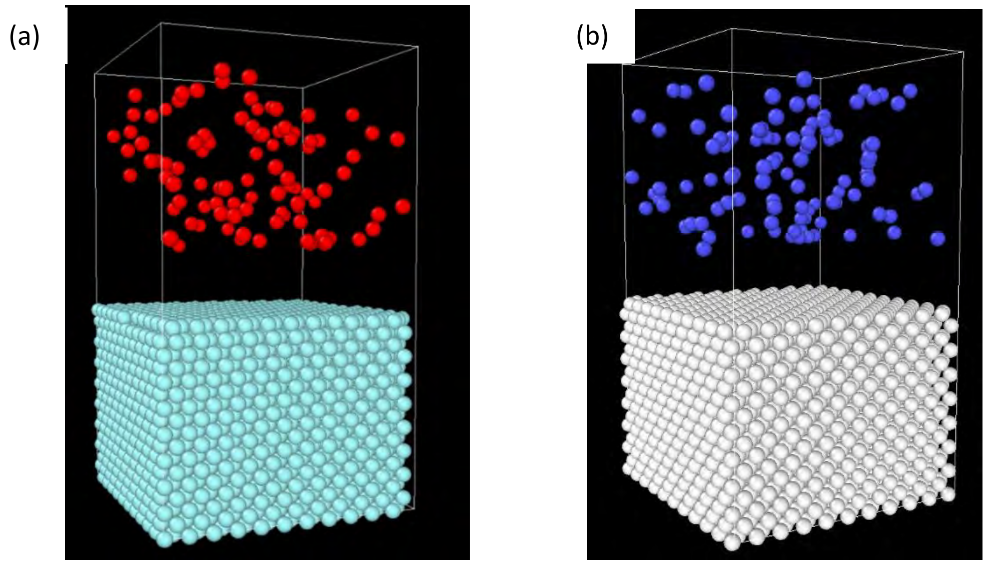

Fig. 12. The initial configuration and placement of oxygen atoms for LAMMPS-based Molecular Dynamics (MD) simulations. (a) Oxygen atoms (red spheres) initially placed above a copper (light green spheres) and, (b) oxygen atoms (purple) placed above platinum (white spheres) slab.

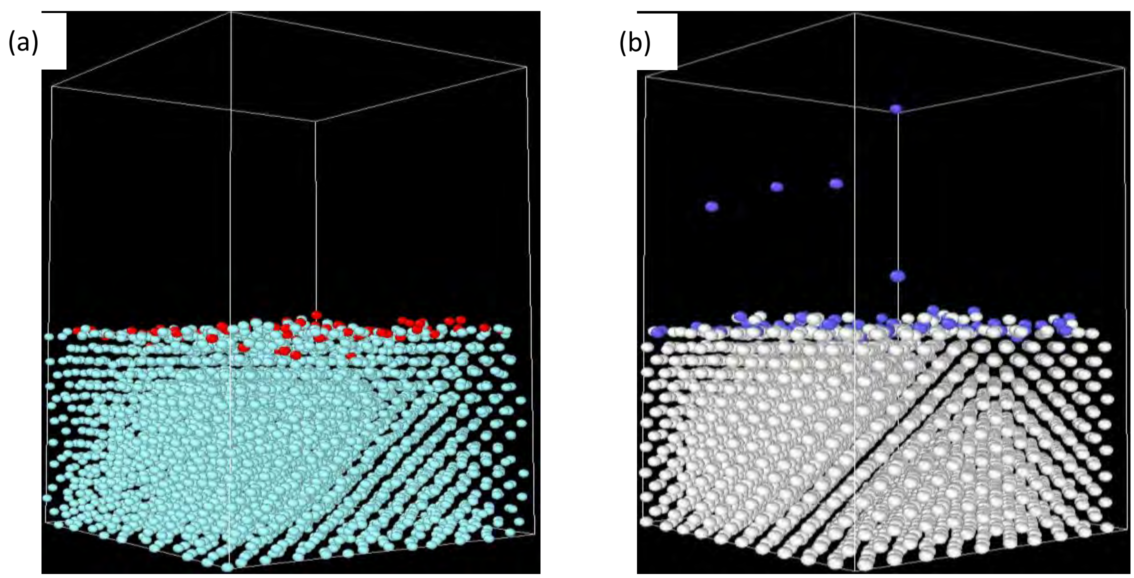

Fig. 13. A 40 ps snapshot of the configuration and placement of oxygen atoms from MD simulations. (a) Oxygen atoms can be seen to penetrate up to 6 monolayers into the Cu material. (b) Partial adsorption of oxygen atoms with a few oxygen atoms still unabsorbed and floating above the platinum surface. Of the adsorbed oxgen atoms, all are seen to stay at the surface with negligible penetration.

3. Plans and Upcoming Events

(a) Plans to carry out simulations for surface temperature and its depth profile based on the A6 magnetron data provided by Prof. Schamiloglu. That should give us realistic predictions for anode heating in a practical HPM system.

(b) Molecular Dynamics simulations to predict the temperature for blow-off of various surface adsorbates. This should yield a mapping between the requisite surface temperatures needed to get rid of different adsorbates. So far, we have obtained temperatures to drive off both CO and CO2 was calculated to be around 650K.

(c) Work in collaboration with Dr. Portillo to simulate his XPS experiments as that data becomes available, for better understanding the surface characteristics.

(d) Complete simulations for Platinum as a surface coating up to longer times to show definitive advantages of that material in blocking out-gassing, and thus helping HPM operation. It would be useful to have experimental data for verification from the University of New Mexico for a more meaningful comparisons and conclusions.

4. Transitions and Impacts

None.

5. Collaborations

Dr. Mahdi Sanati, Physics Department, Texas Tech University

Dr. Salvador Portillo, Electrical Engineering, University of New Mexico

6. Personnel

Principal investigator	Ravindra P. Joshi
Co-investigator or Co-PI	Mahdi Sanati, Physics Department, Texas Tech University
Business Contact	Amy Cook, TTU Associate Vice-President for Research
Team Members	None others
Subs	None

7. Students

Yagnya Pokral – PhD student

Yasir Iqbal – PhD student

8. Technology Transfer

None.

9. Products, Publications, Patents, License Agreements, etc.

<u>Archival Publications #1</u>

a. Article Title: Importance of Surface Morphology on Secondary Electron Emission: A Case Study of Cu covered with Carbon, Carbon Pairs, or Graphitic-like Layers
b. Journal: Scientific Reports (Nature Publishing Group)
c. Authors: L. Diaz, A. A. Karkash, S. Alshahri, R. P. Joshi, E. Schamiloglu, and M. Sanati
d. Keywords: Electron emission, Metal emitters, surface coverage by carbon
e. Distribution Statement: Unrestricted distribution
f. Publication Status: Published
g. Publication Identifier Type: DOI https://doi.org/10.1038/s41598-023-34721-8
h. Publication Identifier: https://doi.org/10.1038/s41598-023-34721-8
i. Publication Date: May 2023
j. Volume: 13
k. Issue: 5
l. First Page Number: 8260
m. Publication Location: New York, USA
n. Acknowledgement of Federal Support? (Yes/No): Yes
o. Peer Reviewed? (Yes/No): Yes

Archival Publications #2

a. Article Title: Simulation Studies of Secondary Electron Yield With Electron Transport From Cu (110) Surfaces Containing C_2, N_2, CO_2, or NO_2 Adsorbates
b. Journal: Frontiers in Materials
c. Authors: M. Maille, N. C. Dennis, Y. M. Pokhrel, M. Sanati, and R. P. Joshi
d. Keywords: SEY, Surface adorbates
e. Distribution Statement: Unrestricted distribution
f. Publication Status: Published
g. Publication Identifier Type: DOI
h. Publication Identifier: doi: 10.3389/fmats.2023.1145425
i. Publication Date: March 2023
j. Volume: 11
k. Issue: 11
l. First Page Number: 1145425
m. Publication Location: New York, NY, USA
n. Acknowledgement of Federal Support? (Yes/No): Yes
o. Peer Reviewed? (Yes/No): Yes

There is currently one other journal article under review.

Y. Pokhrel, Y. Iqbal, M. Sanati, and R. P. Joshi, "Assessing Surface Cleaning to Remove Adsorbates," submitted for publication.

In addition, the following presentations were made at the International Conference on Plasma (ICOP-2023) in Orlando in Santa Fe. This talk at the conference was within the May 21-25, 2023 period. The specific details are:

C. Dennis, Y. Pokhrel, A. Karkash, M. Mille, S. Portillo, M. Sanati, R. P. Joshi, "Selecting Incident Electron Pulse Parameters for Effective Surface Cleaning to Remove Adsorbates," Int'l Conference on Plasma Science (ICOPS), Santa Fe, May 21-25, 2023.

10. Point of Contact in the Navy

None

Distributed Coordination of Aerial Swarms for High-Gain Wireless Transmission

Grant No. N00014-20-1-2389

Annual Report for Fiscal Year 2023

Period of Performance: October 1, 2022 to September 30, 2023

Prepared by:

Dr. Jeffrey Nanzer, Principal Investigator
Associate Professor, Electrical and Computer Engineering
Michigan State University
428 S Shaw Lane, Room 2120 Engineering
East Lansing, MI 48824
Tel: (517) 432-8089
Email: nanzer@msu.edu

This work was sponsored by the Office of Naval Research (ONR), under grant number N00014-20-1-2389. The views and conclusions contained herein are those of the authors only and should not be interpreted as representing those of ONR, the U.S. Navy or the U.S. Government.

Grant or Contract Number: N00014-20-1-2389
Date Prepared: January 30, 2024
Project Title: Distributed Coordination of Aerial Swarms for High-Gain Wireless Transmission
Annual Summary Report: FY23
Principle Investigator: Jeffrey Nanzer, 517-432-8089, nanzer@msu.edu,
Michigan State University, 428 S Shaw Lane, Room 2120 Engineering, East Lansing, MI 48824

Section I: Project Summary

1. Overview of Project

Abstract: This report provides a summary of progress made towards distributed synchronization of separate wireless systems for distributed beamforming operations. Distributed beamforming requires accurate synchronization of the electrical states of the nodes in a distributed array to ensure that transmitted signals arrive sufficiently aligned at the intended destination so that the signals add constructively, yielding significant increases in signal power at the destination. In this report, we summarize the objectives of this effort and report on advancements made in the areas of decentralized electrical state coordination, distributed localization, and experimental implementations of the concepts developed in this effort.

Objective: In this effort, we will develop novel decentralized coordination techniques for high-gain transmission from swarms of hundreds of nodes and evaluate the possibilities of achieving high-gain signal transmission using existing commercial off-the-shelf (COTS) microwave technologies. In particular, we will investigate new techniques for the coordination of large arrays using decentralized consensus algorithms based on physical-layer coordination of array element location, frequency, phase, and time. We will assess the feasibility of achieving high-power transmission under realistic system-level constraints, such as coordination errors, noise, array motion, amplifier efficiencies, and beam steering errors, among others. The results of this effort will inform future high-gain microwave transmission concepts and identify any technology areas for future development to achieve greater capabilities than COTS technologies can provide. The proposed research directions are two-fold:

- Develop a distributed approach enabling the coherent coordination of the spatio-electrical states of arrays consisting of hundreds of nodes, investigate the possibilities of using distributed optimization for high-gain microwave signal transmission, and demonstrate distributed signal transmission in a scaled testbed.
- Develop system design rules for achieving specified high-gain signal requirements, determine bounds on achieving high levels of coherent gain given system specifications, provide notional designs based on COTS technologies, and identify areas for future technology development.

Introduction: Current and future wireless applications, including sensing, communications, and high-power transmission, have driven the need for continual increases in transmitted signal gain. However, the ability to achieve high-gain wireless transmission of microwave signals is restricted by the traditional platform-centric model used to develop wireless systems, where single, large platforms are limited by aperture size, device power handling and efficiency, and heat dissipation, among other factors. Achieving increases in signal gain under the current platform-centric model requires redesigns of devices, apertures, or entire systems, an approach that is not only costly but time-consuming. To overcome these platform-centric challenges, we propose a novel approach to high-gain microwave signal transmission using distributed, scalable arrays of small, low-cost platforms, each with individually low-power transmitters. In particular, coordinating separate wireless systems to create a coherent distributed phased array can yield dramatic system-level gains that cannot feasibly be achieved with a single platform, or even with non-coherent signal coordination on multiple platforms. These benefits include transmit power gains proportional to the number of platforms squared, significant spatial diversity affording robustness to interference and failures, and the ability to directly scale capabilities by simply adding or removing nodes in the array. The ultimate level of flexibility is achieved in an open-loop array, where the nodes self-align without using feedback from the target location. Whereas closed-loop distributed arrays are possible with signal inputs from the target, such approaches are limited in that the array can only direct signals back to the point of the emanating signal. In contrast, open-loop distributed phased arrays can arbitrarily steer beams to any desired angle.

Background: Achieving coherent transmission in distributed arrays requires coordination of the spatio-electrical states of the elements in the array; our group has pioneered efforts in developing technologies for high-accuracy coordination for distributed beamforming in small arrays of 2-4 platforms. Our group has extensive experience developing open-loop distributed phased arrays through our prior efforts developing and demonstrating critical technologies enabling fully open-loop coherent distributed transmission, which have demonstrated the feasibility of achieving and maintaining sufficient phase stability between separate platforms. In prior efforts, a high-accuracy microwave ranging technique using a novel spectrally sparse waveform achieved sub-mm range accuracy and was used to experimentally demonstrate the first open-loop coherent distributed transmission. Other efforts developed a novel one-way wireless frequency locking approach, which was used to demonstrate the first fully wireless open-loop distributed phased array. Current efforts are focused on building cognitive-enabled adaptive coordination algorithms that are robust to changing environmental conditions. The outcome of these efforts is that the basic coordination technology to achieve distributed phase coherence with small array sizes has been largely proven. The challenge for high-gain microwave applications is in creating a framework amenable to coordinating hundreds of nodes or more. The proposed effort is, to our knowledge, the first to investigate approaches to implementing distributed coordination in large-scale arrays of tens to hundreds of nodes, and to explore the implications of array scalability.

2. Activities and Accomplishments

In this reporting period, we made significant progress in the development of technologies and techniques for wireless pico-second time synchronization, decentralized time synchronization, and distributed beamforming. Specifically, in this reporting period we:

- Refined our previously reported time synchronization approach to obtain accuracies on the order of 2 ps and internode range errors on the order of 0.5 mm;
- Demonstrated distributed beamforming using wireless time synchronization, demonstrating wideband operation;
- Implemented wireless time synchronization in our previously developed decentralized consensus averaging approach using software-defined radios.

Our results on these topics are described in the following.

2.1 High-Accuracy Internode Time Synchronization and Internode Range Measurement

In a distributed coherent antenna array application, each element in the array must align its time, phase, and frequency in order to ensure coherent reception at the target location. In this work, we utilize a real-time high-accuracy time transfer technique that relies on a spectrally sparse two-tone waveform and a two-stage delay estimator to obtain high-accuracy internode delay measurements and compensate for internode time offset and internode range. In general, the local time at each node in a system of N wireless nodes with independent clocks can be modeled as $T_n(t) = t + \delta_n(t) + \nu_n(t)$, where $\delta_n(t)$ is a time-varying offset from the global true time, and $\nu_n(t)$ is a zero-mean time-varying noise term due to device noise from all components in the timing chain. The goal of timing synchronization is to determine the offset $\delta_n(t)$ of each node. For simplicity, it may be assumed that node 0 has the true time; thus, we must correct offset relative to node 0, i.e., $\Delta_{0n} = \delta_0 - \delta_n$, where $\delta_0 = 0$.

To estimate this offset, a two-way time transfer (TWTT) technique is used based on the assumptions that the channel is quasi-static during the synchronization epoch and the systems are syntonized (aligned in frequency) (Fig. 1). The synchronization process begins when node n transmits a ranging waveform to node 0 which it locally timestamps at $T_n(t_{\mathrm{TX}n})$ which we denote as $T_{\mathrm{TX}n}$ for brevity. Node 0 will timestamp the received waveform with its local time $T_{\mathrm{RX}0}$ and will then respond with another locally timestamped ranging waveform at $T_{\mathrm{TX}0}$ after some arbitrary processing delay τ_{proc}. Finally, node n will timestamp the received waveform at $T_{\mathrm{RX}n}$ and estimate its offset Δ_{0n} using

$$\Delta_{0n} = \frac{(T_{\mathrm{RX}0} - T_{\mathrm{TX}n}) - (T_{\mathrm{RX}n} - T_{\mathrm{TX}0})}{2}$$

Based on this, the relative timing can also be determined by summing the differences of the two pairs of timestamps, yielding an estimate of the internode distance, which is needed for localization.

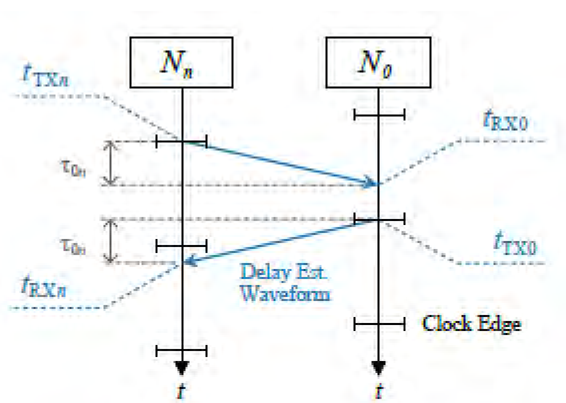

Fig. 1. Timing diagram for two-way time transfer distributed array. Here, node N_n initiates time transfer with the primary node, N_0 and the delay estimation waveform is transmitted between the nodes with timestamps saved at each transmission and reception.

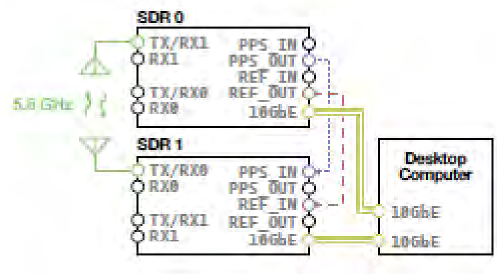

Fig. 2. Schematic diagram of the two-way time-transfer system. Nodes 0 and 1 are represented by two software-defined radios SDR 0 and SDR 1, respectively, both controlled by a single PC running GNU Radio software**.**

The block diagram of the experimental two-way time- transfer circuit is shown in Fig. 2. The system used wireless time transfer with a cabled frequency reference between two software-defined radio (SDR) nodes (Ettus Research X310 SDRs with UBX-160 daughterboards). Both two-tone wave- forms and the more common LFM waveform were used to determine relative accuracy. The two SDRs were connected to two L-Com 8-dBi 2.3–6.5 GHz log-periodic antennas through 6-ft coaxial cables and two Analog Devices HMC427A control transfer switches. The antennas were placed 90 cm apart. The SDRs were controlled through GNU Radio software. A two- tone waveform with pulse duration of 10 µs and 5.8 GHz carrier frequency was exchanged between the two nodes 0 and 1. The experiment consisted of two sub-experiments: measurements of the two-way propagation delay were taken while (1) varying the SNR from 6–36 dB in 3-dB increments at 40 MHz bandwidth, and (2) varying the bandwidth of the two-tone waveform (i.e., the tone separation) and LFM waveform from 5–50 MHz in 5 MHz increments with the SNR fixed at 30 ± 1 dB.

The error of the estimate of the distances between nodes was calculated from one set of measured time delays between two selected nodes. The inter-node distance d_{01} between nodes 0 and 1 was computed from the relation $d_{01} = ct_f$ where t_f is the time-of-flight with bias. Either the tone bandwidth or SNR may be used to improve the accuracy. Two experiments were conducted: one varying the SNR with a fixed bandwidth of 40 MHz; and one varying the bandwidth with a fixed SNR of 30 +/-1 dB. The standard deviation was computed for each data point over one minute of data with a measurement interval of 500 ms. The results versus SNR are shown in Fig. 3. The standard deviation decreased as the SNR increased, reaching a minimum of 0.5 mm at 36 dB for the two-tone waveform, which is equivalent to a timing accuracy of 1.67 ps. Fig. 4 shows the results versus bandwidth, showing a similarly decreasing accuracy as the bandwidth increases, and a significant improvement when using the two-tone wave- form compared to the LFM. Also shown on each figure are the boundaries at which the performance supports a given distributed beamforming frequency. It can be seen that the two-tone approach supports distributed beamforming at frequencies extending up to 40 GHz.

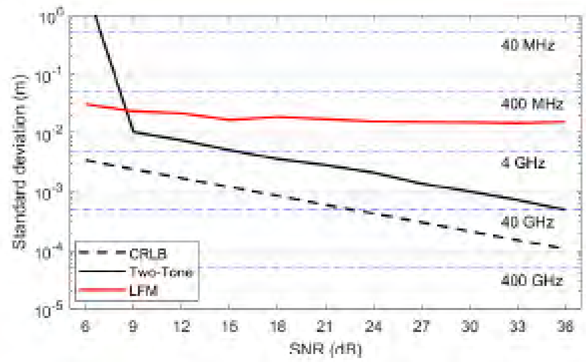

Fig. 3. Accuracy of time ranging for wireless time transfer measured at SNR 6–36 dB with +/-1 dB tolerance with a bandwidth of 40 MHz. The accuracy is the standard deviation of the inter-node distance computed in meters, and the CRLB is the theoretical lower bound using (1) and (2). The horizontal lines represent the beamforming frequency.

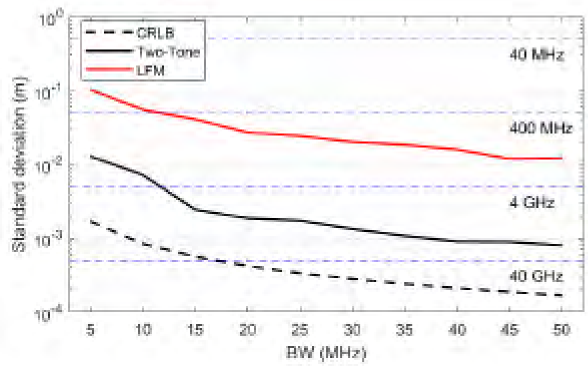

Fig. 4. Accuracy of time ranging for the system as a function of the waveform bandwidth. The standard deviation of the distance was calculated in meters over a bandwidth range of 5–50 MHz in 5 MHz increments at 30 +/-1 dB SNR. The horizontal lines represent the beamforming frequency.

2.2 Distributed Wideband Beamforming Demonstration

The timing and localization approach was next implemented in a two-element distributed beamforming system. To correct for signal processing, cable, and antenna-induced time and phase delays, the system was initially calibrated by transmitting orthogonal linear frequency modulation (LFM) waveforms and estimating their inter-pulse time-delay and phase offsets; these were then saved in a lookup table for compensation at runtime. This may be performed separately in practical systems. After the initial calibration, beam steering was accomplished by adding a time and phase delay to the sampled waveform; this delay included both the calibration delay and phase, as well as the delay and phase required to steer the beam to the desired angle given by

$$\tau_{\mathrm{bf}i} = \frac{D_i}{c}\sin\theta_{\mathrm{bf}} \quad \text{and} \quad \phi_{\mathrm{bf}i} = 2\pi f_c \tau_{\mathrm{bf}i}$$

respectively, where D_i is the internode distance between the first and ith node, θ_{bf} is the beam steering angle, and f_c is the beamforming carrier frequency. To synthesize a wider bandwidth than the instantaneous bandwidth of the system, a coherent pulse train of stepped LFMs was implemented. Thus, the transmitted waveforms were given by

$$s_i(t) = \sum_{n=0}^{N} \exp\left[j\pi(2f_n\tau + k\tau^2) + j\phi_{\mathrm{bfi}}\right]$$

where k is the chirp rate (each node transmitted an up- or down-chirp), defined by chirp bandwidth β over chirp duration T, and N is the number of frequency steps. In this experiment, $\beta = 100$ MHz, $T = 10$ µs , $N = 3$, $I = 2$ and $f_n = [3.1, 3.2, 3.3]$ GHz. The time between any two pulses in the pulse train was dictated by the time it took to retune the local oscillator and generate the next waveform in the pulse train—on the computer used in this experiment, this was typically ~20 ms.

The hardware used in the beamforming experiment, shown schematically in Fig. 5, consisted of two nodes separated by 1.484 m, each with an Ettus USRP X310 SDR controlled by a single desktop computer running GNU Radio 3.10 and UHD 4.3. Each SDR had a sample rate of fs = 200 MSa/s and was connected to the host via 10 Gb Ethernet. To more closely evaluate the performance of timing and ranging, a cable was used for frequency transfer between the nodes in this experiment. A photograph of the configuration is shown in Fig. 6. On initialization, the system used a pulse-per-second (PPS) signal derived from a global navigation satellite system (GNSS) receiver to coarsely align the system to within 100 ns, following which the high-accuracy time-transfer and inter-node ranging process would begin. For the time transfer, each node used log-periodic antennas operating at 5.5 GHz transmitting two-tone pulses with a tone separation of 50 MHz and a duration of 10 µs with a signal-to-noise ratio of 36 dB. Finally, the LFM pulse train was transmitted using log-periodic antennas to a Keysight DSOS804A oscilloscope at the target, located 35.5 m downrange, which sampled the waveform at 20 GSa/s using a similar log-periodic antenna. To determine the inter-pulse time and phase delay of arrival, the two orthogonal up- and down-chirp waveforms were matched filtered; the time delay of each was estimated by using quadratic least- squares interpolation to refine the peak estimate, and the phase was estimated using linear interpolation at the location of the corresponding time delay estimate.

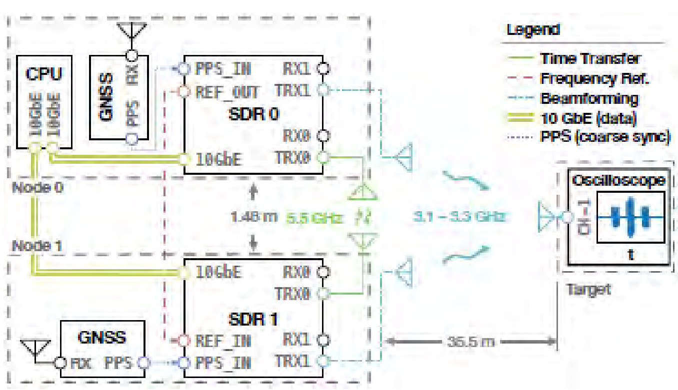

Fig. 5. System schematic. Time synchronization and internode ranging was performed at 5.5 GHz. A pulse-per-second (PPS) signal from a global navigation satellite system (GNSS) receiver was used for an initial coarse time sync on system initialization. Beamforming was performed from 3.1 3.3 GHz. The target oscilloscope was placed 35.5 m downrange.

Fig. 6. Experimental setup. Nodes 0 and 1 are on the left and right, respectively, and the target oscilloscope cart is shown in the inset

The measured inter-pulse time and phase arrival estimates at the target are presented for a beamsteering sweep from θ_{bf} = [0, 50]° in Fig. 7. The error between the expected beamforming delay and phase and the measured result at the target is shown in Fig. 7. The vertical dashed red lines in Figs. 7 and 8 indicate the target location θ_t = 1.854°, at which the inter-node time and phase difference bias standard deviation was 62.46+/-45.74 ps and 0.27+/-2.28° across all f_n. The internode range estimate during the experiment was D_1 = 1.40 m +/- 2.59 mm and included a constant range estimation bias of 88 mm which contributed to beamsteering errors at high angles. After compensating for the constant bias, the time and phase difference errors across all angles were 20.47+/-69.33 ps and 28.13+/-21.59°. This time and phase delay correspond with a maximum beamforming symbol rates and carrier frequencies of ~914 MBd at 710 MHz and ~1.44 GBd at 3.23 GHz across all angles.

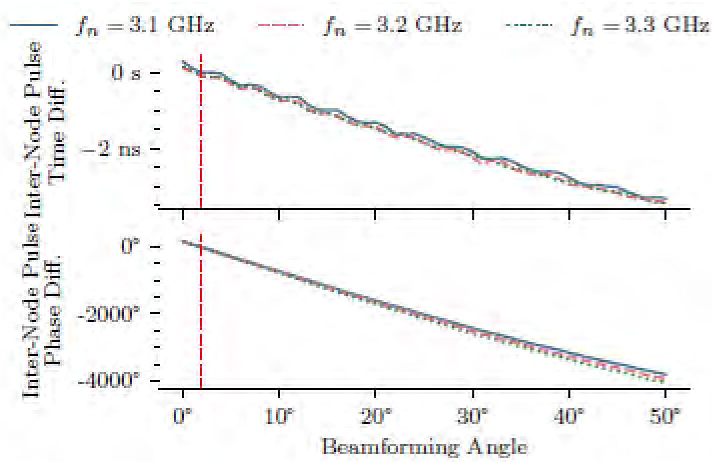

Fig. 7. Measured beamforming results at the target (oscilloscope). The vertical red dashed line indicates the angle where the target was located; at this location the pulse arrival time and phase differences should be zero.

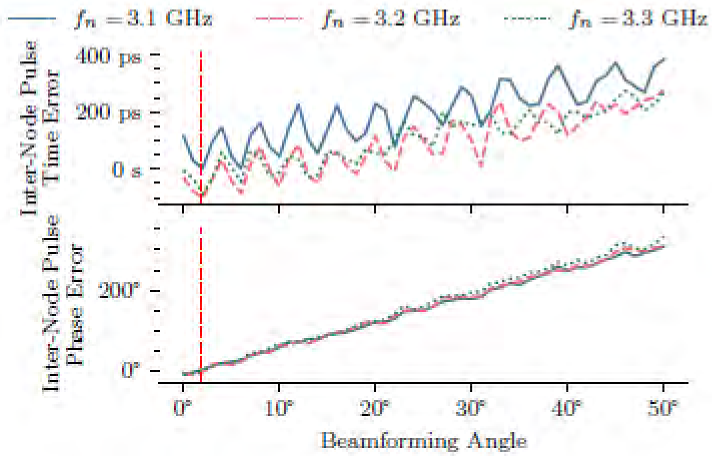

Fig. 8. Error between expected time and phase difference at the target location for a given beamforming angle. The vertical red dashed line indicates the angle where the target was located.

2.3 Decentralized Time Synchronization

Each node in a decentralized antenna array is required to estimate and correct for the average time offsets with respect to the adjacent nodes that are connected to it. Here we describe the average consensus method of an *n*-node distributed antenna array. The average consensus method expresses the average of the time offsets at node i as $(\mathbf{W}\Delta)ii$, where $\mathbf{W} = [w_{ij}]$ is the mixing matrix, which is an *n* x *n* real matrix with nonzero entries corresponding to the edges in the graph and self-loops (diagonal entries). To ensure convergence, the mixing matrix must be symmetric ($\mathbf{W} = \mathbf{W}^T$), doubly stochastic (the elements of each row and column sum to unity, respectively), and decentralized in the sense that $w_{ij} = 0$ if i = j and nodes i and j are not connected. In this work, the mixing matrix was created through the use of the Metropolis–Hastings constant edge weight matrix to ensure that the matrix requires only local information.

The consensus algorithm works in effect by calculating the average value of the offsets seen by a node in its neighborhood, after which the node adjusts its local time base by the average offset value. While the process is based only on local information sharing, as long as the graph is strongly connected (information can flow from a given node to any other node) and a constant edge weighting such as the Metropolis-Hastings weighting is used, the network will converge to the global average in a static case. In realistic systems the time errors are dynamic, however if the synchronization interval is sufficiently shorter than the clock drift they can be assumed to be static. Furthermore, the drift may be alleviated by using a simultaneous syntonization (frequency alignment) approach. The decentralized time alignment algorithm updates the time at each node during each iteration (synchronization epoch) until it reaches convergence. The nodes in the array reach consensus when the clock time in each node reaches the average of the initial clock times in all the nodes of the array or, in other words, when the time offsets between all nodes are relatively small.

The decentralized synchronization algorithm was evaluated experimentally using a four-node system with internode time estimates based on the timing approach described above. Various graph topologies were considered. The experiment was implemented in a loop topology, with two connections per node. The experiment evaluates the number of iterations required to achieve convergence as well as the accuracy of the method. Each experiment was repeated ten times, and the time offsets between the nodes of the system were recorded over 100 iterations. The mean standard deviation and the mean bias were calculated between the ten measurements. These parameters were computed from the measured time offsets between the local clocks of the nodes in the system. Syntonization of the systems was implemented using cabling in all the configurations, which alleviated clock drift, but not the time offsets, since the focus of this is on synchronizing the clocks. Wireless syntonization can be implemented using various techniques, such as those we have discussed in our prior reports. The experiments represented a four-node distributed antenna array and employed four SDRs (Ettus Research Universal Software Radio Peripheral (USRP) X310) (Fig. 9). Each SDR had two UBX-160 daughterboards supporting 160 MHz of instantaneous analog bandwidth. Each of the experiments was repeated ten times with a synchronization epoch of approximately 200 ms and the time offset between the nodes were measured over less than 2 minutes (60 iterations for the first two configurations, 100 iterations for the third and fourth configurations). Figs. 10–12 show the results of the measurement. Convergence was noted after about 20 iterations with error of less than 12 ps.

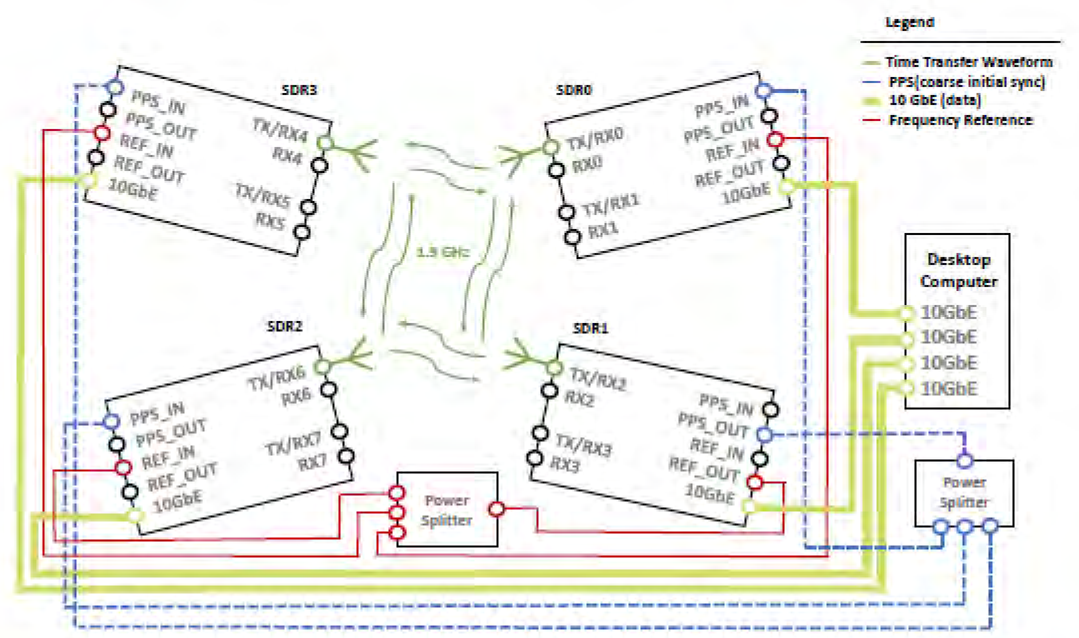

Fig. 9. Schematic of wireless time transfer experiment for four-node distributed antenna array. The four SDRs are connected to dipole antennas for wireless time transfer at carrier frequency of 1.9 GHz. The system has cabled frequency reference and cabled PPS for initial coarse time alignment.

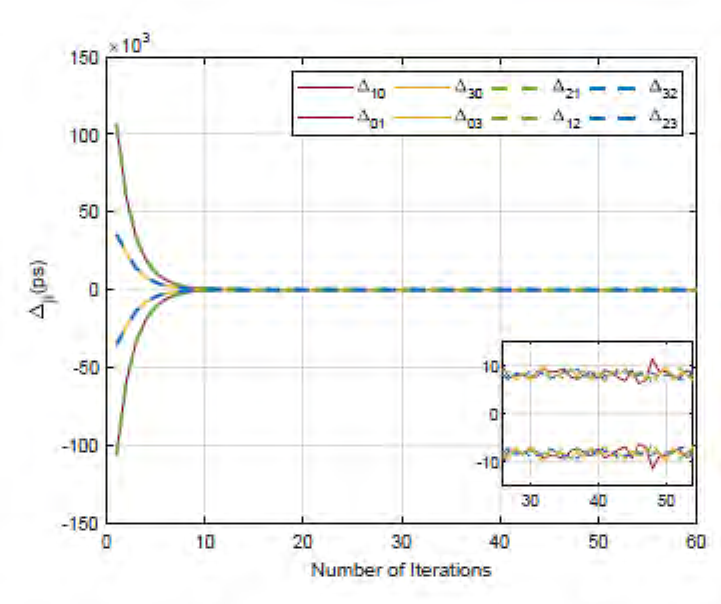

Fig. 10. The time offsets Δji between the connected nodes of a four-node distributed antenna array over 60 iterations for wireless time transfer at 36 dB SNR and 40 MHz tone separation.

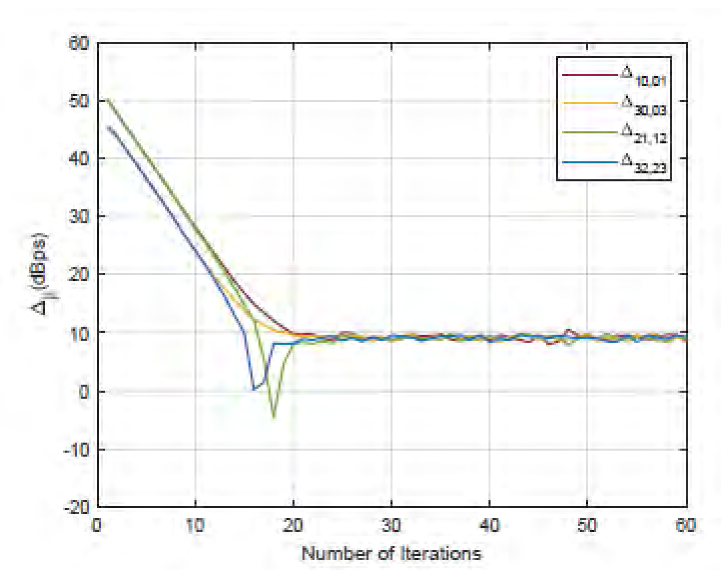

Fig. 11. The log magnitude of the time offsets between the connected nodes of a four-node distributed antenna array over 60 iterations for wireless time transfer at 36 dB SNR and 40 MHz tone separation.

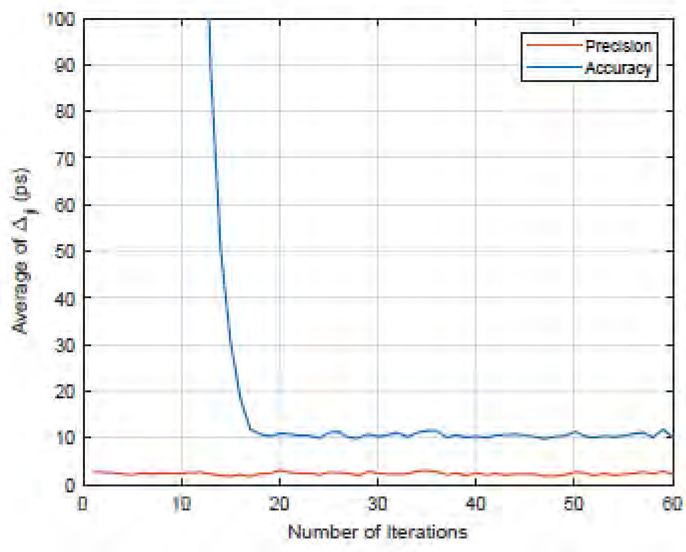

Fig. 12. The average accuracy and precision of the time offsets between the connected nodes of a four-node distributed antenna array over 60 iterations for wireless time transfer at 36 dB SNR and 40 MHz tone separation.

3. Findings and Conclusions

The results of this reporting period provide critical pieces of the foundation of a distributed approach to phase coherent transmission of microwave signals, and demonstrate the feasibility of distributed coherent beamforming from separate wireless systems. Time synchronization is a fundamental coordination aspect, and enables not only the coordination of the transmitted information, but also enables high-accuracy localization, which is necessary for phase alignment. By combining these into a decentralized framework, future systems of large numbers of elements can feasibility transmit coherently, leading to significant power density at the destination. Our ongoing work will focus on implementing transmission from larger sets of nodes using the techniques shown in this report.

4. Plans and Upcoming Events

In the next year we will focus on three principal topics: advanced decentralized coordination algorithms for aligning frequency, phase, and time; hardware implementations of wireless coordination to demonstrate distributed beamforming, and investigating bounds and limitations on transmit power.

5. Transitions and Impacts

N.A.

6. Collaborations

N.A.

7. Personnel

Principal investigator

- Jeffrey Nanzer
- ~1 person month of effort in the reporting period

- National Academy Member: No

Postdoctoral Fellow

- Robert Hipple
- ~1 person month of effort in the reporting period
- National Academy Member: No

Business contact

- Amanda Blank, ProposalTeam2@osp.msu.edu

8. Students

This project supported five PhD students during the reporting period:

- Ahona Bhattacharyya
- Derek Luzano
- Jason Merlo
- Naim Shandi
- William Torres

9. Technology Transfer

N/A

10. Products, Publications, Patents, License Agreements, etc.

Publications resulting from this project in the past year:

Archival Publications

J. M. Merlo, A. Schlegel, and J. A. Nanzer, "High Accuracy Wireless Time-Frequency Transfer For Distributed Phased Array Beamforming," IEEE International Microwave Symposium, 2023, 1st Place Winner Student Paper Competition

N. Shandi, J. M. Merlo, and J. A. Nanzer, "Sub-Millimeter Ranging Accuracy for Distributed Antenna Arrays Using Two-Way Time Transfer," IEEE International Symposium on Antennas and Propagation and USNC-URSI Radio Science Meeting, 2023

J. M. Merlo and J. A. Nanzer, "Wireless Time and Phase Alignment for Wideband Beamforming in Distributed Phased Arrays," IEEE International Symposium on Antennas and Propagation and USNC-URSI Radio Science Meeting, 2023, Honorable Mention, Student Paper Competition

A. Bhattacharyya, J. M. Merlo, A. Schlegel, and J. A. Nanzer, "High-Accuracy Localization Using Spectrally-Sparse Two-Way Time Transfer for Distributed Phased Arrays," IEEE International Symposium on Antennas and Propagation and USNC-URSI Radio Science Meeting, 2023

A. Bhattacharyya, J. M. Merlo, and J. A. Nanzer, "A Dual-Carrier Linear-Frequency Modulated Waveform for High-Accuracy Localization in Distributed Antenna Arrays," European Radar Conference, 2023

11. Point of Contact in Navy

N/A

Pulsed Dielectric Breakdown of Solid Dielectric Insulation Materials

Grant No. N00174-20-1-0025 and N00174-22-1-0023

Annual Report for Fiscal Year 2023

Period of Performance: October 1, 2022 to 30, September, 2023

Prepared by:

Professor David Wetz, Principal Investigator
Associate Professor Electrical Engineering Department
University of Texas at Arlington
Department of Electrical and Computer Engineering
416 Yates Street, Rm. 537
Arlington, TX 76019
Tel: (512) 788-0848
Email: wetz@uta.edu

This work was sponsored by the Office of Naval Research (ONR), under Naval Engineering Education Consortium (NEEC) grant numbers N00174-20-1-0025 and N00174-22-1-0023. The views and conclusions contained herein are those of the authors only and should not be interpreted as representing those of ONR, the U.S. Navy or the U.S. Government

Date Prepared: 1/5/2023
Project Title: Pulsed Dielectric Breakdown of Solid Dielectric Insulation Materials
Annual Summary Report: FY23
Principle Investigator: David Wetz, (512) 788-0848, wetz@uta.edu
The University of Texas at Arlington
416 Yates St. 537 Nedderman Hall
Arlington, Texas 76019

Section I: Project Summary

1. Overview of Project

Abstract:
Liquids and gases are often used as insulating materials in high voltage pulsed power systems and dielectric breakdown is always a concern. Gasses and liquids are conforming and self-healing, but they introduce significant engineering challenges and restrictions when it comes to sealing and/or pressurizing them. Liquid dielectrics are heavy so they may reduce a system's power and energy density, and their dielectric properties are unable to be functionally graded which can lead to boundary conditions that create high electric-field enhancements. Solid dielectrics could be more attractive from a maintenance, power density, and energy density perspective, but they are not self-healing and can be difficult to manufacture, especially around complex geometries. Epoxies have been studied but much more work is needed to fully understand their future uses. The rapid rise of additive manufacturing has also opened new avenues that need to be better explored. Epoxy, thermoset plastics, and additively manufactured materials can be functionally graded using nano-particle additives, potentially minimizing electric field enhancements. In the work presented here, raw and dielectrically altered solid dielectric materials have been modeled using finite element techniques and experimentally studied under pulsed experimental conditions to evaluate their dielectric strength. Additional work was performed this year to study materials with extremely high permittivities, specifically how their frequency-dependent permittivity varies up to 12 GHz.

Objective:
The objective of this effort is to identify and study solid dielectric materials that can be employed to replace gas and liquid insulators in high voltage pulsed power systems. The team is using modeling and simulation (M&S) and experimental techniques to characterize the dielectric properties and pulsed dielectric strength of raw and altered solid dielectric materials. An additional SoW was added to identify dielectric materials that have extremely high relative permittivity values and measure how the permittivity value changes as a function of frequency up to 12 GHz.

Naval Relevance:
Directed energy weapon (DEW) systems introduce significant tactical advantage on the battlefield. Many DEW systems employ high voltage pulsed power supplies. Typically, gas and liquid dielectrics are used to insulate high voltage systems, however, these pose many challenges when it comes to sealing, maintaining, and storing them for extended periods of time. Solid dielectrics solve many of these issues but face many of their own challenges. The significance of finding suitable solid dielectric materials pertains to reduction in size, weight, and maintenance of fielded high voltage pulsed power systems; solid dielectrics require no maintenance under normal storage or operational conditions and can lead to reductions in size and weight of fielded systems. A primary concern comes with a solid dielectric's inability to self-heal, as a single dielectric breakdown can cause electrical and mechanical failure that results in the need for replacement of the entire system. It is imperative that the insulator is well understood and properly designed to ensure reliability under high electric fields. Identifying methods to tune dielectric properties of insulator materials enables functionally graded dielectrics to be employed, which aims to reduce electric field enhancements

along with the size of the system. The experimental and M&S work being performed here is aimed at advancing our understanding of solid dielectrics and their use in DEW systems.

Introduction:

This project serves to investigate the feasibility of using solid dielectric materials as replacements for conventional liquid or gas dielectrics in high voltage pulsed power applications, including high power microwave (HPMs) systems. The solid dielectrics of interest include epoxies and plastic materials. Epoxies are of especially high interest due to their ability to pot complex geometries, since they are formulated and cast in a liquid state that hardens as a solid. Composite solid dielectric materials, which are produced by introducing particulate filler materials into a base material of interest during its formulation, are also being investigated. The motivation for investigating composites is to determine how the dielectric properties of solids can be tuned to achieve specific desired dielectric characteristics that may reduce high electric field enhancements in complex geometries. This effort focuses on using experimental as well as M&S techniques to characterize the dielectric properties and pulsed dielectric strength of raw and altered epoxy materials. Over the course of the four-year project period of performance, several tasks have been executed, listed below, and those performed in this reporting period will be described in detail later.

Task 1: Technology, Raw Epoxy Material, and Dielectric Additives Literature Survey

A review of previously performed research investigating dielectric breakdown of epoxies and plastics has been performed in year 1 and materials to be studied have been chosen. This year an extensive literature review was performed in collaboration with Purdue Univ. identifying materials with extremely high permittivity (UTA) and permeability (Purdue).

Task 2. Testbed Design and Fabrication

A testbed has been designed and fabricated in FY21/22 to apply pulsed electric fields to epoxy and thermoset plastic samples manufactured in house. A 30 stage, 600 J/pulse marx generator is employed as the pulsed power source.

Task 3. Existing Pulsed Power System Survey

UTA has worked with NSWC-DD to identify a marx topology that has been employed in HPM studies and M&S tools are being used to evaluate how solid dielectrics can be employed and functionally graded to reduce the size and weight of the system.

Task 4. M&S and Pulsed Dielectric Breakdown of Raw and Additively Manufactured Dielectrics

EPON 815C base epoxy material is being studied. Over 135 pulsed dielectric breakdown experiments have been performed to characterize its pulsed dielectric strength in raw and dielectrically altered forms. Novel M&S techniques have been developed to quickly study the electric fields present when employing the materials being studied.

Task 5: Permittivity Measurements

A VNA and test fixture are used to study the freq. dependent permittivity of Task 1 materials.

Task 6: Permeability Measurements

Purdue Univ. setup experiments to measure the freq. dependent permeability of Task 1 materials.

Task 7: Reporting

Reporting has been completed monthly to satisfy the ONR and NEEC requirements.

Background:

Many research papers were found in which epoxy dielectrics have been studied in their natural form or with dielectric modification. The results of all these previously published works suggest that it is feasible to alter the dielectric properties of epoxy resins by using many different types of micro and nano sized particles. Most of the previously documented work is focused on studying only low-voltage dielectric properties of altered materials, not on studying their dielectric strength. The work here is focused on not only studying how material properties are altered when they are dielectrically altered, but also what impact the alteration has on the dielectric strength. When coupled with the M&S approaches being taken, a holistic approach to studying solid insulator materials is being taken. Epoxy materials are being altered and cast in-house using careful techniques to minimize the presence of air bubbles. The work with thermoset plastics is limited to date but techniques have been developed and verified for creating dielectrically altered samples.

2. Activities and Accomplishments

Experimental Setup

Using DURIP funding obtained in FY21, a marx and load fixture was procured from Applied Physical Electronics (APELC) in Austin, Texas. It is comprised of a 30-stage, 600kV marx generator along with a 38 Ω electrical load in which samples can be installed and dielectrically loaded. A planetary mixer is used to ensure that the epoxy and additives are well mixed with homogeneous dispersion. Breakdown samples are loaded into the testbed such that when the marx is fired, current will flow through the matched load or through the sample if the electric field is great enough to cause a breakdown event to occur. CVRs (current

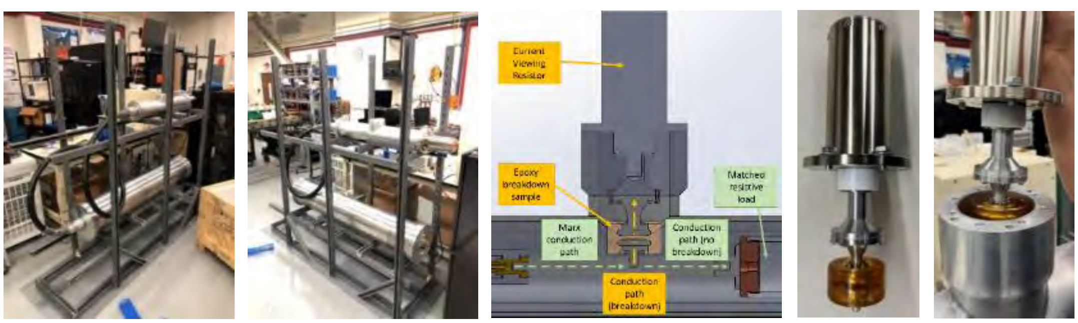

Figure 1. Marx and test fixture (left, second left), rendering of the dielectric sample holder and CVR, (third left), fabricated assembly (second right), sample assembly being loaded into testbed (right).

viewing resistors) are used on the load side as well as the sample side of the load to detect breakdown and measure the voltage. The marx, test fixture, and sample CVR assembly are shown in Figure 1. The epoxy samples are manufactured in house using a custom mould assembly, seen in Figure 2.

The mould casts epoxy around two parallel electrodes at a fixed separation distance that is set by the thickness of the middle section of the mould. The epoxy is mixed in the planetary mixer and then injected into the mould from the bottom using a large syringe. There is a disposable reservoir installed above for ensuring the mould is filled and for degassing it as shown in the left two images of Figure 3. EPON 815C epoxy samples with a 0.025" and 0.015" electrode spacing were made to reliably cause breakdown events. Bruce profile electrodes have been used to apply a near uniform electric field across the sample. In Figure 3, an epoxy sample is seen after it was potted, both before (left) and during (center) the degassing phase. Figure 4 shows an epoxy sample after electrical breakdown event. In the right side of Figure 4, a plot of the electrical data shows the breakdown voltage and current measured during testing. The sudden rise in the orange current trace indicates a breakdown has occurred.

In FY21, significant effort was invested to fabricate our own additive manufacturing filaments with and without additives. It will not be discussed in detail here but in short, the effort was not successful. In FY22, effort was spent identifying vendors that could supply thermoset plastics with additives. Techmer PM in Knoxville, TN was able to supply limited composite plastic stock with and without glass fiber additives and we were able to successfully mould them and test them. This year they were unwilling to work with us due to the low volume we were interested in procuring. This thrust of research should continue but it needs to be dedicated so that sufficient volume can be procured.

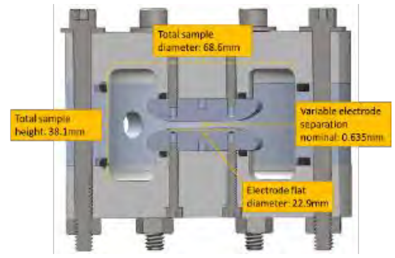

Figure 2. Rendering of epoxy sample mould assembly.

Figure 3. Samples before (left) and during degassing (right).

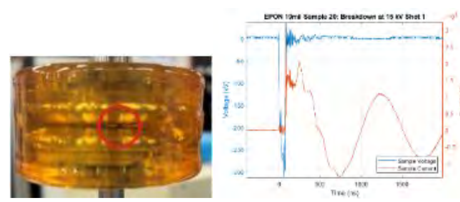

Figure 4. Epoxy sample after breakdown testing (left), carbon tracking is circled. Breakdown voltage and current waveform through the sample (right).

Material Literature Survey & Characterization

Additional funds were awarded in late FY22 to investigate materials with high permittivity or permeability at high frequencies (up to 12GHz) for NLTL applications. The findings from this literature survey are far too long to report on here but they are available upon request. A coaxial airline dielectric fixture, seen in the left side of Figure 5, was procured from MuEpsln and a 20GHz Anritsu Shockline VNA is used with it. The samples loaded into the airline are coaxial samples with an outer diameter of 7 mm, inner diameter of 3 mm, and length of up to 5 cm. A mould fixture, seen in Figure 5, was designed to fabricate samples for study. The mixtures are mixed the same way as the dielectric breakdown samples, with the only difference being the mould used. The selection of materials fabricated was driven by their demonstrated performance in a range of frequencies and from the exhaustive literature survey. These identified materials can be used to modify solid dielectrics and make them more suitable for use in high frequency NLTL applications. The survey was performed collaboratively between UTA who focused on ferroelectrics, their fabrication methods, and applications in systems related to this study. A few results obtained are shown in Figure 6. Purdue focused on ferrite-based composites, the synthesis & manufacturing method of relevant ferrites, their application space, and look at the state of the field. Somnath Sengupta at Powerhouse Consulting was also engaged to provide sintered material. A few of those real permittivity results are shown in Figure 7. Purdue is still actively performing permeability measurements using a Sawyer Tower experimental setup.

M&S Efforts

Simulation efforts, this reporting period focused on three different tasks: improving overall simulation speed for both electrostatic and frequency sweep simulations, continuing to optimize dielectric permittivity for minimizing field enhancements in a marx generator, and determining a simulation method that can produce S-Parameters for use in permittivity calculation for comparison with created samples. This process involves creating a model that reflects the geometry of our sample holder used with the VNA. The parameters related to the sample holder, shown in Figure 8, were applied to a model in CST Studio. Additional parameters, such as additive material and fill percentage, are applied on a per-sample basis. The length of a physical sample influences the frequency where the S-Parameter reflection occurs. If there is a mismatch between the size of the physical sample and the modeled sample, the S-Parameters will have a different reflection frequency. By applying the same geometric properties, the simulated S-Parameters are very close to what we measure with the VNA for a corresponding sample, seen in Figure 9. Using the Nicholson-Ross and Epsilon from Transmission models in the MuEpsln software, the permittivity and permeability of the samples can be estimated using only S-Parameters.

Using an automated script, models were created that used particles of radius 100um, adding particles until the corresponding mass fill percentage was reached. The S-parameters from the simulations are processed by both CST and the MuEpsln's program used to process S-parameters from the VNA. Additionally, the calculation method used by CST to estimate permittivity and permeability is identical to the Nicolson-Ross method used by the MuEpsln program, and for simulation models does not require the de-embedding of S-parameters to obtain permeability and permittivity results. A comparison of measured and simulated permittivity of EPON with varying Al2O3 mass fill percentages, obtained using the Nicolson-Ross method, are seen in Figure 10.

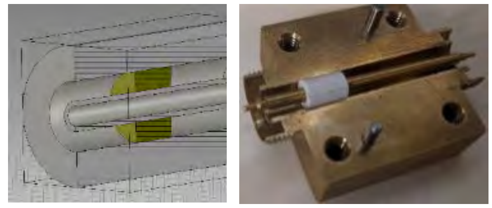

Figure 8. Figure 25. (top) Model used for simulation with a sample length of 10.17 mm. (bottom) Corresponding Epoxy Sample.

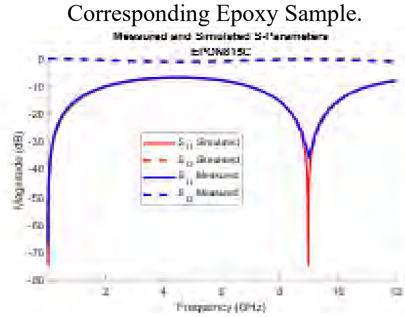

Figu sample

Figure 9. S-Parameters for S11 and S21 for simulated and measured results.

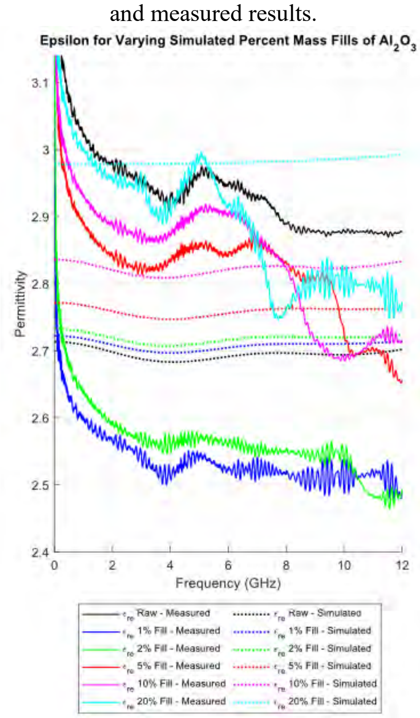

Figure omposite

Figure 10. Comparison of measured and simulated permittivity of EPON with varying Al_2O_3 mass fill percentages obtained using the Nicolson-Ross method.

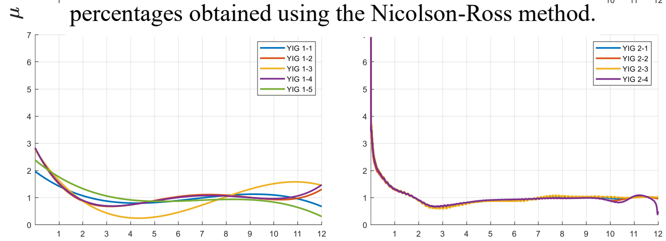

Figure 7. Permeability measurements made from several sintered ceramic material samples studied this FY.

Pulsed Electrical Breakdown Results

By the start of FY23, methods were sufficiently identified to facilitate the production, testing, and data collection of composite solid epoxy samples. With respect to the dielectric breakdown portion of the effort, the goal was solely to continue fabrication and testing of composite epoxy samples to gather a statistically relevant data set to draw conclusions from. At the start of FY23, 32 raw EPON 815C samples had been produced and tested. By the end of FY23, over 135 samples have been made and tested. The samples made and tested in FY23 have been raw and composite samples with various loadings of Alumina, Barium Strontium Titanate (BST), Calcium Copper Titanate (CCTO), or Calcium Titanate (CTO). A lineup of some samples fabricated this year are shown in Figure 11. The goal this year was to identify additive materials that can be used to specifically alter the permittivity of a base material without compromising dielectric strength. The data shown in Figure 12 plots the breakdown strength measured for composites with Alumina, BST, CCTO, and CTO.

Introducing alumina into the base material offers moderate ability to alter the permittivity as seen at loadings under 20%, and dielectric strength of the material does not appear to be significantly compromised. In fact, the dielectric strength has been observed to be largely maintained with alumina loadings up 5%. Going forward, alumina will be investigated under higher loadings (up to 30%) to observe the effects on both the dielectric strength and the permittivity. The performance of alumina as an additive material appears to align with the goals of this effort.

Initial struggles were met when working with various CCTO powders. Initially a CCTO powder from Bonding Chemical was used with extremely poor results optically and on permittivity and breakdown strength testing, which was concerning. Eventually, CCTO powders from American Elements were obtained along with better results. While the permittivity can be altered to a moderate degree even at low loadings, the breakdown strength appears to be affected quite negatively. Only a few breakdown samples had been tested by the end of FY23, so more data is needed and will be obtained going forward. Initial impressions suggest this material may not be suitable for this effort's goals due to poor dielectric strength.

The results from BST and CTO permittivity alteration have been significant, as the permittivity has been able to be substantially altered. Their performance in breakdown testing, however, has been quite disappointing so far. These samples appear to consistently break down early in the rise time. It is worth mentioning that, due to the density of these materials, it has been noticed that there is significant settling on the bottom of the BST samples, and this may also be the case for CTO samples. This issue will continue to be investigated to determine if there is a better mixing/casting process for these heavy materials. Much more work is being performed in FY24 and a more complete matrix of tests and better theoretical understanding will be presented at the end of FY24.

Figure 11. Lineup of some samples fabricated this year, including Alumina (124-125), BST (115-116, 128-129), CCTO (119-123, 130), and CTO (111-114, 117-118, 126-127) composite samples.

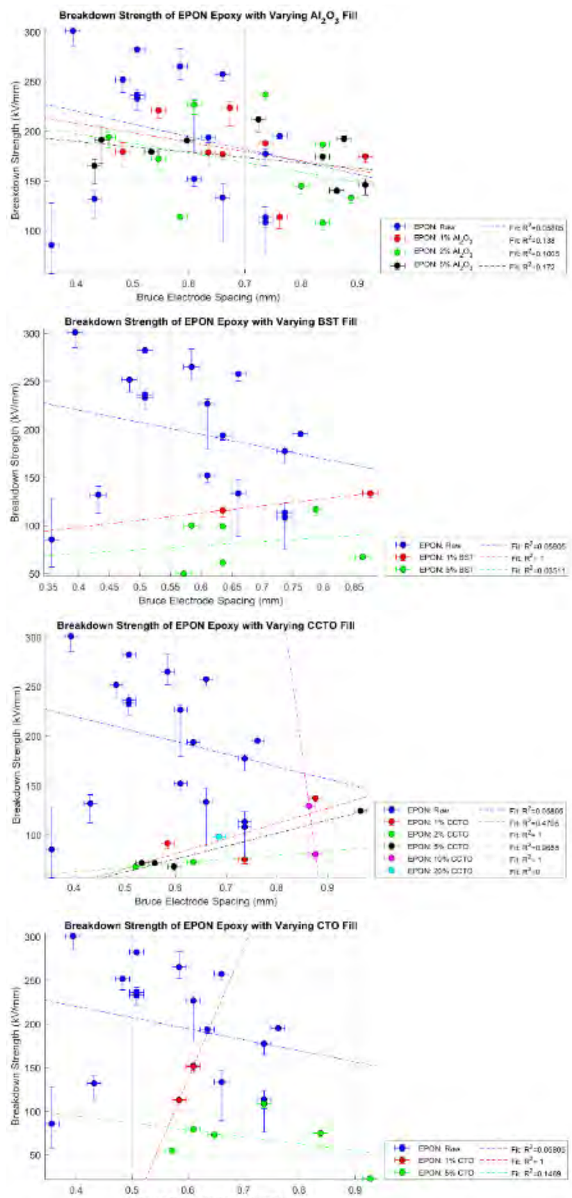

Figure 12. Dielectric breakdown strength measured for composites with Alumina, BST, CCTO, and CTO.

3. Findings and Conclusions

A literature survey by UTA and Purdue identified many different materials with high permittivity and permeability that are being studied. Several different high permittivity nanoparticle additives have been identified and studied within EPON 815C epoxy mixtures at pbw percentages as high as 20%. Alumina and BST look promising while others such as CCTO and CTO appear to negatively impact dielectric strength. Additional testing with more additives is planned in FY24. Unique M&S tools are being used to model the freq. dependent permittivity of the materials being tested so that their full potential for use in existing pulsed power supply tech. can be understood.

Purdue is leading the ferromagnetic study. As full material characterization is crucial for understanding and predicting nonlinear transmission line performance. Hysteresis curves for custom materials were measured to allow for the extraction of material permeability, retentivity, magnetization saturation, coercivity, and hysteresis loss. The resulting parameters can be used to help guide the designer when selecting the material that is to be implemented into a system. For example, materials with higher magnetization saturation may generate higher frequency oscillations compared to their low magnetization saturation counterparts while materials with narrow hysteresis curves indicate lower hysteresis loss. A few sample hysteresis waveforms captured this year are shown in Figure 13 using the setup shown in Figures 14 and 15.

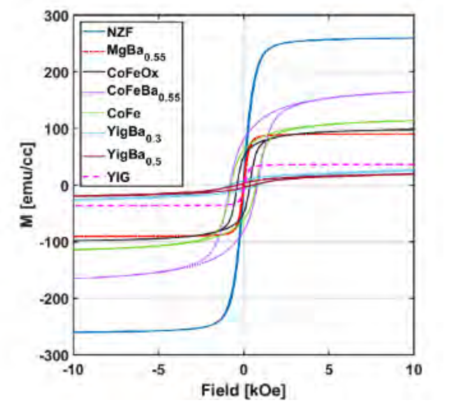

Figure 13. BH curves for custom materials at 300K.

Figure 14. VSM system to measure BH curves.

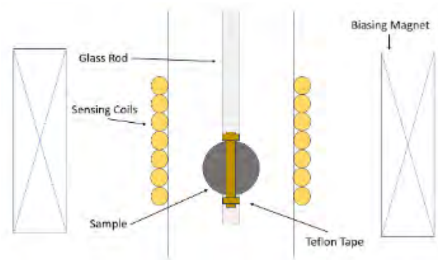

Figure 15. Inside look at VSM and sample mounting solution.

4. Plans and Upcoming Events

The effort should come to an end at or just slightly after the end of FY24. At UTA, experiments are planned with Alumina, Barium Titanate, Titanium Dioxide, and Strontium Titanate. A full test matrix will be completed, and results will hopefully lead to theoretical conclusions and paths forward for the community. Purdue is planning to continue their hysteresis measurements and should report out findings this summer. Additional modeling efforts are planned to demonstrate size implications of using altered dielectrics in pulsed power generators.

Recommendations for Future Work: We would like to study dielectrically altered thermoset plastics as we think that could be a very valuable effort. We tried to lump that into this effort and there just isn't enough funds or bandwidth to make it happen. We are also interested in researching phase change materials and their potential use as dielectric insulators. Something that can be transitioned back to a liquid under moderate heat may be advantageous for many reasons.

5. Transitions and Impacts

There are many ways to transition this work including starting to apply it to relative HPM pulsed power supplies. A proposal was submitted in FY23 to the Joint Directed Energy Transition Office Center of Excellence proposing additional work studying potted dielectrics and particle suspension in liquid dielectrics for employment in pulsed power supplies and especially pulsed transformers. There is significantly more work to do studying raw and altered thermoset plastics that should also be explored based on the methods and preliminary results obtained here.

6. Collaborations

Allen Garner (Purdue University) joined as a co-PI this year as discussed. Collaborations are occurring with Cameron Pouncey (NSWC-DD), Jordan Chaparro (NSWC-DD), Matthew McQuage (NSWC-DD), Andrew Fairbanks (NSWC-DD), and Somnath Sengupta (Powerhouse)

7. Personnel

Principal Investigator: David Wetz, 113 hours, National Academy Member (N)

Hayden Atchison: Postdoctoral Fellow (Grad. in Aug 2023), 85 hours in Sept 23
Co-investigator or Co-PI: Allen Garner (Purdue Univ). 25 hours, National Academy Member (N) (Subcontract)
Business Contact: Sarah Panepinto, Director of Grant and Contract Services, ogcs@uta.edu
Team Members: Listed as students below
Subs: Purdue Univ. added at the start of FY23

8. Students

Tyler Scoggin (UTA PhD Student), Hayden Atchison (UTA PhD Student who graduated in August 2023), Travis Crawford (PhD Student at Purdue)

9. Technology Transfer

None to report

10. Products, Publications, Patents, License Agreements, etc.

Publications resulting from this project:

<u>Archival Publications</u>

None this FY but two have been submitted in FY24 that will be included in next years report. Three additional are in process of being written

<u>Conference Papers</u>

A. Title: Testing of a Compact High-Power Microwave System Utilizing a Novel Composite Based Nonlinear Transmission Line Topology
B. Authors: T. D. Crawford and A. L. Garner
C. Conference Name: Directed Energy Professionals Society Conference
D. Conference Date: April 2023
E. Conference Location: San Antonio, TX.
F. Publication Status: Published
G. Publication Date: April 2023
H. Publication Identifier Type: Not sure
I. Publication Identifier: Not Sure
J. Acknowledgement of Federal Support? Yes

A. Title: Material and System Design Considerations for Nonlinear Transmission Lines used as Combined Pulse Forming Lines and High-Power Microwave Sources
B. Authors: T. D. Crawford and A. L. Garner
C. Conference Name: 24th IEEE International Pulsed Power Conference
D. Conference Date: June 2023
E. Conference Location: San Antonio, TX.
F. Publication Status: Published
G. Publication Date: June 2023
H. Publication Identifier Type: Not sure
I. Publication Identifier: Not Sure
J. Acknowledgement of Federal Support? Yes

<u>Books</u>

None this FY

<u>Book Chapter</u>

None this FY

Theses

None this FY

Websites

None

Patents

None

Other Products:

Presentations without associated papers

S.T. Scoggin, H.L. Atchison, N.E. Jennings, and D.A. Wetz,' Pulsed Dielectric Breakdown of Altered Solid Dielectric Insulation Materials,' 2023 IEEE Pulsed Power Conference, June 25 – 29, 2023, San Antonio, Texas.

H.L. Atchison, S.T. Scoggin, N.E. Jennings, and D.A. Wetz, 'Study of Solid Dielectric Insulator Materials using Finite Element Modeling,' 2023 IEEE Pulsed Power Conference, June 25 – 29, 2023, San Antonio, Texas.

S. Scoggin, H. Atchison, N.E. Jennings, and D. Wetz, 'High Voltage Breakdown of Altered Dielectrics,' Office of Naval Research (ONR) Basic Research Conference, September 6, 2022, Held Virtually.

11. Point of Contact in Navy

Mr. Matthew McQuage, matthew.mcquage@navy.mil, NSWC-DD, Last Contacted on December 15, 2023
Mr. Andrew Fairbanks, andrew.j.fairbanks5.civ@us.navy.mil, Last Contacted on December 15, 2023

An Accessible Platform for Simultaneous Macro, Meso and Microscopic Measurements of Polymeric Materials at High Loading Rates and Temperatures

Grant No. N00014-22-1-2490

Annual Report for Fiscal Year 2023

Period of Performance: October 1, 2022 to September 30, 2023

Prepared by:

Research Professor Sal Portillo, Principal Investigator
Department of Electrical and Computer Engineering
University of New Mexico
Albuquerque, NM 87131-0001
Tel. 505-417-9822
Email: sportil@unm.edu

This work was sponsored by the Office of Naval Research (ONR), under grant number N00014-22-1-2490. The views and conclusions contained herein are those of the authors only and should not be interpreted as representing those of ONR, the U.S. Navy or the U.S. Government.

Grant or Contract Number: N00014-22-1-2490
Date Prepared: January 31, 2024
Project Title: An Accessible Platform for Simultaneous Macro, Meso and Microscopic Measurements of Polymeric Materials at High Loading Rates and Temperatures[2]
Annual Summary Report: FY23 (01 September 2022 – 30 September 2023)
Principal Investigator: Sal Portillo, 505-417-9822, sportil@unm.edu
University of New Mexico, Department of Electrical and Computer Engineering, Albuquerque, NM 87131-0001

Section I: Project Summary

1. Overview of Project

The overall goal of this project is to develop high energy, long pulse, High Power Microwave (HPM) sources that provide the Naval Warfighter with an asymmetric lethal capability against electronics. HPM sources are limited to relatively short pulses due to the outgassing of molecules from the surfaces of these devices. To overcome this, our project focuses on changing the surfaces of these HPM sources via laser exposure or via compressive means so that these molecules find it more difficult to adhere to the topmost surface layers and more difficult to disassociate from these layers if they do bind. This project is in collaboration with Texas Tech scientists carrying out numerical models of this adsorption and surface modification. Ultimately, we are looking for not an academic solution but a practical answer to this problem and will couple this solution to an HPM source.

The relevance to the Naval Warfighter is that this technology will enable the design and build of novel HPM sources that can deposit more energy, punch harder, on combatant electronic threats, especially those that are dynamically changing and adapting thereby defeating the threat in littoral as well as in land scenarios. This is of critical importance as demonstrated by recent events in eastern Europe as well as near the red sea and Persian Gulf.

Abstract: This document details 6.1 research efforts funded by the Office of Naval Research (ONR) to develop higher energy and longer pulse HPM sources, specifically by decreasing the effect of outgassing, technology which can be implemented on Magnetically Insulated Line Oscillators as well as Magnetrons.

Objective: The principal objective of this work is to carry out experimental investigation in order to develop mitigation techniques that will reduce the outgassing of molecules in HPM devices and thus increase the pulse length and energy that these sources can deliver making them more lethal to electronic threats.

Introduction: As electronic targets of interest, from small components to full-fledged systems, are brought online these present new threats to American interests. These new threats require different operational parameters such as wavelength and higher energy density, and thus, the need to develop devices that can produce and deliver these higher energies in order to interdict present and future threats. These crossed field devices utilize the movement of electrons past cavities whereby under certain condition, called synchronicity, the electrons transfer energy to the seeded EM waves within the cavity thereby increasing the amplitude of these waves until they are released to carry out the required interdiction. They are called crossed field devices as the forces generating the movement of the electrons to synchronicity arise due to the perpendicular (crossed) currents and induced or applied magnetic fields. The principal mechanism limiting the energy creation of these devices us outgassing of adsorbed molecules from the internals of the device into the vacuum or interaction space. The University of New Mexico (UNM) experimental and

[2] This work was sponsored by the Office of Naval Research (ONR), under grant number N00014-22-1-2490. The views and conclusions contained herein are those of the authors only and should not be interpreted as representing those of ONR, the U.S. Navy, or the U.S. Government.

computational HPM group has developed world class leading plasma experimental facilities and numerical models that focus on the development of advanced HPM sources. We are designing and developing the next generation of HPM sources capable of delivering higher energies on target.

Administrative Info:

- PI: Sal Portillo, Research Professor, sportil@unm.edu, 505-269-3525
- Business Contact: osp@unm.edu, 505-277-4186

Background: Our approach is to carry out experimental plasma physics research on cathode and anode materials with the goal of developing cathode geometries and surface treatment of anodes that reduce this outgassing. We are focusing on modifying the surface of various anode materials so as to remove the dangling bonds of the surface and increase the path length or passivate the surface so inner bound molecules find it more difficult to move into the interaction space of these HPM sources. This modification occurs via laser irradiation across various wavelengths, power levels, exposure time and materials. Additionally, we have developed an extensive suite of temporally resolved plasma diagnostics – along with advanced analysis tools- which allow us to measure the amount and type of molecules in short time scales as well as how they evolve from onset of voltage application and how these affect the crossed field device. The experiments are carried out on a pulsed power accelerator/test bed that is a surrogate for an HPM device. Similarly, we are utilizing the same diagnostics on cathode materials and will generate new cathodes using similar laser irradiation techniques that modify the surface and lead to electron emission with reduced adsorbate load.

2. Activities and Accomplishments

Our work on cathodes/anode measuring plasma creation and evolution has been quite a success as we have demonstrated not only temporal resolution but also spatial resolution. This means we can observe when and where the plasmas, arising from the adsorbed molecules, form and how they evolve. All of these experiments are carried out on the Lobo Linear Transformer Driver accelerator which produces an output pulse that is a good surrogate for an HPM device. For reference, figure 1 shows a series of images showing the Lobo LTD, its experimental chamber and typical cathodes fired on in FY23. The image on right shows plasmas arising from the cathode as well as the anode. Clearly a spatially resolved diagnostic is needed that tells us where these are born and where they move to. Further we wish to know how much plasma is there, the constituents of the plasma, and the status of the plasma (temperature) which tells us how it interacts with the incident electron beam which is not visible as it does not emit light but is traversing from cathode to anode. These plasmas destroy the desired behavior of the electron beam, and they are dynamic; they grow and shrink in time with respect to the applied voltage pulse and hence the need for time resolved diagnostics. HPM UNM group has now developed and implemented a Moire deflectometer and a Mach Zehnder interferometer to obtain the needed time resolved and a spatially resolved information.

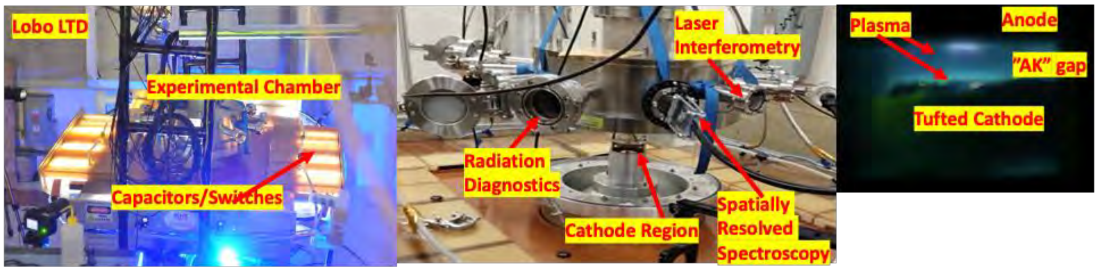

Figure 1 Image of the LTD firing, the experimental chamber and a typical shot cathode anode experiment. The latter clearly shows plasmas from both the anode and the cathode.

Figure 2 shows the results of a time resolved interferometer from the rightmost image on figure 1. The interferometer is one of a kind utilizing a framing camera to take snapshots of the interference pattern at discrete times during the pulse. These snapshots are analyzed to yield information about the plasma at that particular time.

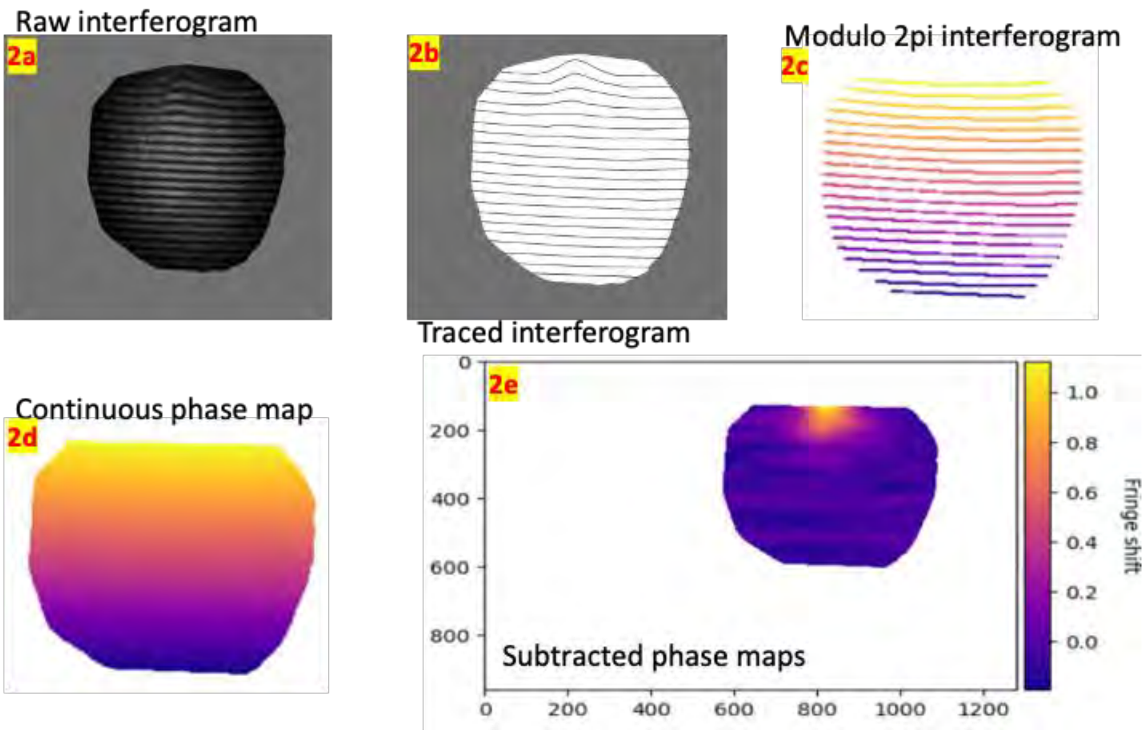

Figure 2. Composite image of an interferometric shot. Figure 2a shows raw data, 2b-2d show the complex mathematical process to remove the 2Pi Modulo and finally one arrives at 2e which shows density of the plasma.

Figure 3 shows 6 images from one test event that give the evolution of the plasma in time from 365 ns until near the end of the pulse at 1165 ns. The plasma density increases and then evolves until it covers most of the interaction space. The ions in the plasma interact with the electron beam from cathode to anode and disrupt its behavior – in this case the current is decreased or staunched which also occurs in HPM devices as well as altering the synchronism mechanism that produces EM energy.

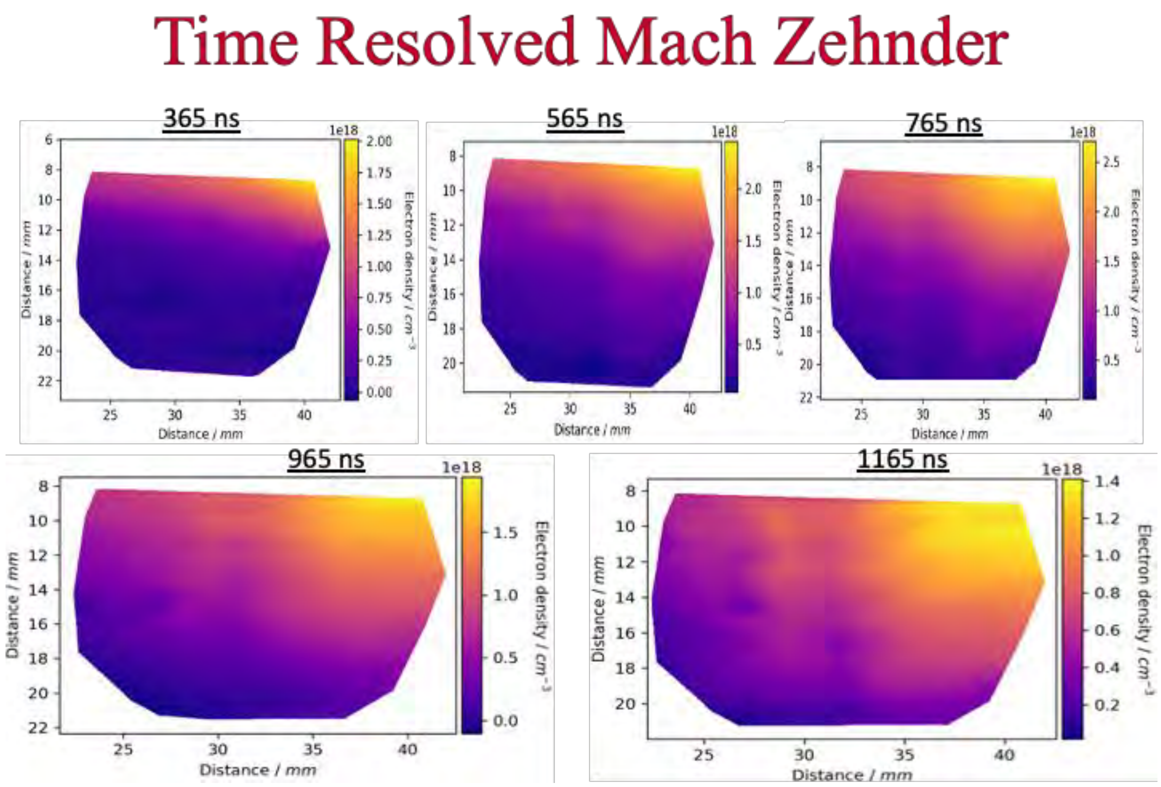

Figure 3. Time resolved images showing evolution of anode plasma as a function of time

There is clearly a relationship with applied voltage which ties in both spatially and temporally and so we have carried out experiments showing this effect, and which are shown in figure 4. It is not necessarily a linear relationship with voltage, that is to say that as the voltage increases one would expect a growth in the amount of plasma which in turn alters the beam more and so the dynamics change in time. The Mach Zehnder time resolved interferometer can be changed so that we have a time resolved deflectometer and figure 5 shows the temporal progression captured by this diagnostic and the resultant analysis which also gives density albeit in a lineout. The issue with the Mach Zehnder is that in order to get density we must carry out a mathematical process called abel inversion and this specifically assumes that the plasma is symmetric about the vertical axis and as one can see from the temporal images this is not necessarily the case.

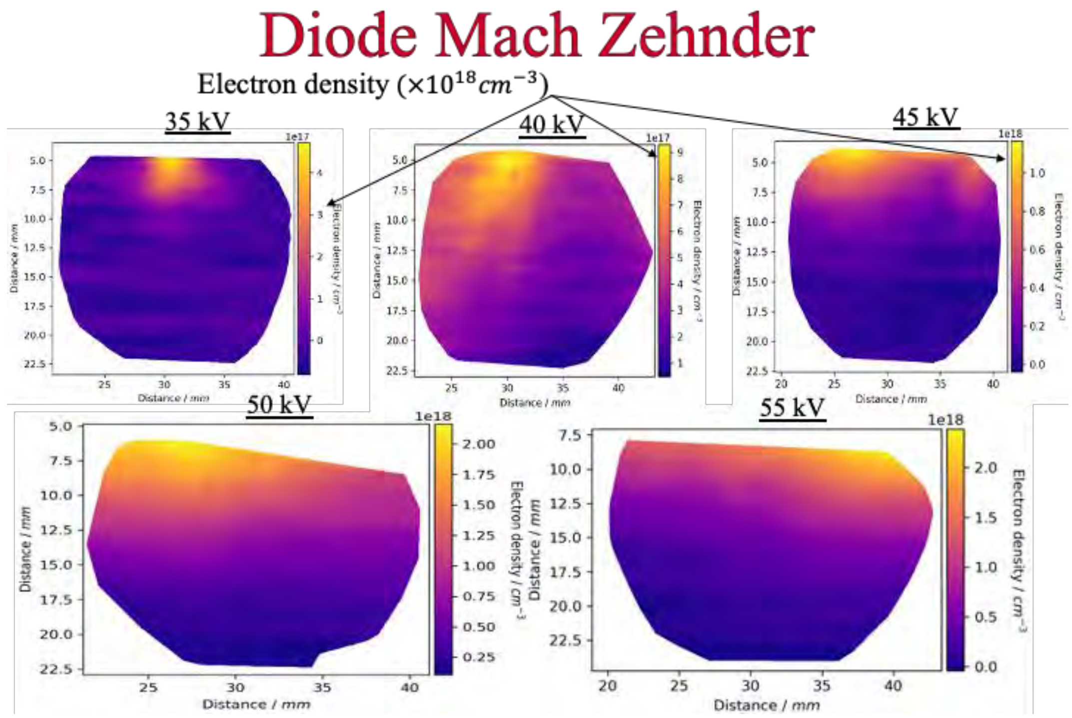

Figure 4. Mach Zehnder interferometric images as a function of voltage at same time in the pulse.

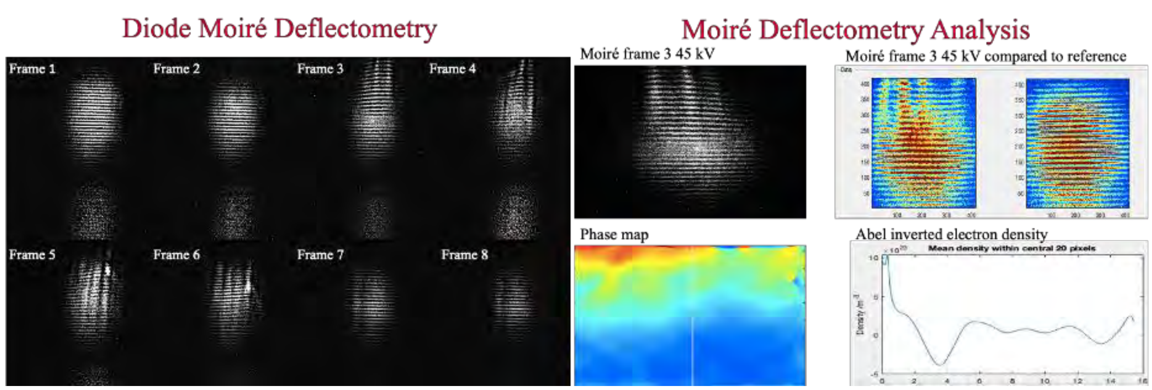

Figure 5. Time resolved reflectometry of our 'Diode' anode cathode shots.

We have started to modify the surface of anode materials, first standard materials such as Al and Cu using laser energy deposition. The parameters of energy, wavelength and material (not just bare but 'dirty' with typical technical surface) are all interrelated. Figure 6 shows our set up for a 488 nm laser irradiating an anode sample. Work remains as FY23 saw the beginning of the campaign and surface analysis needs to be carried out in the upcoming year.

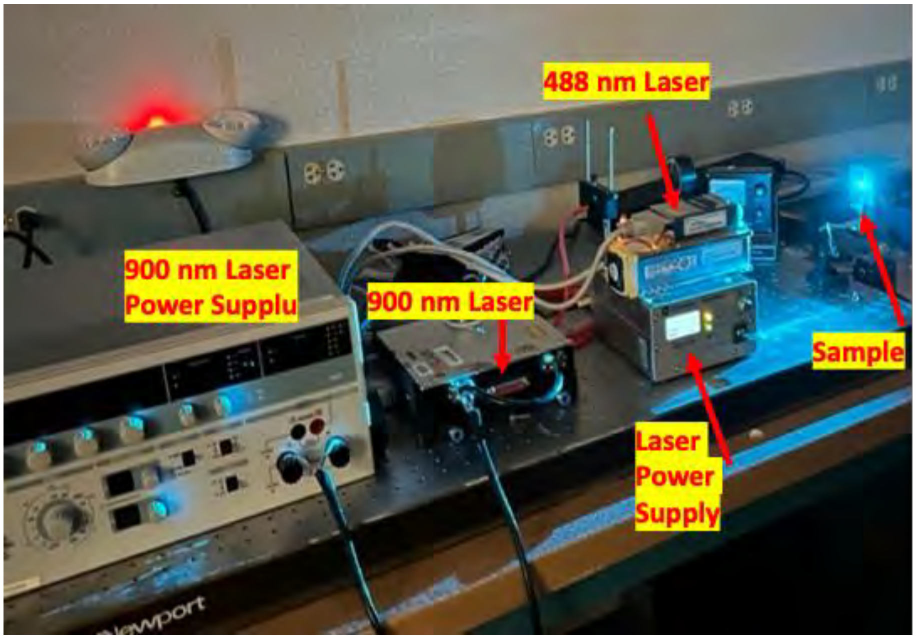

Figure 6. Experimental set up for our surface laser modification work.

3. Findings and Conclusions

Plasmas from anode and cathode desorbates have been measured both temporally as well as spatially. Densities, content and evolution have been measured. Our work on modification of surface has begun.

4. Plans and Upcoming Events

In the next fiscal year we will move towards modifying surface via isentropic compression and continue our work with laser modification. We will carry out exhaustive analysis on the surface adsorbates via X-ray Photon Spectroscopy and Scanning electron Microscope. Additionally, we will continue to develop additional diagnostics that will yield key metrics within these plasmas and we will in-situ cathode experiments with best in class modified materials.

We will increase our numerical modeling footprint utilizing a Particle-In-Cell (PIC) code to model the effects of reduced adsorbate loads utilizing a kinetic-fluid hybrid model. We will also begin atomic numerical simulations to understand the generation of plasmas, specially highly ionized and non neutral plasmas found in HPM devices. We will additionally begin to design a modern high frequency HPM source with new geometries and materials for possible build and test.

5. Transitions and Impacts

None yet.

6. Collaborations

1. Ravi Joshi, Texas Tech University, DFT numerical simulations and molecular dynamics sumulations of anode surface modification

2. Steven Fairchild, AFRL/RX, Cathode development for HPM sources.

3. Brad Hoff, AFRL/RD, Felt cathode for HPM sources

4. Genevieve Dion, Drexel University, woeven cathode assembly

5. Dmitri Tsentalovich, DexMat Corp., Carbon fiber construction

6. Peter Duselis, SemSol, Magnetic Insualted Line Oscillator Design

7. Ken Hara, Stanford University, Cathode adsorbates

8. Jack Hare, Massachussets Institute of Technology, complex analysis of interferometric data

9. Simon Bland, Imperial College, Pulsed Power and Isentropic Compression of materials

7. Personnel

Principal investigator – Sal Portillo (2.5-person month)
Business Contact – osp@unm.edu

8. Students

1 Graduate Student and 2 undergraduate students supported

9. Technology Transfer

None to-date.

10. Products, Publications, Patents, License Agreements, etc.

Archival Publication (publication reference information (article title, authors, journal, date, volume, issue) can be automatically entered using a DOI)

a. Upper-hybrid oscillations of high current relativistic electron beam under conditions of magnetic self-insulation
b. Physics of Plasmas
c. K. Ilyenko, T. Yatsenko, V. Vekslerchik and S.Portillo
d. Keywords: Magnetic Insulated Line Oscillator, Plasma Physics, high power microwaves
e. Distribution Statement: Distribution Statement A. Approved for public release: distribution is unlimited.
f. Publication Status: Submitted
g. Publication Identifier Type: N/A
h. Publication Identifier: N/A

i. Publication Date: N/A
j. N/A
k. N/A
l. N/A
m. Publication Location: Melville, NY
n. Acknowledgement of Federal Support? (Yes)
o. Peer Reviewed? (Yes)

Conference Paper

a. Anode Cathode Time Resolved Plasma Measurements
b. R. Beattie Rossberg, S. Portillo
c. 2023 IEEE International Conference on Plasma Science
d. May 21-25, 2023
e. Santa Fe, NM, USA
f. Submitted
g. N/A
h. Publication Identifier Type – unknown
i. Unknown
j. Acknowledgement of Federal Support? (Yes)

Theses - None

Websites

a. High Power Microwaves and Pulsed Power at the University of New Mexico (www.unm.edu/~sportil)

Patents – None

Other Products: None

11. Point of Contact in Navy

None

High Power Electromagnetic Sources from X-Band to Ka-Band

Grant No. N00014-23-1-2072

Annual Report for Fiscal Year 2023

Period of Performance: October 1, 2022 to September 30, 2023

Prepared by:
Distinguished Professor Edl Schamiloglu, Principal Investigator
Department of Electrical and Computer Engineering
University of New Mexico
Albuquerque, NM 87131-0001
Tel: 505-269-3525
Email: edls@unm.edu

This work was sponsored by the Office of Naval Research (ONR), under grant (or contract) number N00014-23-1-2072. The views and conclusions contained herein are those of the authors only and should not be interpreted as representing those of ONR, the U.S. Navy or the U.S. Government.

Grant or Contract Number: N00014-23-1-2072
Date Prepared: January 30, 2024
Project Title: High Power Electromagnetic Sources from X-Band to Ka-Band[3]
Annual Summary Report: FY23 (01 December 2022 – 30 September 2023)
Principal Investigator: Edl Schamiloglu, 505-269-3525, edls@unm.edu
University of New Mexico, Department of Electrical and Computer Engineering, Albuquerque, NM 87131-0001

Section I: Project Summary

Overview of Project

This project seeks to advance the state-of-the-art in high power sources of RF (HPRF) from X-band to Ka-band. This is accomplished through a combination of simulation (particle-in-cell simulations – PIC) and experiment. A large portion of the effort in Year 1 has been to perform a comprehensive literature review. In addition, pervious work on the Magnetically Insulated Line Oscillator (MILO) is being pushed to much higher frequencies than previous designs. This includes development of novel high-power microwave (HPM) geometries to deliver higher energy electromagnetic (EM) pulses to give the naval warfighter an asymmetric capability to interdict electronic devices.

In terms of Navy relevance of the project, our goal is to address, via focused and translational HPM research, some of the critical problems facing Navy operations due to asymmetric electronic threats, such as those faced by Marine warfighters in forward operating bases to those in littoral waters, and protection of high value targets, such as U.S. embassies in potential hot spots around the globe.

Abstract: This annual report summarizes activity on the FY2023 awarded ONR grant "High Power Electromagnetic Sources from X-Band to Ka-Band" covering the period December 01, 2022 – September 30, 2023.

Objective: The objective of this effort is to perform a comprehensive literature review of high-power EM sources from X-band to Ka-band in Year 1 and then in Year 2 select a source concept and frequency range to design and implement an experiment that can be performed using the facilities at UNM. In addition, PIC simulations are being performed to advance the MILO to higher frequency with a secondary objective to understand and overcome the limitations imposed by the smaller separation distances within this class of high frequency cross-field device.

Introduction: The UNM group excels in designing novel HPRF source concepts of relevance to the Navy using PIC simulations, and then validating the source designs in experiment. We are advancing the capabilities of such sources to higher frequency, specifically from X-band to Ka-band, including advancing the MILO to higher frequency.

Administrative Info:

- PI: Edl Schamiloglu, Distinguished Professor ECE, edls@unm.edu, 505-269-3525
- Business Contact: osp@unm.edu, 505-277-4186

Background: "The Nation has entered an age of warfighting wherein U.S. dominance in air, land, sea, space, cyberspace, and the electromagnetic spectrum (EMS) is challenged by peer and near peer adversaries. These challenges have exposed the cross-cutting reliance of U.S. Forces on the EMS and are driving a change in

[3] This work was sponsored by the Office of Naval Research (ONR), under grant number N00014-23-1-2072. The views and conclusions contained herein are those of the authors only and should not be interpreted as representing those of ONR, the U.S. Navy, or the U.S. Government.

how the DoD approaches activities in the EMS to maintain an all-domain advantage." This is the opening paragraph from the Foreword written by Mark Esper to the October 2020 DOD Electromagnetic Spectrum Superiority Strategy (Fig. 1).[4] This is what is motivating this effort at UNM, advancing HPRF sources to higher frequency.

1. Activities and Accomplishments

Survey of Sources from X-Band to Ka-Band

In our literature review we focused mostly on publications over the last 20 years. The key research groups outside of the US that have published in the literature in the frequency bands 8.2-15.0 GHz, 12.4-18.0 GHz, 18.0-26.5 GHz, 26.5-40 GHz with a minimum of 100 MW output power have been noted.

We are working on PIC simulations of the UESTC RKA in Ka-band to verify its performance indicated in the publications.

Extending the MILO to Higher Frequency

We have designed a 12.25 GHz MILO. The design is a classical one, based on our 1.1 GHz MILO, but scaled. The PIC design is shown in Fig. 1. This operates at 12.5 GHz and it is generating energy in simulations.

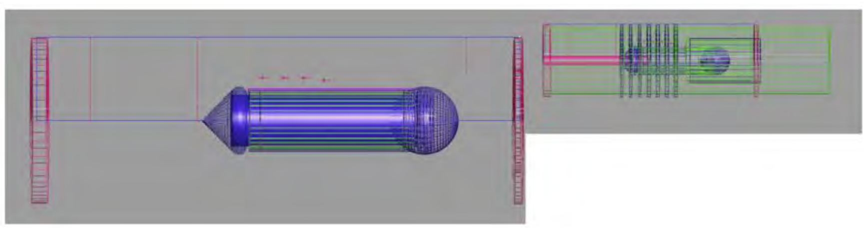

Figure 1. Cut-away cross section of inner part of the 12.25 GHz MILO. This is a modern design incorporating most of the technical features needed for generating high power. The inset shows the cross section of the outer and inner parts of same design.

The device is highly sensitive to initial voltage, risetime as well as peak voltage with this playing a larger role in the operation of the device. Whereas our larger canonical device operates consistently over a broad voltage range, the 12.5 GHz model does not. Even small deviations lead to poor operation. Therefore, the simulations must be carried out with high resolution of the applied voltage. Figure 2 shows the EM fields produced by the model at two different voltages. The abscissa is time with units of nanosecond while the ordinate is the electric field in kV/cm. The first image shows operational behavior that mirrors the canonical design. While the right image shows similar operation at a slightly different voltage. One can see that the startup time is much faster for the optimized applied voltage and if the voltage is varied by a small amount the startup is slow. The radiation pulse completely disappears if the voltage is changed even more. The probes corresponding are on cavity 3 which is the 2nd right most cavity in the figure.

Figure 3 shows the energy distributions of electrons within the model on the above design if the voltage is increased further. First, the startup time increases, and the amplitude of oscillations decreases. The 2nd image shows this behavior explicitly. We do not understand the dynamics leading to this anomalous behavior and why there is such sensitivity. It is possible that our model may be off, the resolution could be

[4] https://media.defense.gov/2020/Oct/29/2002525927/-1/-1/0/ELECTROMAGNETIC_SPECTRUM_SUPERIORITY_STRATEGY.PDF

too low, although we have done our due diligence by looking at the entire model and the parameters of the run and nothing comes out as a problem. It is likely that the dynamics of the crossed field device are closely coupled such that even a small variation in voltage leads to a reduction in magnetic field thereby affecting the crossed field force and this calls for additional analytical investigations.

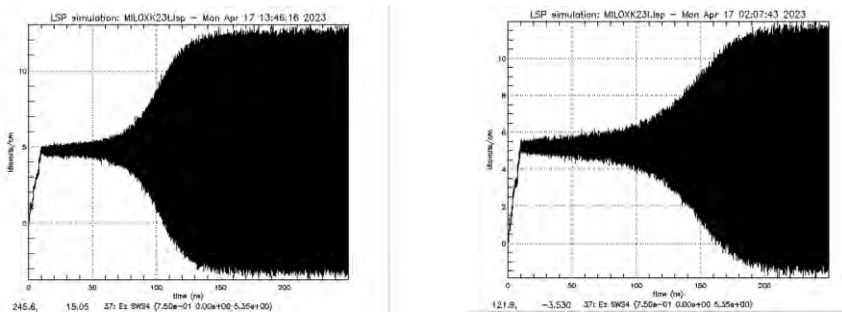

Figure 2. Plots of electric field at cavity four for two different operating voltages, actually very close to each other. There is a very large sensitivity to input voltage variations (these were fairly close to each other) and also to turn-on time.

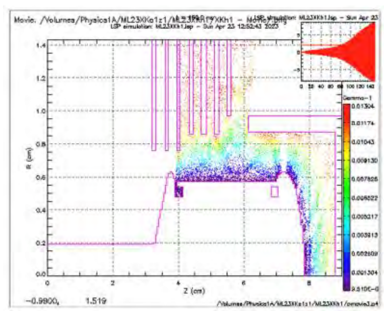

Figure 3. PIC simulations of MILO under very similar conditions with slight voltage variation leading to different behavior and anomalous (yet to be understood) output. The image shows electron particles as a function of energy at a particular snapshot in time.

2. Findings and Conclusions

The literature review gave us a good picture as to what the state-of-the-art is in HPRF sources ranging from X-band to Ka-band. We are working on simulating the Ka-band RKA using our PIC codes. This is in progress. The scaled MILO is very sensitive to voltage, and we are working on trying to understand this sensitivity.

3. Plans and Upcoming Events

We are working on PIC simulations of the UESTC Ka-band RKA to verify its operation.

In Year 2 we will select a device to pursue in experiments at UNM. Our short pulselengths may limit or ability to do this.

Our work has shown that a MILO at much higher frequencies than previously built can be designed. Work remains to be carried out to understand the upper frequency limit and how to mitigate the voltage sensitivity if needed but this lays the foundation for an actual design and build for a device that can be put on a high voltage test bed.

4. Transitions and Impacts

None yet.

5. Collaborations

We are loosely collaborating with the Ukrainian Academy of Science researchers as they have provided their model of a very high frequency HPM source. We are also collaborating with resesearchers at the Technion who are pursuing X-band cross-field devices. We are also in discussion with researchers at Seoul National University to start a collaboration. Our collaborators are indicated in Table 6.

Table 6. List of collaborators.

Agency/Org	Performer	Project Name	Purpose of Research/ Collaboration
NSWCDD	John Kreger, Jack Chen, and Jon Cameron Pouncey	HPM collaboration	We discussed proceeding with MDO and transparent cathode testing at NSWC
AFRL/RX	Steven Fairchild	HPM cathode collaboration	We are discussing collaborative research on HPM cathodes
AFRL/RD	Brad Hoff and Sterling Beeson	HPM cathode and switch collaboration	We are discussing collaborative research on HPM cathodes and pulsed power switches/CsI coatings
Technion, Haifa, Israel	Yakov Krasik and John Leopold	Comparison of magnetic mirror vs. cathode rod and reflector	Optimize suppression of magnetron leakage current via an electron beam in a squeezed state – now in X-band
Weizmann Institute of Science	Yitzhak Maron	Diagnostics	Time-resolved spectroscopic diagnostics in high power, cross-field devices
Drexel University	Genevieve Dion	Cathodes	Large area cathode assembly
DexMat	Dmitri Tsentalovich	Cathodes	Providing base material for sewn cathodes
Verus Research	Sameer Hemmady	MILO	High impact outcomes
Stanford University	Ken Hara	Cathodes, MILO, MDO	Spectroscopy
Texas Tech University	Ravi Joshi	Cathodes, MILO, MDO	Effects of outgassing
Sem-Sol	Peter Duselis	MILO	X-band
Collins Clark Technologies	Collins Clark	Pulser	Potential acquisition of a longer pulse pulser

6. Personnel

Principal investigator – Edl Schamiloglu (0.5-person month)
Co-investigators or Co-PIs – Salvador Portillo (4 person-months), Andrey Andreev (1 person-month), Ahmed Elfrgani (3 person-months)
Business Contact – osp@unm.edu

7. Students

3 undergraduate students supported; no graduate students supported to-date.

8. Technology Transfer

None to-date.

9. Products, Publications, Patents, License Agreements, etc.

Publications resulting from this project:
[Please list all publications or other products in the following order. The format below is that for the Army system and has been used here for your convenience. Other standard reference formats, such as ASME, AIAA, etc. can be used for this report as long as they are complete and consistent.]

Archival Publication (publication reference information (article title, authors, journal, date, volume, issue) can be automatically entered using a DOI)

a. Observation of the Diocotron Instability in a Diode with a Split Cathode

b. Physics of Plasmas
c. Y.P. Bliokh, Ya.E. Krasik, J.G. Leopold, and E. Schamiloglu
d. Keywords: relativistic magnetron, diocotron instability, split cathode, high power microwaves
e. Distribution Statement: Distribution Statement A. Approved for public release: distribution is unlimited.
f. Publication Status: published
g. Publication Identifier Type: ISSN 1070-664X (print); 1089-7674 (web)
h. Publication Identifier: 10.1063/5.0103120
i. Publication Date: December 06, 2022
j. Volume 29
k. Issue
l. First Page Number: 23901
m. Publication Location: Melville, NY
n. Acknowledgement of Federal Support? (Yes, prior award)
o. Peer Reviewed? (Yes)

Archival Publication (publication reference information (article title, authors, journal, date, volume, issue) can be automatically entered using a DOI)

a. Diocotron and Electromagnetic Modes in Split-Cathode Fed Relativistic Smooth Bore and Six-Vane Magnetrons
b. Physics of Plasmas
c. J. G. Leopold, Y. Bliokh, Ya.E. Krasik, A. Kuskov, and E. Schamiloglu
d. Keywords: relativistic magnetron, diocotron instability, split cathode, high power microwaves
e. Distribution Statement: Distribution Statement A. Approved for public release: distribution is unlimited.
f. Publication Status: published
g. Publication Identifier Type: ISSN 1070-664X (print); 1089-7674 (web)
h. Publication Identifier: 10.1063/5.012951
i. Publication Date: January 19, 2023
j. Volume 30
k. Issue
l. First Page Number: 013104
m. Publication Location: Melville, NY
n. Acknowledgement of Federal Support? (Yes, prior award)
o. Peer Reviewed? (Yes)

Archival Publication (publication reference information (article title, authors, journal, date, volume, issue) can be automatically entered using a DOI)

a. Characterizing the High-Power-Microwaves radiated by an axial output compact S-band A6 segmented magnetron fed by a split cathode and powered by a Linear Induction Accelerator
b. Journal of Applied Physics
c. O. Belozerov, Y. Krasik, J. Leopold, S. Pavlov, Y. Hadas, K. Kuchuk, and E. Schamiloglu
d. Keywords: relativistic magnetron, linear induction accelerator, LIA, split cathode, high power microwaves
e. Distribution Statement: Distribution Statement A. Approved for public release: distribution is unlimited.
f. Publication Status: published

g. Publication Identifier Type: ISSN 0021-8979 (print); 1089-7550 (web)
h. Publication Identifier: 10.1063/5.0138769
i. Publication Date: April 05, 2023
j. Volume 133
k. Issue
l. First Page Number: 133301
m. Publication Location: Melville, NY
n. Acknowledgement of Federal Support? (Yes, prior award)
o. Peer Reviewed? (Yes)

Archival Publication (publication reference information (article title, authors, journal, date, volume, issue) can be automatically entered using a DOI)

a. Frequency Agility in the 24-Cavity Relativistic Magnetron with Diffraction Output Using Rectangular Void Ring Metamaterials
b. IEEE Transactions on Plasma Science
c. M. Liu, C. Liu, E. Schamiloglu, Y. Li, X. Liu, Q. Wu, and W. Jiang
d. Keywords: relativistic magnetron with diffraction output, metamaterials, high power microwaves
e. Distribution Statement: Distribution Statement A. Approved for public release: distribution is unlimited.
f. Publication Status: published
g. Publication Identifier Type: ISSN 1939-9375
h. Publication Identifier: 10.1109/TPS.2023.3279430
i. Publication Date: July 04, 2023
j. Volume 51
k. Issue
l. First Page Number: 1917
m. Publication Location: Piscataway, NJ
n. Acknowledgement of Federal Support? (Yes, prior award)
o. Peer Reviewed? (Yes)

Archival Publication (publication reference information (article title, authors, journal, date, volume, issue) can be automatically entered using a DOI)

a. Guest Editorial Special Issue—Golden Anniversary of TPS
b. IEEE Transactions on Plasma Science
c. E. Schamiloglu
d. Keywords: plasma science
e. Distribution Statement: Distribution Statement A. Approved for public release: distribution is unlimited.
f. Publication Status: published
g. Publication Identifier Type: ISSN 1939-9375
h. Publication Identifier: 10.1109/TPS.2023.3292333
i. Publication Date: July 2023
j. Volume 51
k. Issue
l. First Page Number: 1583
m. Publication Location: Piscataway, NJ
n. Acknowledgement of Federal Support? (Yes)
o. Peer Reviewed? (Yes)

Conference Paper

a. Experiments on A6 Relativistic Magnetron Fed by a Solid Cylindrical Cathode: 350 MW of High-Power Microwaves at 4.675 GHz (2π-mode) During 25 ns for Directed Energy (DE) and Non-DE Applications
b. A. Andreev, C. Rodriguez, M. Felix, and E. Schamiloglu
c. 24th IEEE International Pulsed Power Conference
d. June 25-29, 2023
e. San Antonio, TX, USA
f. Published
g. November 13, 2023
h. Publication Identifier Type – unknown
i. 10.1109/PPC47928.2023.10310900
j. Acknowledgement of Federal Support? (Yes)

Conference Paper

a. The Diocotron Mode Develop- ing in a Smooth Bore Coaxial Diode and the Electromagnetic Modes in a Six-Vane Magnetron Fed by a Split Cathode
b. J. Leopold, Y. Bliokh, Ya.E. Krasik, A. Kuskov, and E. Schamiloglu
c. 24th IEEE International Pulsed Power Conference
d. June 25-29, 2023
e. San Antonio, TX, USA
f. Unpublished
g. November 13, 2023
h. Publication Identifier Type – unknown
i. N/A
j. Acknowledgement of Federal Support? (Yes)

Conference Paper

a. Recent High Power Electromagnetics Research at the University of New Mexico
b. E. Schamiloglu and C. Christodouloue
c. ICEAA (International Conference on Electromagnetics in Advanced Applications 2023)
d. October 09-13, 2023
e. Venice, Italy
f. Published
g. October 31, 2023
h. Publication Identifier Type – unknown
i. 10.1109/ICEAA57318.2023.10297686
j. Acknowledgement of Federal Support? (Yes)

Book

a. Recent Advances in High Power Electromagnetics
b. F. Vega, N. Mora, E. Schamiloglu, and C. Kasmi
c. First
d. Volume
e. IET
f. 2024
g. London, England
h. awaiting publication

i. Publication Identifier Type – unknown
j. Publication Identifier – unknown
k. Acknowledgement of Federal Support? (Yes)

Book Chapter

a. Reference Manual on Scientific Evidence
b. Chapter 17, Engineering
c. C. Abdallah, B. Black, and E. Schamiloglu
d. Fourth Edition
e. Volume
f. National Academies Press
g. 2024
h. Washington, DC
i. Editor - Unknown
j. Publication Status: awaiting publication
k. Publication Identifier Type – unknown
l. Publication Identifier – unknown
m. Acknowledgement of Federal Support? (No)

Theses - None

Websites

a. Directed Energy Center at the University of New Mexico (DEC@UNM)
b. https://dec.unm.edu/
c. This website is currently under development and will be fully developed by March 01, 2024

Patents – None

Other Products: None

10. Point of Contact in Navy

Dr. Jon Cameron Pouncey
Engineer
HPM Technology Development Branch E52
NSWC DD
jon.c.pouncey.civ@us.navy.mil
Desk: 540-653-2882
Cell: 540-604-6679

Last contact was in-person visit at the University of New Mexico. We have been emailing frequently.

ONR Young Investigator Program (YIP) Reports

Direct Generation of Electromagnetic Radiation with a Compact, Air-Stable, Optically Modulated Electron Emitter

Grant No. N00014-21-1-2634

Annual Report for Fiscal Year 2023

Period of Performance: October 1, 2022 – September 30, 2023

Prepared by:
Prof. Rehan Kapadia, Principal Investigator
University of Southern California
Dept. of Electrical and Computer Engineering
3737 Watt Way, PHE 626
Los Angeles, CA, 90089-0271
Tel: (213) 821-0845
Fax: (213) 740-8677
Email: rkapadia@usc.edu

This work was sponsored by the Office of Naval Research (ONR), under grant (or contract) number N00014-21-1-2634. The views and conclusions contained herein are those of the authors only and should not be interpreted as representing those of ONR, the U.S. Navy or the U.S. Government.

Grant or Contract Number: N00014-21-1-2634
Date Prepared: 1/20/2024
Project Title: Direct Generation of Electromagnetic Radiation with a Compact, Air-Stable, Optically Modulated Electron Emitter
Annual Summary Report: FY23
Principle Investigator: Rehan Kapadia, 213-821-0845, rkapadia@usc.edu, University of Southern California
Section I: Project Summary

1. Overview of Project

1.1 Abstract

In this report, we will cover the objectives, background, accomplishments, and future plans for the grant titled "Direct Generation of Electromagnetic Radiation with a Compact, Air-Stable, Optically Modulated Electron Emitter". Through this grant we aim to demonstrate a new type of electron source that enables rapid modulation of emitted electron density but allows the use of established telecommunications photon sources to excite the electron source. In this way, an optical signal imprinted on the incident photon source can be converted into an elecron density modulation. Using this density modulated electron beam, we then aim to design a vacuum electron device that can convert the density modulated electron beam into a high-power RF signal.

1.2 Objective

The first goal of this proposal is to continue to develop and demonstrate a simple *planar* silicon-insulator-graphene structure to create an air-stable, *electrically tunable*, negative electron affinity surface by applying a bias between the graphene and silicon, termed Hot Electron Light Assisted Cathode (HELAC). A continuous or pulsed photon source may then be used to excite electrons in the silicon, which will then be emitted into vacuum when a small (4-10 V) bias is applied across the device. This electron source can be compact, environmentally robust, and use low energy photons in the near-IR to visible range. Based on initial simulations, modulation frequencies of
>250 GHz and 1 A/cm^2 emission currents should be achievable through device optimization. Initial experimental prototypes have already demonstrated 1 mA/cm^2, despite a relatively unoptimized structure.

Using this electron source, we will then design and build a device similar to an Inductive Output Tube (IOT), where an electron beam is density modulated by incident light, then accelerated to a desired voltage, and finally RF power is extracted from the beam using an output cavity. We refer to this device as a Light Modulated IOT (LM-IOT). Unlike IOTs, which have frequency and total current limitations due to the grid-cathode spacing and uniformity, this approach is expected to overcome those issues by eliminating the need for a grid and input cavity. We will build a prototype LM-IOT, where the beam generation, confinement, and collector segments are fixed, and the output frequency will be determined by swapping output cavity. Specifically, we will carry out simulations to establish basic operation principles, design the overall device, and then fabricate and assemble the device. This will be used to establish the proof of principle operation for LM-IOTs as well as make projections about device parameters.

Finally, we aim to explore multi-frequency devices, where we simultaneously excite the electron emitter with multiple modulation frequencies, creating an electron beam with multiple frequencies, and then use multiple output cavities to extract and emit those frequencies separately. In this task, the goal is to understand interaction between multifrequency beams and multiple cavities, the limitations in power distribution between frequencies, and any non-linear effects due to the electron source itself that could take two input frequencies and generate different output frequencies. These limits would be driven by a combination of the physics of the electron source and the beam-cavity interactions.

1.3 Background

The

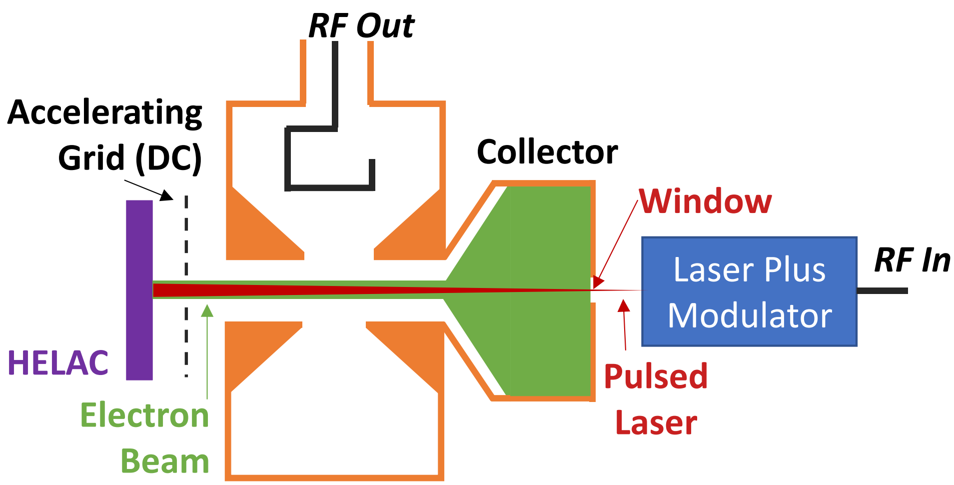

Figure 1: A schematic view of our device. In this structure, the cathode (HELAC) is excited by a modulated laser beam, generating a density modulated electron beam. This beam is accelerated by a grid held at a DC bias. The beam will then pass through an RF cavity to extract the high frequency content of the beam. The HELAC will be excited by a laser beam that travels in reverse through the electron beam tunnel. The size of the laser spot on the cathode, and therefore the area of the beam will be determined by the divergence of the spot, which can be tuned by an optical lens at the source.

modern day congested and contested electromagnetic spectrum has placed stringent demands on electronic systems[1, 2]. A single electromagnetic (EM) source that change transmission bands, multiple frequencies, or even frequency bands, and be able to quickly switch frequencies when the desired communication channels becomes contested is of value in a contested environment. Additionally, directed EM sources which can temporarily or permanently deny communications are of significant value. One approach to this may be the direct generation of EM radiation from a modulated electron source. This approach could enable compact, high-frequency, high-power HPM sources which could serve the needs of directed energy systems[3-14]. An Inductive Output Tubes (IOT) is a source which utilizes a directly modulated, where a continuous beam of electrons is modulated by a grid, and an output cavity converts the high frequency component in the beam to electromagnetic radiation. IOTs, however, use a high voltage grid which couples to an input RF signal, this limits the frequency of operation due to electron transit time between the grid and cathode, and also limits scaling of the cathode due to grid spacing uniformity requirements. Here, we propose utilizing an optically modulated cathode technology to directly create a density modulated electron beam, and then extract the high frequency content from the beam using an output cavity. By eliminating the use of a grid to modulate the electron density, this approach would enable (i) higher frequency operation, (ii) larger cathodes for increased drive current, (iii) higher beam voltages, (iv) a reduction in size and weight, and (v) multi-frequency operation from a single device.

Electron emission cathodes are used in a wide variety of applications, including but not limited to, electron microscopes[15, 16], electron beam lithography[17], space propulsion[18], high power microwave (HPM) devices[19-21,], free electron lasers[22], and displays[23]. HPM sources for millimeter-wave and terahertz radiation are of great interest for military and defense applications such as radar, electronic counter measures, and communications[20, 24]. While photo-assisted field emission devices have been explored in the past[25,26,27,28,29], as promising high frequency emitter, these are generally studied utilizing free-space optics to directly focus a laser on a tip or tip array, and use p-type silicon to enable photogating of field emission. Recently, simulation and experimental results have shown that optically driven emitters[30-37] could play a valuable role in cathodes for high power microwave and vacuum electron devices in general.

2. Activities and Accomplishments

We have carried out activities focused on (i) HELAC development, (ii) electron gun and LM-IOT development, (iii) HELAC simulation, and (iv) IOT simulation.

a) Rear Junction Contact Resistance Studies

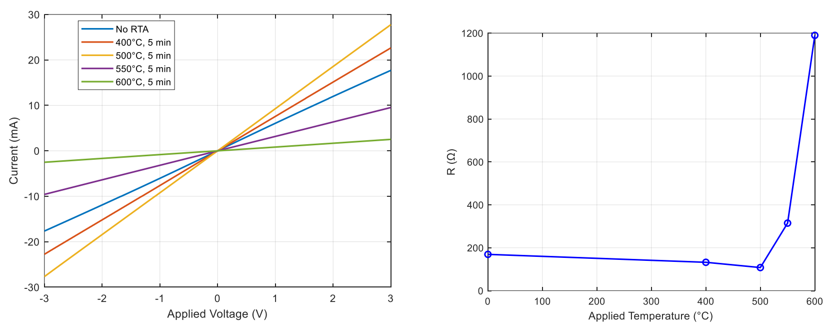

Figure 2: Two terminal contact resistance test results. I-V plots for various temperature (left). Contact resistance vs. RTA temperature plot (right)

To reduce the contact resistance at the back contact-semiconductor junction, we are carried out contact anneal studies as summarized in Figure 2. The aluminum forms an ohmic contact with the p-type semiconductor for this case as $\Phi_{Metal} > \Phi_{Semi}$. But annealing introduces a heavily doped layer immediately below the metal semiconductor junction. Higher temperature causes carriers from metal to diffuse to the semiconductor side and that contributes to the doping of the area near the interface of the semiconductor

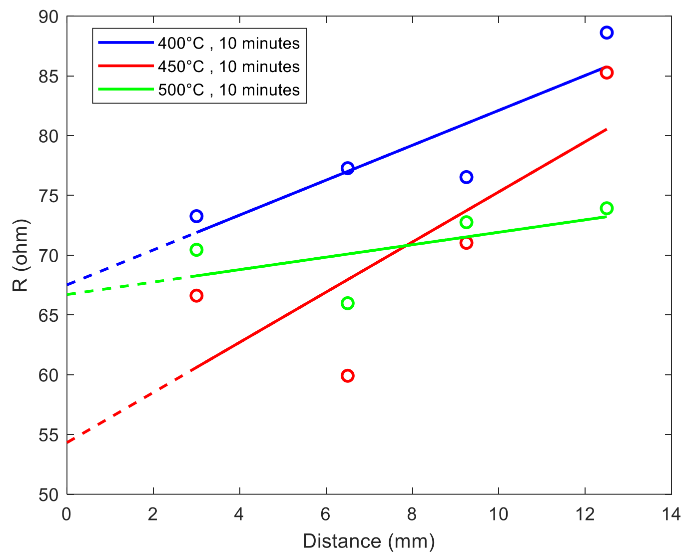

Figure 3: TLM measurement results for various temperature RTA. Best temperature was found to be 450°C

and the metal. This reduces the resistivity of the contact resulting in the overall reduction of the series resistance of a device.

One of the key limiting factors towards getting faster emission from our HELAC devices is the series resistance (R_s). The high resistance increases the RC constant of the overall system, and as a result, we are having a slower response. By reducing the R_s we will be able to get higher frequency optical modulation response from our HELAC devices. Rapid thermal annealing (RTA) for various temperatures and durations was tested and characterized. Both the two-terminal resistance test and TLM (Transfer Length Method) measurements indicated that annealing at 450°C - 500°C for several minutes reduces the contact resistance as shown in Figure 3.

(b) Atomic Layer Deposited Al_2O_3 dielectrics for HELACs

We explored structures of HELACs using Al2O3 tunnel oxide layer deposited using Atomic Layer Deposition (ALD) technique as these gave us ~90 uA of emission current (Fig. 4). We are trying to optimize the structure to get stable high emission current from these devices. One issue that we are facing is, these devices tend to display increased leakage current after applying a certain amount of voltage. These likely occur because as we are applying high electric fields across the oxides introducing defect states that cause conduction. Due to these newly introduced defects, we often see the oxide layer will eventually fail. Therefore, we need an oxide layer that has less defects and hence lower tendency to breakdown. We are now exploring devices with dry thermal oxide (SiO2) tunnel oxide. As the dry oxidation results in more controlled, dense and cleaner thin oxide layers, the breakdown field is much higher. Our experiments also verify the results (Fig. 5). Although we applied high electric field across these devices, they did not exhibit leakage. The dark diode current plot shows that the device maintained its performance under high voltage across the oxide and showed negligible hysteresis which is promising. The emission current is however, lower than previously measured.. We are planning to deposit ALD Al2O3 on top of dry thermal SiO2 to get a combined effect of the two materials.

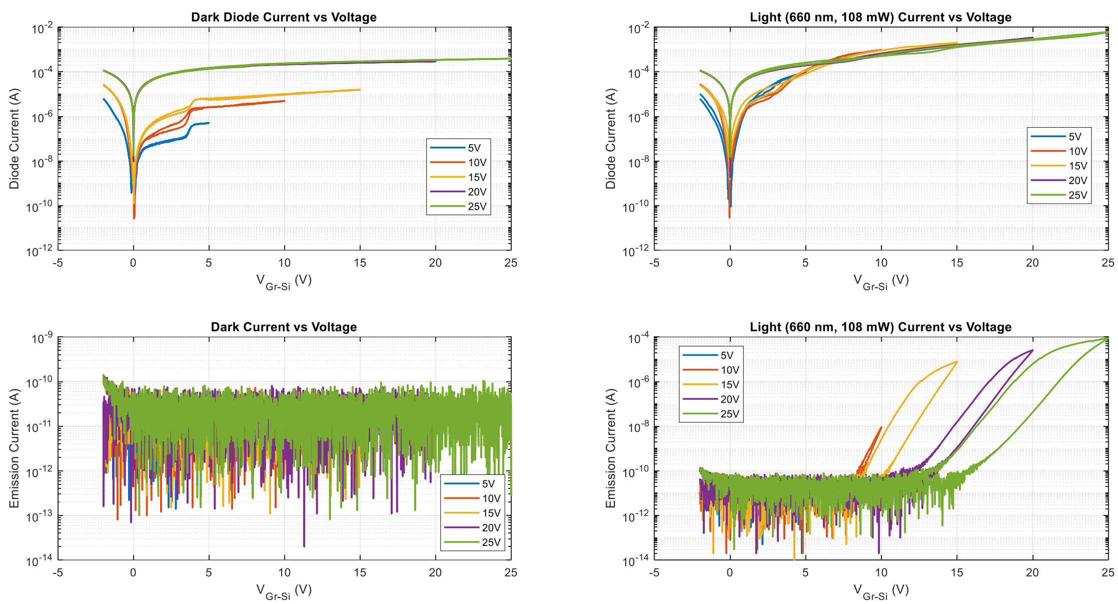

Figure 4: I-V characteristics of HELAC with Al2O3 Tunnel Oxide. Diode I-V plot at dark (top left). Diode I-V plot with light excitation (top right). Emission I-V plot at dark (bottom left). Emission I-V

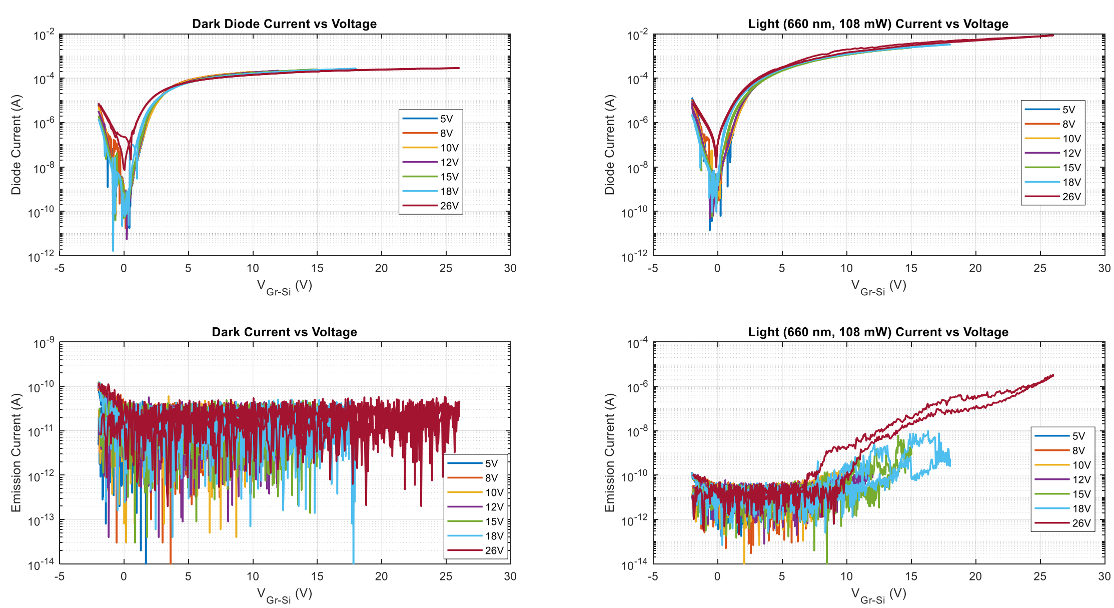

Figure 5: I-V characteristics of HELAC with dry thermal SiO2 Tunnel Oxide. Diode I-V plot at dark (top left). Diode I-V plot with light excitation (top right). Emission I-V plot at dark (bottom left).

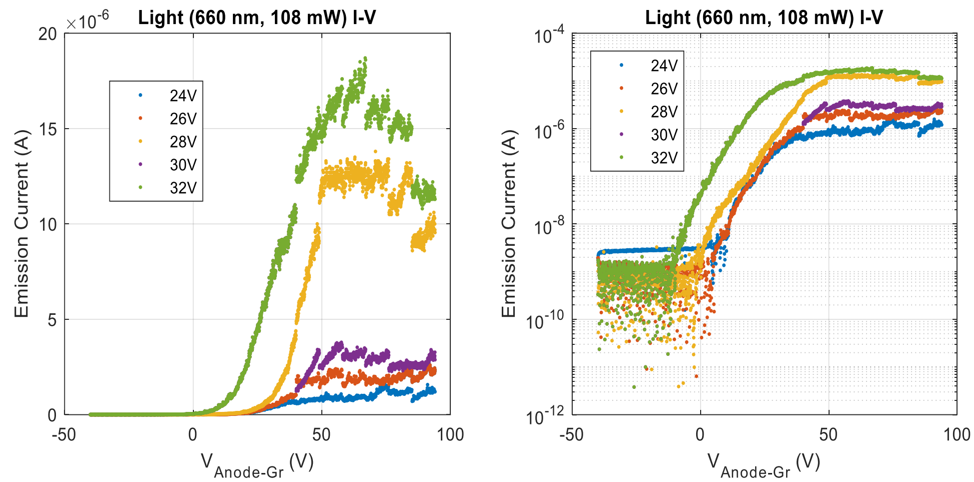

Figure 6: Results of HELAC with SiO2 Tunnel Oxide in Anode Voltage Sweep Experiment. Linear plot (left), Log scale plot (right)

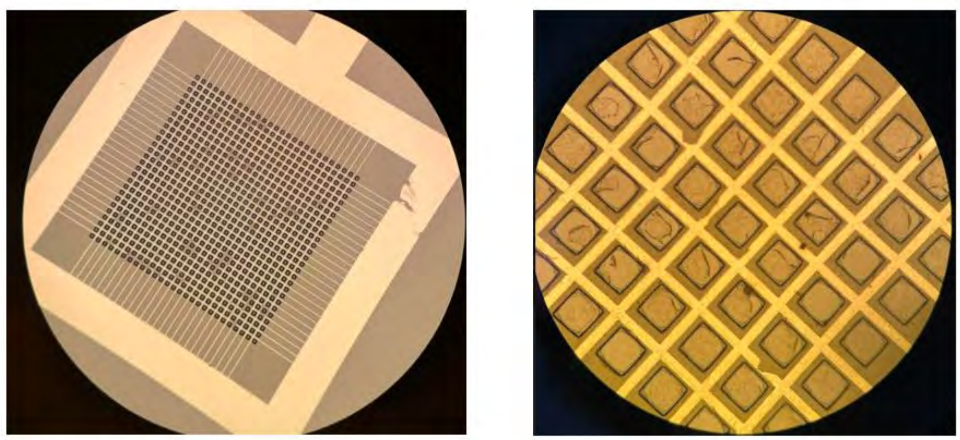

Figure 7: Fabricated gridded or mesh HELAC structure, each active area here is 10um x 10um (left). Zoomed in picture with transferred graphene on top (right).

Additionally, by carrying out an anode voltage sweep (Figure 6), we see two interesting results from our SiO_2 devices. Two intriguing results from this measurement are shown in Figure 6. First as we increase the extraction voltage from 0V – 100 V, we see a significant increase in the emission current. This suggests that while these devices are indeed acting as photoemitters, there is also a field based component in the emission.

(c) Gridded HELAC fabrication to reduce series resistance

We have explored HELACs with dry thermal SiO_2 tunnel oxide layer with resulting mesh structure shown in Figure 7. This better quality oxide has lower amount of defects and traps and showed much higher breakdown fields and time to breakdown. These devices also sustained under comparatively higher electric field. One challenge that we face with these devices is a large series resistance in the device I-V characteristics that dominates the diode behavior. We believed the reason behind it is the resistance introduced by graphene. To reduce this challenge, we are fabricating HELACs having a mesh like structure where we have an array of smaller active areas. These smaller HELACs are connected in parallel to each other. So as a result, the overall resistance of the device decreases. So it is expected that faster HELAC devices could be made in this way.

(d)

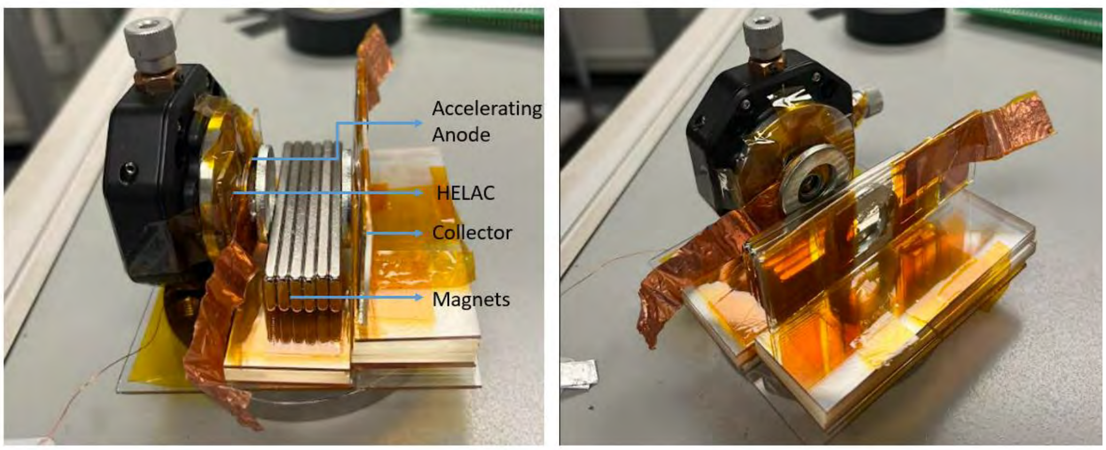

Figure 8: V0.1 LM-IOT setup without the output cavity

Accelerating structure/electron gun design for LM-IOT

We have started developing the Light Modulated Inductive Output Tube (LM-IOT) setup and in the past month have made progress in building the necessary components. In order to induce electron emission, we have applied a laser through an ITO glass collector on our Hot Electron Laser Assisted Cathode (HELAC). Our prior calculations and simulations have indicated the requirement for an accelerating anode to generate a sufficiently high electric field for the extraction and acceleration of the emitted hot electrons from the HELAC. To focus and direct the electron beam towards the collector, magnets have been used to create the necessary magnetic field. According to our simulations a uniform magnetic field of at least 200mT throughout the beam path is required to collimate the electron beam. As for this primary test setup shown in Figure 8 we are using neodymium magnets we were only able to apply ~150mT and it's quite non-uniform at this point. We intend to use solenoid for applying the uniform magnetic field and also place an output cavity between the accelerating anode and collector in the future to extract RF signal from the modulated electron beam. Preliminary results indicate that optimization of the magnet setup is required to ideally collimate the electron beam and maximize carrier collection in the collector. The results attached in Figure 9 illustrates the current collection at different positively biased nodes in the setup. As the system is not properly optimized yet, we can observe a part of the emitted electrons are collected at the accelerating anode. Our target is to reduce it down to a negligible amount by properly focusing the electron beam.

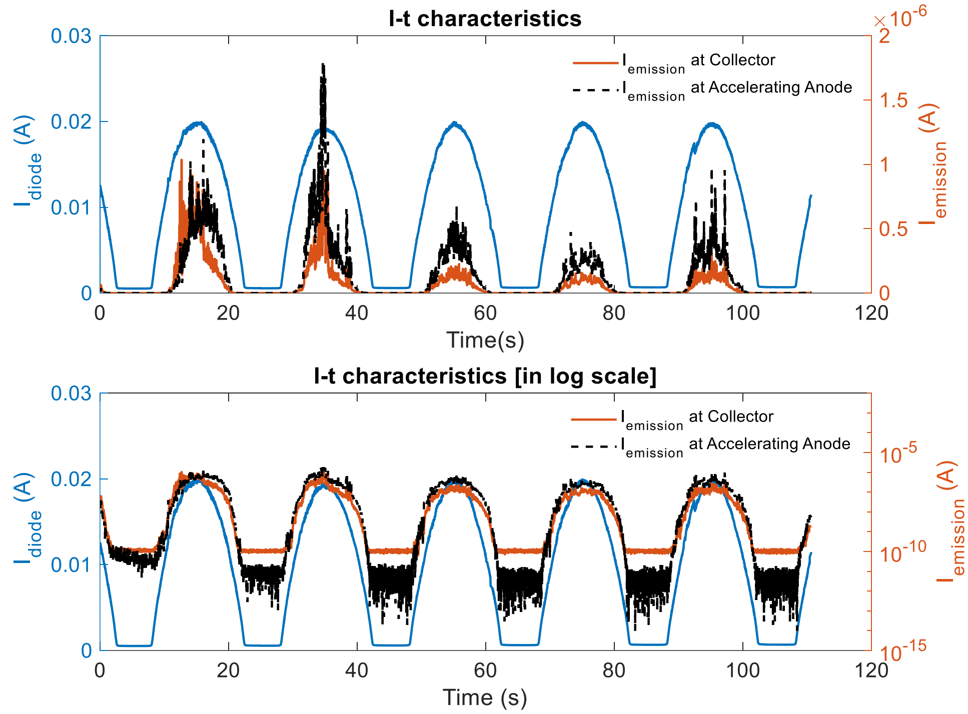

Figure 9: I-t characteristics of HELAC in response to sinusoidally modulated optical beam in linear sale (top) and in log scale (bottom)

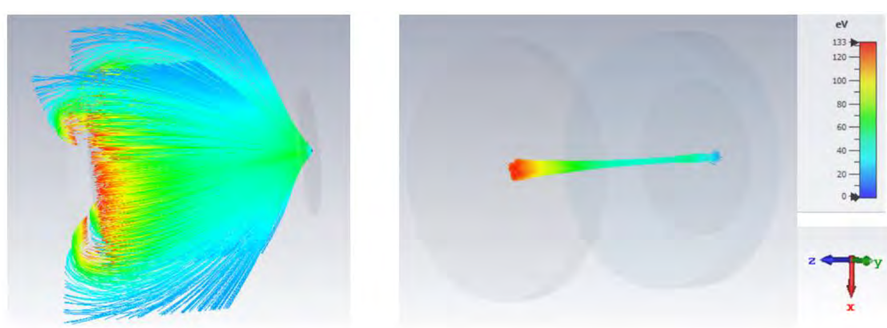

Figure 10: Electron trajectory without any magnetic field and unoptimized parameters (left). Electron trajectory with 0.5 T magnetic field, optimized accelerating anode voltage and spacing between the magnet and emitter (right)

(e) CST Simulations and design of Light Modulated Inductive Output Tube (IOT) Simulation and Experiment

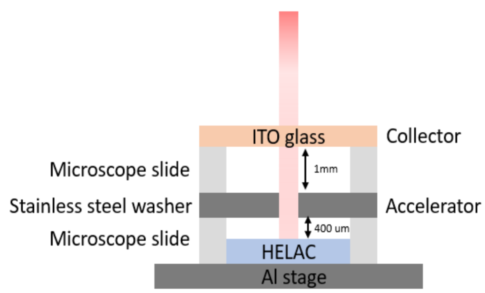

Figure 11: Proof-of-concept LM-IOT structure setup.

Our IOT will have an electron emitter, an annular accelerating anode that will create enough electric field to extract the electrons, a magnet or solenoid to keep the electron beam focused, a cavity for extracting the RF power and a collector. Figure 10 shows CST simulations without the cavity to find the optimum parameters such as accelerating anode voltage, required magnetic field and spacing between the magnet and emitter. Figure 11 shows a proof-of-principle experiment carried out to explore the effect of focusing magnets on the electron beams from the HELACs, and the HELAC.

3. Findings and Conclusions

We have identified several critical factors that determine the behavior of HELACs, including an understanding of what determines quantum efficiency, temporal response, and stability. We have also begun to fabricate the LM-IOT and have identified challenges associated with integrating these cathodes into guns, and taken steps to overcome those challenges. These set the stage for the completion and testing of the entire system.

4. Plans and Upcoming Events

We are currently planning on completing our electron gun fabrication experiments and testing laser modulated emission this year. We expect to be able to obtain the first VED/HPM device based generation of radiation from laser-modulated cathodes.

5. Transitions and Impacts

We presently do not have any transitions but aim to share the emission devices fabricated in our group beyond the present collaborations as noted in section 6.

6. Collaborations

Our collaboration with Prof. Peng Zhang at MSU has continued and grown. Previously, his team is theoretically exploring material combinations and structures that may be used to improve our device performance. This resulted in a theory paper on how a tunneling can be used to dramatically improve emission energy spread for field emitters. Now we are exploring how structured electron beams from optically modulated cathodes can be used to generate radiation. This collaboration is also aided by the support of Dr. Carter Armstrong, who periodically joins our meetings and offers invaluable suggestions on how we can do DoD and industrially relevant work.

We also have an on-going collaboration with Prof. John Booske and Prof. Nader Behdad where we send them HELAC devices for use in x-ray generation devices for the purposes of communications. We have sent them some multiple generations of HELACs, and they are doing testing on those devices. There have been interesting results on thermionic emission from these devices as a result of this collaboration.

7. Personnel

Principal investigator: Rehan Kapadia, 2 person months, NA Member: N
Business Contact: Cindy Huynh (cynthimh@usc.edu)

8. Students

A total of 4 Graduate students have assisted with this work: Subrata Das, Hyun Uk Chae, Ragib Ahsan, and Anika Tabassum.

9. Technology Transfer

We have previously applied for a patent on the general HELAC structure, U.S. Serial No. 17/940,113, but have not applied for any more this year.

10. Products, Publications, Patents, License Agreements, etc.

Conference Papers

a. Hot Electron Laser Assisted Cathode by Electronically Tunable Negative Electron Affinity Surfaces – Prospects and Challenges
b. Hyun Uk Chae, Anika Tabassum Priyoti, Juan Sanchez Vazquez, Ragib Ahsan, and Rehan Kapadia
c. 24th International Vacuum Electronics Conference
d. 4-26-2023
e. Chengdu, China. (Presentation given remotely)
f. Publication Status: Awaiting publication
g. Publication Date
h. Publication Identifier Type
i. Publication Identifier
j. Acknowledgement of Federal Support? Yes

a. An Air stable, electronically tunable negative electron affinity silicon photocathode
b. Anika Tabassum Priyoti, Ragib Ahsan, Hyun Uk Chae, Juan Sanchez Vazquez, Subrata, Das, and Rehan Kapadia
c. 24th International Vacuum Nanoelectronics Conference
d. 7-10-2023
e. Cambridge, MA
f. Publication Status: Awaiting publication
g. Publication Date
h. Publication Identifier Type
i. Publication Identifier
j. Acknowledgement of Federal Support? Yes

a. A vacuum insulator negative electron affinity electron emitter with high quantum efficiency

b. Juan Sanchez Vazquez, Anika Tabassum Priyoti, Ragib Ahsan, Hyun Uk Chae, and Rehan Kapadia
c. 24th International Vacuum Nanoelectronics Conference
d. 7-10-2023
e. Cambridge, MA
f. Publication Status: Awaiting publication
g. Publication Date
h. Publication Identifier Type
i. Publication Identifier
j. Acknowledgement of Federal Support? Yes

Patents

a. None

11. Point of Contact in Navy

Matthew McQuage, updated via email Jan 19th 2024.

Surface Breakdown and Plasma Formation in Cross-Field High Power Microwave Sources

Grant No. N00014-21-1-2698

Annual Report for Fiscal Year 2023

Period of Performance: October 1, 2022 to September 30, 2023

Prepared by:

Professor Ken Hara, Principal Investigator
Assistant Professor, Department of Aeronautics and Astronautics
Stanford University
DURAND 252
Stanford, CA 94305
Tel: (650) 725-6309
Email: kenhara@stanford.edu

This work was sponsored by the Office of Naval Research (ONR), under grant number N00014-21-1-2698. The views and conclusions contained herein are those of the authors only and should not be interpreted as representing those of ONR, the U.S. Navy or the U.S. Government.

Grant or Contract Number: N00014-21-1-2698
Date Prepared: January 18, 2024
Project Title: Surface breakdown and plasma formation in cross-field high power microwave sources
Annual Summary Report: FY23
Principle Investigator: Ken Hara, 650-725-6309, kenhara@stanford.edu, Department of Aeronautics and Astronautics, Stanford University

Section I: Project Summary

1. Overview of Project

Plasma dynamics in high power microwave (HPM) sources are considered a detriment to the operation of vacuum electronic devices (VED) to generate electromagnetic signals. The formation and existence of the plasma flows become more and more critical, particularly when operating the HPM sources at a high-frequency range, which is of great interest to the future of U.S. naval missions. While HPMs theoretically must operate in high vacuum conditions, due to available materials and operating conditions, outgassing can occur from materials. This issue becomes more problematic for compact HPM devices because the volume-to-area ratio worsens, and the plasma-wall interactions greatly influences the electromagnetic wave properties. For instance, pulse shortening of the microwave output signal due to gap closure and lifetime of the device can highly depend on the charged particles[5]. A self-consistent plasma simulation model is required to understand the power scaling of these devices as they operate at higher applied voltages up to a few hundred volts or megavolts.

The goal of this research project is to advance the understanding of surface breakdown and plasma formation in cross-field HPM devices. Specific research objectives include: (**R-I**) to develop and test electromagnetic plasma fluid and kinetic models; (**R-II**) to characterize the space charge limited sheath due to the plasma formation near explosive emission cathodes; and (**R-III**) to investigate the anode plasma formation and radiofrequency wave-driven surface breakdown mechanisms.

2. Activities and Accomplishments

a. Plasma formation in anode-cathode gaps

To study the plasma formation and expansion, a 1D particle-in-cell Monte Carlo collision (PIC-MCC) simulation model is developed, assuming that due to the surface flashover mechanism, a thin neutral layer of gas forms near the cathode. Specifically, we investigate the effect of the outgassed neutral layer, collisions (electron-neutral, ion-neutral, and Coulomb collisions), and different waveforms on plasma formation and expansion. Coulomb collisions are included using the Langevin approach. We have reviewed the papers carefully and propose a modification to the existing methodology. The 1D PIC-MCC simulation includes a self-consistent Fowler-Nordheim field emission (FNFE) current[6] from the velvet cathode, which ionizes the outgassed neutral layer from the velvet material, forming plasma. The development of the model is aligned with R-I (development of a plasma model) and the study conducted using the PIC-MCC model is aligned with R-II (the investigation of cathode plasma formation).

We report the simulations assuming the following assumptions. Neutral layer[7] is atomic hydrogen and 100 μm thick with density of $1.3\text{x}10^{23}$ m^{-3} . Field enhancement parameter (β) is assumed to be 500[8]. It was

[5] Hadas et al., *J. Appl. Phys.* 104, 064125 (2008); Rose et al., *Phys. Plasmas* 20, 034501 (2013)
[6] Feng et al., Phys. Plasmas, 15, 043301 (2008)
[7] Miller, J. Appl. Phys. 84, 3880–3889 (1998)
[8] Kobayashi et al., Appl. Surf. Science 146, 148-151 (1999)

observed from our simulation that FNFE cannot ignite plasma without the inclusion of a field enhancement factor (β) to account for micro-protrusions. AK gap is 1 cm and we varied the cell size from 400 to 40000 for grid convergence. Voltage pulse has a 20 ns ramp up, 40 ns flat top at 600 kV, and 40 ns ramp down.

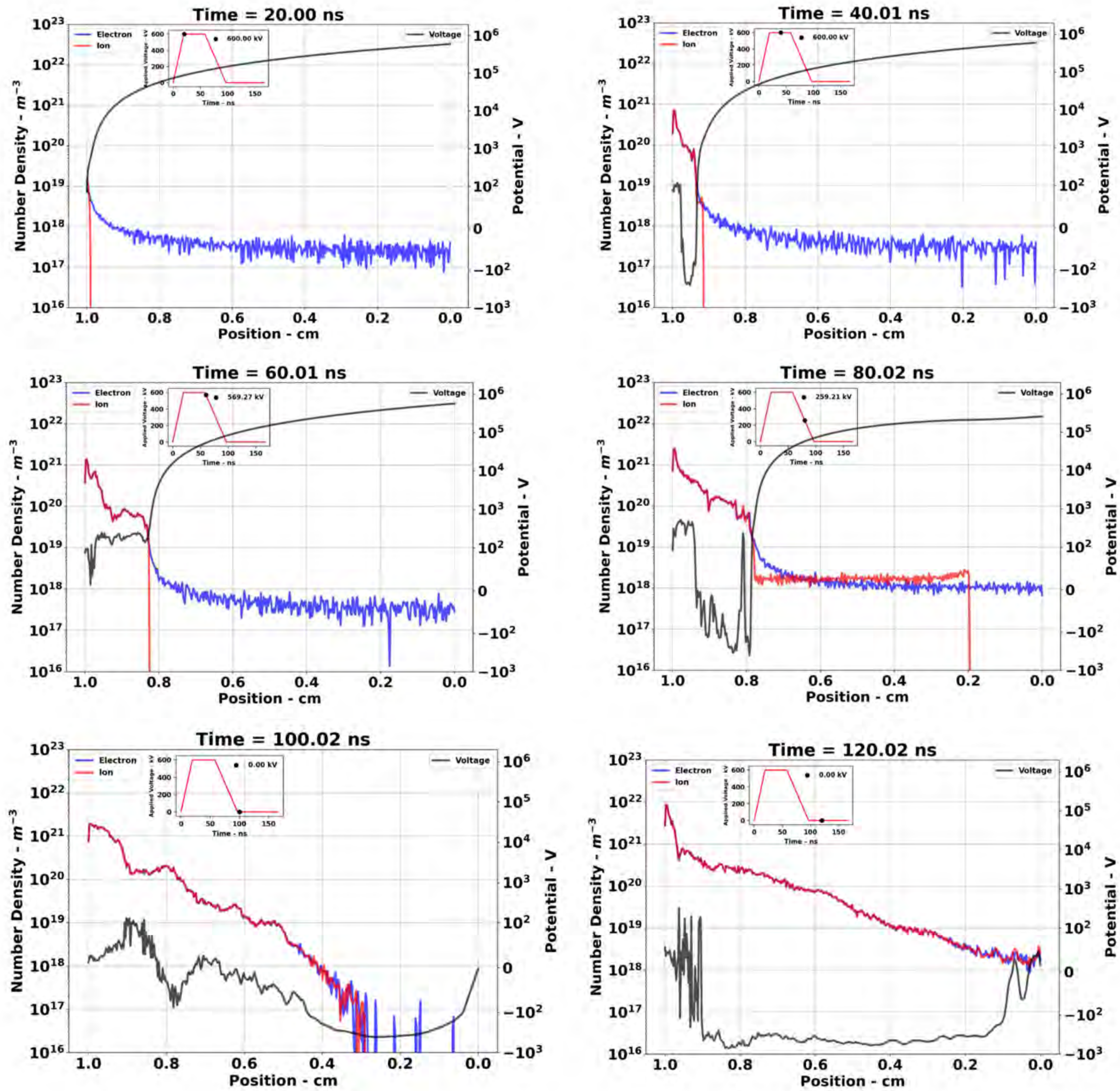

Figure 1. Snapshot of plasma properties at different stages of pulse

Snapshots of plasma density (electron & ion) and the plasma potential at 20 ns intervals in the AK gap are shown in Figure 1. The anode and cathode are located at x = 0 and 1 cm, respectively. A quasineutral plasma formation is observed during the pulse and the propagation of this plasma front from the cathode to the anode can be seen. During the pulse, the plasma front speed during the generation phase from the 1D PIC-MCC simulation is 7.26 cm/μs, which agrees well with experimental observations[9] (1-10 cm/μs). In addition, we observe a faster self-expansion speed towards the end of the pulse (51.89 cm/μs) due to diffusion.

A grid-convergence study was conducted to resolve the Debye length and study the effect of grid size on the simulation results. The high plasma density near the cathode leads to low Debye lengths close to the

[9] Shefer et al., The Phys. of Fluids 31, 930-939 (1988)

cathode. On the other hand, the high acceleration of the electron beam in the high-applied voltage setup leads to relativistic electrons near the anode, violating the CFL condition. If we are to resolve both the Debye length near the cathode and CFL condition near the anode in our simulations, we must use variable grid size PIC-MCC code, which we can investigate as future work.

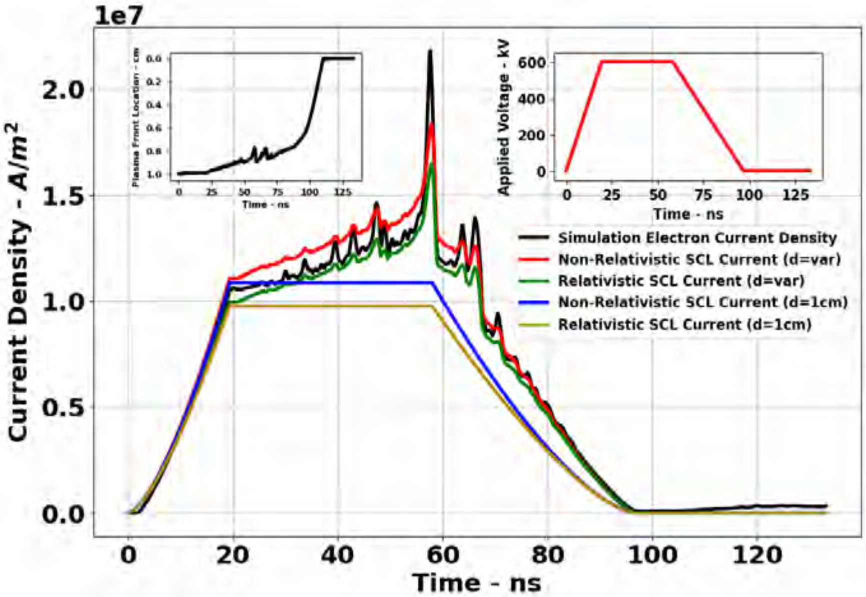

Figure 2. Comparison of simulation current density with space charge limited (SCL) theory.

The electron current density in the simulation was computed and compared with the theoretical space charge-limited current density value, as shown in Figure 2. The simulations show good agreement with the relativistic SCL current theory if we account for cathode plasma expansion leading to a lower AK gap.

b. Plasma sheaths for magnetized plasmas

Using a different 1D particle-in-cell (PIC) simulations, the plasma sheath with an applied oblique magnetic field has been studied. The results showed that monotonic sheaths could be obtained by injected ions along the magnetic field while meeting the Bohm condition normal to the wall for field angles $\theta \leq 70°$ and for higher field angles a standing potential oscillation is observed at the injection and/or near the sheath edge. Note that $\theta = 90°$ is parallel to the wall. For $\theta \geq 50°$, the sheath potential drop decreases with increasing field angle. The most significant observation from the PIC results is the unique truncation of the electron VDF. The electron sheath edge VDF has a cone-shaped truncation due to the electron gyromotion near the wall; the gyration causes for electrons to be absorbed by the wall before they can be repelled. An example of the cone-shaped truncation is seen in Fig. 3 for various magnetic field angles.

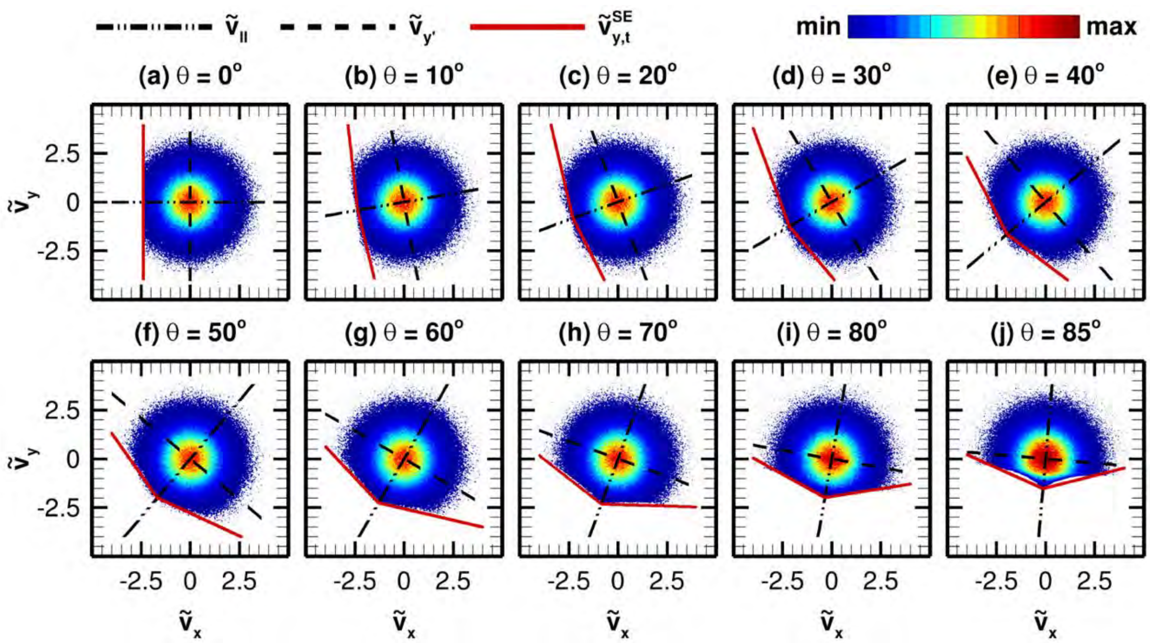

Figure 3. Sheath edge electron VDFs for various magnetic field angles.

From the PIC simulation results, we constructed a plasma sheath theory for magnetized plasma to discuss the Bohm condition. As shown in Figure 4, the ion bulk velocity at the sheath edge and the sheath potential are obtained as a function of the magnetic field angle.

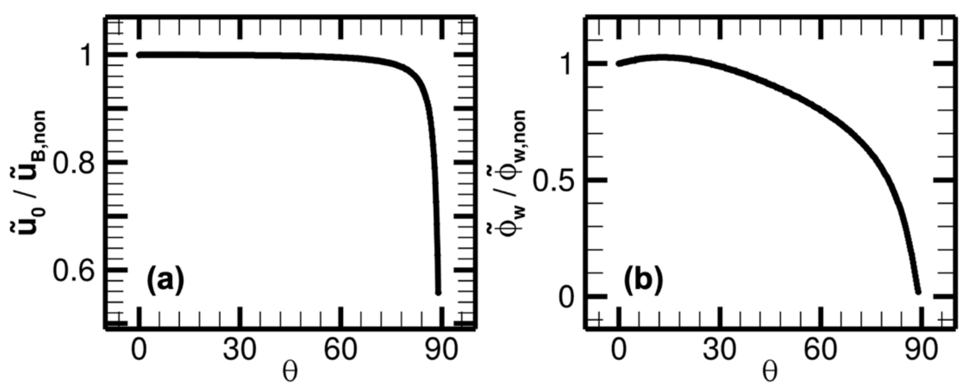

Figure 4. (a) Sheath edge bulk velocity and (b) wall potential for a range of field angles. Results are normalized by the non-magnetized solutions, $u_{B,non}$ and $\phi_{B,non}$.

c. Gas breakdown using fluid moment (FM) approach

Breakdown has been studied for over a century, with the behavior relating the breakdown voltage V_b to the gas pressure p multiplied by the anode-cathode gap distance d being classically described by Paschen's law. The curve is governed by two empirical, gas-dependent parameters fitted from experimental data, and is derived by considering electron continuity, the current balance between ions and electrons, and a phenomenological expression of the number of ionization events per unit length.

The first study is a benchmark for DC breakdown using a particle-in-cell/Monte Carlo collisions (PIC-MCC), a full-fluid moment (FFM) and a drift-diffusion (DD) models, simulating breakdown conditions across a wide range of pd values and constructing breakdown curves. Additionally. RF breakdown has also been simulated using the PIC-MCC and the FFM models, studying the effect of varying the initial plasma density on the eventual breakdown condition. While the former is aligned with R-I (development of fluid model), the latter is aligned with R-III (plasma formation due to microwave).

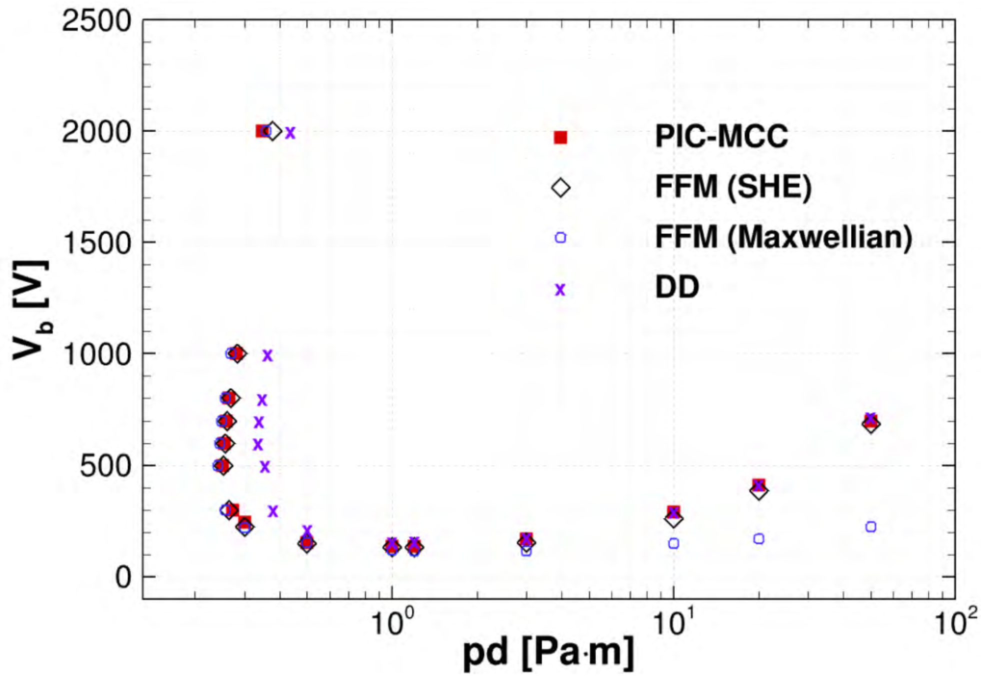

Figure 5 Breakdown criteria for PIC/MCC, FFM, and DD for a range of pd values.

Figure 5 shows the breakdown curves for the three models, showing FFM using Maxwellian rate coefficients and rate coefficients calculated using a two-term spherical harmonic expansion on BOLSIG+. The models show good agreement with each other, particularly FFM-SHE with PIC-MCC. In the right branch (i.e., high pressure), the Maxwellian rates underestimate the breakdown voltage, and this is due to the overestimation of the ionization coefficient. Assuming Maxwellian VDFs for rate calculations neglects the depletion of the high-energy tail of the electrons, which contributes significantly to ionization at low electron mean energies. The rest of the models show excellent agreement in the right branch, where the high collisionality enforces a Maxwellian distribution and cause the electrons to equilibrate, removing velocity and temperature gradients, as will be shown next. This makes the DD approximation valid, converging FFM to the DD approach.

In the left branch, FFM and PIC-MCC show excellent agreement, despite the rarefied nature of the gas in this regime. This can be attributed to the fact FFM solves for the fluid inertia, thus allowing the species to be propagated by their own momentum even in the absence of collisions. By self-consistently solving for the energy as well, FFM successfully captures the breakdown conditions that PIC-MCC exhibit. The DD results in the left branch show the most significant deviation from the other models, and this is because the DD approximation requires sufficient collisions for the model to work, thus requiring the minimum pressure to be pushed to a higher value.

Preliminary results have been obtained using the FFM model for RF breakdown, which are compared to the PIC-MCC results. In the RF breakdown setup, space charge is accounted for, and as such, Poisson's equation is solved for the potential to acquire the RF field. The results are sensitive to the initial plasma density, so the initial density is varied to study the trend.

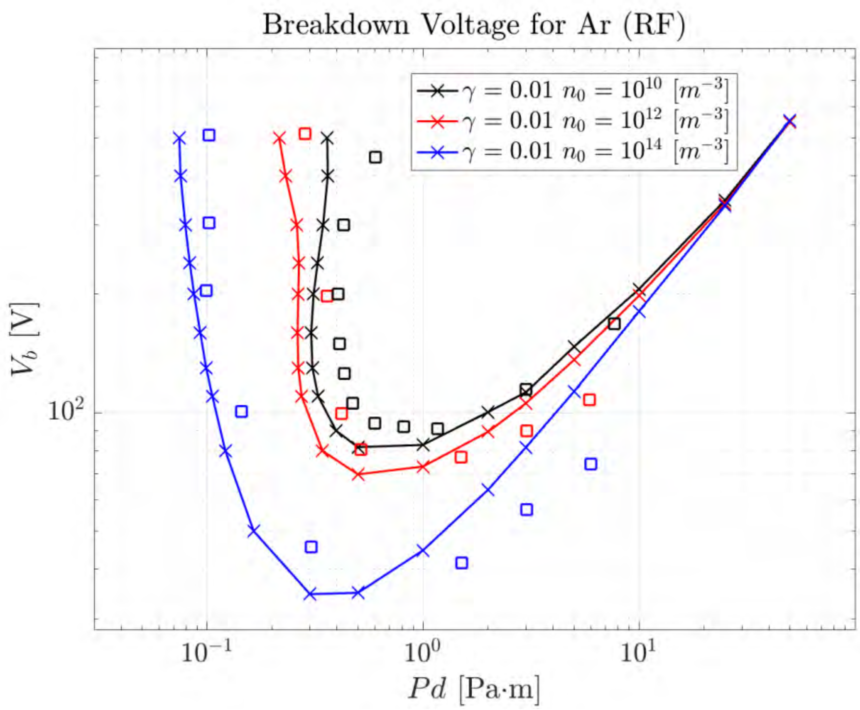

Figure 6. Figure 6. RF Breakdown curve using FFM and PIC-MCC for various initial plasma densities.

Figure 6 shows the breakdown results for RF breakdown using FFM, compared to the results from PIC-MCC. Note that by nature of the fluid formulation, the fluid model in its current form is unable to capture the high energy tail of the electron VDF, which is critical to the operation of RF devices. Nonetheless, the results from FFM are qualitatively close to the PIC-MCC results in all cases. As the initial density decreases, the results become invariant since the space charge plays a lesser role. Poisson's equation becomes Laplace's equation as the right-hand side becomes negligible compared to the imposed RF field. At high pressures, where the gas density is high and the ionization degree of the plasma naturally becomes lower, the results converge to nearly the same breakdown conditions. Further investigations are necessary to study the behavior of the plasma profiles, and to see if the results converge at high initial densities as well.

3. Findings and Conclusions

The development of high-order (five- and ten-moment) fluid models can have immense impact for the plasma studies, as particle-based kinetic models are usually much more computational expensive to run. If the fluid models work, this will significantly accelerate any plasma formation/expansion investigations in the future. Such findings can also be directly implemented in existing codes that are of interest to the DOD (e.g., Magic, ICEPIC).

Plasma formation study sheds light into the physical processes associated with plasma expansion. The numerical results that show good agreement with experimental observation is promising. The 1D model development has given us more confidence in the 2D development if resources are available. Throughout this ONR project, the model has been elevated to a level where it can be used to study emission physics in pulsed power systems in detail (cf. collaboration with Sandia).

The research outcomes can help (i) address existing issues in the HPM sources developed and deployed by the U.S. Navy, and (ii) improve the optimization and design processes of the future HPM sources using the predictive modeling capabilities developed through this project. In addition, advancing the fundamental understanding of the interaction between plasma flows, electromagnetic waves, and plasma-immerse materials possesses further immense impacts to other DoD applications and missions, including space propulsion, fusion energy, space weather, aerodynamics, combustion, and material processing.

4. Plans and Upcoming Events

We have currently submitted one paper to Phys Plasmas (received positive review) on magnetized sheath. We are writing another paper for Journal of Plasma Physics regarding another magnetized sheath paper. In addition, several papers have been submitted and are revised related to DC breakdown. The plasma formation study is now completed and we currently started writing a draft, aim to be submitted to Journal of Applied Physics. Therefore, we expect several more publications by the end of this project.

As planned, anode plasma formation study (R-III) will be conducted. The numerical results will be compared with literature. The team is also considering development of fluid moment (FM) model for the cathode plasma formation study. Another student will be required to do so.

PI Hara has been invited to several departmental seminars, including Georgia Institute of Technology (Aerospace Engineering) and Princeton University (Mechanical and Aerospace Engineering). He is also organizing a workshop on breakdown in the APS Gaseous Electronics Conference in October 2024. PI has also been invited as a lecturer at the 3rd US Low temperature plasma summer school and is serving as a technical chair for the next International Conference on Plasma Science at Beijing in June 2024.

Recommendations for Future Work: two-dimensional simulations of surface flashover can help understand the microscale plasma formation near the carbon velvet and carbon fiber cathodes. For this work, initially, we plan to use a simplified metal-dielectric-vacuum geometry to study the surface flashover mechanism. In the first stage of this study, we will use a 2D PIC to self-consistently model the secondary electron emission avalanche (SEEA) due to field emission from the triple point (CTJ). Collaboration with experimentalists on plasma formation will also be a good way to increase the impact of this work.

5. Transitions and Impacts

Graduate student Andy Castillo was selected as an intern at Sandia National Laboratories, where he worked on plasma global model for high-voltage power switches. The work supported by this ONR project also helped Andy Castillo win the Laboratory Residency Graduate Fellowship (LRGF) from Department of Energy, National Nuclear Security Administration. The key hypothesis of the LRGF project is that the shear flow instabilities lead to increased plasma expansion in the MITL gap, which is detrimental to the system. The current approach is to use a 1D magnetostatic PIC code to generate 1D profiles in relevant properties, such as charge and current density and the electric and magnetic fields. Linear stability analysis can be performed (informed by these profiles), and the susceptibility of the system to these instabilities can be determined for a wide range of parameters. The next step will involve a 2D magnetostatic or electromagnetic code to model the instability itself in an idealized configuration.

Work resulting from this ONR project is contributing to the research collaboration with Lam Research and Applied Materials to study physical processes in semiconductor manufacturing devices. In addition, PI is involved in collaborative projects with Sandia National Laboratories on gas breakdown.

6. Collaborations

- Sandia National Laboratories: Matt Hopkins & Nicki Bennet – collaboration regarding high voltage gap simulation and plasma formation in magnetically insulated transmission lines (MITLs). Matt Hopkins & Chris Moore – collaboration on breakdown.

- Lam Research: Saravanapriyan Sriraman – we are collaborating with Lam research to study RF breakdown in low-pressure capacitively coupled plasma source. We have been awarded the Unlock Ideas and Elevate Ideas, which are Lam's internal research development funding.
- Applied Materials: Shahid Rauf – we collaborate on development of a 2D cylindrical PIC-MCC model for low-temperature plasmas and high-order closure of fluid moment approaches.
- Georgia Institute of Technology: Sedina Tsikata – collaboration on cross-field plasma discharge physics, particularly focusing on the kinetic and fluid instabilities in partially magnetized plasmas.
- NRL: Ian Rittersdorf and Joe Schumer – visited lab and exchanged ideas about simulations.

7. Personnel

- Principal investigator: Ken Hara, 0.3-person month, National Academy Member (N)
- Business Contact: Simon Tang, Associate Research Administrator

8. Students

3 graduate students (two post-quals PhD candidates and one pre-quals PhD student) are conducting this research.

2 postdocs, not supported by this ONR project directly, are helping the breakdown simulations and kinetic model development.

9. Technology Transfer

We discussed our research with Joe Schumer, Ian Rittersdorf, Alexander Vlasov, and Simon Cooke at NRL before the proposal. PI visited NRL in September 2022. We hope to continue the relationship.

PI visited the Air Force Research Laboratory to visit the ICEPIC team in Albuquerque in 2021.

PI has strong connection with AFRL in Edwards AFB (In-space propulsion branch), e.g., Justin Koo, Dan Eckhardt, and David Bilyeu.

10. Products, Publications, Patents, License Agreements, etc.

Publications resulting from this project:

Archival Publications (publication reference information (article title, authors, journal, date, volume, issue) can be automatically entered using a DOI)

a. Title: Theory of gradient drift instabilities in low-temperature, partially magnetized plasmas
b. Journal: Journal of Plasma Physics
c. Authors: K. Hara, A. R. Mansour, and S. Tsikata
d. Keywords: plasma devices, plasma dynamics, plasma instabilities
e. Distribution Statement: Open Access
f. Status: Published
g. Publication Identifier Type: DOI
h. Publication Identifier: doi:10.1017/S002237782200068X
i. Publication Date: 2022
j. Vol: 88
k. Issue: -
l. Number: 905880408

m. Publication Location: The city and country where article was published
n. Acknowledgement of Federal Support? Yes
o. Peer Reviewed? Yes

Conference Papers

a. Title: Monotonic sheath conditions of partially magnetized plasma sheaths
b. Authors: A. M. Castillo and K. Hara
c. Conference Name: 65th Annual Meeting of the APS Division of Plasma Physics
d. Conference Date: October 2023
e. Conference Location: Denver CO
f. Publication Status: Published
g. Publication Date: October 2023
h. Publication Identifier Type: none
i. Publication Identifier: none
j. Acknowledgement of Federal Support? Yes

a. Title: Full-fluid Moment Modeling and Theory of DC Breakdown
b. Authors: A. R. Mansour, Y. Yamashita, and K. Hara
c. Conference Name: 65th Annual Meeting of the APS Division of Plasma Physics
d. Conference Date: October 2023
e. Conference Location: Denver CO
f. Publication Status: Published
g. Publication Date: October 2023
h. Publication Identifier Type: none
i. Publication Identifier: none
j. Acknowledgement of Federal Support? Yes

a. Title: Gradient-drift instability in partially ionized, partially magnetized plasmas
b. Authors: K. Hara, A. R. Mansour, and S. Tsikata
c. Conference Name: 65th Annual Meeting of the APS Division of Plasma Physics
d. Conference Date: October 2023
e. Conference Location: Denver CO
f. Publication Status: Published
g. Publication Date: October 2023
h. Publication Identifier Type: none
i. Publication Identifier: none
j. Acknowledgement of Federal Support? Yes

a. Title: Modeling of plasma formation and expansion in a high-voltage anode-cathode gap
b. Authors: V. Sharma, A. M. Castillo, Y. Yamashita, and K. Hara
c. Conference Name: 65th Annual Meeting of the APS Division of Plasma Physics
d. Conference Date: October 2023
e. Conference Location: Denver CO
f. Publication Status: Published
g. Publication Date: October 2023
h. Publication Identifier Type: none
i. Publication Identifier: none
j. Acknowledgement of Federal Support? Yes

a. Title: Plasma chemistry modelling of SF6 replacement gas for high voltage switches
b. Authors: A. M. Castillo, M. Hopkins, A. Lietz, and K. Hara
c. Conference Name: 76th Annual Gaseous Electronics Conference
d. Conference Date: October 2023
e. Conference Location: Ann Arbor, MI
f. Publication Status: Published
g. Publication Date: October 2023
h. Publication Identifier Type: none
i. Publication Identifier: none
j. Acknowledgement of Federal Support? Yes

a. Title: Plasma global model of Novec 4710/CO2 mixture for high voltage switches
b. Authors: A. M. Castillo, A. Lietz, M. Hopkins, and K. Hara
c. Conference Name: IEEE Pulsed Power Conference 2023
d. Conference Date: June 2023
e. Conference Location: Santa Antonio, TX
f. Publication Status: Published
g. Publication Date: June 2023
h. Publication Identifier Type: none
i. Publication Identifier: none
j. Acknowledgement of Federal Support? Yes

a. Title: 1D PIC-MCC modeling of cathode plasma formation and expansion in vacuum diode
b. Authors: V. Sharma, Y. Yamashita, A. M. Castillo, and K. Hara
c. Conference Name: IEEE Pulsed Power Conference 2023
d. Conference Date: June 2023
e. Conference Location: Santa Antonio, TX
f. Publication Status: Published
g. Publication Date: June 2023
h. Publication Identifier Type: none
i. Publication Identifier: none
j. Acknowledgement of Federal Support? Yes

a. Title: Particle-in-cell simulation of magnetized plasma sheath
b. Authors: A M Castillo and K Hara
c. Conference Name: 50th IEEE ICOPS
d. Conference Date: May 2023
e. Conference Location: Santa Fe, NM
f. Publication Status: Published
g. Publication Date: June 2023
h. Publication Identifier Type: none
i. Publication Identifier: none
j. Acknowledgement of Federal Support? Yes

a. Title: Towards self-consistent modeling of cathode plasma formation and expansion
b. Authors: V. Sharma, Y. Yamashita, A. M. Castillo, and K. Hara
c. Conference Name: 50th IEEE ICOPS
d. Conference Date: May 2023
e. Conference Location: Santa Fe, NM

f. Publication Status: Published
g. Publication Date: June 2023
h. Publication Identifier Type: none
i. Publication Identifier: none
j. Acknowledgement of Federal Support? Yes

a. Title: Kinetic modeling of plasma-wall interactions with magnetic field and secondary emission effects
b. Authors: A M Castillo and K Hara
c. Conference Name: International Electric Propulsion Conference
d. Conference Date: June 2022
e. Conference Location: Cambridge MA
f. Publication Status: Published
g. Publication Date: June 2022
h. Publication Identifier Type: none
i. Publication Identifier: IEPC-2022-382
j. Acknowledgement of Federal Support? Yes

a. Title: Kinetic simulation of plasma sheath relevant to cross-field diodes
b. Authors: A M Castillo and K Hara
c. Conference Name: International Conference on Plasma Sciences
d. Conference Date: May 2022
e. Conference Location: Seattle WA
f. Publication Status: Abstract Published
g. Publication Date: May 2022
h. Publication Identifier Type: none
i. Publication Identifier: none
j. Acknowledgement of Federal Support? Yes

a. Title: Kinetic simulation of magnetized plasma sheaths with oblique magnetic fields
b. Authors: A M Castillo and K Hara
c. Conference Name: APS Far West Section Fall 2022 Meeting
d. Conference Date: October 2022
e. Conference Location: Honolulu HI
f. Publication Status: Abstract Published
g. Publication Date: October 2022
h. Publication Identifier Type: none
i. Publication Identifier: none
j. Acknowledgement of Federal Support? Yes

11. Point of Contact in Navy

Joe Schumer and Ian Rittersdorf, Naval Research Laboratory.
Last contact: September 2022. PI visited NRL for a discussion.

Multi-frequency High Power Microwave Generation and Amplification via Optically Gated Electron Beams

Grant No. N00014-20-1-2681

Annual Report for Fiscal Year 2023

Period of Performance: October 1, 2022 to September 30, 2023

Prepared by:

Prof. Peng Zhang, Principal Investigator
Department of Electrical and Computer Engineering
Michigan State University
428 S. Shaw Ln
East Lansing, MI 48824
Tel: 517-353-3654
Email: pz@egr.msu.edu

This work was sponsored by the Office of Naval Research (ONR), under grant number N00014-20-1-2681. The views and conclusions contained herein are those of the authors only and should not be interpreted as representing those of ONR, the U.S. Navy or the U.S. Government.

Grant or Contract Number: N00014-20-1-2681
Date Prepared: Jan 10, 2024
Project Title: Multi-frequency High Power Microwave Generation and Amplification via Optically Gated Electron Beams
Annual Summary Report: FY2023
Principle Investigator: Peng Zhang, 517-353-3654, pz@egr.msu.edu
Department of Electrical and Computer Engineering, Michigan State University

Section I: Project Summary

1. Overview of Project

Abstract: Electron beam based high power microwave (HPM) devices are critical to a variety of defense applications for Navy and more broadly the Department of Defense (DOD). This project explores the fundamental physics of density modulation of electron beam emission via combined mechanisms of thermionic/field/photo-emission and the interaction of such premodulated beams with circuits for HPM generation and amplification. This report provides an executive summary of our recent theoretical modeling efforts. We provided a comprehensive analysis on direct density modulation of high-current electron beam emission from an Radio Frequency (RF) cold cathode using optical excitation. We theoretically studied the photo-assisted field emission of periodically bunched electron beams of various pulse shapes under the combined excitation of an RF field and an optical field, using an exact quantum model. Our results show the optical gating/modulation offers substantially strong flexibility to control the pulse shape as well as the frequency components in beam current emission. We developed an exact analytical quantum theory for field emission from surfaces with a nearby quantum well. It is found that the quantum well can lead to resonant tunneling enhanced field emission up to several orders of magnitude larger than that from bare cathode surfaces. In the meantime, the electron-emission energy spectrum is significantly narrowed. We also investigated the Smith-Purcell Radiation (SPR) operation frequency and growth rate using cold- and hot-tube dispersion relations. We demonstrated that the growth rate calculation using the hot-tube dispersion relation can be used to predict the optimal grating parameters to minimize the starting current of SPR. We also employed a dimensional method to evaluate the microscale gas breakdown characteristics at atmospheric pressure, resulting in a universal breakdown curve applicable to different types of gases. Our results will be useful in the development of advanced cathodes, electron sources, and electromagnetic interaction circuits with density modulation, enabling new advances for the development of high power electromagnetic sources and amplifiers.

Objective: The objective of this project is to provide a foundational understanding of the underlying physics in optically gated electron emission and its interaction with microwave circuits. The goal is to provide guidelines for the design of compact HPM devices with high power output and extremely flexible frequency tunability. The ultrafast electron emission due to pulsed lasers, or optical gating, would potentially provide unrivaled precision in phase-control of electromagnetic signals from electron based HPM devices. The potential of selective gating of multiple beams would provide strong flexibility for multi-frequency HPM applications.

Introduction: Traveling wave devices utilize the collective interaction of an electron beam with a periodic structure to convert electron beam energy into electromagnetic radiation. They are key elements in telecommunication systems, satellite-based transmitters, military radar, communication data links, and electronic countermeasures. There continues to be strong interests in increasing the output power, frequency tunability, and bandwidth of traveling wave devices, for uses as radiation sources and power amplifiers, from GHz to THz and beyond. For the development of coherent radiation sources, it is desirable to minimize the threshold beam current for triggering oscillation. In contrast, for high power traveling wave tube (TWT) amplifiers, unwanted oscillations pose a major threat to their operation. For novel contemporary traveling wave devices, such as metamaterial-, photonic crystal- and advanced Smith-Purcell-based traveling wave devices, improving efficiency remains a major challenge.

In vacuum microwave tubes, the energy conversion from electron beams into electromagnetic radiation relies on beam modulation, by either density modulation or velocity modulation. Density modulation is achieved by controlling the electron emission from the cathode. Velocity modulation is achieved by passing the electrons through an RF electric field that modulates the velocities of the electrons. At present, TWTs mainly rely on velocity modulation of the electron beam for power amplification. After the electron velocities are modulated, there is a substantial delay before velocity modulation becomes density modulation, and useful gain is produced. Significant improvements in TWT performance can be enabled by density modulation during emission. In particular, with density modulation, velocity dispersion in the beam can be minimized and the portion of the interaction circuit used for converting velocity modulation into density modulation can be eliminated. This would result in compact devices with reductions in overall dimensions and weight, through the elimination of the pre modulation circuit. Furthermore, density modulation during emission would eliminate the launching loss of the input RF signal, which is a serious intrinsic problem in TWTs based on velocity modulation.

In this project, we will explore density modulation in optically gated electron emission. This is motivated by the recent rapid development in ultrafast lasers and photonics, which has opened up unprecedented possibilities for the control of electron beam dynamics at ultrashort spatial-temporal scales. The research on implementing both high power and frequency tunability in HPM devices will enable a critical disruptive capability for high power microwave systems. The theory will also be valuable to neighboring fields such as novel miniaturized electromagnetic radiation sources, nano-optoelectronics, ultrafast physics, material science, and accelerator technology.

Background: The idea of using direct current modulation of electron beams in microwave amplifiers has existed for decades. Historically, density modulation was accomplished with a grid that lays over the surface of a thermionic emitter to control the electron emission. Because of the finite transit time of the electrons across the cathode-grid space, this modulation technique is only effective up to 2 GHz for state-of-the-art devices. With the advancement of vacuum microelectronics and field emitter arrays (FEAs), the gate-to-emitter spacing has been reduced into submicron scale, which significantly decreases the electron transit time. Density modulation up to about 5 GHz by gate modulating of the FEA has been demonstrated; however, there are significant challenges for using FEAs in high power tubes, because the premature failure due to arcing often occurs at current levels much smaller than the design requirements. Breakdown is a major challenge for FEAs because of the high fields within the structure and the thin-film gate electrode. An electrical short between the gate and any individual emitter will burn out the entire FEA and render it unusable. While shields can be added to mitigate the damaging effects of the electrical shorts, high operating voltage is needed to field emitter arrays to draw sufficient current.

Photoemission provides an alternative method to generate premodulated electron beams, which relaxes the requirement of high operating voltage in field emission, thus eliminating possible arcing and circuit breakdown. More importantly, pulsed laser induced (or assisted) electron emission offers the possibility of manipulation and control of coherent electron motion in ultrashort spatiotemporal scales. These advantages would greatly benefit the development of advanced compact HPM devices.

2. Activities and Accomplishments

The main new activities and accomplishments during this performance period (1 October 2022 to 30 September 2023) include: 1) study of direct density modulation of photo-assisted field emission from an

RF cold cathode; 2) Resonant tunneling enhanced field emission; 3) direct correlation between spatial growth rate and starting current for grating optimization for Smith–Purcell radiation; and 4) Dimensional analysis on microscale gas breakdown with electric field nonuniformity and positive space charge effects.

DIRECT DENSITY MODULATION OF PHOTO-ASSISTED FIELD EMISSION FROM AN RF COLD CATHODE

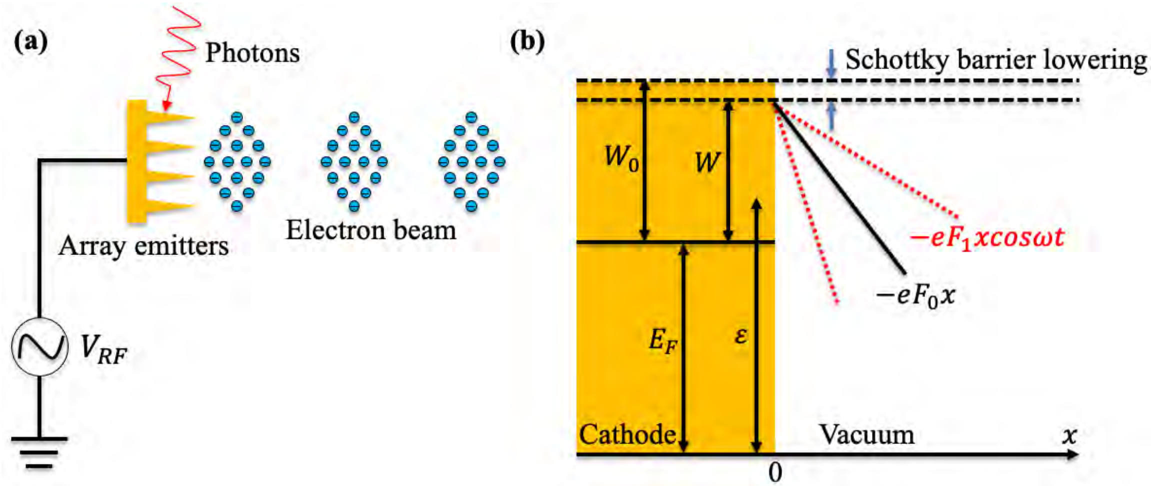

Figure 1. (a) The periodical emission bunched beam produced from a sharp emitters array under an RF field and a laser field. (b) The quantum model with a one-dimensional solid-vacuum interface under an RF field F_0 and a laser field $F_1\cos\omega t$, with E_F being the Fermi energy of the metal, W_0 being the work function of the cathode, ε being the initial energy, W being the effective work function considering the Schottky effect [1].

We have studied direct density modulation of photo-assisted field emission from an RF cold cathode [1]. This is motivated by the recent rapid development in ultrafast lasers and photonics, which has opened up enormous opportunities to control electron beam dynamics at ultrashort spatial-temporal scales, thus offering unprecedented scientific advances. Pulsed laser-induced (or assisted) electron emission, offers the possibility of manipulation and control of coherent electron motion in ultrashort spatiotemporal scales. The timing of electron beam emission, and therefore of the electron beam density modulation, can be achieved in femtosecond scale, by laser illuminating DC-biased sharp metallic tips. This ultrafast electron emission due to pulsed laser, or optical gating, would potentially provide unrivaled precision in phase-control of electromagnetic signals from electron-based devices.

We theoretically study the photo-assisted field emission of periodically bunched electron beams of various pulse shapes under the combined excitation of an RF field and an optical field (Figs.1 and 2), using an exact quantum model. Both continuous-wave (CW) and pulsed optical fields are considered. The emission current pulse amplitude, pulse width, electron number density per pulse, as well as pulse shape and its harmonic contents are investigated in detail. For CW photon sources in the UV to optical range (i.e., 200 nm – 1200 nm), increasing the optical intensity under an RF bias tends to change the current pulse from Gaussian to sinusoidal-like shape, thus offering strong flexibility to control the frequency components in beam current emission. Pulsed photon sources combined with an RF field can produce sharp, high-current electron bunches with pulse duration comparable with or even less than that of the optical pulse. A contour map of the density modulation depth is constructed for different combinations of RF and laser fields (Fig. 3).

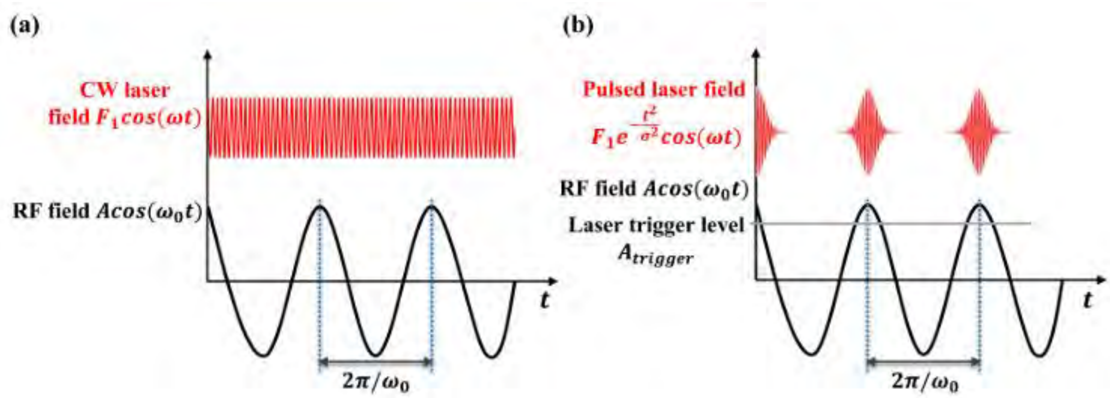

Figure 2. Cathode excitation using (a) an RF field and a CW laser field, (b) an RF field and a pulsed laser field.

Figure 3 shows contours of constant average current density J_{avr} and the ratio of average over the peak of current density J_{avr}/J_{pk} calculated using our quantum electron emission model, where Fig. 3(a) is for CW laser, and Fig. 3(b) is for pulsed laser with duration $\tau_p = 0.025$ ns. It shows that both density J_{avr} and J_{avr}/J_{pk} can be adjusted over a wide range of values by controlling RF amplitude, laser field, and laser pulse duration. It shows significantly increased flexibility to achieve density modulation during electron emission over a wide range of parameter space by using optical means, as compared to voltage-controlled field emission (cf. Fig. 14 of D. R. Whaley, et al, "Experimental demonstration of an emission-gated traveling wave tube amplifier," IEEE Trans. Plasma Sci. 30(3), 998–1008 (2002).). The J_{avr}/J_{pk} is as small as 0.04 can be achieved using pulsed lasers (Fig. 3(b), which is an order of magnitude smaller than the typical value of $J_{avr}/J_{pk} > 0.3$ from voltage-controlled field emission.

The results provide insight into unlocking new opportunities to achieve direct density modulation during electron current emission by optical means. This work will provide a foundation for many exciting opportunities in the exploration of premodulated beams to generate and/or amplify high power electromagnetic radiation.

The work is published in Journal of Applied Physics [1].

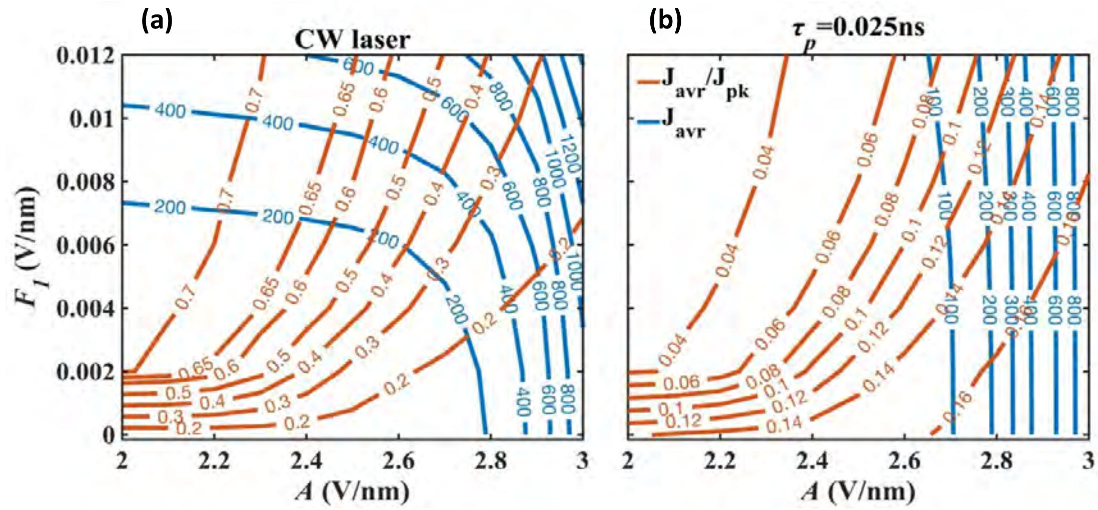

Figure 3. Average current density J_{avr} [A/cm^2] and the ratio of average over the peak of current density J_{avr}/J_{pk} in various RF amplitude (A V/nm) and laser field (F_1 V/nm) with 200 nm wavelength for (a) CW laser, and (b) pulsed laser of duration $\tau_p = 0.025$ ns.

THEORETICAL ANALYSIS OF RESONANT TUNNELING ENHANCED FIELD EMISSION

We performed theoretical analysis of resonant tunneling enhanced field emission [2]. This is a joint work with Prof. Rehan Kapadia's group at USC. We develop an exact analytical quantum theory for field emission from surfaces with a nearby quantum well, by solving the one-dimensional (1D) time-independent Schrödinger equation. The quantum well, which may be introduced by ions, atoms or nanoparticles etc, is simplified as a square potential well with depth H, width d, and distance to the surface L. The theory is used to analyze effects of the quantum well (d, H, and L), cathode properties (work function W and Fermi energy E_F) and dc field F. It is found that the quantum well can lead to resonant tunneling enhanced field emission up to several orders of magnitude larger than that from bare cathode surfaces. In the meantime, the electron emission energy spectrum is significantly narrowed. The strong enhancement region is bounded by the conditions $eFL + H \geq W + C$ and $eFL \leq W$, with e being the elementary charge (positive) and C a constant dependent on dc field F. It is also found that the linear shift of resonance peaks in the electron emission energy spectrum with dc field F follows $\varepsilon_p = \varepsilon_{p0} - eFL$, with ε_{p0} approximately the eigenenergies for electrons confined in a square potential well without dc field. The theory provides insights for the design of high efficiency field emitters which can produce high current and highly collimated electron beams.

The 1D model considers electrons inside the metal ($x < 0$) with the initial longitudinal energy ε emitted to the vacuum under an externally applied dc electric field F, as shown in Fig. 4. A quantum well is formed near the metal surface due to ions, atoms, and nanoparticles etc, with well depth H, well width d, and distance from left edge of the well to metal surface L.

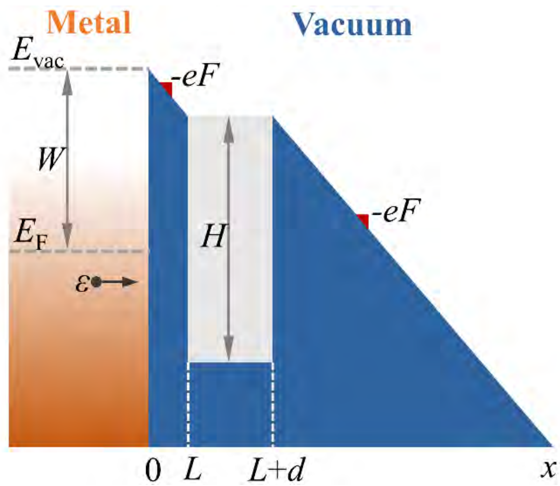

Figure 4. Energy diagram of field electron emission through a triangular barrier deformed by a quantum well under the externally applied dc field F. The incident electron has an initial longitudianl enegy of ε. The metal has Fermi energy E_F and work function W. The quantum well has depth H, width d, and distance from left edge of the quantum well to metal surface L.

Figure 5 shows a representative comparison of field emission from a bare metal surface and that with a nearby quantum well. The metal is gold, with work function $W = 5.1$ eV and Fermi energy $E_F = 5.53$ eV. Unless stated otherwise, these are the default properties of metal in this study. The energy diagram for bare metal and metal surfaces with a quantum well ($d = 3$ nm, $L = 1.5$ nm and $H = 6$ eV), under dc field $F = 2.8$ V/nm, is shown in Fig. 5(a). With the presence of quantum well, electrons with initial energy between 0.43 eV and 6.43 eV have to tunnel through two seperate barriers with the quantum well in between, which can produce resonant tunneling behavior. It can be found that the field emission current density per energy $J(\varepsilon) = eD(\varepsilon)N(\varepsilon)$ has a maximum resonance peak orders of magnitude higher than that for a bare metal surface, i.e., 2.15×10^4 A/m^2/eV vs 8.90 A/m^2/eV, as shown in Figs. 5b and 5c. The corresponding total emission current densities are 105 A/m^2 and 3.07 A/m^2 respectively, showing a significantly enhanced emission current density with a quantum well. In the meantime, the energy spread of the emitted electrons with a quantum well is orders of magnitude narrower than that from the bare metal surface, with a full width half maximum (FWHM) of < 0.008 eV vs ~ 0.3 eV in $J(\varepsilon)$, as shown in Figs. 5b and 5c.

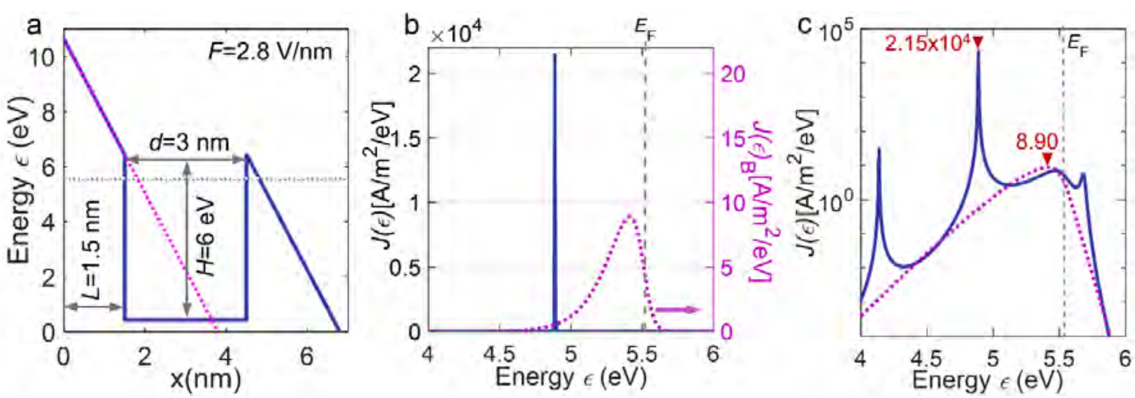

Figure 5. (a) Energy diagram for a bare metal (magenta dashed line) and a metal surface with a quantum well of d = 3 nm, L = 1.5 nm and H = 6 eV (blue solid line) under a dc field F = 2.8 V/nm; (b) Emission current density energy spectrum for field emission without (calculated from Eq.(7) in Ref. [62]) and with a quantum well (calculated from Eq. (10)) as a function of electron initial energy ε; (c) semi-log plot of (b). The metal is gold, with work function W = 5.1 eV and Fermi energy E_F = 5.53 eV. The temperature in Eq. (10) is taken at T = 300 K.

The theory provides insights for the design of high-efficiency field emitters, which can produce high current and highly collimated electron beams.

The work is published in Physical Review Applied [2].

GRATING OPTIMIZATION FOR SMITH–PURCELL RADIATION: DIRECT CORRELATION BETWEEN SPATIAL GROWTH RATE AND STARTING CURRENT

We examined the starting current of Smith-Purcell radiation (SPR), which shows the same scaling as the spatial growth rate as a function of the grating parameters [3]. High power, efficient, and low-cost electromagnetic sources have significant uses in high resolution imaging, biomedical scanning, material analysis, security systems, high-data-rate communications, and so on. As a special case of backward wave oscillator (BWO), Smith–Purcell radiation (SPR) has attracted strong interest in producing terahertz (THz) radiation.

The dependence of starting current on grating parameters for SPR is analyzed in previous studies, which typically calculate the growth rate in time (i.e., imaginary component of frequency) and rely on the boundary conditions at the ends of the interacting structure. In this work, we systematically studied the cold-and hot tube dispersion relations for THz SPR at different grating parameters (groove's heights and widths) with a fixed grating period (Fig. 6). The change of the SPR operating points with different grating parameters was obtained from the cold-tube dispersion relation. We then solved the hot-tube dispersion relation to find the spatial growth rate (i.e., imaginary component of wavenumber), which is compared with the starting current calculated from particle-in-cell (PIC) simulations [P. Zhang, et al., "Enhancement of coherent Smith-Purcell radiation at terahertz frequency by optimized grating, prebunched beams, and open cavity", Phys. Rev. ST Accel. Beams, 18, 020702 (2015)]. Strong correlation between the starting current and spatial growth rate is demonstrated, without considering the boundary conditions at the ends of the interaction structures. In contrast to previous studies based on the time growth rate and on the end boundary conditions of the grating, our simple approach by only calculating the spatial growth rate based on the hot-tube dispersion relation can be used to determine the optimal grating parameters for minimization of the starting current efficiently.

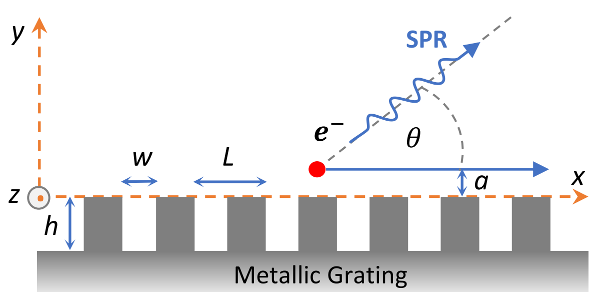

Figure. 6. Schematic of Smith-Purcell grating and beam configuration.

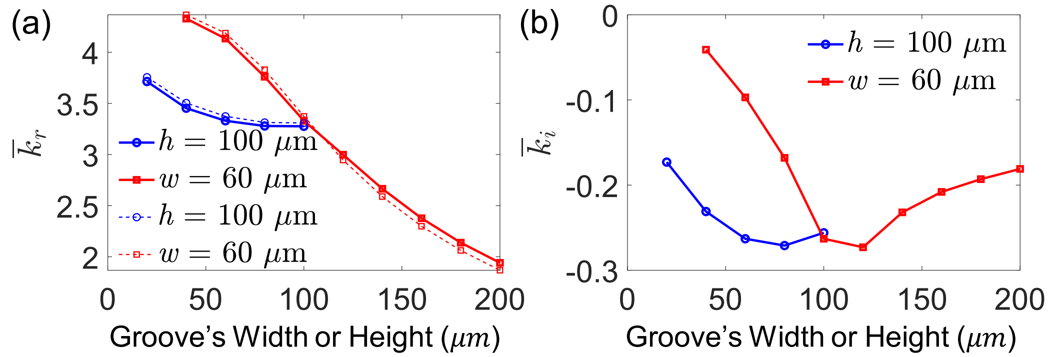

Figure. 7. (a) Real and (b) imaginary part of the wavenumber at the operating frequency $\overline{\omega} = 2\pi f_{ev}L/c$, as a function of the groove height h (squares, groove width w fixed at 60 μm) as well as groove width w (rounds, h fixed at 100 μm), calculated from the hot dispersion relation. Dashed lines in (a) are for the wavenumber at f_{ev} calculated from the cold-tube dispersion.

Figure 7 plots the real and imaginary part of the complex wavenumber $\overline{k} = \overline{k}_r + j\overline{k}_i$ with a negative $\overline{k}_i$ at the operating frequency $\overline{\omega}$ ($= 2\pi f_{ev}$) determined by the cold-tube dispersion, as a function of the groove height h (width w is kept at 60 μm) and groove width w (h is kept at 100 μm), while the period of the grating fixed at 120 μm and beam energy at 50 keV. As compared to the cold-tube dispersion calculation (dashed line in Fig. 7(a)), $\overline{k}_r$ (solid line in Fig. 7(a)) calculated from the hot-tube dispersion is slightly shifted, due to the detuning effect of the electron beam. Just as the real part, $\overline{k}_i$ also depends strongly on the grating parameters. As shown in Fig. 7(b), there is a maximum spatial grow rate $-\overline{k}_i$ around h = 100 μm and 120 μm for fixed w; and around w = 80 μm for fixed h. It is important to note that these maximum grow rates occur when the corresponding operating points become closest to the upper band edge of the cold-tube dispersion curve, where the band edge is known to be susceptible to instabilities to trigger oscillation.

In Fig. 8, we compare the spatial growth rate in Fig. 7(b) with the starting currents from PIC simulations in P. Zhang, et al., Phys. Rev. ST Accel. Beams, 18, 020702 (2015). It can be seen that the pattern of $\overline{k}_i$ follows very closely that of the starting current. This is the key result of this work. Note the linear and log scale used to plot the $-\overline{k}_i$ and the starting current respectively, which precisely confirms that the exponential wave growth $e^{-k_i x}$ follows the scaling of the starting current as a function of w and h. Note also that in our calculation here, the boundary conditions at the two ends of the interacting grating are not considered, which is in contrast of the traditional method for BWO analysis based on Johnson's approach, where the boundary conditions are critical.

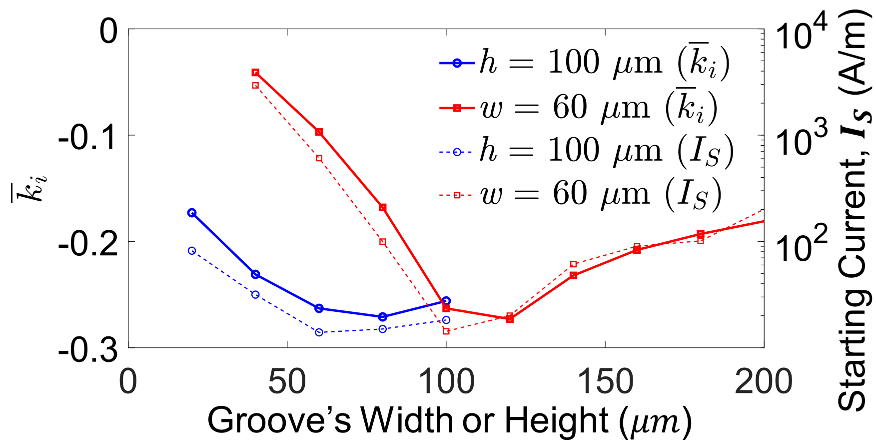

Figure 8. Imaginary part of wavenumbers and the corresponding starting current values obtained from PIC simulations [2] as a function of the groove height h (squares, groove width w fixed at 60 μm) as well as groove width w (rounds, groove height h fixed at 100 μm).

We confirmed that the growth rate calculation using the hot-tube dispersion relation can be used to predict the optimal grating parameters to minimize the starting current of SPR. This approach has a significantly reduced computational cost compared to either direct PIC simulations or the traditional Johnson's approach using the BWO condition of zero-drive instability. As both the operation frequency of SPR and its growth rate depend strongly on the grating parameters, both the cold- and hot-tube dispersion relations can be used in combination to minimize the starting current at the desired radiation frequency. While we applied our analysis to the effects of grating parameters on SPR, we expect that our dispersion relation treatment to grating optimization is applicable to study linear free-electron beam-based vacuum devices in general and in various geometries (e.g., cylindrical geometry).

The work is published in IEEE Transactions on Electron Devices [3].

DIMENSIONAL ANALYSIS ON MICROSCALE GAS BREAKDOWN WITH ELECTRIC FIELD NONUNIFORMITY AND POSITIVE SPACE CHARGE EFFECTS

We employed a dimensional method to evaluate the microscale gas breakdown characteristics at atmospheric pressure, resulting in a universal breakdown curve applicable to different types of gases (e.g., Ar, Xe, Ne, and N2). As the gap distance decreases, the breakdown mode transitions from ion-induced secondary electron emission to the field emission regime. In the field emission regime, the positive space charge effect becomes more significant. We discovered that incorporating the positive space charge effect in the field emission regime can be achieved by modifying the local electric field enhancement factor β. Consequently, we propose an effective electric field enhancement factor, β_{eff}, which scales linearly with β, to accurately reproduce the breakdown curve while considering the positive space charge effect. This proposed approach significantly simplifies the numerical model. Additionally, we examined the effects of gas pressure, gap distance, cathode properties (e.g., work function and secondary electron emission coefficient), and electric field nonuniformity.

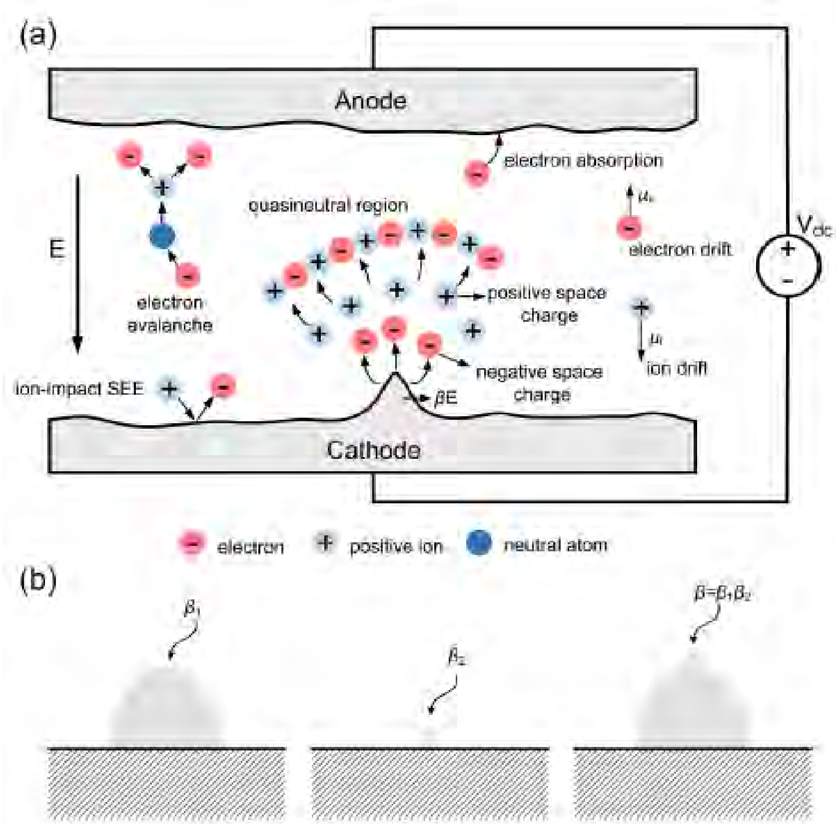

Figure 9. (a) Schematic of the microgap breakdown physical mechanisms, including field emission (FE), ion-impact secondary electron emission (SEE), electron avalanche (EA), electron absorption, electron drift, and ion drift. (b) A large surface protrusion produces a macroscopic field nonuniformity with a field enhancement of β_1 on the tip (left), whereas a small protrusion leads to a localized field enhancement factor β_2 (middle). The combined geometrical effects result in both the electric field nonuniformity across the gap and a relatively large total electric field enhancement factor $\beta = \beta_1\beta_2$ (right).

Figure 9(a) illustrates the fundamental physical mechanisms involved in microscale gas breakdown, including ion-impact secondary electron emission, field emission, electron avalanche (EA), electron absorption, and electron and ion drift motion. In such breakdown processes, a negative space charge region can form when electron emission is strong, whereas a positive space charge region is formed when bulk ionization dominates. Consequently, a positively charged plasma sheath is formed when a quasi-neutral region simultaneously exists.

By employing dimensional analysis, we have established a universal Paschen's curve that encompasses both the field emission and secondary electron emission regimes, which is independent of the gas type. The breakdown voltage is influenced by both macro- and microscopic field enhancement factors, with the former playing a more significant role in the secondary electron emission regime while the latter in the field emission regime. Additionally, we presented a two-dimensional dependence map, depicting V as a function of p and d, which is universal for N2, Ar, Ne, and Xe. Our findings contribute to a comprehensive understanding of microscale gas breakdown characteristics, and the adoption of nondimensional methods significantly simplifies the analysis of parameter dependencies across a wide range of dimensions and pressure scale regimes.

The work is published in Journal of Applied Physics [4] and is selected as an Editor's Pick article.

During this performance period, the PI served as a Guest Editor for the Nineteenth Special Issue on High-Power Microwave and Millimeter-Wave Generation in IEEE Transactions on Plasma Science [5].

The PI is also currently coauthoring the fourth edition of the classical book: J. Benford, J. A. Swegle, E. Schamiloglu, J. Stephens, and P. Zhang, High Power Microwaves, 4th ed. (CRC Press), which is expected to be published in 2025.

[1] L. Jin, Y. Zhou, and P. Zhang, "Direct density modulation of photo-assisted field emission from an RF cold cathode", J. Appl. Phys. 134, 074904 (2023).

[2] Y. Zhou, R. Ahsan, H. Chae, R. Kapadia, and P. Zhang, "Theoretical Analysis of Resonant Tunneling Enhanced Field Emission", Phys. Rev. Applied 20, 014043 (2023).

[3] M. A. Faisal, and P. Zhang, "Grating Optimization for Smith–Purcell Radiation: Direct Correlation Between Spatial Growth Rate and Starting Current", IEEE Trans. Electron Devices 70, 2860 (2023).

[4] C. Lin, J. Chen, A. Iqbal, P. Zhang, and Y. Fu, "Dimensional analysis on microscale gas breakdown with electric field nonuniformity and positive space charge effects", J. Appl. Phys. 134, 053301 (2023). [Editor's Pick]

[5] J. Browning, N. Jordan, J. Stephens, and P. Zhang, "Guest Editorial The Nineteenth Special Issue on High-Power Microwave and Millimeter-Wave Generation", IEEE Trans. Plasma Sci., 51, 1839 (2023).

3. Findings and Conclusions

We explored direct density modulation of high-current electron beam emission from an RF cold cathode using optical excitation. We theoretically studied the photo-assisted field emission of periodically bunched electron beams of various pulse shapes under the combined excitation of an RF field and an optical field, using an exact quantum model. Our results show the optical gating/modulation offers substantially stronger flexibility to control the pulse shape as well as the frequency components in beam current emission. We developed an exact analytical quantum theory for field emission from surfaces with a nearby quantum well. It is found that the quantum well can lead to resonant tunneling enhanced field emission up to several orders of magnitude larger than that from bare cathode surfaces. In the meantime, the electron-emission energy spectrum is significantly narrowed. We also analyzed the Smith-Purcell radiation operation frequency and growth rate using cold- and hot-tube dispersion relations. We confirmed that the grow rate calculation using the hot-tube dispersion relation can be used to predict the optimal grating parameters to minimize the starting current of SPR. Finally, we employed a dimensional method to evaluate the microscale gas breakdown characteristics at atmospheric pressure, resulting in a universal breakdown curve applicable to different types of gases. Our results will be useful to the development of advanced cathodes and electromagnetic circuits with density modulation, enabling new advances for the development of high power electromagnetic sources and amplifiers.

4. Plans and Upcoming Events

[*Short term plans*] We are currently applying our newly developed models for emission current density modulation in RF field emitters to study their effects on beam-structure interaction for radiation generation. In particular, we would like to determine the scaling dependence of RF output power on the input parameters for a given operation frequency, including emitter properties, laser and RF fields. We have been looking at Inductive Output Tubes (IOTs) as an initial example and analyzing the effect of beam bunching on efficiency and output power. The results will be used to determine the optimized combination of input parameters (emitter properties, laser, and RF fields) to give the desired level of density modulation to maximize the efficiency and performance for a given device.

[*Long term plans*] Based on this initial study of density modulated IOTs, we plan to focus on travelling wave tubes (TWTs) and backward wave oscillators (BWOs) using emission modulated beams from photo/light assisted emission. We have existing collaborations with experimentalists at AFRL, University of Southern California, and Sandia National labs. We have also been discussing with experimentalists at Texas Tech University, France, and Singapore to identify possible collaboration opportunities. We plan to explore the possibility of tailoring the emission energy spread using optical fields. We also plan to develop a new general theory for beam-circuit interaction for density modulated beams using optical means. Our goal is to identify the optimized parameter combinations relative to beam dynamics and RF output. We will further explore the space charge effects and explore waveform controllability using emission modulated beams. We also plan to run CST and XOOPIC simulations to test the beam-circuit theory and provide guidance to the source and circuit design of amplifiers and oscillators.

Optical control of electron beams is envisioned to provide unprecedented new advances in the development of novel high power electromagnetic radiation sources owing to its ultrafast and precise control electron bunching with extremely high spatiotemporal resolution. Integration of existing device platforms with economical lasers will significantly enhance their performance and enable new capabilities. We plan to pursue this for HPM development beyond the current YIP project.

5. Transitions and Impacts

Not Applicable.

6. Collaborations

John Luginsland, AFOSR.
Matt Franzi, Air Force Research Laboratory.
Steve Fairchild, Air Force Research Laboratory.
Tyson Back, Air Force Research Laboratory.
Jacob Stephens, Texas Tech University.
Edl Schamiloglu, University of New Mexico.
Lin Wu, international collaborator, Institute of High Performance Computing, Singapore.
Y. Y. Lau, University of Michigan.
John Verboncoeur, Michigan State University.
Rehan Kapadia, University of Southern California.
Sneha Banerjee, Sandia National Labs.
Brain Bentz, Sandia National Labs.

7. Personnel

Principal Investigator: Peng Zhang, 1 person-month, National Academy Member (N).

Team Members:
Asif Iqbal, postdoc, 3 person-months, National Academy Member (N).
Yang Zhou (currently postdoc at Argonne National Lab), graduate student, postdoc, 12 person-months, National Academy Member (N).
Lan Jin, graduate student, 12 person-months, National Academy Member (N).
Md Faisal, graduate student, 6 person-months, National Academy Member (N).

Business Contact: Casie Medina
Subs: None

8. Students

3 graduate students assisting during reporting period.

9. Technology Transfer

We have filed a US Provisional Patent on optically gated field emission: P. Zhang, L. Jin, and Y. Zhou, "Optically gated field emission cathodes", US Patent Provisional filed on 8/14/2023.

10. Products, Publications, Patents, License Agreements, etc.

Publications resulting from this project during the performance period of 10/1/2022-9/30/2023:

Archival Publications

1. L. Jin, Y. Zhou, and P. Zhang, "Direct density modulation of photo-assisted field emission from an RF cold cathode", J. Appl. Phys. 134, 074904 (2023). Peer-reviewed, Distribution A, Federal Funding Acknowledged. https://doi.org/10.1063/5.0156328

2. Y. Zhou, R. Ahsan, H. Chae, R. Kapadia, and P. Zhang, "Theoretical Analysis of Resonant Tunneling Enhanced Field Emission", Phys. Rev. Applied 20, 014043 (2023). Peer-reviewed, Distribution A, Federal Funding Acknowledged. https://doi.org/10.1103/PhysRevApplied.20.014043

3. M. A. Faisal, and P. Zhang, "Grating Optimization for Smith–Purcell Radiation: Direct Correlation Between Spatial Growth Rate and Starting Current", IEEE Trans. Electron Devices 70, 2860 (2023). Peer-reviewed, Distribution A, Federal Funding Acknowledged. https://doi.org/10.1109/TED.2022.3208846

4. C. Lin, J. Chen, A. Iqbal, P. Zhang, and Y. Fu, "Dimensional analysis on microscale gas breakdown with electric field nonuniformity and positive space charge effects", J. Appl. Phys. 134, 053301 (2023). [Editor's Pick] . Peer-reviewed, Distribution A, Federal Funding Acknowledged. https://doi.org/10.1063/5.0160504

5. J. Browning, N. Jordan, J. Stephens, and P. Zhang, "Guest Editorial The Nineteenth Special Issue on High-Power Microwave and Millimeter-Wave Generation", IEEE Trans. Plasma Sci., 51, 1839 (2023). Peer-reviewed, Distribution A, Federal Funding Not Acknowledged. https://doi.org/10.1109/TPS.2023.3292334

Conference Papers

1. Peng Zhang, "Electron Emission Physics at Ultrafast and Ultra-Small Scale", 4th International Symposium on Plasma and Energy Conversion (iSPEC2022) (November 25-27, 2022, Foshan, Guangdong, China). [via Zoom] **[Invited Tutorial]** Federal Funding Acknowledged.

2. Y. Zhou, and Peng Zhang, "Effects of dc bias on quantum pathways interference in two-color laser induced photoemission", 36th IEEE International Vacuum Nanoelectronics Conference (IVNC) (July 10 - 13, 2023, Cambridge, MA, USA). [Oral] Federal Funding Acknowledged.

3. L. Jin, Y. Zhou, and Peng Zhang, “Modulated electron beam emission under rf and laser fields”, 36th IEEE International Vacuum Nanoelectronics Conference (IVNC) (July 10 - 13, 2023, Cambridge, MA, USA). [Poster] Federal Funding Acknowledged.

4. Peng Zhang, Y. Luo, Y. Zhou, and L. Jin, “Exact Analytical Quantum Theory for Strong-field Pulsed Photoelectron Emission from Biased Surfaces and Nanogaps”, PhotonIcs and Electromagnetics Research Symposium (PIERS) (July 3 - 6, 2023, Prague, Czech Republic). [Oral] Federal Funding Acknowledged.

5. Y. Zhou, R. Ahsan, H. Chae, R. Kapadia, and Peng Zhang, “Enhanced Field Emission by Resonant Tunneling Through a Quantum Well”, the American Vacuum Society (AVS) Michigan Chapter 2023 Spring Symposium (June 7th, 2023, Ann Arbor, MI, USA). [Poster] Federal Funding Acknowledged.

6. Y. Heri, and Peng Zhang, “Space Charge Effects on the Evolution of Gaussian Short-Pulse Beam Profiles”, the American Vacuum Society (AVS) Michigan Chapter 2023 Spring Symposium (June 7th, 2023, Ann Arbor, MI, USA). [Poster] Federal Funding Acknowledged.

7. L. Jin, Y. Zhou, and Peng Zhang, “Density modulation of electron beam emission using laser and rf fields”, the American Vacuum Society (AVS) Michigan Chapter 2023 Spring Symposium (June 7th, 2023, Ann Arbor, MI, USA). [Poster] Federal Funding Acknowledged.

8. M. W. Rahman and Peng Zhang, “Large Signal Analysis for Space Charge Effect on Electron Beam-Cavity Interaction”, the American Vacuum Society (AVS) Michigan Chapter 2023 Spring Symposium (June 7th, 2023, Ann Arbor, MI, USA). [Poster] Federal Funding Acknowledged.

9. Y. Zhou, R. Ahsan, H. U. Chae, R. Kapadia, P. Zhang, “Effects of resonant tunneling in field emission”, 2023 IEEE International Conference on Plasma Science (ICOPS) (May 21-25, 2023, Santa Fe, NM, USA). [Oral] Federal Funding Acknowledged.

10. M.A. Faisal, P. Zhang, “Minimizing starting current of smith-purcell radiation by grating optimization using dispersion relation”, 2023 IEEE International Conference on Plasma Science (ICOPS) (May 21-25, 2023, Santa Fe, NM, USA). [Oral] Federal Funding Acknowledged.

11. L. Jin, Y. Zhou, P. Zhang, “Density Modulated Electron Emission Using RF and Laser Fields”, “Characterization of Plasma Breakdown Induced by Pulsed Photoemission”, 2023 IEEE International Conference on Plasma Science (ICOPS) (May 21-25, 2023, Santa Fe, NM, USA). [Oral] Federal Funding Acknowledged.

12. M.W. Rahman, P. Zhang, “Parametric Analysis of Electron Beam-Cavity Interaction”, 2023 IEEE International Conference on Plasma Science (ICOPS) (May 21-25, 2023, Santa Fe, NM, USA). [Poster] Federal Funding Acknowledged.

13. A. Iqbal, B. Bentz, Y. Zhou, K. Youngman, P. Zhang, “Characterization of Plasma Breakdown Induced by Pulsed Photoemission”, 2023 IEEE International Conference on Plasma Science (ICOPS) (May 21-25, 2023, Santa Fe, NM, USA). [Oral] Federal Funding Acknowledged.

14. Y. K. Heri, P. Zhang, “Space charge effects on the short pulse beam profile”, 2023 IEEE International Conference on Plasma Science (ICOPS) (May 21-25, 2023, Santa Fe, NM, USA). [Poster] Federal Funding Acknowledged.

15. M. A. Faisal, Peng Zhang, "Smith-Purcell Radiation by a Two Layer Grating Structure", 2023 24th International Vacuum Electronics Conference (IVEC) (April 25-28, 2023, Chengdu, Sichuan, China). [Oral] Federal Funding Acknowledged.

16. Y. Zhou, and Peng Zhang, "Quantum Pathways Interference in Photoemission from Biased Metal Surfaces Induced by Two-color Lasers", 13th Annual MIPSE Graduate Student Symposium (November 16, 2022, Ann Arbor, MI, USA). [Poster] Federal Funding Acknowledged.

17. A. Paudel, Peng Zhang, P. Wong, J. Luginsland, and M. Franzi, "A Discrete Cavity Analysis of Coupled-cavity Travelling Wave Tubes", 13th Annual MIPSE Graduate Student Symposium (November 16, 2022, Ann Arbor, MI, USA). [Poster] Federal Funding Acknowledged.

18. M. Faisal, and Peng Zhang, "Grating Optimization for Smith-Purcell Radiation: Direct Correlation between Spatial Growth Rate and Starting Current", 13th Annual MIPSE Graduate Student Symposium (November 16, 2022, Ann Arbor, MI, USA). [Poster] Federal Funding Acknowledged.

19. B. Z. Bentz, K. Youngman, A. Iqbal, Y. Zhou, and Peng Zhang, "Photoemission induced plasma breakdown", DOE Center for Low Temperature Plasma Interactions with Complex Interfaces and User Facilities Annual Meeting (October 28-29, 2022, Arlington, VA, USA). [Oral] Federal Funding Acknowledged.

20. Peng Zhang, B. Bentz, A. Iqbal, Y. Zhou, K. Youngman, "YO08.00010: Effects of pulsed photoemission in plasma breakdown", 64th Annual Meeting of the APS Division of Plasma Physics (October 17–21, 2022, Spokane, Washington, USA). [Oral] Federal Funding Acknowledged.

21. Y. Zhou, and Peng Zhang, "PO08.00011: Quantum pathways interference in photoemission from metals induced by two-color lasers with a dc bias", 64th Annual Meeting of the APS Division of Plasma Physics (October 17–21, 2022, Spokane, Washington, USA). [Oral] Federal Funding Acknowledged.

22. B. Bentz, K. Youngman, A. Iqbal, Y. Zhou, Peng Zhang, "DT1.00001: Photoemission induced plasma breakdown", 75th Annual Gaseous Electronics Conference (October 3-7, 2022, Sendai, Japan). [Oral] Federal Funding Acknowledged.

<u>Theses</u>

1. Y. Zhou, "Photoemission from biased metal surfaces: quantum efficiency, laser heating, dielectric coatings, and quantum pathways interference", Ph.D. dissertation, Dept. Elect. Comput. Eng., Michigan State Univ., East Lansing, MI, USA, 2022. Federal Funding Acknowledged.

<u>Patents</u>

1. P. Zhang, L. Jin, and Y. Zhou, "Optically gated field emission cathodes", US Patent Provisional filed on 8/14/2023.

11. Point of Contact in Navy

Kevin Jensen, NRL, 10 MAY2023; Jason Marshall, NRL, 10MAY2023

Infrared Optics with Engineered Materials

Grant No. N00014-20-1-2297

Annual Report for Fiscal Year 2023

Period of Performance: October 1, 2022 to September 30, 2023

Prepared by:

Professor Mikhail Kats, Principal Investigator
University of Wisconsin-Madison
Engineering Hall, 1415 Engineering Drive, Room 3441, Madison, WI, USA - 53706
Tel: 608 890 3984
Email: mkats@wisc.edu

This work was sponsored by the Office of Naval Research (ONR), under grant number N00014-20-1-2297. The views and conclusions contained herein are those of the authors only and should not be interpreted as representing those of ONR, the U.S. Navy or the U.S. Government.
Grant or Contract Number: N00014-20-1-2297

Date Prepared:
Project Title: Infrared Optics with Engineered Materials
Annual Summary Report: FY23, 1 October 2022 to 30 September 2023
Principle Investigator: PI Mikhail Kats, 608-890-3984, mkats@wisc.edu, University of Wisconsin-Madison

Section I: Project Summary

1. Overview of Project

Abstract: The major goals of this project are to explore innovative ways to engineer and characterize existing and emerging optical materials to enable next-generation infrared optics for emitting, manipulating, absorbing, and detecting infrared light. The ability to emit, manipulate, absorb, and detect infrared light has substantial long-term Naval relevance, especially due to the rapid development of infrared sensors and cameras, as well as high-power lasers that may be used to blind these instruments. This document describes progress made in FY23 toward these fundamental-science goals, and includes the demonstrating and understanding of colossal optical birefringence in the mid infrared, the demonstration of VO_2-metasurface-based optical limiters, switches and power diodes, the demonstration of metasurface-based spectrochemical sensing, and advances in mid-infrared spectroscopic ellipsometry.

Objective: The proposal had three key sections (chapters). In Chapter 1, we proposed new approaches to modify materials properties, focusing on spatial control of infrared optical properties, such that they can be engineered into devices. In Chapter 2, we proposed the development of new and improved methods of materials metrology to better understand infrared optical materials and to better characterized engineered optical structures. In Chapter 3, we proposed new infrared optical and optoelectronic devices for polarization control and infrared photodetection, based on materials-engineering and characterization techniques (to be) developed in Chapters 1 and 2. Specifics goals include the development of new spectroscopic techniques for materials analysis, new types of flat and thin optical components for imaging and beam control, more-robust control over polarization of infrared light, new optical protective technologies, and new optical technology for thermoregulation using engineered thermal radiation.

Background: Our approach to reach the objectives described above is to carry out an interdisciplinary, integrated program where we simultaneously investigate new spectroscopic techniques for materials characterization, new ways of modifying materials, and new devices, with the devices building on the materials innovations developed within the project.

2. Activities and Accomplishments

Colossal optical anisotropy

As briefly described in the FY22 Annual Report, we have discovered and been studying the existence of colossal optical anisotropy in strontium titanium sulfide (STS), setting a world record for a uniaxial material (refractive index = 2.4 for one polarization, and 4.5 for an orthogonal polarization). This work is in collaboration with Jayakanth Ravichandran's group at USC and Rohan Mishra's group at WUSTL.

This observation of optical anisotropy in this material is unsurprising given our past results and the expected ABX_3 quasi-1D crystal structure, but the magnitude of it is very surprising and potentially very important. For a long time, we have been unable to determine the precise physical mechanism enabling such colossal optical anisotropy. I am happy to report that, as of this reporting period, the physical mechanism has been identified and understood. In particular, what leads to the large enhancement to optical anisotropy in

$Sr_{9/8}TiS_3$ is atomic-scale structural modulations resulting from excess Sr atoms in this nonstoichometric configuration of strontium titanium sulfide (it turns out that the stoichiometric configuration is not stable, but the nonstoichiometric and modulated configuration is stable). The structural modulations increase the unit cell of the crystal manyfold from the stoichiometric case, and the additional electrons from the extra Sr form highly oriented electron clouds whose polarizability is strongly asymmetric.

We have now published a comprehensive manuscript in *Advanced Materials* that describes this finding, including comprehensive optical measurements from the ultraviolet to the mid infrared, careful structural analysis based on x-ray diffraction and high-resolution electron microscopy, and density functional theory based on the structural analysis that explains the electronic origin of the dramatic anisotropy. The first figure of the manuscript is shown as Fig. 1 here.

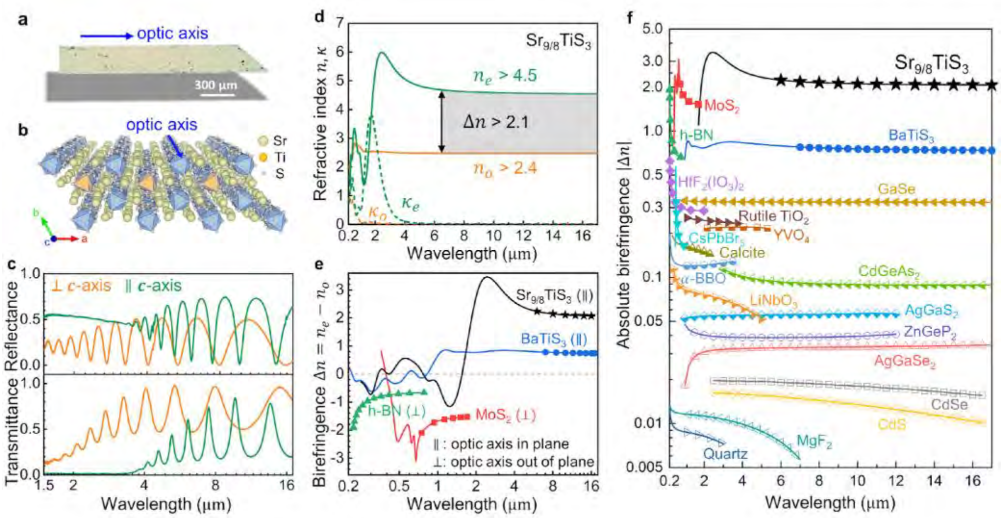

Figure 1. Infrared birefringence n > 2.1 in $Sr_{9/8}TiS_3$ single crystals. a. Optical image of a $Sr_{9/8}TiS_3$ crystal. **b**. Perspective schematic of a $Sr_{9/8}TiS_3$ crystal with the optic axis along the TiS_6 chains. **c**. Polarized reflectance and transmittance of a $Sr_{9/8}TiS_3$ crystal plate with thickness = 3.2 μm measured across the mid infrared (the wavelength axis uses the log scale). **d**. Extracted complex refractive-index values of uniaxial $Sr_{9/8}TiS_3$ for the ordinary (perpendicular to *c*-axis, orange) and extraordinary (parallel to *c*-axis, green) directions spanning the visible through the mid infrared, based on a combination of spectroscopic ellipsometry and transmittance/reflectance measurements. For wavelengths longer than ~6 μm, the material is highly transparent and maintains a large birefringence, $\Delta n > 2.1$ (gray shaded region). **e.** Comparison of the birefringence of two representative hexagonal quasi-1D chalcogenides ($Sr_{9/8}TiS_3$ and $BaTiS_3$) with highly anisotropic 2D materials (h-BN and MoS_2). The transparent regions of these materials are identified using symbols. **f.** Comparison of the absolute birefringence values of $Sr_{9/8}TiS_3$ and a variety of anisotropic materials [from the literature], showing that $Sr_{9/8}TiS_3$ has by far the largest birefringence among reported anisotropic crystals. The symbols indicate regions of transparency.

<u>Optical limiting, nonlinear isolation, and switching using VO_2-enabled metasurfaces</u>

In this reporting period, we continued our work on VO_2-based devices for tunable infrared functionality. In particular, we recently published a paper in *Nature Photonics* describing a multifunctional device comprising a metasurface, a phase-transition layer, and electrical controls that can serve as a mid-infrared modulator, limiter, and limiting diode (nonlinear isolator), depending on how it is used (Fig. 2)

Previously in this project, we published a paper in Laser & Photonics Reviews titled "Ultrathin broadband reflective optical limiter", where we used a similar concept to design a structure which was transparent at low input power but reflective at high input power. The structure in Fig. 2 is similar, except we can now drive a current through the frequency selective surface and provide a temperature bias to the VO_2, changing its threshold intensity. The devices have already been fabricated, and we have demonstrated the performance of the device in various modes, using a quantum cascade laser that we purchased that has a peak wavelength around 3.9 micron. This wavelength range has various applications of Naval relevance.

The structure comprises metallic metasurfaces made of aperture antennas on top of a VO_2 layer, which features a phase transition, and the entire metallic structure is used as a microheater to which electrical leads are attached. By sending current through the leads, we can control the temperature of the VO_2 layer, enabling current-driven infrared modulation. The current biasing also enables the tuning of the threshold of VO2, enabling optical limiting with different threshold. Because we engineered the device to feature different absorption depending on the direction of incident light, there exists a range of optical powers where the device is transparent in one direction but opaque from the other, this serving as a nonlinear optical isolator or a limiting power diode. The experimental optical limiting performance is shown in Fig. 3, tested with the 3.9 micron continuous-wave quantum cascade laser.

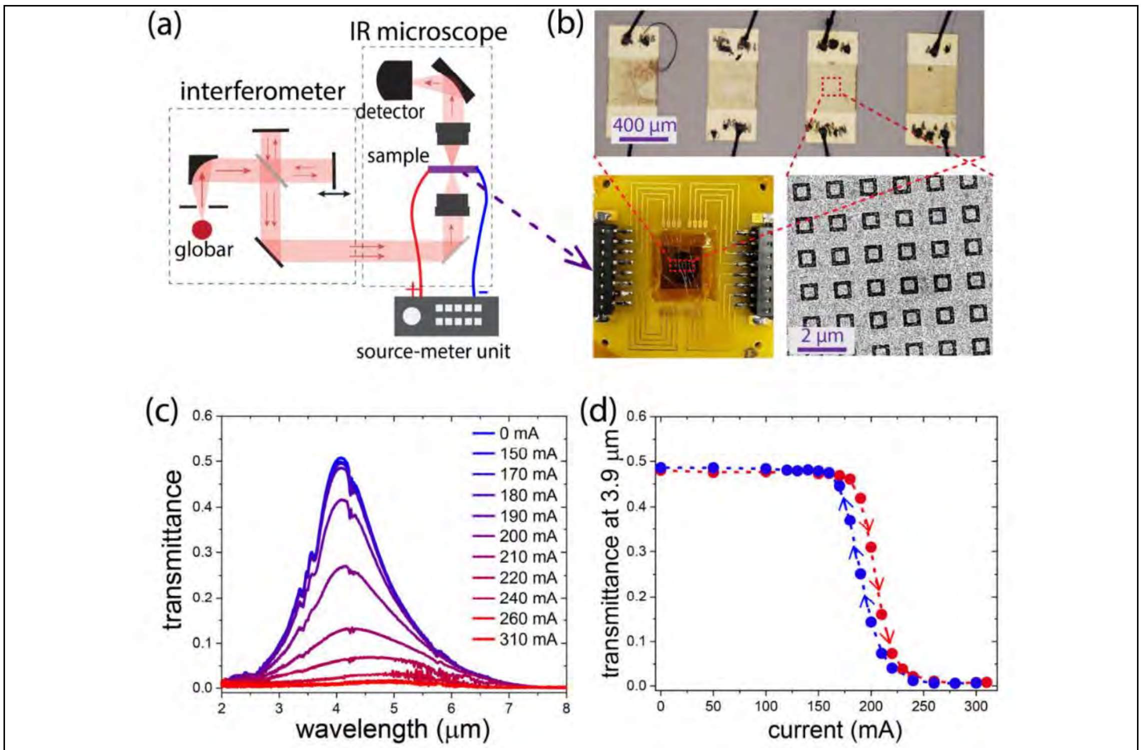

Figure 2. (a, b) Schematic of transmittance measurements through our multifunctional VO_2-metasurface device, and image of the circuit board on which several devices are mounted. The measurements in this paper all come from the device boxed in red. (c) Transmittance spectrum of our device for varying current (0 to 310 mA), initially at ambient temperature. (d) Transmittance at λ = 3.9 µm for ascending and descending current.

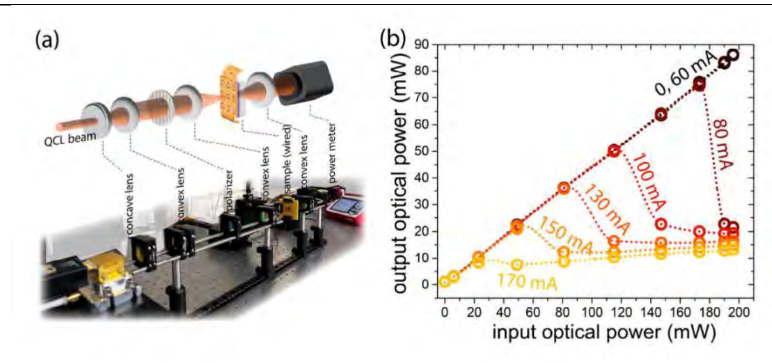

Figure 3. (a) Schematic of optical limiting measurement apparatus using a quantum cascade laser (QCL) at 3.9 µm. (b) Output-vs-input curves for optical limiting, for different levels of bias current.

The current biasing also enables the tuning of the threshold of VO2, enabling optical limiting with different threshold. Because we engineered the device to feature different absorption depending on the direction of incident light, there exists a range of optical powers where the device is transparent in one direction but opaque from the other, this serving as a nonlinear optical isolator or a limiting power diode. The experimental optical limiting performance is shown in Fig. 4,

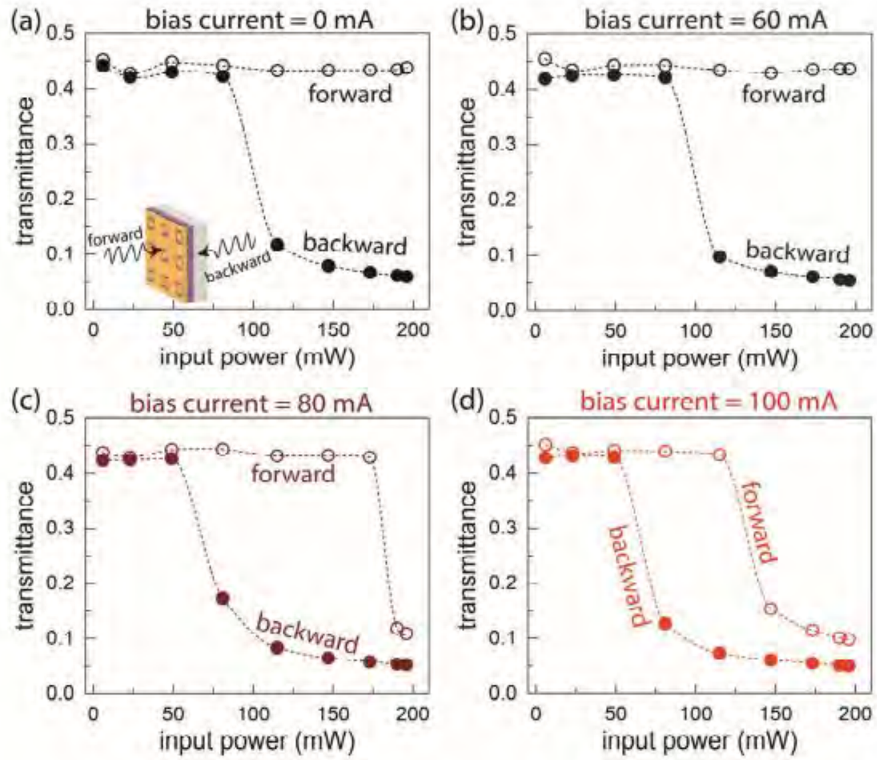

Figure 4. Device transmittance when it is functioning as a nonlinear isolator (limiting optical diode) for bias currents from 0 (a) to 100 mA (d). As the current is increased, electrical heating begins to dominate over optical heating, reducing the transmittance asymmetry while the limiting threshold in both directions is decreased.

We have also started looking into the possibility of further engineering these devices using defect engineering via ion bombardment. As we demonstrated in a couple of previous publications, including one from the present project, the bombardment of VO_2 with ion beams results in damage to the film, creating localized strain, which is known to affect the phase transition of VO_2. We believe that we can use this technique to engineer the phase transition of localized regions after the entire device is fabricated, including via ion implantation through the metal frequency selective surface. Preliminary data on this topic is shown in Fig. 5 below. Basically, we were able to create an optical switch or limiter, similar to our in-press paper, and then irradiate regions using an Ar ion beam, resulting in a shift in the phase transition temperature and therefore changing the triggering threshold of the device. This kind of post-fabrication engineering of the phase transition of VO_2 is (we believe) the first of its kind. We plan to publish a paper describing this advance in FY24.

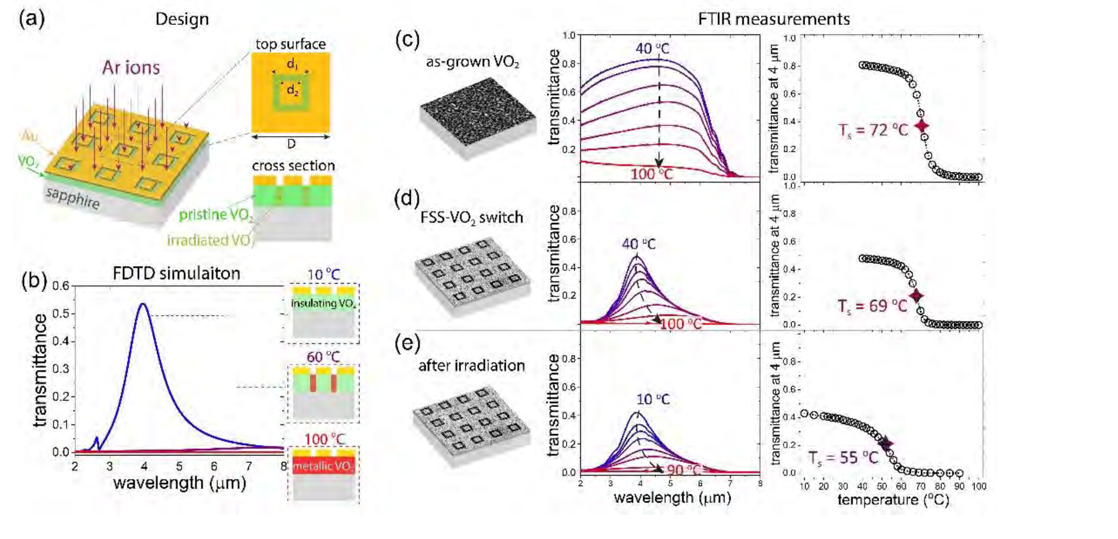

Figure 5. **(a)** We irradiated a fabricated FSS-VO_2 optical switch using 75-keV Ar ions with a fluence of $6x10^{13}$ cm^{-2}, resulting in lower IMT temperature in the exposed VO_2 while leaving the VO_2 under the Au regions unaffected. **(b)** Simulated optical transmittance of the design shown in (a) when the VO_2 is in the insulating phase (blue curve), when only the irradiated VO_2 is transformed to the metallic phase (purple curve), and when the entire VO_2 is in the metallic phase (red curve). **(c – e)** Temperature-dependent FTIR transmittance measurement of the as-grown (intrinsic) VO_2 film, fabricated FSS-VO_2 optical switch, and the post-irradiation optical switch, respectively. In each panel, the left figures are schematics with SEM images incorporated. The middle figures are FTIR transmittance of the corresponding samples for temperature increasing from 10 to 100 °C. The right figures are normalized transmittance at λ = 3.9 μm (i.e., peak transmittance) and their derivatives with respect to increasing temperature. The switching temperature, T_s, is determined in the derivative curve.

Mid-infrared metasurfaces for spectrochemical sensing

While this was not an initial goal of the present project, the mid-infrared infrastructure and measurement expertise built over the duration of the project helped enable a new colleague, Filiz Yesilkoy (Biomedical Engineering at UW-Madison) to design and measure plasmonic metasurfaces that have multiple resonances that can be activated by different polarizations of mid-infrared light, enabling a new type of bio-imaging with very high resolution and polarization sensitivity. In Fig. 5, we show the fabricated structures to Yesilkoy's group and our mid-infrared measurements. The structures were then used by Yesilkoy to perform surface-enhanced infrared absorption imaging using a tunable quantum-cascade-laser system combined with focal-plane-array imaging in an infrared microscope.

The result is a label-free and nondestructive mid-infrared vibrational hyperspectral imaging tool that can provide spatially resolved biochemical information critical to understanding physiological and pathological processes. A paper describing this work has now been published as S. Rosas et al, "Metasurface-Enhanced Mid-Infrared Spectrochemical Imaging of Tissues", *Advanced Materials* 35, 2301208 (2023). It was also highlighted as an "Editor's Choice" paper, indicating that it was selected as one of the best papers published in this top journal.

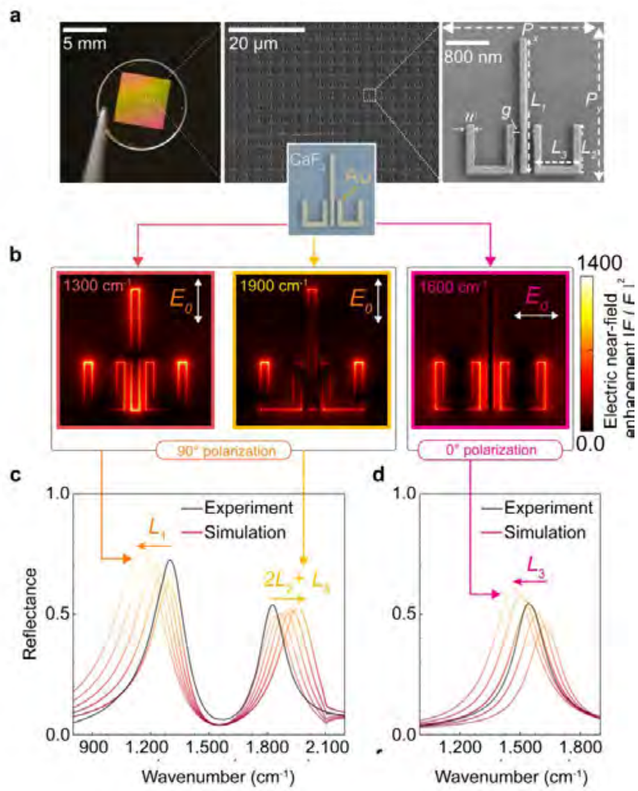

Figure 5. Polarization-multiplexed multi-resonant broadband plasmonic metasurface. (a) Photograph and SEM image of the two-dimensional array of plasmonic ulu nanostructures. b, Numerically Simulated electric near-field intensity enhancement $|E/E_0|^2$ maps at different resonance wavenumbers for 0° and 90° polarizations. c, d, Experimentally measured (black curves) and simulated (red-yellow gradient) reflectance spectra of the polarization-multiplexed multiresonant plasmonic metasurface. The three resonant peaks are independently tuned by adjusting the geometrical parameters of the ulu structures, such as L_1, L_2, and L_3, to spectrally match the absorption fingerprints of important biomolecules in the mid-Infrared region

Advances in the fitting of spectroscopic ellipsometric data

We have been taking precise measurements of temperature-dependent optical properties over a broadband range of amorphous SiO_2, which we regularly use in infrared measurements as a reference material, but whose temperature-dependent infrared properties are not well known. This is important for us to be able to perform well-calibrated infrared measurements of all types, but in particular reflectance and emission measurements which need a well-known reflectance and emissivity. Because the optical properties of all materials, including any we can use as references, are expected to change with temperature, we need to pre-characterize our references as a function of temperature very precisely.

Some of our results (not published at this time) are shown in Fig. 6. We can see the vibrational resonances of amorphous SiO_2 (Corning wafers of different grades) around 9, 12, and 21 micron, resulting from various modes of Si-O bonds. This data was acquired using variable-angle spectroscopic ellipsometry, and then we fit it using an oscillator model using Gaussian oscillators. Fitting this data, and most ellipsometric data is nontrivial, especially if one aims to build a model that has physical meaning. In particular, it is very easy to overfit the data—add oscillators that end up fitting the noise rather than some underlying physical mode.

We have recently started using the fact that the vibrational resonances are expected to gradually and monotonically evolve with temperature to check our model for overfitting. Whether or not this is observed in our modeling can be a test of whether or not we have overfitted our data. We are presently refining this technique, and plan to publish a paper on this topic in FY24.

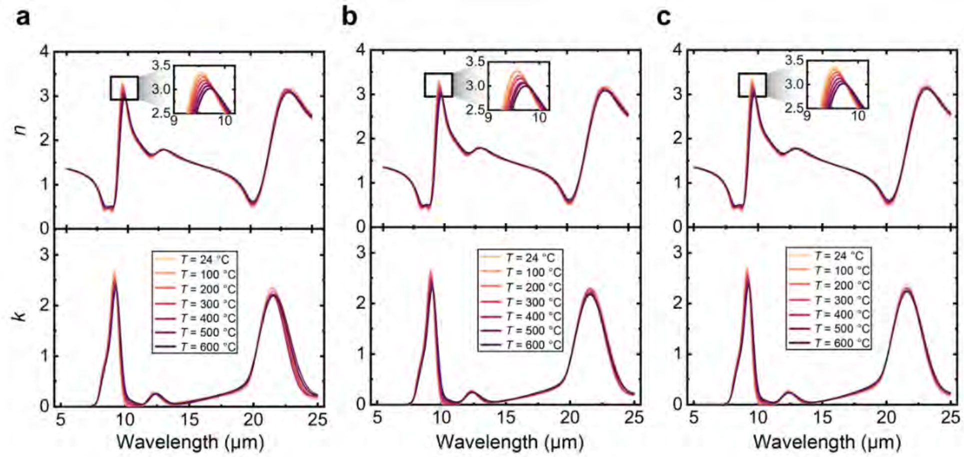

Figure 6. (Upper) Refractive index (n) and (lower) absorption coefficient (k) values of (a) Corning HPFS 8655 UV grade fused silica, (b) Corning HPFS 7979 IR grade fused silica, and (c) Corning HPFS 7980 standard grade fused silica.

3. Findings and Conclusions

- Demonstrated and elucidated the mechanism of colossal mid-infrared optical anisotropy in strontium titanium sulfide
  - Related to Chapter 1 goals enabling new mid-infrared optical materials
- Designed and demonstrated a multifunctional device using tunable VO2-based metasurfaces, enabling mid-infrared optical switching, limiting, and nonlinear isolation
  - Meeting a Chapter 3 goal, demonstrating new optical and optoelectronic devices
- Demonstration of mid-infrared metasurfaces for spectrochemical sensing
  - Related to a Chapter 2 goal, demonstrating a new sensing/metrology technique, albeit for biosensing rather than for metrology of mid-infrared materials for devices
- Made an advance in the fitting of spectroscopic ellipsometric data, in particular to prevent overfitting issues in mid-infrared ellipsometry
  - Meeting a Chapter 2 goal, helping improve methods of infrared materials metrology

4. Plans and Upcoming Events

The plans are unchanged from the proposal. Prof. Kats has an upcoming seminar at AFRL, which will in part cover the work on the present project, as well as invited talks at the Optica Imaging Congress (Toulouse) and SPIE Optics + Photonics (San Diego).

5. Transitions and Impacts

We have initiated discussions with AFRL about our work on colossal optical materials, and I will visit AFRL in September 2024 to further these discussions that may lead to a transition.

We have applied for and received an ONR DURIP to build a photothermal commonpath interferometry (PCI) system to enable new modelities of materials characterization over a broadband range that includes the mid-infrared. During the next FY, the system will be built.

We have also started the Wisconsin Center for Semiconductor Thermal Photonics with seed funds from the Wisconsin Alumni Research Foundation, based in part on the fundamental research carried out via this project.

We received a Phase I STTR titled "F-MECCs for Thermal Regulation", where certain materials concepts were developed as part of the present project. This is a subcontract from Physical Sciences Inc, funded by the Air Force.

6. Collaborations

In this reporting period on this project, we have collaborated with the following groups:

- Group of Carsten Ronning, University of Jena, Germany
- Group of Shriram Ramanathan, Rutgers University
- PIs David Woolf, Joel Hensley, and others, Physical Sciences Incorporated
- Group of Jayakanth Ravichandran, University of Southern California
- Group of Rohan Mishra, Washington University in St. Louis
- Group of Jun Xiao, UW-Madison
- Group of Filiz Yesilkoy, UW-Madison

7. Personnel

Principal investigator: Mikhail Kats, 0.1 person months [not a National Academy Member]

Team Members: Jin-Woo Cho, postdoc, 1.5 person months [not a National Academy Member]; Tanuj Kumar, graduate student, 2 person months [not a National Academy Member]; Hongyan Mei, graduate student, 4 person months [not a National Academy Member]; Shenwei Yin, graduate student, 1.5 person months [not a National Academy Member]; Yuzhe Xiao, Assistant Scientist, 1 person-months [not a national Academy Member]

Note that Yuzhe Xiao (Postdoc, then Assistant Scientist) departed early on in this reporting period, and is now an Assistant Professor at the University of North Texas. e

8. Students

Four (4) graduate students

9. Technology Transfer

No new patent this FY, though two patents have been filed based on work performed on this project:

Y. Xiao, C. Wan, J. Salman, M. A. Kats, "Planck spectrometer", Patent application filed Dec 2020, published 2022. Issued Jan 2024. US Patent 11,879,783 B2.

S. Niu, G. Joe, M. A. Kats, S. Ravichandran, "Anisotropic materials and method of forming anisotropic materials exhibiting high optical anisotropy". Provisional patent application filed May 2018. Published July 2021 (pending).

10. Products, Publications, Patents, License Agreements, etc.

Publications resulting from this project:

Archival Publications (all peer reviewed)

A. Koch, H. Mei, J. Rensberg, M. Hafermann, J. Salman, C. Wan, R. Wambold, D. Blaschke, H. Schmidt, J. Salfeld, S. Geburt, M. A. Kats, C. Ronning, "Heavily Doped Zinc Oxide with Plasma Frequencies in the Telecommunication Wavelength Range", *Advanced Photonics Research* 2200181 (2022)

H. Mei, G. Ren, B. Zhao, J. Salman, G. Y. Jung, H. Chen, S. Singh, A. S. Thind, J. Cavin, J. A. Hachtel, M. Chi, S. Niu, G. Joe, C. Wan, N. Settineri, S. J. Teat, B. C. Chakoumakos, J. Ravichandran, R. Mishra, M. A. Kats, "Colossal optical anisotropy from atomic-scale modulations", *Advanced Materials* 35, 2303588 (2023)

S. Rosas, K. A. Schoeller, E. Chang, H. Mei, M. A. Kats, K. W. Eliceiri, X. Zhao, F. Yesilkoy, "Metasurface-enhanced mid-infrared spectrochemical imaging of tissues", *Advanced Materials* 35, 2301208 (2023)

J. King, C. Wan, T. J. Park, S. Deshpande, Z. Zhang, S. Ramanathan, M. A. Kats, "Electrically tunable VO2-metal metasurface for mid-infrared switching, limiting, and nonlinear isolation", *Nature Photonics* 18, 74 (2024) [note: final publication in FY24, but paper was up on arXiv and accepted in FY23]

Conference Papers

Note: in our group/field, we typically do not submit "conference papers", but we do have conference presentations which are either oral or poster presentations. Sometimes (but not always) the abstract is published, but we do not typically submit full conference papers.

H. Mei, G. Ren, B. Zhao, J. Salman, G.-Y. Jung, H. Chen, A. Thind, S. Singh, N. Settineri, S. Teat, B. Chakoumakos, J. Ravichandran, R. Mishra, M. Kats, "Infrared optics with highly anisotropic Materials", Materials Research Society Fall Meeting, Boston (2023)

H. Mei, G. Ren, B. Zhao, J. Salman, G. Y. Jung, H. Chen, A. Thind, J. Cavin, J. Hachtel, M. Chi, S. Niu, G. Joe, C. Wan, N. Settineri, S. Teat, B. Chakoumakos, J. Ravichandran, R. Mishra, M. A. Kats, "Colossal Birefringence From Periodic Structural Modulations", Conference on Laser and Electro-Optics (CLEO), San Jose (2023)

J. King, C. Wan, S. Deshpande, T. J. Park, Z. Zhang, S. Ramanathan, M. A. Kats, "Electrically Tunable High-Contrast Optical Modulator Based on the Phase Transition of Vanadium Dioxide", Conference on Laser and Electro-Optics (CLEO), San Jose (2023)

T. Kumar, D. Feng, S. Yin, P. Lin, M. Mah, M. Fortman, G. Jaffe, C. Wan, C. Fang, R. Warzoha, V. Brar, J. Talghader, M. Kats, "Photothermal Commonpath Interferometry of Silicon Nitride Membranes for Laser Light Sails", Conference on Lasers and Electro-Optics (CLEO), San Jose (2023)

B. Zhao, G. Ren, H. Mei, V. Wu, S. Singh, G. Y. Jung, H. Chen, R. Giovine, N. Settineri, S. Teat, R. Clément, M. A. Kats, R. Mishra, J. Ravichandran, B. Chakoumakos, "Correlated Disorder of the Sub-Angstrom Atomic Displacements in BaTiS3 Causes Giant Optical Anisotropy", Bulletin of the American Physical Society (2023)

Books

None

Book Chapter

None

Theses

None

Websites

None

Patents

None this FY

Other Products: Identify any other significant products that were developed under this project. Describe the product and how it is being shared.

N/A

11. Point of Contact in Navy

None at this time

ONR Global

Geodesic Luneburg Lenses for High Power Applications

Grant No. N62909-20-1-2040

Annual Report for Fiscal Year 2023

Period of Performance: October 1, 2022 to September 30, 2023

Prepared by:

Dr. Oscar Quevedo-Teruel, Principal Investigator
KTH Royal Institute of Technology
Brinellvägen 8, 114 28
Stockholm, Sweden
Tel: +46-72-844 41 64
Email: oscarqt@kth.se

This work was sponsored by the Office of Naval Research (ONR), under grant number N62909-20-1-2040. The views and conclusions contained herein are those of the authors only and should not be interpreted as representing those of ONR, the U.S. Navy or the U.S. Government.

Grant or Contract Number: N62909-20-1-2040
Date Prepared: 10th Jan. 2024
Project Title: Geodesic Luneburg Lenses for High Power Application
Annual Summary Report: FY23
PI: Prof. Oscar Quevedo-Teruel, +46-72-844 41 64, oscarqt@kth.se
KTH Royal Institute of Technology

Section I: Project Summary

1. Overview of Project

Abstract:

This project investigated the suitability of fully-metallic geodesic Luneburg lens antennas for high power applications. As the project ended in September 2023, the primary aim of this reporting period was to finalize the investigations initiated in previous reporting periods. The most important was the manufacture and experimental testing of the X-band rotationally symmetric Luneburg lens, designed for operation from 10-20 GHz. The measurements were conducted using facilities at both KTH (Stockholm) and the NRL (Washington D.C.), independently verifying the lens performance. In addition to the measurements conducted at the NRL, the team from KTH hosted seminars to discuss the work performed during the project at NSWC-DD and John Hopkins APL during their visit to Washington D.C. in August, 2023. To complete the study on the addition of loss terms to the generalized ray-tracing code, an elliptical lens prototype was manufactured monolithically using metallic 3D printing. The results obtained from ray tracing were verified using both full-wave simulation and measurements and have been published in an IEEE Transactions on Antennas and Propagation article. The ray tracing code for a non-rotationally symmetric case where the outline of the footprint is defined has been completed and verified with full-wave simulations. This modification to the ray tracing algorithm has been presented at the 13th International Conference on Metamaterials, Photonic Crystals and Plasmonics 2023 in Paris and has been accepted for presentation and publication at the 2024 edition of the European Conference on Antennas and Propagation to be held in Glasgow. Additionally, a refined version of the half-Luneburg lens with an integrated reflectarray using square patches was presented at both the Swedish Microwave Days held in Stockholm and at the 2023 Edition of the European Conference on Antennas and Propagation held in Florence.

Objective:

The primary objective of this project was to investigate the suitability of geodesic lenses for high-power antenna applications, which can be utilized in radar systems. As geodesic lenses can take a significant amount of time to model using commercial software, the development of a time-efficient model was deemed necessary. In addition to this, the project aimed to determine the fundamental limitations of geodesic lenses and their limitations at high-power. The project also explored the use of fully metallic geodesic lenses at X- and Ku- bands.

Introduction:

A Luneburg lens is a graded-index lens that transforms a spherical/cylindrical wave into a planar wave at the opposing side of the excitation. Luneburg lenses are an attractive solution for communications and radar systems since they have low scan losses. However, their principal drawback for high-power applications is that they are typically implemented with dielectric materials, which are lossy and limit the amount of handled power. Equivalents to dielectric Luneburg lenses can be achieved with geodesic lenses. As geodesic lenses are fully metallic, they can cope with high-power.

Geodesic lenses consist of two parallel curved conductive plates, with a homogenous refractive index between the plates. The refractive index profile of a conventional dielectric lens is then replicated with an appropriate height profile. A rotationally symmetric structure is assumed during the calculation of the height profile. This lens profile can be reduced in the *z*-direction via the introduction of folds, which maintain the optical path length required of the lens.

Geodesic Luneburg lenses are highly relevant for both naval and civilian applications as they can be used in radar systems; 5G/6G communications systems and satellite communications.

<u>Background:</u>

Ray tracing has been successfully implemented in the design process of a wide range of microwave technologies where commercial software is either inefficient or inconvenient. In this approach the propagation of electromagnetic waves is modelled in terms of rays, where each ray is defined as the normal to the wave front at that location. In doing so, the problem is simplified allowing for the possibility of an algorithm to be developed.

The ray tracing model that has been engineered over the course of this project can be split into three regimes, firstly geometric optics to determine the ray path through the lens, secondly the concept of ray tubes to approximate the amplitude at the lens edge and finally Kirchhoff diffraction to determine the radiation pattern exhibited by the lens.

2. Activities and Accomplishments

Rotationally symmetric cases have been explored extensively in previous reporting periods with the results disseminated in several conference papers and journal publications. The project was developed further with the exploration of non-rotationally symmetric cases. These investigations were continued into the reporting period discussed in this report.

Losses due to the conductivity and the surface roughness of the metallic plates have been previously introduced to the generalized ray-tracing model, allowing for an easy comparison between manufacturing techniques/materials and their impact on the radiation pattern displayed by the lens. In this reporting period the modified model was verified with a manufactured prototype designed for operation from 24-32 GHz. An elliptical lens with a compression of 30% along the *y*-axis and a water-drop height profile was manufactured monolithically using metallic 3D printing. The material selected was the aluminum alloy AlSi10Mg. An image of the manufactured lens and the radiation patterns generated from ray tracing, full-wave simulation and measurements are shown in Fig. 1. These results have been published in an IEEE Transactions on Antennas and Propagation article with the title ‘Evaluation of Losses in 3D-Printed Geodesic Lenses Using a Ray-Tracing Model’.

(a)

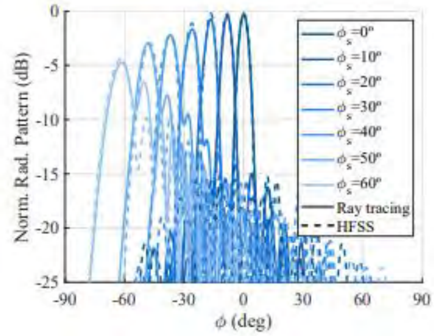

(b)

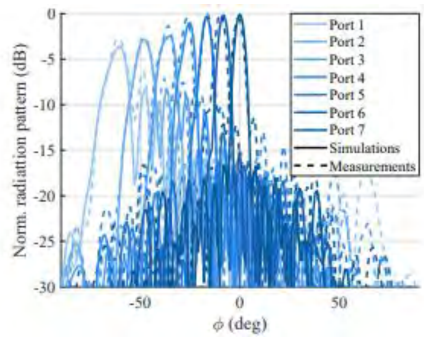

(c)

Figure 1: (a) Manufactured elliptical lens mounted for measurement at KTH, (b) radiation patterns for each port of the designed lens at 30 GHz generated from the modified ray tracing code and full-wave simulation and (c) the radiation patterns for each port of the designed lens at 28 GHz from measurement and full-wave simulation.

The investigation into non-rotationally symmetric full-lens structures with defined footprints was completed in this reporting period. For this profile, a spline function was used to create a footprint in the *xy*-plane that reduced the size of the lens in both the *x* and *y* directions (Fig. 2). This variation in shape is more complex than the compressions applied in the elliptical lens case, allowing for more degrees of freedom to generate the desired radiation response from each port. The ray tracing model required modification to the meshing of the lens profile and how the waveguide port was represented at different positions, which was initiated in the previous reporting period but finalized during the current one. An example case operating at 100 GHz was presented at the 13th International Conference on Metamaterials, Photonic Crystals and Plasmonics in Paris, France. A paper reporting the impact of the profile shape on the radiation pattern has been accepted for presentation at the European Conference on Antennas and Propagation (EuCAP) to be held in Glasgow, Scotland (Fig. 2 (a)), and an article featuring a prototype designed for operation at 60 GHz will be submitted to IEEE Antennas and Wireless Propagation Letters (Fig. 2 (b)).

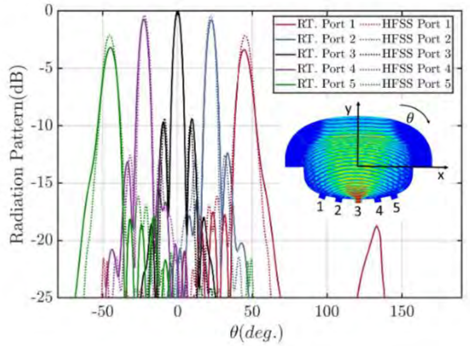

(a) **(b)**

Figure 2: (a) Radiation patterns exhibited by the lens with a defined profile that will be presented at EuCAP 2024 and (b) photograph of the manufactured prototype operating at 60 GHz.

The rotationally symmetric manufactured prototype (Fig. 3 (a)) was measured using the facilities at KTH and the NRL during this reporting period. The broadband behavior of the lens was verified, with the radiation patterns at 10 and 20 GHz matching closely with the anticipated results from simulation, as shown in Fig 3(b) and (c). The deviation in measured position seen in in the outer ports is a result of a shifted phase center in the feeding waveguide, and not the lens.

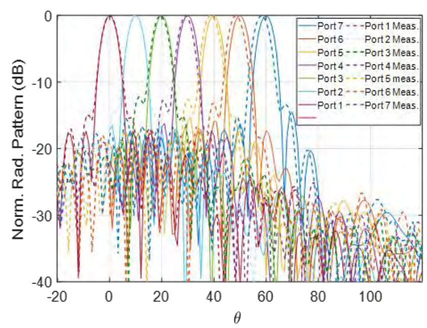

(a) **(b)**

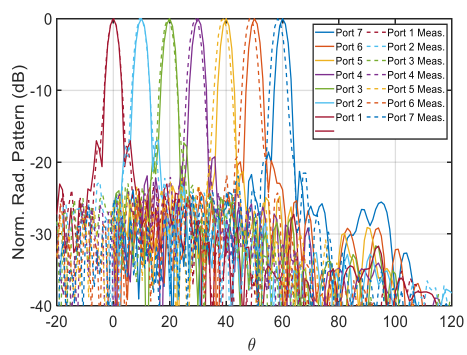

(c)

Figure 3: (a) Manufactured X-band prototype and (b) measured and simulated radiation patterns at 10 GHz and (c) 20 GHz.

3. Findings and Conclusions

The rotationally symmetric prototype has proved to be capable of operating over a wide bandwidth and presents radiation patterns that match the simulated results. It was also shown that the ray tracing code with the inclusion of loss terms can be used when selecting the material or manufacturing method for geodesic lens prototypes.

The footprint of geodesic lenses can be reduced by defining the outline using splines, and the features of the radiated beams can be tailored by careful selection of the shape of the spline. This is useful for scenarios where volume limited, but good performance over a range of scanning angles is still desired.

4. Plans and Upcoming Events

As the project has come to an end the final report will be submitted. Additionally, articles reporting the final developments of the project are expected to be submitted to various journals. The content of these submissions will cover the non-rotationally symmetric geodesic lens with a defined outline and the half-lens with an integrated reflectarray.

In terms of dissemination, a paper titled 'Tailoring the Performance of Geodesic Lens Antennas By Defining their Footprint', has been accepted to be presented at the 2024 European Conference on Antennas and Propagation (EuCAP) held in Glasgow. This is the largest European conference relevant to our research.

5. Transitions and Impacts

Prof. Oscar Quevedo-Teruel and Dr. Sarah Clendinning participated in the Visiting Scientist Program in August 2023, which allowed them to visit NSWC-DD, John Hopkins APL and NRL. Seminars were held at NSWC-DD (team lead: Dr. Jack Chen, yeong-jer.chen.civ@us.navy.mil) and APL (team lead: Dr. Brendan Sievers, brendan.sievers@jhuapl.edu), where the investigations conducted over the course of the project was presented in depth. This allowed for discussions about possible future work or areas of applications that were not thought of before the visit. The measurement facilities at NRL were used, with the assistance of Dr. Mark Dorsey (william.m.dorsey4.civ@us.navy.mil) and Dr. Zachary Drikas (zachary.drikas@nrl.navy.mil) to independently verify the radiation patterns displayed by the manufactured X-band prototype featured in this report. High-power testing was also conducted on the lens, which was only possible using the facilities at NRL. Further high-power testing was conducted on the lens at the NRL after the visit from the team at KTH.

6. Collaborations

The team at KTH have collaborated with Prof. Francisco Mesa (University of Seville in Spain) to further develop the ray tracing tool for non-rotationally symmetric cases.

7. Personnel

All the participants in this project are at KTH Royal Institute of Technology, Stockholm Sweden.

Principal investigator: Prof. Oscar Quevedo-Teruel (Full Professor) (450hr)
Team Members:

- Dr. Sarah Clendinning (Post-doc). 1800 hr
- Ms. Pilar Castillo-Tapia (PhD student). 450 hr

8. Students

In 2023, PhD student Ms. Pilar Castillo-Tapia contributed to the project.

9. Technology Transfer

Oscar Quevedo-Teruel sent a copy of the ray tracing code which can model rotationally symmetric geodesic lenses and elliptical geodesic lenses to Ryan Hoffman (ryan.b.hoffman.civ@us.navy.mil), Suchitra Ramani (suchitra.ramani.ctr@us.navy.mil) and Charles R. Eddy, Jr. (charles.r.eddy12.civ@mail.mil) on the 15th of January, 2023.

10. Products, Publications, Patents, License Agreements, etc.

Publications resulting from this project:
Archival Publications (publication reference information (article title, authors, journal, date, volume, issue) can be automatically entered using a DOI)

a. Geodesic Lens Antennas for 5G and Beyond
b. IEEE Communications Magazine
c. Oscar Quevedo-Teruel, Qingbi Liao, Qiao Chen, Pilar Castillo-Tapia, Francisco Mesa, Kun Zhao and Nelson Fonseca
d. 5G Mobile Communication, Spatial Diversity, Dielectric Materials, Prototypes, Directive Antennas, Geometrical Optics and Propagation Losses
e. -
f. Published
g. DOI: 10.1109/MCOM.001.2100545
h. -
i. 1 January 2022
j. 60
k. 1
l. 40
m. Publication Location: The city and country where article was published
n. Acknowledgement of Federal Support? (**Yes**/~~No~~)
o. Peer Reviewed? (**Yes**/~~No~~)

Archival Publications

a. Near-Field Focusing Multibeam Geodesic Lens Antenna for Stable Aggregate Gain in Far-Field
b. IEEE Transactions on Antennas and Propagation
c. Omar Orgeira, German Leon, Nelson Fonseca, Pedro Mongelos and Oscar Quevedo-Teruel
d. Lenses, Gain, Ray Tracing, Mathematical Models, Antennas, Focusing, Antenna Arrays
e. -

f. Published
g. DOI: 10.1109/TAP.2021.3139093
h. -
i. 10 January 2022
j. 70
k. 5
l. 3320
m. -
n. Acknowledgement of Federal Support? (**Yes**/~~No~~)
o. Peer Reviewed? (**Yes**/~~No~~)

Archival Publications

a. Ray-Tracing Model For Generalized Geodesic Lens Multiple Beam Antennas
b. IEEE Transactions on Antennas and Propagation
c. Qingbi Liao, Nelson Fonseca, Miguel Camacho, Angel Palomares-Caballero, Francisco Mesa and Oscar Quevedo-Teruel
d. Lens Antennas, Geodesic Lenses, Parallel Plate Waveguides, Ray Tracing and Non-Euclidean Transformation Optics
e. Distribution Statement: Text (200 characters) describing how distribution should be restricted
f. Early Access
g. DOI: 10.1109/TAP.2022.3233643
h. -
i. N/A
j. -
k. -
l. -
m. -
n. Acknowledgement of Federal Support? (**Yes**/~~No~~)
o. Peer Reviewed? (**Yes**/~~No~~)

Archival Publications

a. Evaluation of Losses in 3D-Printed Geodesic Lenses Using a Ray-Tracing Model
b. IEEE Transactions on Antennas and Propagation
c. Pilar Castillo-Tapia, Jose Rico-Fernandez, Sarah Clendinning, Francisco Mesa and Oscar Quevedo-Teruel
d. Additive Manufacturing, Geodesic Lenses, Losses, Radiation Efficiency, Ray-Tracing
e.
f. Early Access
g. DOI: 10.1109/TAP.2023.3319156
h. -
i. N/A
j. -
k. -
l. -
m. -
n. Acknowledgement of Federal Support? (**Yes**/~~No~~)

o. Peer Reviewed? (**Yes**/~~No~~)

Conference Papers

a. Numerical aspects of the application of ray-tracing to geodesic lenses
b. Sarah Clendinning, Shiyi Yang, Qingbi Liao, Pilar Castillo-Tapia, Francisco Mesa, Nelson Fonseca and Oscar Quevedo-Teruel
c. European Conference on Antennas and Propagation
d. 26th March – 1st April 2022
e. Madrid, Spain
f. Published
g. 11th May 2022
h. -
i. -
j. Acknowledgement of Federal Support? (**Yes**/~~No~~)

Conference Papers

a. Ray-Tracing Model for Elliptical Half-Geodesic Lens Antennas
b. Sarah Clendinning, Francisco Mesa and Oscar Quevedo-Teruel
c. International Symposium on Antennas and Propagation
d. 31st October – 3rd November 2022
e. Sydney, Australia
f. Published
g. 2nd January 2023
h. -
i. -
j. Acknowledgement of Federal Support? (**Yes**/~~No~~)

Conference Papers

a. Ka-Band Implementation of a Geodesic Half-Maxwell Fisheye Lens Antenna
b. Shiyi Yang, Qiao Chen, Francisco Mesa, Nelson Fonseca and Oscar Quevedo-Teruel
c. International Symposium on Antennas and Propagation
d. 31st October – 3rd November 2022
e. Sydney, Australia
f. Published
g. 2nd January 2023
h. -
i. -
j. Acknowledgement of Federal Support? (**Yes**/~~No~~)

Conference Papers

a. Radiation Efficiency Estimation of Lossy Geodesic Lens Antennas Based on a Ray-Tracing Technique
b. Pilar Castillo-Tapia, Shiyi Yang, Qiao Chen, Francisco Mesa, and Oscar Quevedo-Teruel
c. European Conference on Antennas and Propagation
d. 26th-31st March 2023
e. Florence, Italy
f. Published
g. 31st May 2023
h. -
i. -
j. Acknowledgement of Federal Support? (**Yes**/~~No~~)

Conference Papers

a. Reducing the Refractive Index Range of GRIN Lenses Through the Integration of a Reflectarray
b. Sarah Clendinning, Oskar Zetterstrom, Francisco Mesa, and Oscar Quevedo-Teruel
c. European Conference on Antennas and Propagation
d. 26th-31st March 2023
e. Florence, Italy
f. Published
g. 31st May 2023
h. -
i. -
j. Acknowledgement of Federal Support? (**Yes**/~~No~~)

Books

N/A

Book Chapter

N/A

Theses

N/A

Websites

N/A

Patents

N/A

Other Products: Identify any other significant products that were developed under this project. Describe the product and how it is being shared.

N/A

11. Point of Contact in Navy

The main contacts during the 2023 reporting period were:

- ONR Global London: Charles R. Eddy, Jr. (charles.r.eddy12.civ@mail.mil)

New Ideas for Advanced Relativistic Magnetrons

Grant No. N62909-21-1-2006

Annual Report for Fiscal Year 2023

Period of Performance: October 1, 2022 – September 30, 2023

Prepared by:
Prof. Yakov Krasik, Principal Investigator
Physics Department
Technion-Israel Institute of Technology,
Haifa 32000, Israel
Tel: +972-545509951 (+972-48293559);
Email: fnkrasik@physics.technion.ac.il

This work was sponsored by the Office of Naval Research (ONR), under grant (or contract) number N62909-21-1-2006. The views and conclusions contained herein are those of the authors only and should not be interpreted as representing those of ONR, the U.S. Navy or the U.S. Government.

Grant Number: N62909-21-1-2006
Date Prepared: January 5th, 2024
Project Title: New Ideas for Advanced Relativistic magnetrons
Annual Summary Report: FY23
Principle Investigator: Prof. Yakov E. Krasik, Tel: +972 4 829 3559, +972 550 9951,
email: fnkrasik@physics.technion.ac.il, affiliation: Physics. Dept., Technion, Haifa 3200003.

Section I: Project Summary

1. Overview of Project

Abstract

We report in this document our accomplishments in this project during FY23 and since it is our last report we summarize our achievements over the entire period of three years for which this project was planned. This project ends with success as we can report a major advancement in that a relativistic magnetron has been developed fed by our novel idea of the *split cathode* which overcomes the problem of pulse shortening in such devices. Moreover, during the course of the project we came up with another novel idea, that is, that slits can be cut in the magnetron's conducting anode wall and this segmented magnetron can be placed in a dielectric vacuum tube. This allows to reduce considerably the power required to feed the magnetic field producing pulsed power system and consequently its size and weight to levels acceptable for deploying a split cathode fed *segmented* relativistic magnetron. We demonstrated both ideas successfully. This work is the result of a research collaboration between our Technion, Plasma Physics and Pulse Power Laboratory (T4PL) directed by Prof. Ya. E. Krasik and Prof. E. Schamiloglu's research team at the University of New Mexico (UNM).

Objectives

The original major goal of the project was to build an efficient relativistic magnetron [RM] operating with a split cathode with no pulse shortening. Later, we suggested to build the magnetron from longitudinal anode segments which allows a magnetron to operate with significant increase in the overall efficiency of microwaves generation.

A RM is a pulsed high-power microwave [HPM] source of high efficiency in transforming the energy of the electrons into electromagnetic power. There are two major problems limiting the practical application of a RM as an HPM source. One is related to the explosive emission plasma formed at the surface of the cathode coaxial to the hollow anode block which contains resonators distributed along its circular circumference. This conducting plasma, generally non-uniform and unstable, expands towards the anode while decreasing the effective cathode-anode distance, which changes the resonance conditions of the structure leading to the termination of microwave generation while the applied voltage is still on. This effect is known as *pulse shortening* and is a major defect not only of the RM but of other such HPM producing devices, and how to overcome it, was studied for many years.

A split cathode contains an explosive emitter which is placed outside the anode and upstream from it so that the expanding cathode plasma does not affect the resonance conditions of the plasma free RM. The upstream emitter, is connected by a conducting rod to a downstream reflector, so that the electron charge accumulates in the space between the emitter, the rod and the reflector, all three at nearly the same voltage, and the anode. The accumulated charge screens the rod from emitting electrons. The electrons are originally emitted at cathode potential but enter the anode at a higher potential than that of the rod (cathode potential) because they first accelerate toward the anode outside the RM active volume. The accumulated charge oscillates axially between the emitter and the reflector and when it becomes too large it either *squeezes* (reduces its energy to overcome Coulomb repelling forces) or it expands towards the cathode depending on the value of the magnetizing applied static axial magnetic field. This electron dynamics is completely different from that of an ordinary RM studied during the last 50 years and to confirm its advantage, studying its dynamics was a basic goal.

The second major problem of RMs and other similar HPM devices is the need to apply a relatively large axial magnetic field (of the order of 1 T). This requires a pulsed power supply with stored energy of several kJ operating in the ms-timescale necessary for the magnetic field to diffuse through the conducting walls of the anode. Thus, considering such power requirements, the overall efficiency of the entire system does not exceed a few percent even if the electronic efficiency of the RM itself is very high. Moreover, this pulsed power system is large and heavy and recharging it makes repetitive operation of the RM challenging. We suggested a solution to this problem by cutting longitudinal slits through the entire anode structure which allows almost immediate magnetic field penetration. When the RM is built from such segments separated by gaps, a micro-second timescale magnetic field is sufficient which can be produced by a pulsed power supply of only 100 J stored energy. A segmented RM is placed inside a dielectric (i.e., Perspex) vacuum tube over which a single layer of solenoid wires is wound.

Thus, the major objective of the project was to prove these concepts by designing by simulations, building and testing by experiments a prototype RM fed by a split cathode and built with a segmented anode and to confirm that the problems of pulse-shortening and magnetic field diffusion are solved in practice.

Introduction and Background

The subject of generation of HPM pulses is related to high-current relativistic electronics. The latter is based on high-voltage and high-current pulsed generators[5] which are used to generate electron beams with current amplitudes of tens of kA, electron energy in the range 0.1 – 1 MeV, and total electron beam energy as large as 10^4 J and greater. The energy of these beams is transferred to microwave energy using various microwave tube technologies among which relativistic magnetrons can be considered as one of the most promising HPM devices.[6] Indeed, studies show that relativistic magnetrons can operate in S- and L-bands generating pulses of several GW power over tens of nanoseconds.[1] The main disadvantages of relativistic magnetrons are the need to apply strong DC magnetic fields produced by external coils which require powerful and large power supplies, thus reducing the total efficiency of the system, and the cathode which is usually an explosive cathode plasma which evolves while changing the magnetron's impedance during its operation leading to what is known as pulse shortening.

Recent research carried out at UNM showed novel avenues towards operating magnetrons with increased efficiency. In Fig. 1 one can see a partial timeline of the evolution of advanced relativistic magnetrons.[6]

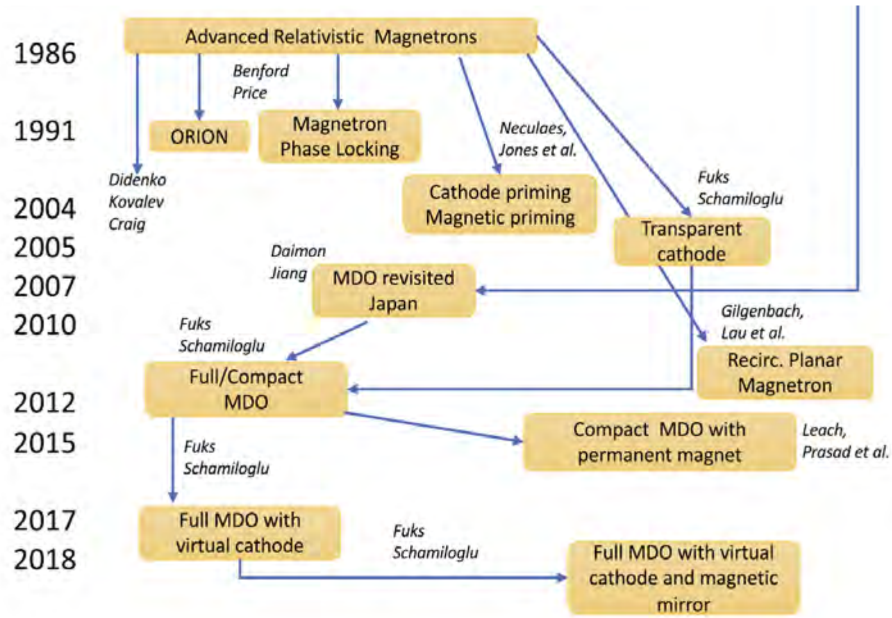

Fig. 1. Part of the timeline of the evolution of the relativistic magnetron (from Ref. [6]).

In the timeline of Fig. 1 one can see the advances introduced by the UNM group (Fuks and Schamiloglu). The use of the transparent cathode[7] allowed for better coupling between the rotating electron spokes and the electromagnetic field in the cathode-anode space. It was also found that using a diffraction output magnetron increases its operation efficiency to 70%.[8] A magnetron with the magnetic field producing coils and current generator replaced by modern compact permanent magnets was also studied.[9]

The T4PL group has been involved in relativistic magnetron research during more than a decade. Several important findings in the study of relativistic S-band magnetrons made recently by the group are summarized in Ref. [6]. By resonant coupling of the magnetron anode to external cavities, stabilization of the HPM frequency was achieved.[10] The operation of a compact magnetron with permanent magnets inserted into the anode vanes was also demonstrated.[11]

Recently, the UNM group suggested the use of a virtual cathode[2] as the magnetron's electron source which is advantageous because there is no cathode plasma to cause pulse shortening. A virtual cathode usually forms near the surface of a real cathode where electrons are emitted. When too much space charge accumulates in a volume near the emitting surface the Coulomb forces cause the charge flow to stop at a certain point downstream from the cathode surface from where it flows both downstream toward the anode and upstream toward the emitter. This point is called a virtual cathode.[12] The idea introduced in Ref. [2] by the UNM group uses a variant of the virtual cathode concept known as a *squeezed state.*

The concept of the squeezed state has been introduced in the former USSR[13] where it has been studied for many years. It did not find too much attention in western science until recently.[2] An electron beam (annular or solid) propagating in a cylindrical tube immersed in a strong axial magnetic field can carry a current limited by space charge Coulomb forces. For a thin annular beam of radius r_b, this limiting current is given by

$$I_{LC} = 17\left(\gamma^{2/3} - 1\right)^{3/2} / [2 \ln\left(\frac{R}{r_b}\right)] \text{ [kA]}, \qquad (1)$$

where R is the tube radius, $\gamma = 1 + eV/mc^2$ is the relativistic factor, eV is the energy of electrons, and 17 kA is the Alfvén current. For a tube consisting of sections of various radii, the limiting current I_{LC} is determined in the tube with the largest radius. An injected current I_{inj} from an upstream electron source exceeding the limiting current, $I_{inj} > I_{LC}$, leads to the formation of a virtual cathode in this section and a return current from the virtual cathode towards the electron source which can be far upstream. These reflected electrons form a sufficiently large negative space charge near the electron source to decrease the emitted current. The space charge of the circulating electrons accumulates in the entire space between the source and the virtual cathode, an unstable situation which relaxes to a state of high density, low energy electrons, a *squeezed state*. The idea of the UNM group was to form this squeezed state in the volume encircled by a magnetron block and they demonstrated by simulations that it can act efficiently as the magnetron's electron source.[2] The advantage of such a scheme is that within the magnetron's interaction space there is no cathode, or cathode plasma, which causes pulse shortening, the most commonly known problem with relativistic magnetrons.[1] The UNM magnetron is of a diffraction output type; that is, the microwave exits along exits in the plane perpendicular to the axis (Fig. 2).

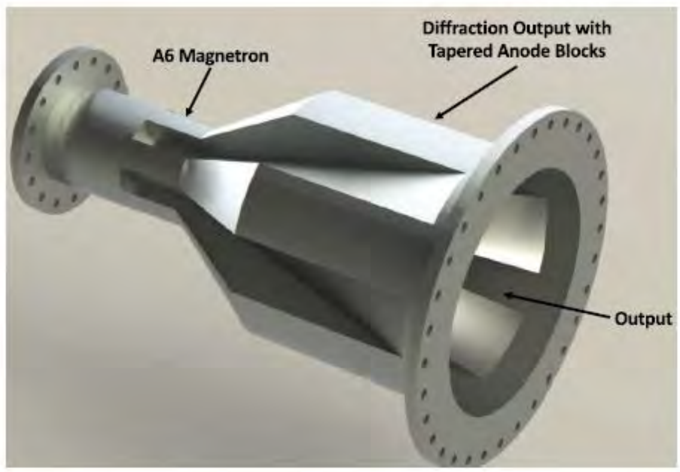

Fig. 2. Drawing of the UNM S-band magnetron. (From Ref. [3].)

Fig. 3 (PIC simulation) shows the effect of positioning the cathode outside from the magnetron anode block and designing the anode tube's outline in three sections with increasing radii, on the electron dynamics. The annular cathode is placed in the lowest radius section followed by the magnetron anode block of radius R_2 and an exit section of radius R_3. Initially two virtual cathodes form near the radius transition points seen clearly in the bottom left panel in Fig. 3 as zero energy points. Then very soon, a squeezed state forms between the cathode and the most downstream virtual cathode.

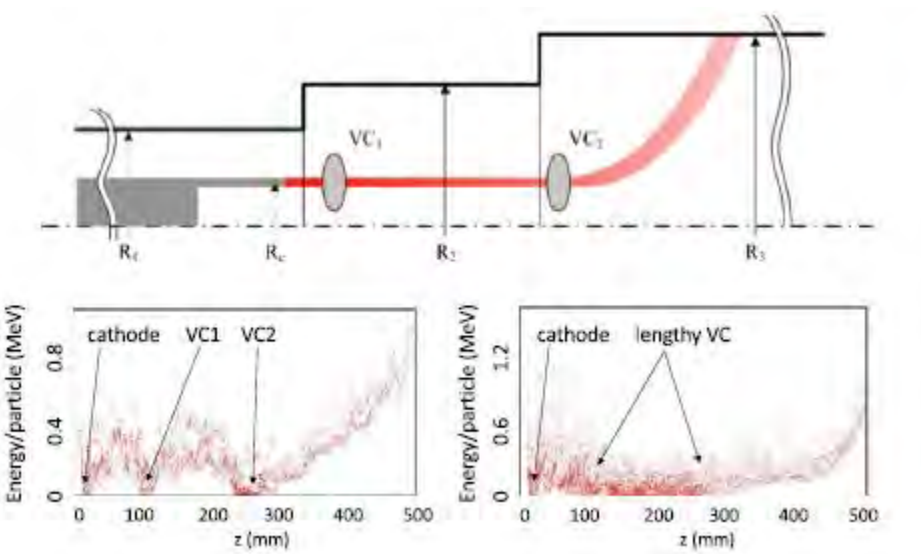

Fig. 3. Top: The MDO interaction region consisting of the three uniform drift tubes of progressively increasing radii $R_1 < R_2 < R_3$. Bottom: Electron particles at 2 ns showing the formation of the two VCs (left) and the low-energy state of electrons between the VCs (at 4 ns).[3]

The remaining problem in this scheme is the current which flows to the walls which interferes with the radiated microwaves and is to be considered as lost with respect to the system's electronic efficiency. So, the UNM group has come up with a more advanced idea to recover this current by increasing the external axial magnetic field exponentially in a magnetic mirror like scheme.[3] For an adiabatic increase of the axial component of the magnetic field from B_1 to B_2 the annular beam radius decreases from r_{b1} to r_{b2} as[14]

$$r_{b2} = r_{b1}\left(\frac{B_1}{B_2}\right)^{1/2}. \qquad (2)$$

It was shown[3] that by considering the additional current in the magnetron interaction region the electronic efficiency of the magnetron could increase to 92%.[3] This idea (exponentially increasing magnetic field) was immediately picked up and tested in simulations of a radial extraction L-band magnetron, performed by a group from the High-Power Radiation Laboratory, School of Electronic Science and Engineering, University of Electronic Science and Technology of China, Chengdu.[15] These ideas have not yet been realized in the laboratory.

Intrigued by the science of squeezed state and interested in producing high frequency, high current electron bunches to be injected in microwave producing slow wave structures, the T4PL, have come up with the idea that the charge in the squeezed state can be made to oscillate rather than relax and these oscillations may produce electron bunches.[16] Simulations showed that high current, high frequency bunches may form in particular in the presence of a cavity which increases the interaction with the oscillating squeezed state. The experiment following these ideas was less successful in the sense that high current bunches were indeed obtained but at a different frequency than predicted.[17] The discrepancy is explainable, and more work is needed to follow this idea. In this scheme the Technion group introduced a new type of device, that is, a partially transparent surface (a conducting grid) connected to the annular cathode on axis by a conducting rod as seen in Fig. 4 and denoted as the central rod and the reflector. A 1 T axial magnetic field is present everywhere.

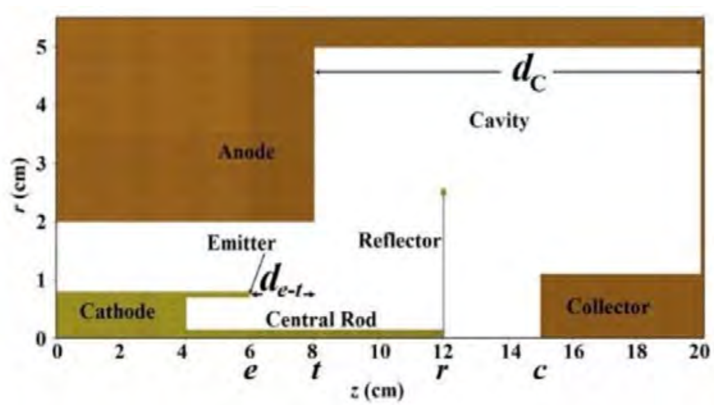

Fig. 4. The cylindrical symmetrical geometry of the PIC simulated system. *e, t, r,* and *c* point out the position of the emitter edge, the RT, the reflector and the collector, respectively.[17]

The effect of the reflector compared to the case where there is only a simple radial transition in the anode tube has been numerically simulated and the results are seen in Fig. 5.

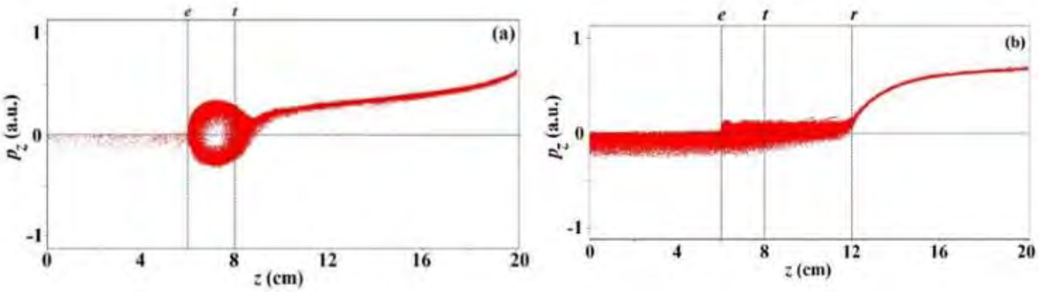

Fig. 5. (a) The longitudinal momentum [z, p_z] phase space at t = 35 ns for the geometry of Fig. 4 but without the central rod, the reflector and the collector. (b) The same but with the rod and the reflector included. ***e***, ***t*** and ***r*** point out the position of the emitter, the radial transition point and the reflector respectively.[17]

Without the reflector [Fig 5(a)] a virtual cathode develops between the cathode emitter and the radial transition point, but the charge is insufficient for full squeezing. The addition of the transparent reflector returns more charge which causes full squeezing to develop [Fig. 5(b)]. The reason for this behavior is simple. The reflector is at the same potential as the cathode and it slows down the electron beam and, just like a virtual cathode, returns part of the current. Moreover, the annular electron beam screens the central rod from emitting electrons and, therefore, it has no effect in that sense. A squeezed state forms here but current also flows downstream in a similar manner to that seen in Fig. 3. Note that there is also flow upstream from the cathode which for this case carries only a small current and can be returned as well using a different cathode holder design.

This work raised the idea that if the reflector is opaque rather than transparent (replace the grid by a solid surface), it can replace the exponentially increasing magnetic field suggested in Ref. [3]. This is a very simple way to make the virtual cathode magnetron realizable, because the design of the magnetron can be made much simpler. Moreover, the presence of the central rod introduces a radial potential difference, important to the operation of a magnetron, without electron emission because of screening. This idea was discussed by the two groups resulting in a joint paper (Ref. [4]). In this paper, we showed that the effect of the reflector is the same as that of the increased magnetic field. We named the cathode attached to the reflector with the central rod a *split cathode* as all connected parts are at the same potential. In Fig. 6, a picture of the split cathode built at the Technion is seen. All parts have been hard anodized (with a layer of oxide) to avoid parasitic emission. The emitter consists of carbon fiber tubes placed in an annular structure.

Fig. 6. Photograph of the hard-anodized cathode, the emitter, and the attached rod and reflector.[4]

The split cathode was introduced in the experimental setup seen in Fig. 7. The system is fed by a Marx-generator providing a few hundred ns long voltage pulse of ~200 kV amplitude. The split cathode is held on the axis of a 6.2 cm radius vacuum tube around which a solenoid produces a uniform axial magnetic field of ~1 T. An anode insert of radius 2 cm surrounds the central rod of the split cathode. Simulations of this system show that a squeezed state forms between the cathode and the reflector and that the current rotates between these two parts at a frequency of ~350 MHz which is close to the single electron round trip transit time assuming that the energy of the electron is ~25 keV, the maximum average energy of the electrons in the squeezed state. Note that the applied voltage is ~200 kV and to avoid current flowing upstream, the cathode holder radius was designed to be large.

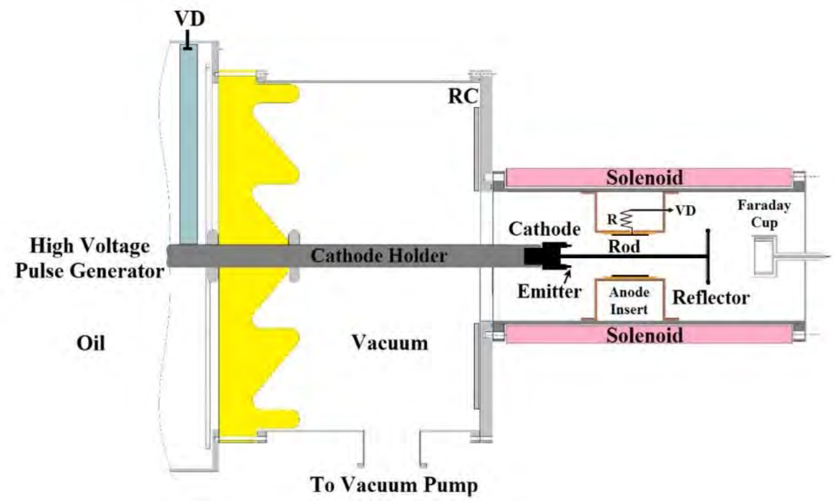

Fig. 7. The experimental setup for the split cathode design. The split cathode (Fig. 6) consisting of the cathode, the reflector and the rod is colored black and is placed along the axis of the anode insert.

Note that in this scheme no current should flow between the cathode and the anode even though electrons are emitted, and the charge accumulates and squeezes in the space in between. Indeed, no current was observed experimentally. Moreover, the presence of the low energy high density electron cloud was also confirmed by various diagnostic means, including the rotation frequency.[4]

This was the point when the ONR collaborative project started. Next we summarize our activities and achievements since, and point out in particular those of FY23 the last year of the project.

References

1. J. Benford, J. Swegle, and E. Schamiloglu, *High Power Microwaves*, 3rd ed. (CRC Press, Boca Raton, FL, 2015).
2. M.I. Fuks, S. Prasad, and E. Schamiloglu, IEEE Trans. Plasma Sci. **44**, 1298 (2016).
3. M.I. Fuks and E. Schamiloglu, Phys. Rev. Lett. **122**, 224801 (2019).
4. J.G. Leopold, Y.P. Bliokh, Ya.E Krasik, and E. Schamiloglu, Phys. Plasmas (2020) (under review).
5. H. Bluhm, *Pulsed power systems. Principles and applications*, (Springer, Berlin, 2006).
6. D. Andreev, A. Kuskov, and E. Schamiloglu, Matter Radiat. Extremes **4**, 067201 (2019).
7. M. Fuks, E. Schamiloglu, Phys. Rev. Lett. **95**, 205101 (2005).
8. M.I. Fuks, E. Schamiloglu, IEEE Trans. Plasma Sci. **38**, 1302 (2010).
9. C. Leach, S. Prasad, M. Fuks, and E. Schamiloglu, in Proceedings of the 2012 IEEE International Vacuum Electronics Conference (IEEE, Monterey, CA, 2012), pp. 491–492.
10. A. Sayapin, A. Levin, and Ya.E. Krasik, IEEE Trans. Plasma Sci. **41**, 3001 (2013).
11. Ya.E. Krasik, J. Leopold and U. Dai, IEEE Trans. Plasma Sci. **47**, 3997 (2019).
12. P. Zhang, Á. Valfells, L. K. Ang, J. W. Luginsland, and Y. Y. Lau, Appl. Phys. Rev. **4**, 011304 (2017).
13. A.M. Ignatov and V.P. Tarakanov, Phys. Plasmas **1**, 741 (1994).
14. A.V. Gromov, M.B. Goykhman, N.F. Kovalev, A.V. Palitsin, M.I. Fuks, and E. Schamiloglu, Tech. Phys. Lett. **44**, 949 (2018).

15. R. Cheng , T. Li, F. Qin, L. Lei, D. Wang, H. Wang, F.M. Ghannouchi, and B. Hu, IEEE Trans. Electron Dev. **67**, 2165 (2020).
16. J.G. Leopold, Y.P. Bliokh, M. Siman-Tov, and Ya.E. Krasik, Phys. Plasmas **26**, 093107 (2019).
17. M. Siman-Tov, J.G. Leopold, Y.P. Bliokh, and Ya.E. Krasik Phys. Plasmas **27**, 0831003, (2020).

2. Activities and Accomplishments

Our thesis explaining the idea of a split cathode supported by numerical simulations and first experiments with a smooth bore anode [no magnetron resonators] confirming that the principle of the split cathode is correct, was published in Phys. Plasmas **27**, 103102 (2020). In an additional article, [J. Appl. Phys. **130**, 034501 (2021)], we confirmed experimentally by comparison to a solid cathode that no pulse shortening develops in a non-radiating magnetron fed by a split cathode.

Our thesis explaining the idea of the segmented anode and simulations confirming that the longitudinal slits do not introduce serious deviations in the operation of this device was published in IEEE Trans. Electron Devices **68**, 5227 [2021]. In this work we introduced a modified version of a compact axial output magnetron (MDO) proposed by Xu et al., Phys. Plasmas **25**, 083301 (2018), but with a split cathode as the electrons source and an anode built from 3 separate segments [see Figs. 8, 9[b] and 9[d]]. The magnetron design continues three of the vanes into the space between the outer wall of the magnetron and the outer tube of the system separating this space into three empty sectors. These separators are longer than the anode length. The additional important design feature is the conical tube continuing the outer cylindrical tube containing the magnetron. This conical tube leads the radiation formed in the resonators (in the π mode) to a TM_{01} mode at the output window.

To realize fast magnetic field penetration through the anode structure we cut longitudinal slits through the entire conducting volume making up the RM. Thus, one can apply a μs-timescale magnetic field produced by a solenoid powered by a considerably smaller power supply. In this work we demonstrated by PIC simulations that the axial output magnetron designed by us operates well with a split cathode and that the segmented anode performs well.

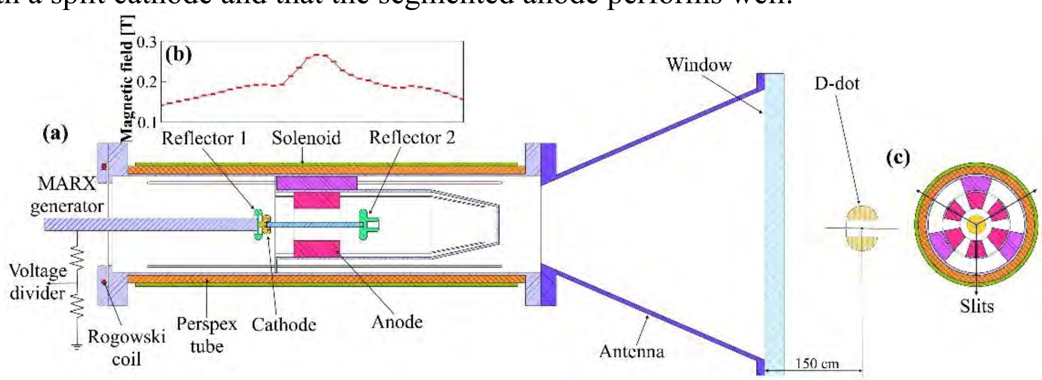

Fig. 8. A cut image of the RM fed by a split cathode (a); axial distribution of magnetic field (b) and a cross section across the center of the magnetron showing the elongated vanes (c).

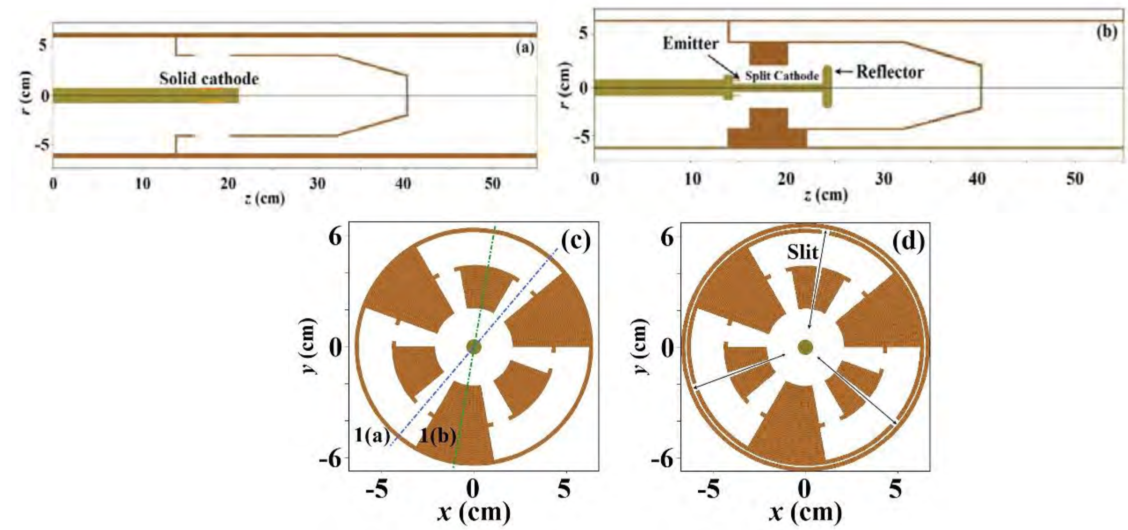

Fig. 9. (a) Cross section of a RM fed by a solid cathode in the plane showing two opposite resonators and axial output channels [see line designated by 1(a) in frame (c)]. (b) Cross section across two opposite vanes [see line designated by 1(b) in frame (c)] with a split cathode replacing the solid cathode. (c) Transverse cross section of the magnetron at its axial center, showing the sectorial separators. (d) Same as (c) but with three longitudinal slits.

Next, we tested the predictions described above experimentally. We manufactured the axial output RM the with the segmented anode fed by the split cathode and attached it to our small pulse power generator. We summarized this work in an article which has been published in the J. Appl. Phys. **131**, 023301 (2022). For these experiments, the magnetron system (see Fig. 8) was fed by an oil filled Marx generator (200 kV, 2 kA, 250 ns). We also designed and built an external solenoid which was used to magnetically insulate the electron beam. The solenoid was constructed from a single wire layer wound around the Perspex tube using a $6 \times 1\text{mm}^2$ rectangular cross section copper wire. The solenoid is energized by a current pulse with a half-period of 15 ms produced by the discharge of a 4 mF capacitor charged to a voltage ranging from 180–600 V corresponding to a magnetic field ranging from 0.16 to 0.48 T.

The results of these experimental research showed that the split cathode allows significantly longer microwave generation without the pulse shortening observed for a solid cathode (See Fig. 10). Also, it was showed that the operation of the RM with the split cathode requires significantly smaller magnetic field – another remarkable advantage of the split cathode. This is due to the smaller potential energy of the electrons in the squeezed state compared to electrons emitted from the solid cathode. The total power of the microwave radiation was of 25 MW with the split compared to and 42 MW with solid cathode.

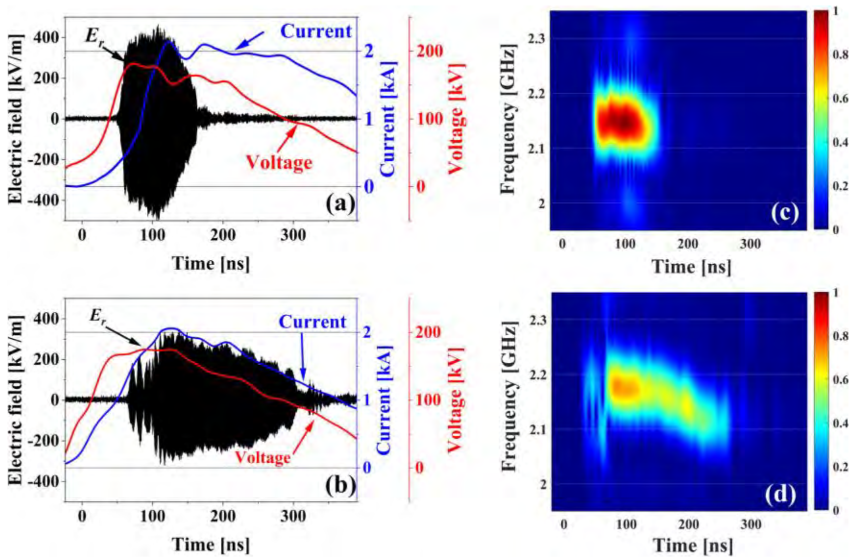

Fig. 10. Waveforms of the voltage and current and radial electric field for a solid carbon cathode, $B_z = 0.25$ T (a) and for a split cathode, $B_z = 0.15$ T (b). (c) and (d) are the normalized frequency/time contours of the microwave signals (a) and (b), respectively.

In parallel, we performed theoretical studies of the squeezed state. We built a model, which gives a physical interpretation to the specific state of an ensemble of electrons continuously injected into an electrostatic potential well immersed in a strong magnetic field preventing radial expansion. This work was published in Phys. Plasmas **28**, 072106 (2021).

During 2022 we carried out a major refurbishment of our Linear Induction Accelerator (see Fig. 11). The purpose of this project was to use the LIA to power the above RM at higher levels than the experiments performed so far. Dissembling of the LIA revealed severe electrical breakdown channels which required manufacturing and replacing some major parts of the accelerator. The successfully refurbished LIA produced 400 kV, 4 KA, 150 ns long pulses. The results of this work were published in J. Appl. Phys. **133**, 133301 (2023).

Fig. 11. The LIA - Linear Induction Accelerator with the 3-segment axial output RM attached at its front end.

It was found that the operation of the RM for a split cathode or a common explosive emission cathode differs significantly. For a split cathode, we optimize for best microwave output, its geometrical parameters, the external magnetic field, and the LIA's charging voltages. For the optimal choice of these parameters, the RM generates ~160 ns long microwave pulses of ~130MW, 1.78 GHz frequency with an electronic efficiency of ~40%, without pulse shortening. On the other hand, a common solid cathode fed RM showed microwave pulse shortening (See Figs. 12 and 13). We demonstrated that the segmented anode allows using a μs-timescale magnetic field, making it possible for the RM to operate repetitively.

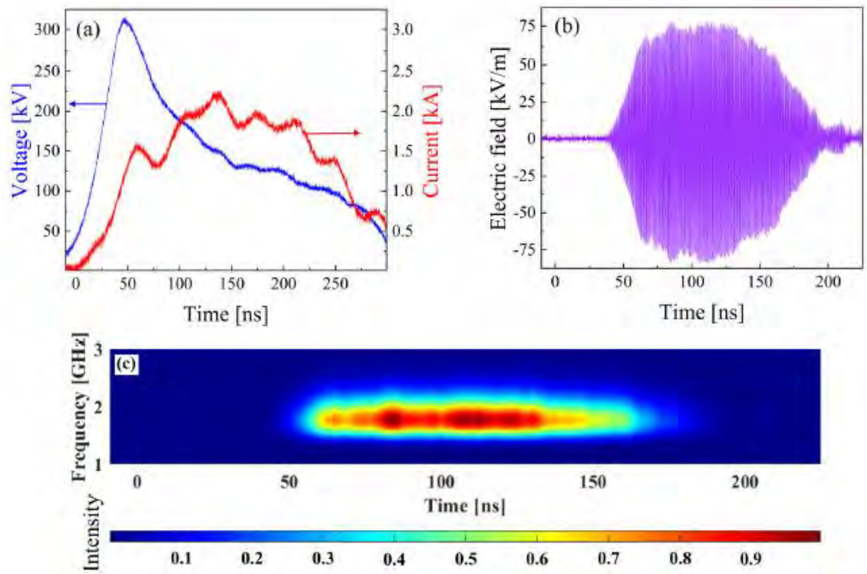

Fig. 12. (a) Waveforms of the voltage and RM current, (b) the electric field obtained by the D-dot with vertical polarization, and (c) time-frequency plot of the signal in (b); the colors represent the intensity (unitless) of the signal as a function of time and frequency and is normalized to the maximum intensity. Parameters: 60 mm long anode, split cathode with 11.5 mm diameter cathode emitter, 6 mm diameter rod, G = 15 mm, B_z = 0.32 T, and φ_{ch} = 2.6 kV.

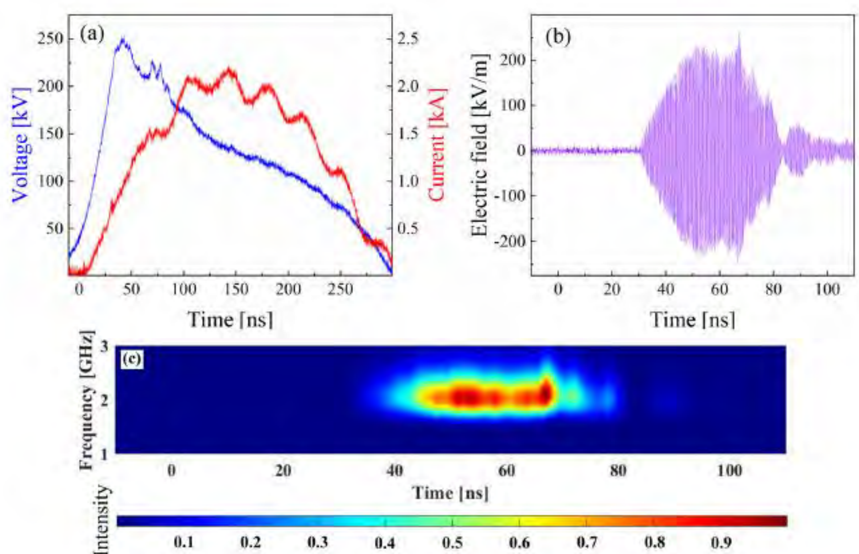

Fig. 13. Waveforms of the voltage and RM current (a), the HPM electric field measured by the D-dot probe with vertical polarization (b), and time-frequency analysis of the microwave pulse (c) [the color bar represents the same value as in Fig. 2(c)]. Parameters: 40 mm long anode, 16 mm diameter, 30 mm long solid cathode, B_z = 0.35 T and φ_{ch} = 2.6 kV.

Theoretical work continued to better understand the dynamics of the squeezed state of the charge accumulated in the longitudinal potential between the two ends of the split cathode and the anode. A smooth bore anode was studied to understand the conditions and properties of the diocotron instability developing in the presence of the axial charge counterflow. An extensive theory has been developed and numerical results were compared with experiments. The two agreed very well and diocotron modes of low [< 4] diocotron mode numbers were observed for magnetic fields strong enough for producing squeezed states. This work was published in Phys. Plasmas **29**, 123901 (2022).

We also studied the diocotron instability by PIC simulations to understand the connection between the diocotron mode number and the RM electromagnetic mode. The diocotron mode is a result of the axial counterflow in the electron cloud whereas the magnetron mode is the result of the interaction of the azimuthally drifting electrons and the resonators. We found that there are two regions of interest. For magnetic fields in the region between a Hull and Buneman-Hartree type limits, the RM electromagnetic mode is independent of the axial flow. For higher magnetic fields, microwave power is still produced but squeezing starts and the counterflow produces a different diocotron mode which is the same as the RM electromagnetic mode. These two regions are evident in Fig. 14 where for 0.25 T $\leq B_z < 0.4$ T the electric field resulting from the electromagnetic interaction increases slightly with magnetic field and for $B_z \geq 0.45$ T where these fields are lower and appear with increasing delay as squeezing sets in. These two regions are distinguishable also by the magnetron π-mode which for the higher magnetic field changes to 2π-mode (See Fig. 15). The latter displays the same diocotron mode number 4 as that observed for the same conditions in a smooth bore magnetron where no magnetron modes can form but squeezing is the same (See Fig. 16). This work was published in Phys. Plasmas **30**, 013104 (2023).

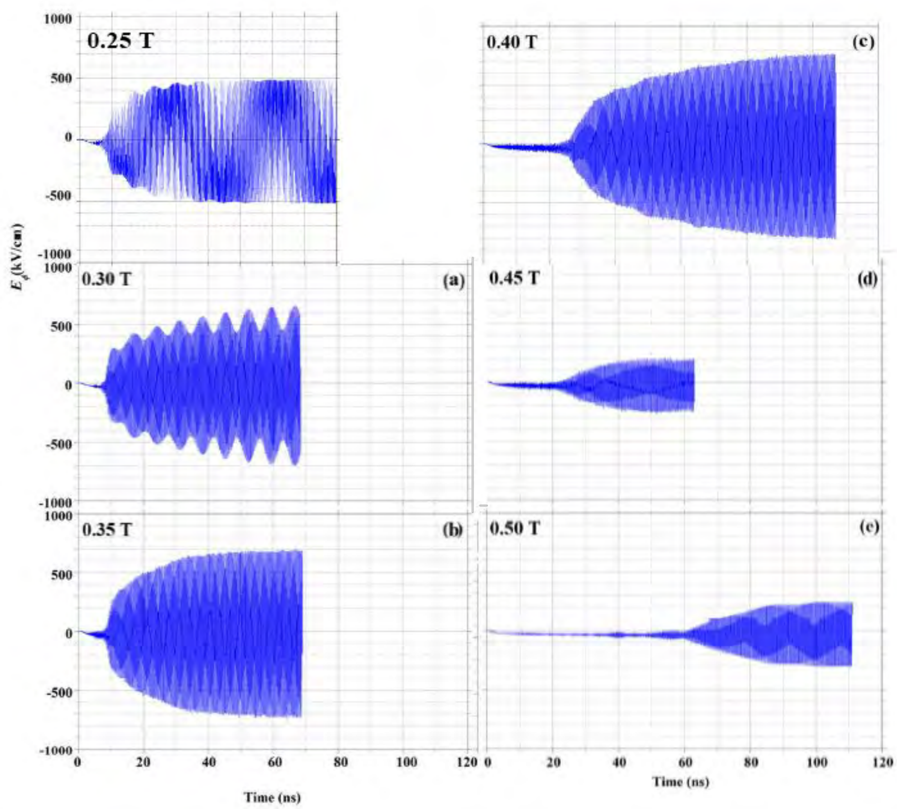

Fig. 14. The azimuthal electric field vs time at r_{in} in one of the magnetron cavities for different applied axial magnetic fields.

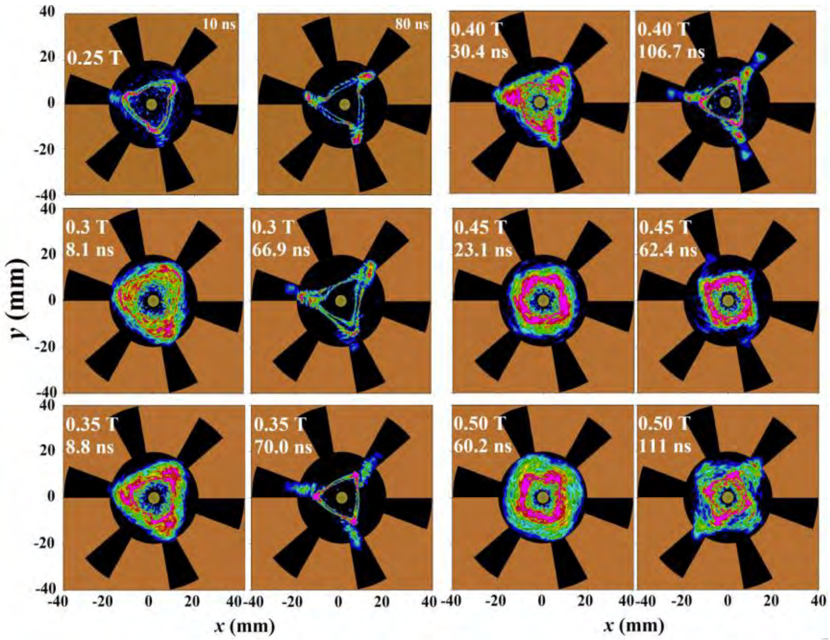

Fig. 15. Snapshots of the azimuthal charge distribution at the magnetron center for different magnetic field amplitudes at two times.

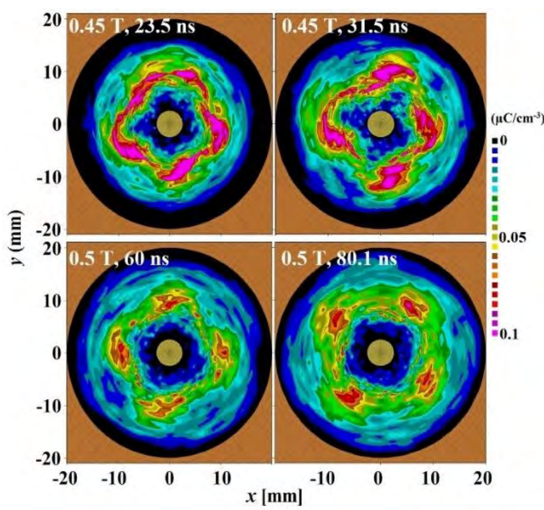

Fig. 16. Snapshots of the azimuthal charge distribution at the coaxial diode center for 0.45 and 0.5 T at two times.

Finally, we tested our split cathode fed segmented RM powered by our long pulse generator [~350 kV, ~500ns], Considerable refurbished of this generator was required and performed during the first few months of 2023.

Fig. 17. The 300 kV pulse generator with the magnetron attached to it.

The reason for testing the split cathode with a long applied pulsed power, was to ascertain the advantage of the split cathode over a solid cathode with respect to pulse shortening. In work with generators providing shorter pulses ≤ 200 ns, this advantage was evident. For the long pulse generator of Fig. 17, the main results can be seen in Fig. 18.

The results seen in Fig. 18 are to be compared to the simulation results in Fig. 14. For the lower magnetic fields, the HPM pulse shortens but it does so while the voltage is still on. On the other hand, for high magnetic fields we observe intermittency, that is, the HPM pulsates over the entire voltage pulse length. While this happens, we observe changes in the voltage and current which are affected by changes in the electron dynamics in the RM (see Figs. 15 and 16). No intermittency is observed in the simulations, because these do not consider that a generator of given impedance is attached. In the experiment when the dynamics changes it affects the RM impedance which causes a change in the voltage/current and the resonance conditions which can cause to no microwaves being produced. For low magnetic fields the electron cloud expands fast so that resonance conditions do not recur. For high magnetic fields microwaves are produced with longer delays and intermittency (recurring resonance conditions) can continue over the entire period of the pulse.

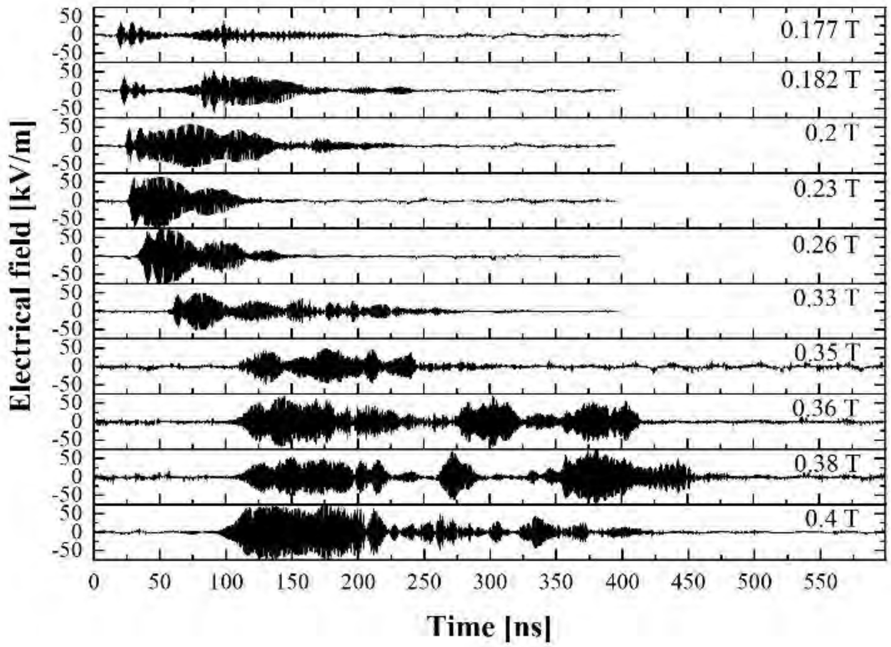

Fig. 18. The microwave electric field component measured on axis at a distance of 1.5 m from the RM for different values of the magnetic field for 25 mm cathode-anode distance, and generator charging voltage φ_{ch} = 20 kV.

For comparison we also tested solid cathodes. The behavior of a solid cathode was similar to that of a split cathode, but a solid cathode produces overall, shorter pulses and lower power for the same parameter region as that studied for the split cathode. The conclusion from this work is that one must take care of impedance matching between the split cathode fed magnetron and the power generator feeding it.

This work has been summarized in a manuscript submitted to IEEE-Trans. Electron Devices is at present under review and received good opinions in its first round of reviewing.

With this work this project has reached its successful completion.

3. Findings and Conclusions

This project provides proof of principle for the advantage of a split cathode over a solid cathode and other proposed pulse shortening solutions. A split cathode fed RM has been developed, manufactured, tested and its advantages proved.

A segmented anode RM works as well as one with a regular solid anode. Its advantage in that the requirements (long pulse, high power) pulsed power system feeding the axial magnetic field producing solenoid can be seriously relaxed so that the system's overall efficiency becomes considerably higher while the weight and size of it considerably lowered have been tested and proved.

This work makes a split cathode segmented anode RM the highest efficiency candidate for a HPM source but one must be careful in providing correct impedance matching between the RMs power supply and the RM for best performance.

4. Plans and Upcoming Events

We have no plans to continue this work which has been completed with no further major unanswered questions that our proof of principle research has not answered.

5. Transitions and Impacts

Recently there is interest in developing HPM sources in the X-ban (8-12 GHz). A RM operating in the X-band is of much smaller dimensions than the S-band (2-3 GHz) RM we studied in this project. Because of this pulse shortening may be a more serious problem when the cathode-anode distance is only a few mm. A split cathode can be even more advantageous for S-band RMs. We intend to test the split cathode's applicability by designing an appropriate X-band RM.

6. Collaborations

This project was performed as a collaboration between the Technion, Plasma Physics and Pulse Power Laboratory's research group directed by Prof. Ya. E. Krasik and Prof. E. Schamiloglu's research team at the University of New Mexico.

7. Personnel

Key Personnel:
Principal investigator: Yakov Krasik (fnkrasik@physics.technion.ac.il; +972-545509951), 1.8 Person Months, National Academy Member – No, Israel

Team Members:
Dr. John Leopold (leopoldjg@technion.ac.il)
Dr. Yurii Bliokh (bliokh@physics.technion.ac.il)
Engineer Yevgene Flyat (flyat@technion.ac.il)
Engineer Svetlana Gleizer (sgleizer@technion.ac.il)

8. Students

PhD student Yang Cao
PhD student Meital Siman Tov

9. Publications

1. M. Siman-Tov, J. G. Leopold, Y. P. Bliokh, and Ya. E. Krasik, *Periodic bunches produced by electron beam squeezed states in a resonant cavity*, Phys. Plasmas **27**, 083103 (2020); https://doi.org/10.1063/5.0014620
2. J. G. Leopold, Ya. E. Krasik, Y. P. Bliokh, and E. Schamiloglu *Producing a magnetized low energy, high electron charge density state using a split cathode*, Phys. Plasma **27**, 103102 (2020); https://doi.org/10.1063/5.0022115
3. J. G. Leopold, Ya. E. Krasik, Y. Hadas and E. Schamiloglu, *An axial magnetron fed by a split cathode and magnetically insulated by a low power solenoid*, IEEE Trans. Electron Dev. **68**, 5227 (2021); https://doi.org/10.1109/TED.2021.3105942
4. J. G. Leopold, M. Siman Tov, S. Pavlov, V. Goloborodko, Ya. E. Krasik A. Kuskov, D. Andreev and E. Schamiloglu *Experimental and numerical studies of relativistic magnetron with a split cathode*, J. Appl. Phys. **130**, 034501 (2021); https://doi.org/10.1063/5.0055118

5. Y. Bliokh, J. G. Leopold, and Ya. E. Krasik, *Squeezed state of an electron cloud as a "quasi-neutral" one-component plasma*, Phys. Plasmas **28**, 072106 (2021); https://doi.org/10.1063/5.0056881
6. Ya. E. Krasik, J. G. Leopold, Y. Hadas, Y. Cao, S. Gleizer, E. Flyat, Y. P. Bliokh, D. Andreev, A. Kuskov, and E. Schamiloglu, *An advanced relativistic magnetron operating with a split cathode and separated anode segments*, J. Appl. Phys. **131**, 023301 (2022); https://doi.org/10.1063/5.0080421
7. Y. Bliokh, Ya. E. Krasik,1, J. G. Leopold, and E. Schamiloglu, *Observation of the diocotron instability in a diode with split cathode* Phys. Plasmas **29**, 123901 (2022); https://doi.org/10.1063/5.0103120
8. O. Belozerov, Ya. E. Krasik, J. G. Leopold, S. Pavlov, Y. Hadas, K. Kuchuk, and E. Schamiloglu, *Characterizing the high-power-microwaves radiated by an axial output compact S-band A6 segmented magnetron fed by a split cathode and powered by a linear induction accelerator*, J. Appl. Phys. **133**, 133301 (2023); https://doi.org/10.1063/5.0138769
9. J. G. Leopold, Y. Bliokh, Ya. E. Krasik, A. Kuskov, and E. Schamiloglu, *Diocotron and electromagnetic modes in split-cathode fed relativistic smooth bore and six-vane magnetrons*, Phys. Plasmas **30**, 013104 (2023); https://doi.org/10.1063/5.0129515
10. G. Liziakin, O. Belozerov, J.G. Leopold, Yu. Bliokh, Y. Hadas, Ya. E. Krasik and E. Schamiloglu, *Experimental research on a split cathode fed magnetron driven by long high voltage pulses*, Phys. Plasmas 2024 (Under Review).

Conference Papers:

11. J. G. Leopold, Y. Krasik, Y.P. Bliokh, and E. Schamiloglu, *Squeezing a Magnetized Relativistic Electron Beam Using a Split Cathode*, ICOPS 2020 (Virtual, December 2020).
12. J. G. Leopold, M. Siman Tov, S. Pavlov, V. Goloborodko and Ya. E. Krasik, A. Kuskov, D. Andreev, and E. Schamiloglu, *Experimental and numerical studies of a relativistic magnetron fed by a split cathode* EAPPC-BEAMS-MEGAGAUSS (Virtual, 29 August - 2 Sept. 2021).
13. J. G. Leopold, Ya. E. Krasik, M. Siman Tov, S. Pavlov, V. Goloborodko, Y. Bliokh, D. Andreev, A. Kuskov and E. Schamiloglu, *A relativistic magnetron with no pulse shortening and small footprint pulsed magnetic field generating system* (IEEE PPC-2021 (Virtual, December, 2021).
14. A. Kuskov, J. G. Leopold, Y. Cao, Y. P. Bliokh, Ya. E. Krasik, D. Andreev, and E. Schamiloglu, *A study of the electron dynamics in a split-cathode* (ICOPS 2022 Seattle, USA, May 2022).
15. Ya. E. Krasik, J. G. Leopold, Y. Hadas, Y. Cao, S. Pavlov, V. Goloborodko, S. Gleizer,1 E. Flyat, Y. P. Bliokh, D. Andreev, A. Kuskov, and E. Schamiloglu, *Experiments on a segmented axial magnetron fed by a split cathode*, (ICOPS 2022 Seattle, USA, May 2022).
16. Ya. E. Krasik, S. Pavlov, J. G. Leopold, Y. Hadas, S. Gleizer, E. Flyat,1 Y. P. Bliokh, Y. Cao, D. Andreev, A. Kuskov, and E. Schamiloglu, *An advanced relativistic magnetron with a segmented anode and fast magnetic field* (EAPPC, Seoul, South Korea, September 2022).
17. J. G. Leopold, Y. P. Bliokh, Ya. E. Krasik, Y. Hadas, S. Gleizer, E. Flyat,1 Y. Cao, D. Andreev, A. Kuskov, and E. Schamiloglu, *Diocotron instability in the electron flow of a split cathode magnetron source* (EAPPC, Seoul, South Korea, September 2022).
18. J. G. Leopold, Y. Bliokh, Ya. E. Krasik, A. Kuskov, and E. Schamiloglu, *The diocotron mode developing in a smooth bore coaxial diode and the electromagnetic modes in a six-vane magnetron fed by a split cathode* (PPC, San-Antonio, US, June, 2023).

10. Point of Contact in Navy

This is an ONRG project. The authors had no direct Navy contact. The investigators were represented by their collaborator Prof. E. Schamiloglu vis a vis the Navy.

Homoepitaxial Ga_2O_3 Structures for Power Device Applications

Grant No. N62909-20-1-2055

Annual Report for Fiscal Year 2023

Period of Performance: October 1, 2022 to September 30, 2023

Prepared by:

Akito Kuramata, Principal Investigator
Novel Crystal Technology, Inc.,
2-3-1 Hirosedai, Sayama,
Saitama, 350-1328, Japan
Email: kuramata@novelcrystal.co.jp

This work was sponsored by the Office of Naval Research (ONR), under grant number N62909-20-1-2055. The views and conclusions contained herein are those of the authors only and should not be interpreted as representing those of ONR, the U.S. Navy or the U.S. Government.

Grant or Contract Number: N62909-20-1-2055
Date Prepared: 1/31/2024
Project Title: Homoepitaxial Ga_2O_3 Structures for Power Device Applications
Annual Summary Report: FY23
Principle Investigator: Akito Kuramata, +81-4-2900-0072, kuramata@novelcrystal.co.jp
Novel Crystal Technology, Inc. (http://www.novelcrystal.co.jp/index.html)
2-3-1 Hirosedai, Sayama, Saitama, 350-1328 Japan

Section I: Project Summary

1. Overview of Project

Monoclinic Gallium Oxide (β-Ga_2O_3) is a very attractive semiconducting material for next generation power devices due to its excellent material properties and ease of mass production. Ga_2O_3 has extremely large bandgap of 4.5-4.8 eV and high breakdown electric field strength of about 8 MV/cm, yielding a nearly ten-fold higher Baliga's figure of merit than that of 4H-SiC. Therefore, realization of Ga_2O_3 power devices will bring huge reduction of energy loss for industrial instruments, power plant, or military equipment, etc.

In this project, we will develop the high-quality growth of Ga_2O_3 bulk substrates by using edge-defined, film-fed growth (EFG) and homoepitaxial thick films by using halide vapor phase epitaxy (HVPE), both with large size up to 4-inch in diameter. The Ga_2O_3-based power devices will be optimized for doping scheme, termination structure, etc. to fully take advantage of the material properties. The techniques of wafer bonding onto foreign substrates with higher thermal conductivity and integrating $(Al_xGa_{1-x})_2O_3/Ga_2O_3$ heterostructures will also be developed as a solution to the heat dissipation issue in Ga_2O_3 devices. By using those techniques, we will be able to demonstrate the ultra high power Ga_2O_3 diode and transistor of kV-class.

Since 2015, NCT/NRL have been a leader in the Ga_2O_3 field with a number of vertical Schottky barrier diode demonstrations. However, only recently has the quality of epitaxy been sufficiently optimized to fully take advantage of the predicted 8 MV/cm critical field of Ga_2O_3.

Abstract:
β-Ga_2O_3 is a very attractive semiconducting material for next generation power devices due to its excellent material properties and ease of mass production. Ga_2O_3 has extremely large bandgap of 4.5-4.8 eV and high breakdown electric field strength of about 8 MV/cm, yielding a nearly ten-fold higher Baliga's figure of merit than that of 4H-SiC. Therefore, realization of Ga_2O_3 power devices will bring huge reduction of energy loss for industrial instruments, power plant, or military equipment, etc.

In this project, we will develop the high-quality growth of Ga_2O_3 bulk substrates by using EFG and homoepitaxial thick films by using HVPE, both with large size up to 4-inch in diameter. The Ga_2O3-based power devices will be optimized for doping scheme, termination structure, etc. to fully take advantage of the material properties. The techniques of wafer bonding onto foreign substrates with higher thermal conductivity and integrating $(Al_xGa_{1-x})_2O_3/Ga_2O_3$ heterostructures will also be developed as a solution to the heat dissipation issue in Ga_2O_3 devices. By using those techniques, we will be able to demonstrate the ultra-high power Ga_2O_3 diode and transistor of kV-class.
Objective:
Advance the state-of-the-art of ultra-wide bandgap steady-state and pulsed power electronics by developing benchmark device structures based on high quality homoepitaxial Ga_2O_3 on native β-Ga_2O_3 substrates. Demonstrate that high quality, large-area Ga_2O_3 substrates and low-defect density epilayers grown by Novel Crystal Technology are a viable platform for the development of commercial β-Ga_2O_3-based high voltage, high power devices. Demonstrate a vertical Ga_2O_3 power SBD with breakdown voltage of 5-10 kV while

maintaining on resistance Ron below 1 mΩ-cm^2. Building on this technology, demonstrate a vertical Ga_2O_3 power transistor with breakdown voltage limited only by the intrinsic breakdown of the dielectrics in the device.

Introduction:

The single-crystal gallium oxide (Ga_2O_3) is an advantageous material for high-power, high-temperature electronic device applications due to its high energy direct gap (~4.9 eV) and high breakdown field (8 MV/cm), yielding a nearly ten-fold higher Baliga figure of merit than that of 4H-SiC ($BFOM_{Ga2O3}$ = 3444, $BFOM_{4H\text{-}SiC}$ = 300). An additional feature of the gallium oxide technology is that commercially available large diameter gallium oxide substrates, grown inexpensively from the melt, are available with 2-inch diameter with prototype 4-inch diameter substrates having been demonstrated (Figure 1). Additional important feature of the gallium oxide technology is that high quality homoepitaxial growth of gallium oxide epitaxial layers on gallium oxide substrates with growth rates of 8 microns/hour have been demonstrated for hydride vapor phase epitaxial (HVPE) growth. In addition, good N-type doping control has been demonstrated with doping from the range of low 10^{15}cm^{-3} to 10^{19} cm^{-3} (Figure 1). Highly doped N-type regions by ion implantation has also been demonstrated. Thus, the gallium oxide material technology has many of the features needed for low cost, high performance next generation high voltage power switch technology.

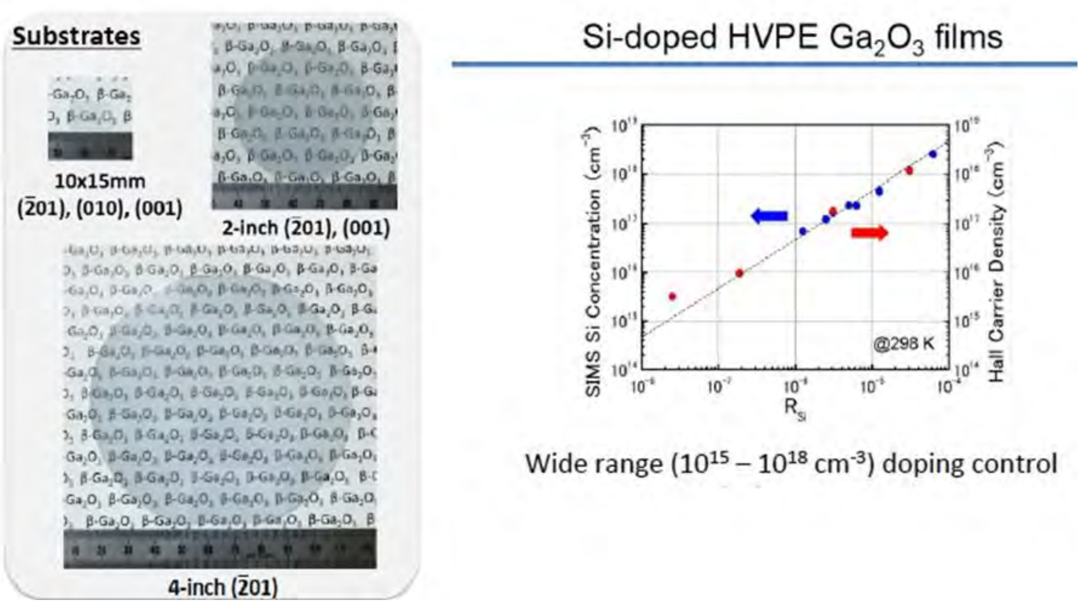

Figure 1. Examples of gallium oxide substrates and N-type doping control.

2. Activities and Accomplishments

During the first year of the NICOP program, a total of 91 Ga_2O_3 and $(Al_xGa_{1-x})_2O_3$ substrates and epiwafers were provided to NRL as program deliverables. This number includes both custom growths for novel experiments such as $(Al_xGa_{1-x})_2O_3$ critical thickness to commercialized 100 mm Ga2O3 epiwafers. In addition, a number of boules of Ga_2O_3 are currently at Novel Crystal technology and are expected to provide additional samples of Ga_2O_3 to NRL in the near future.

During the second year, a further quantity of 378 Ga_2O_3 and $(Al_xGa_{1-x})_2O_3$ substrates and epiwafers were provided to NRL as program deliverables.

During the third year, a total of 72 Ga_2O_3 and $(Al_xGa_{1-x})_2O_3$ substrates and epiwafers have been provided or planned to be provided by the end of CY2024.

Our planned and delivered samples of Year 3 are listed as below.

1. Ga_2O_3 substrates –
   a. Float-zone and Vertical Bridgman substrates, UID (delivered)
   b. (010) Fe-doped substrates, off-axis (to be delivered CY2024)
   c. (100) Fe-doped substrates, off-axis (to be delivered CY2024)
   d. (010) Fe-doped substrates, on-axis (to be delivered CY2024)
   e. (001) 100 mm HVPE substrate, on-axis (to be delivered CY2024)
2. MBE epitaxial films
   a. HFET structures for lateral power devices (to be delivered CY2024)
   b. MBE regrowth on thinned, bonded Ga_2O_3/SiC compound wafer (to be delivered CY2024)
3. HVPE epitaxial films (all wafers are (001) orientation)
   a. N-doped epiwafers with n- UID layer, on Sn-doped substrate (delivered)
   b. 4-inch epiwafers for vertical power device development (to be delivered CY2024)

Specific substrate and epiwafer quantities are summarized in the table below.

Sample detail	Qty
Float zone substrates	20
Vertical Bridgman substrates	10
Off-axis (010) substrates	10
Off-axis (100) substrates	10
On-axis (010) substrates	10
(001) 100 mm substrate	1
HFET MBE heterostructures	5
MBE regrowth	1
N-doped HVPE epiwafers	3
4-inch epiwafers, (001)	3
Dicing	As needed

Specific activities and research results obtained in FY23 are outlined next:

1. Structural, Electrical, and Thermal Characterization of CIS-MOCVD Ga_2O_3 Epitaxial Buffer Layers

Epitaxial growth of β-Ga_2O_3 using metalorganic chemical vapor deposition (MOCVD) has seen great advancements demonstrating high-quality films with high growth rates, low point defect concentrations, and high mobility with low doping concentrations [1]. In this study, we investigate the impact of buffer layer thickness for these MOCVD epitaxial films on electrical characteristics, thermal conductivity, and defect concentrations.

MOCVD films were grown on commercial (Novel Crystal Technology) Fe-doped (010) β-Ga_2O_3 substrates using Agnitron Technology's Agilis close-injection showerhead MOCVD (CIS-MOCVD). The unintentionally doped (UID) buffer layer thickness was varied on the 3 samples: A – 300 nm, B – 500 nm, and C – 1000 nm. The UID layers were followed by a 10 nm thick n^+ (~10^{19} cm^{-3}) Ga_2O_3 layer for improved channel conductivity. A 100 nm highly n^+ Ga_2O_3 layer was selectively regrown following ref. [2]. Ohmic contacts were formed in the regrown areas with an annealed 20/200 nm thick Ti/Au metal stack (475 °C, 1 min., N_2). Mesa isolation was formed with an etch of ~170 nm. Transmission line measurements (TLM) showed sample C had the lowest specific contact resistance of 2.25×10^{-6} $\Omega\cdot cm^2$ and sample A had the highest of 1.99×10^{-4} $\Omega\cdot cm^2$. Room temperature Hall effect measurement showed similar mobility for samples B and C of ~115-116 $cm^2/V\cdot s$, while sample A showed a much lower mobility of 71 $cm^2/V\cdot s$. Samples B and C, both showed high open-gated source-drain current (I_D) (>0.05 A/mm at V_{DS} = 5 V) and low isolation (mesa-mesa) current of < 0.1 µA/mm at V_{DS} = 10 V. Sample A (300 nm thick buffer layer), showed 10X lower open-gated I_D and a high isolation current of ~3 mA/mm at V_{DS} = 10 V. Higher isolation leakage current for samples with thin buffer layers, such as sample A, have been frequently attributed to a peak in Si concentration at the epilayer/substrate interface observed in secondary-ion mass spectroscopy [1]. Here, we offer further insight on this effect via frequency-domain thermoreflectance (FDTR) and positron annihilation spectroscopy (PAS). Preliminary FDTR data showed decreasing thermal conductivity for thicker epilayers. PAS data fitted with a 3-layer model consistently showed higher density of Ga-related vacancies in the epilayers compared to each substrate. More detailed measurements, including XRD and device-level FDTR, will be performed. This preliminary data suggested that MOCVD Ga2O3 was affected by both unintentional impurities and point defects in addition to the known issue of interfacial Si accumulation. [1] A. Waseem, et al., Physica Status Solidi (A), p. 2200616, 2022. [2] Z. Xia, et al., IEEE EDL, 39(4), 568–571, 2018.

Table 1. Specific contact resistance from TLM and mobility, sheet resistance, and sheet carrier concentration from room temperature Hall measurements on each MOCVD stack.

Sample	Specific R_C (Ω*cm^2)	Mobility ($cm^2/V\cdot s$)	R_{sh} (Ω/sq.)	N_{sh} (cm^{-2})
A (0.3 µm)	1.99×10^{-4}	71	4082	2.15×10^{13}
B (0.5 µm)	1.77×10^{-5}	115	4513	1.20×10^{13}
C (1.0 µm)	2.25×10^{-6}	116	6585	8.12×10^{12}

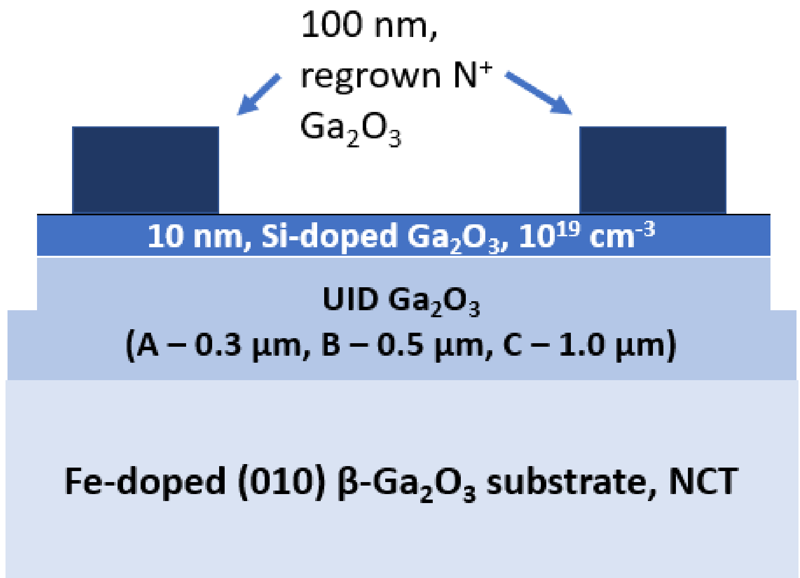

Fig. 1. Cross-section schematic of the MOCVD structures grown on Fe-doped (010) β-Ga_2O_3 substrates from NCT.

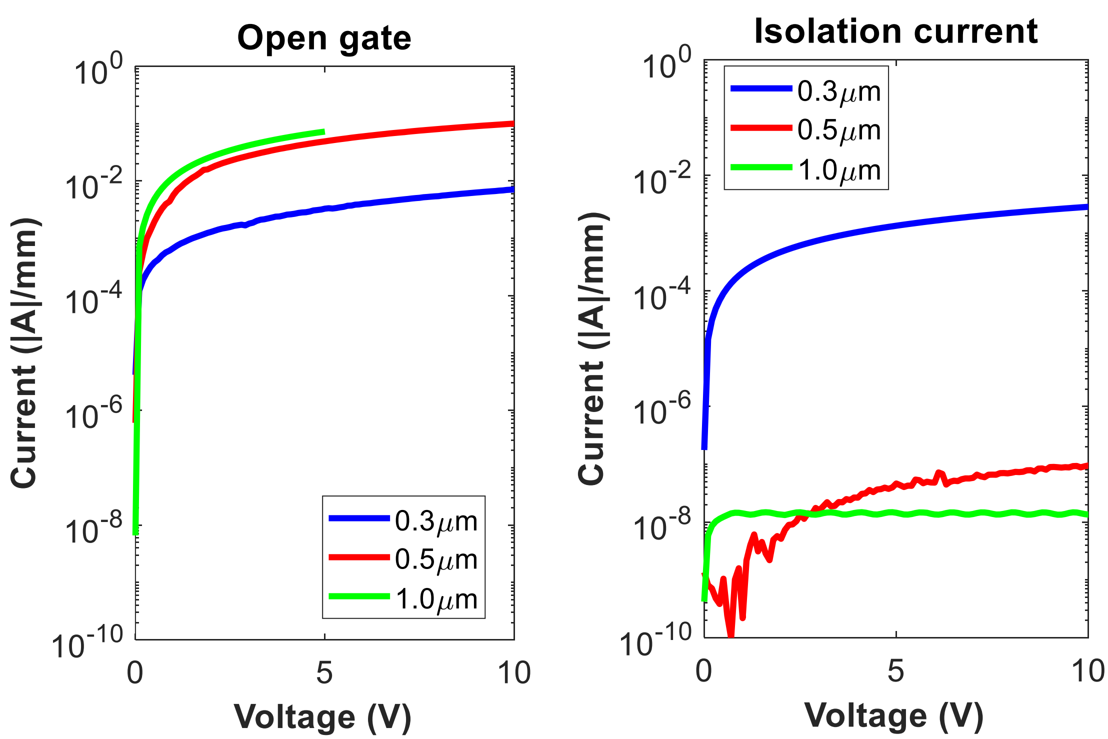

Fig. 2. (a) Open gate *J-V* characteristics and (b) isolation current of each MOCVD sample (A – blue), (B – red), (C – green).

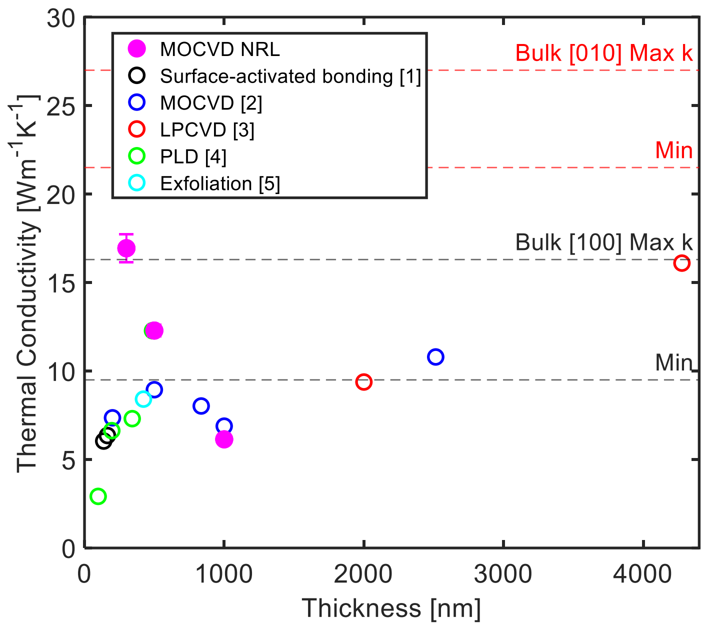

Fig. 3. Thermal Conductivity of this work measured by FDTR compared to literature. References: [1] Z. Cheng et al., ACS Appl Mater Interfaces, vol. 12, no. 40, pp. 44943–44951, Oct. 2020. [2] Y. Song et al., ACS Appl. Mater. Interfaces, vol. 13, p. 38490, 2021. [3] Y. Song et al., ACS Appl. Mater. Interfaces, vol. 13, p. 38490, 2021. [4] N. Blumenschein et al., Oxide-Based Materials and Devices IX (2018). [5] Z. Cheng et al., APL Mater, vol. 7, 031118, Mar. 2019.

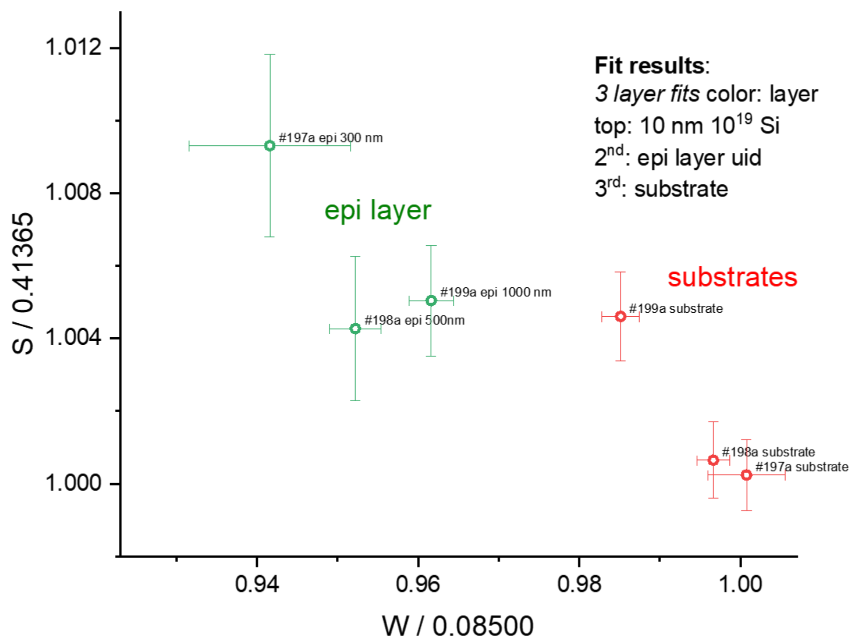

Fig. 4. Normalized S vs. W plot for 3-layer fit of positron annihilation spectra for the three samples.

2. Fabrication of Self Aligned β-Ga_2O_3 Junction Barrier Schottky Diodes with NiO Field Termination

Despite the ultra-wide bandgap (4.8 eV) and the high critical field (6-8 MV/cm) of Ga_2O_3, the lack of shallow acceptors and the self-trapping of holes prevents this material from being doped p-type. Without the availability of p-type Ga_2O_3, Ga_2O_3 power devices must rely on a heterojunction for forming critically-important pn junctions. The naturally p-type nickel oxide (NiO, 3.6-4.5 eV [1]) forms a heterojunction with Ga_2O_3 and has been used to demonstrate Ga2O3 JBS diodes [2, 3]. A self-aligned process is required in order to etch Ga2O3, remove plasma etch damage, and deposit NiO into the etched regions without misalignment.

In this work we have developed a self-aligned JBS diode fabrication process with about 1 μm resolution that is capable of withstanding high-temperature thermal and chemical treatments such as annealing and relevant acid cleaning for Ga_2O_3 (e.g., HCl, H_3PO_4). This novel dry lift-off process incorporates a XeF_2 etch for the undercut and lift-off steps. A tri-layer mask consisting of, in order of deposition, amorphous Silicon (a-Si), PECVD SiO_2, and e-beam evaporated Ni, allow for the dry etching of the Ga_2O_3 epilayer prior to NiO self-aligned deposition. The Ni, SiO_2, and a-Si layers were patterned using Transene Ni-etchant, a CF_4-plasma, and an SF6-plasma dry etching, respectively. Subsequently, a ~250 nm deep trench in the Ga_2O_3 epilayer was etched via BCl_3 plasma, and a post-dry etch clean in warm (80 °C) H_3PO_4 was performed for 10 minutes, wherein the Ni hard mask was also removed. The a-Si mask layer was undercut using a 1" burst of dilute XeF2 in a Xactix XeF2 etcher. P-type NiO with 10% O2 was sputtered (200 W, 12.5 mTorr) in the trench regions, followed by a dry lift-off of the remaining mask (a-Si/SiO_2) in XeF_2 gas by selective undercutting of the a-Si layer. At the conclusion of this self-aligned process, a tri-layer NiO junction termination extension (JTE) region was deposited around the anode perimeter in order to facilitate electric field spreading and improve VBR [4]. Ni/Au anode was deposited atop the JBS region and the inner portions of the NiO JTE to conclude device fabrication (Figs. 1-4). Current-voltage characteristics in forward and reverse bias are shown in Figs. 5-6, respectively. This novel self-aligned process as shown by the fabrication of Ga_2O_3 NiO JBS diode serves to advance Ga_2O_3 heterojunction device technology and fabrication capabilities.

References:
[1] Spencer. J.A, et al., Applied Physics Reviews, 2022.
[2] Lv, Y. et al., IEEE Transactions of Electron Devices, 2021.
[3] Gong, HH et al., Applied Physics Letters, 2021.
[4] Wang, B. et al., IEEE Electron Device Letters, 2022.

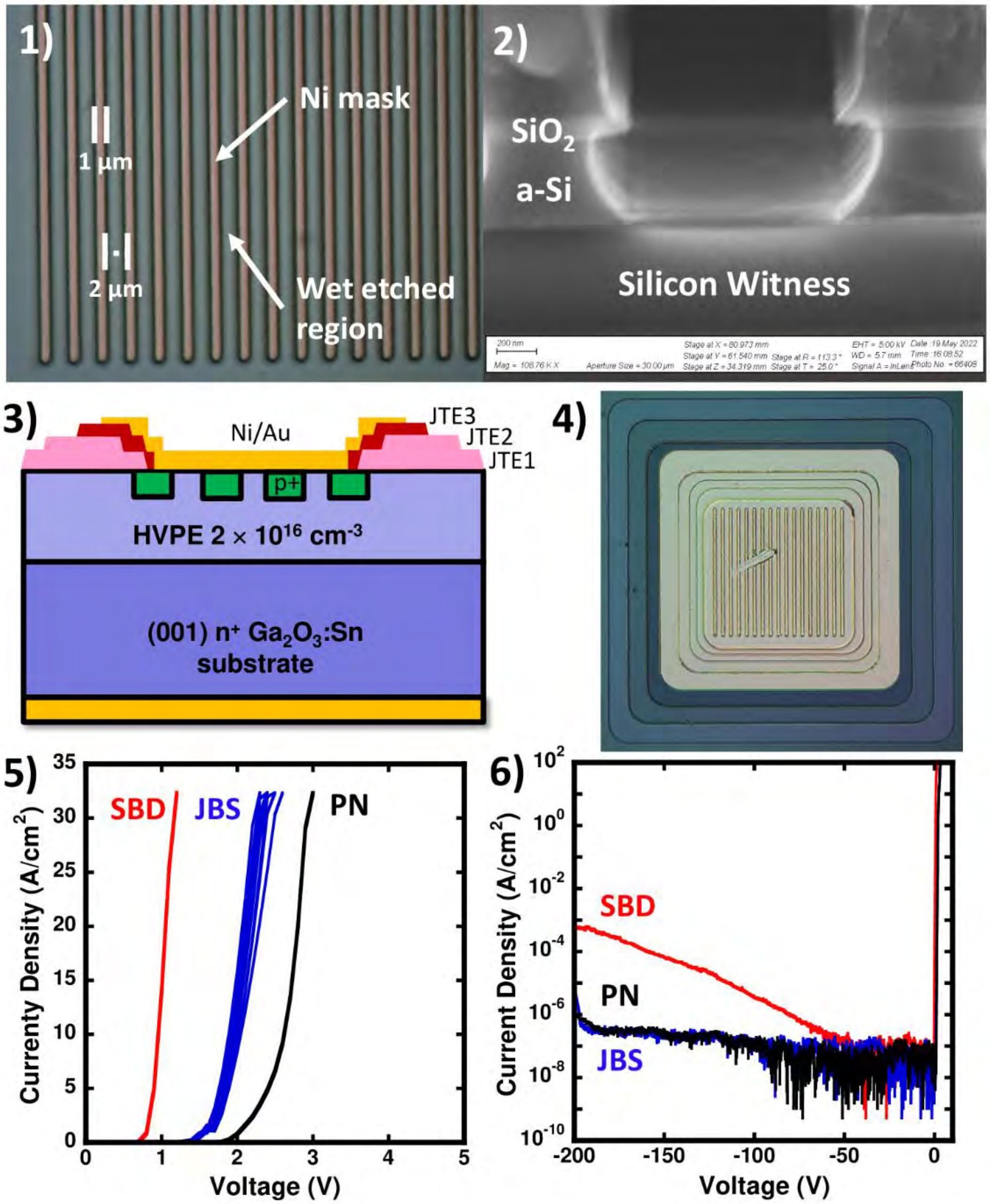

Figure 1. Demonstration of nickel wet etching down to 1 µm. 2) XeF_2 undercut of the amorphous silicon layer for the lift-off process 3) Schematic of the Ga_2O_3 NiO JBS diode 4) Fully fabricated Ga_2O_3/NiO JBS diode with NiO JTE 5) Forward and 6) reverse I-V characteristics of the JBS, SBD, and PN diodes.

3. Towards Controlled Transfer of (001) β-Ga_2O_3 to (0001) 4H-SiC Substrates

We demonstrate successful blistering of He-implanted (001) β-Ga_2O_3, bonding to (0001) 4H-SiC, and initial results towards large-area transfer of (001) β-Ga_2O_3 to 4H-SiC. Compatible with large-scale processing, exfoliation is an important step in controlled-thickness transfer of films for heterogeneous integration. Furthermore, integration of β-Ga_2O_3 to high thermal conductivity materials will be crucial for thermal management of β-Ga_2O_3-based power devices. Two-inch (001) β-Ga_2O_3 wafers were implanted with He^+ at an energy of 160 keV and a dose of 5×10^{16} cm^{-2}, which are the same implant parameters used previously to successfully exfoliate (010) β-Ga_2O_3 [1]. Strain fringes were observed after the implant which corresponded to a maximum strain of ~1.7%, which is higher than the ~1% strain when implanting (010) β-Ga_2O_3 likely due to the larger Poisson's ratio of (001) β-Ga_2O_3 [2] The implanted substrates were then bonded to (0001) 4H-SiC at room temperature using a ~5 nm thin Ti interlayer to assist with the bond. Both unbonded implanted substrates and the bonded structures were first annealed at 200 °C for 10 hours to simultaneously initiate He bubble nucleation at the implanted projected range (~0.68 μm) and strengthen the bond. Then, even after annealing at 500 °C for 10 hours to initiate He bubble growth, the (001) β-Ga_2O_3 did not transfer to the (0001) 4H-SiC. Unlike what was observed for (010) β-Ga_2O_3 blistering did not even occur at this temperature. Annealing at 800 °C for up to 12 hours resulted in ~10 μm blisters for the unbonded substrates, which is typically an indication that large wafer-area transfer can be achieved if bonding was done prior to annealing [3]. However, the β-Ga_2O_3 substrate did not wafer split from the bonded structure, and instead only small area transfers up to ~200 μm were achieved. Only ~7% of the total bonded area transferred while the entire structure remained bonded. Strategies to improve transfer will be presented, including initiating a cold split prior to exfoliation and refined annealing strategies to improve He bubble nucleation and larger bubble growth at the projected range. These are promising results towards achieving large wafer-scale (001) β-Ga_2O_3 composite wafers, and when combined with subsurface damage-free chemical mechanical polishing [4], these composite wafers would be suitable for subsequent devices and/or epitaxial growth.

References

[1] M.E. Liao, et al., ECS J. Solid State Sci. Technol., 8(11), P673 (2019).
[2] K. Adachi, et al., J. Appl. Phys., 124, 085102 (2018).
[3] M. Bruel, et al., Jpn. J. Appl. Phys., 36, 1636 (1997).
[4] M.E. Liao, et al., J. Vac. Sci. Technol. A, 41, 013205 (2023).

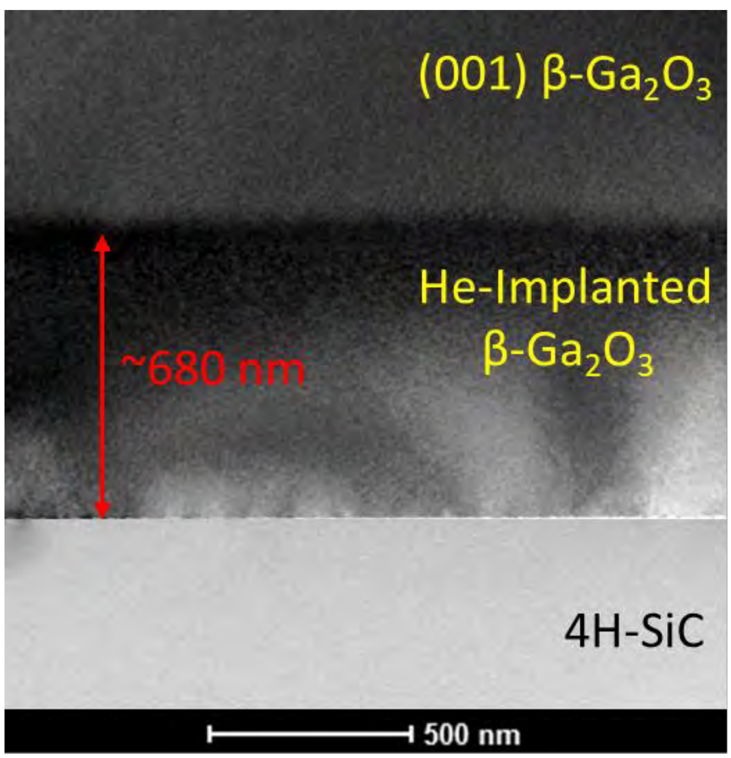

Figure 1. Cross-sectional bright field scanning transmission electron microscopy image aligned along the [100]* β-Ga_2O_3 zone axis.

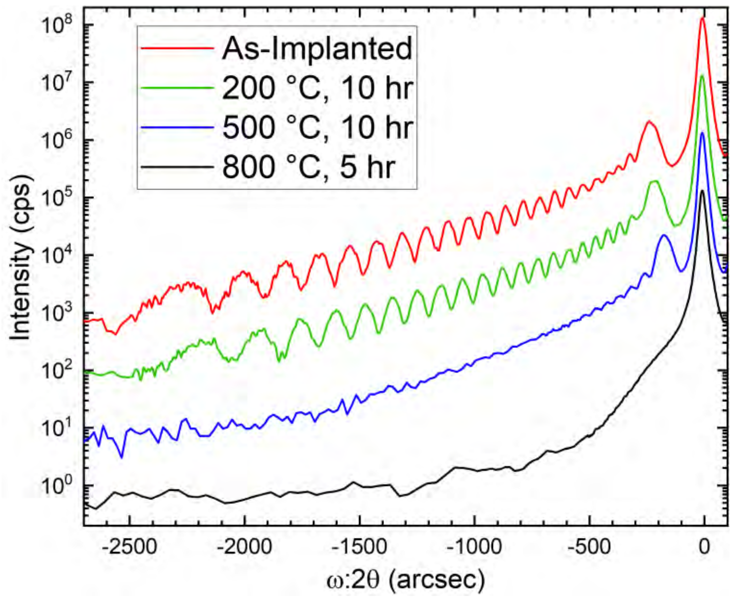

Figure 2. Triple-axis X-ray diffraction symmetric (004) β-Ga_2O_3 ω:2θ scans. The anneal order was: 200 °C, 500 °C, then 800 °C. Fringes correspond to strain from the He implant and each subsequent anneal reduced the fringe intensity and shifted towards 0” ((004) substrate peak), which corresponds to strain reduction.

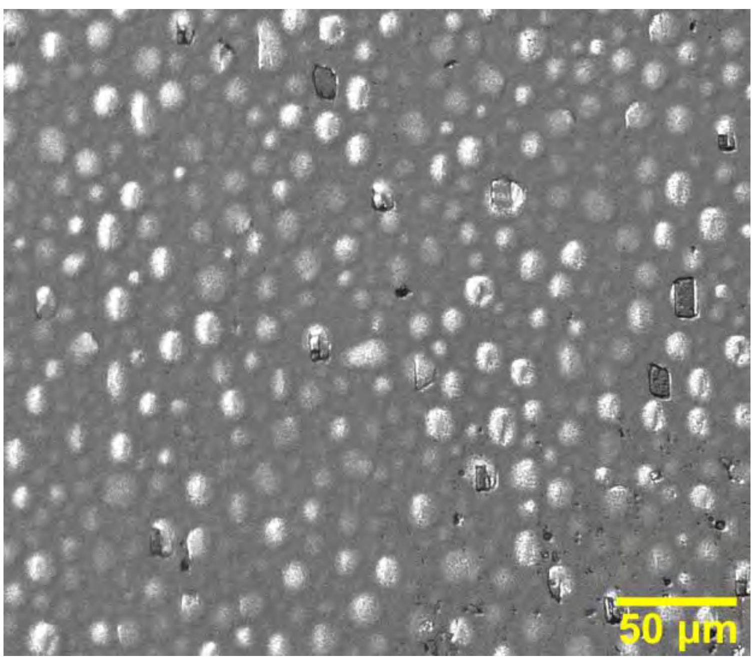

Figure 3. Planview optical Nomarski image of the unbonded (001) β-Ga_2O_3 surface after annealing 200 °C, 500 °C, then 800 °C. The round light contrast features are He surface blisters. The dark rectangular features are exfoliated regions, with the vertical edges corresponding to the (100) primary cleavage plane.

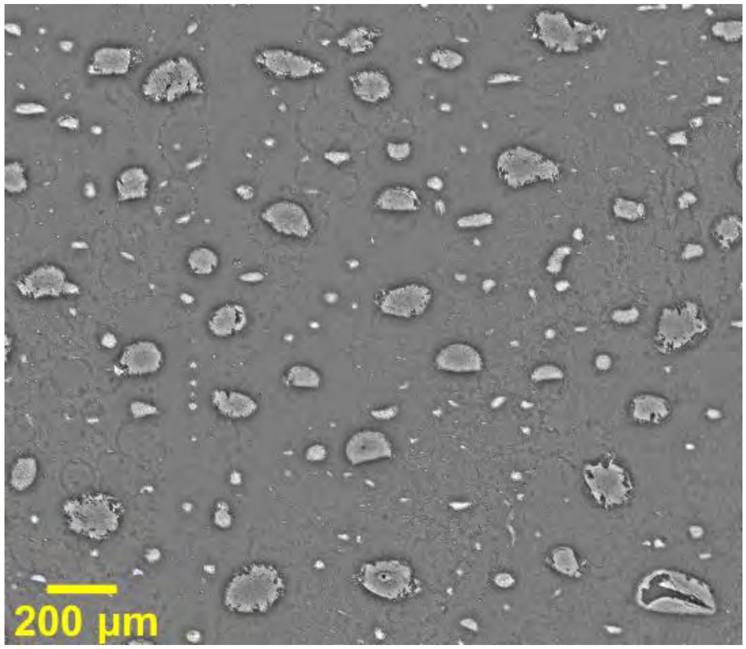

Figure 4. Planview optical Nomarski image of the bonded structure viewed through the β-Ga_2O_3 wafer after annealing. ~7% of the total bonded area transferred to the (0001) 4H-SiC (round light contrast features). The structure remained bonded and the β-Ga_2O_3 did not wafer split.

4. Operation of β-Ga_2O_3 field-effect transistors at 650 °C – this is the highest reported operating temperature for a Ga_2O_3 device

The ultrawide bandgap of β-Ga_2O_3 (~4.8 eV) allows for high voltage and high temperature operation, making it enticing for extreme environment electronics. [1] Potential applications include space exploration, deep drilling, aeronautics, and defense, which can have operating environments with temperatures greater than 600 °C. [2,3] As such, performance and reliability at these high operating temperatures (>600 °C) must be characterized and understood in order to optimize devices for expected, reliable, and stable operation. In this work, we report operation and electrical characterization of β-Ga_2O_3 metal-oxide-semiconductor field-effect transistors (MOSFETs) at temperatures up to 650 °C to lay the groundwork for potential deployment in extreme environments.

Using Agnitron Technology's Agilis 100 MOCVD reactor, 300 nm thick UID β-Ga_2O_3 buffer, 30 nm thick 10^{18} cm^{-3} β-Ga_2O_3 (Si-doped) channel, and 10 nm thick 10^{19} cm^{-3} β-Ga_2O_3 (Si-doped) contact layers were homoepitaxially grown on Fe-doped (010) β-Ga_2O_3 substrates. Ti/Au Ohmic contacts were deposited using e-beam evaporation, lifted off, and annealed (470 °C, 1 min, N_2 ambient). Subsequently, a 20 nm thick Al_2O_3 gate dielectric was deposited using atomic layer deposition. Finally, Pt/Au gate contacts were deposited using e-beam evaporation. The devices had a channel length of 15.5 µm, channel width of 75 µm, gate length of 3 µm, and a drain-source spacing of 10 µm. A cross-sectional schematic of the device structure is shown in Fig. 1. The β-Ga_2O_3 MOSFETs had a Hall mobility of 170 cm^{2}V^{-1}s^{-1}, sheet carrier concentration of 1.74×10^{12} cm^{-2}, sheet resistance of 21.02 kΩ/sq, and specific contact resistivity of 5.26×10^{-4} Ωcm^2. For high temperature measurements, a DC/RF MicroXact probe station was used along with a Keithley 4200 parameter analyzer. All measurements were performed under vacuum at base temperatures from 30 °C to 654 °C. DC output and transfer characteristics of a Ga_2O_3 MOSFET are shown in Fig. 2. From Fig. 2(a), at 654 °C, there is >3× increase in the maximum I_{ds} (at V_{gs} = 5 V) as compared to at 30 °C. From Fig. 2(b), it can be seen that there is a negative threshold voltage shift as the base temperature is increased. Furthermore, the increase in base temperature also led to a significant increase in the OFF-state leakage current; from 30 °C to 654 °C, the leakage current increased by five orders of magnitude. In Fig. 3, both I_{ds} and I_g are plotted as a function of V_{gs} for four different MOSFETs operated at 654 °C. As shown, I_g is three orders of magnitude smaller than I_{ds} in the OFF-state, indicating that the gate is not the primary leakage path at high temperatures.

[1] M.A. Mastro *et al.*, *ECS J. Solid State Sci. Technol.* 2017*,* 6(5), P356-P359.
[2] M.R. Werner *et al.*, *IEEE Trans. Ind. Electron.* 2001*,* 48(2), 249-257.
[3] J. Noh *et al.*, *IEEE Trans. Electron Devices* 2021*,* 68(5), 2515-2521.

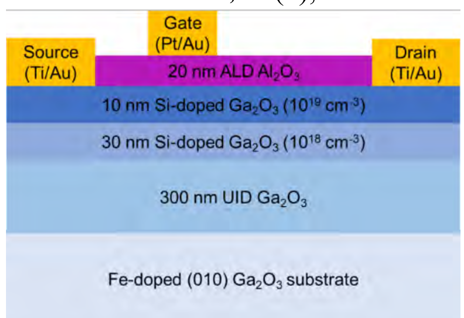

Figure 1. Cross-sectional schematic of the β-Ga_2O_3 MOSFET.

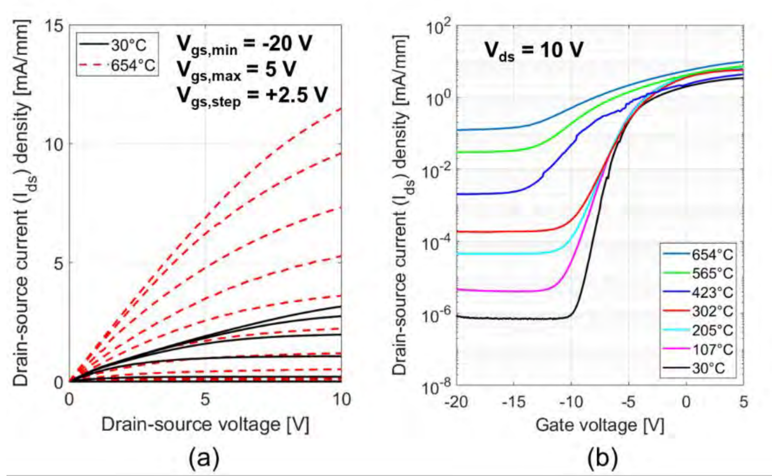

Figure 2. (a) DC output characteristics of a β-Ga_2O_3 MOSFET at 30 °C and 654 °C. (b) DC transfer characteristics of a β-Ga_2O_3 MOSFET from 30 °C to 654 °C.

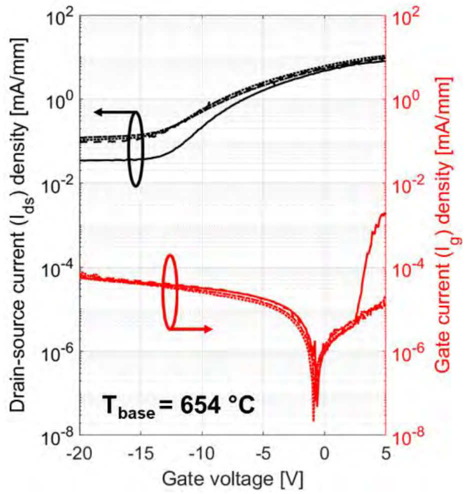

Figure 3. DC transfer characteristics of four different β-Ga_2O_3 MOSFETs operating with a base temperature of 654 °C. The left axis shows the drain-source current density (I_{dss}) and the right axis shows the gate current density (I_g).

5. Platinum oxide Schottky contacts to degenerately-doped (-201) β-Ga_2O_3

Ga_2O_3 is an ultra-wide bandgap semiconductor that has gained much interest in the materials and electrical engineering research fields. Ga_2O_3 has numerous favorable material properties such as substrate melt and homoepitaxial growth, excellent doping control, low background acceptor concentrations, and the potential for a high critical field strength of ~6 MV/cm. It is these properties and the potential for advancing the field of power electronics beyond SiC and GaN that has spurred interest into Ga_2O_3. The rapidly advancing epitaxial growth methods have resulted in high quality drift regions as thick as 20 µm. However, if such a voltage cannot be obtained in order to fully deplete the drift layer, it only serves as added resistance to a vertical diode. Leakage current over the Schottky contact of both a Schottky barrier diode (SBD) and a junction barrier Schottky (JBS) diode are a common cause of premature breakdown and reduced breakdown voltage that prevent the full depletion of the drift layer from being reached. Nickel and platinum are two commonly used Schottky contacts in SBDs with nickel having a lower work function than platinum and thus a lower breakdown voltage. The metallic oxide platinum oxide (PtOx) has a higher work function than both nickel and platinum carrying with it the potential for improved breakdown voltages. In this work, we highlight the increased barrier height of a PtOx Schottky contact to highly doped Ga_2O_3 and its impact on vertical power diodes.

It is well known that a Schottky contact formed on a highly, or degenerately doped semiconductor will be poor in nature. As EF becomes closer to the conduction band energy with increased doping, the electron affinity of the semiconductor decreases, thus decreasing the barrier height of the formed Schottky contact (insert the simple formula here). Reduced barrier height contributes to increased reverse leakage current, reducing the blocking voltage capabilities of the rectifier. Thus, one solution is to develop higher work function Schottky contacts to ultra-wide bandgap materials such as Ga2O3. This was demonstrated with PtOx and other sputtered oxides recently on low-doped Ga_2O_3 [Martin Allen et al., IEEE EDL 2019]. In this work, we demonstrate that PtOx is an effective Schottky contact to highly conductive Ga_2O_3:Sn.

Platinum oxide (PtOx) Schottky contacts were deposited using reactive sputtering on highly doped (8×10^{18} cm^{-3}) (-201) β-Ga_2O_3:Sn substrates grown by the edge-defined film-fed method. Electron-beam evaporated Ni and Pt Schottky contacts were deposited as reference. All Schottky metals were capped with evaporated gold. Capacitance-voltage measurements as well as temperature dependent current-voltage measurements were performed in order to extract the barrier height of the PtOx Schottky contact. PtOx was shown to increase the barrier height by 85% and 64% when compared to nickel and platinum Schottky contacts, respectively. At low reverse bias, the leakage current of the PtOx Schottky barrier diodes was approximately 5-6 orders of magnitude lower when compared to the nickel and platinum anodes. These results highlight the increase in Schottky barrier height provided by PtOx as evidenced by the fabrication of a rectifying Schottky contact to highly doped β-Ga_2O_3.

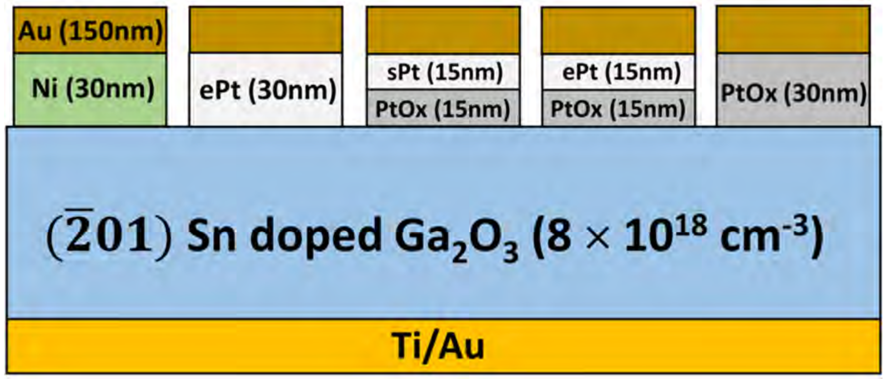

Figure 1. Configuration of the five different Schottky contacts deposited onto ($\bar{2}$01) β-Ga_2O_3:Sn substrates. All anode metal stacks are a total of 180 nm thick. sPt and ePt denote sputtered and evaporated platinum, respectively.

	V_{bi} (eV)	$R_{on,spec}$ (mΩ·cm^2)	V_{on} (V)	J_R* (A/cm^2)	$\Phi_{B,CV}$ (eV)	$\Phi_{B,JVT}$ (eV)	n_{RT}	Δn
Ni / Au	0.92	3.73	0.84	5 x 10^2	0.84	0.57	1.57	-0.41
Pt / Au	1.27	3.58	0.97	3 x 10^1	1.19	0.64	1.54	-0.39
PtOx / sPt / Au	1.61	4.61	1.47	1 x 10^0	1.53	0.97	1.54	-0.35
PtOx / ePt / Au	1.72	4.72	1.51	9 x 10^{-3}	1.64	1.06	1.31	-0.16
PtOx / Au	1.67	4.46	1.48	3 x 10^{-1}	1.59	0.92	1.37	-0.14

Table 1. Characteristics of the Schottky Barrier Diodes including built-in potential (V_{bi}), specific on-resistance ($R_{on,spec}$), turn-on voltage (V_{on}) , barrier height from *C-V* ($\Phi_{B,CV}$) temperature dependent *I-V* ($\Phi_{B,JVT}$), leakage current (J_R), room temperature ideality factors (n_{RT}) and the change in ideality (Δn) from room temperature to 180°C. * J_R measured at V_R = -8 V.

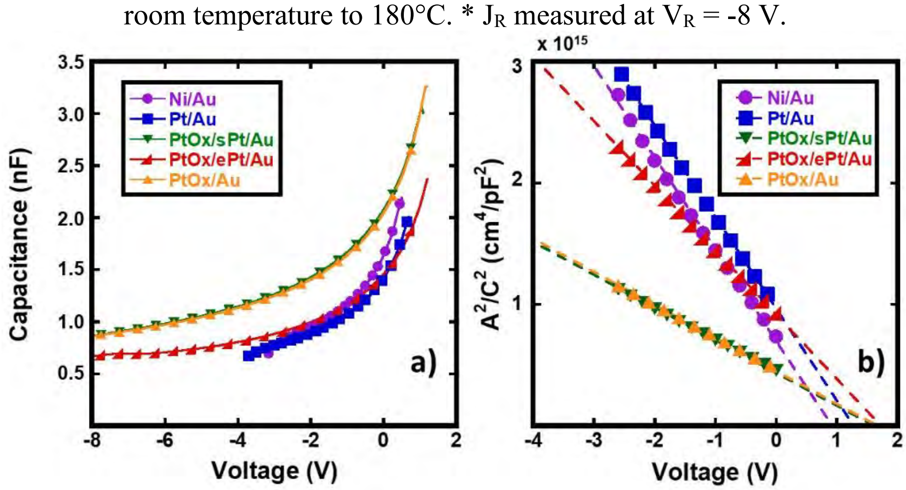

Figure 2. a) Capacitance-voltage characteristics of the five Schottky barrier diodes. b) 1/C^2 is shown in order to extract the doping concentration and the built-in-potential V_{bi}.

6. Silicon Ion Implant Activation in β-$Al_{0.4}Ga_{1.6}O_3$

Gallium oxide β-Ga_2O_3 (GO) devices have generated great interest for next generation power and RF devices, in no small part due to the availability of large area, high quality, melt grown, bulk substrates in multiple orientations. Many structures take advantage of heteroepitaxial growth of aluminum gallium oxide β-$(AlGa)_2O_3$ (AlGO) pseudomorphically for heterjunction AlGO/GO devices. A key challenge for HFET and similar devices remains in obtaining low contact resistance, enabling high drain-source current density with minimal contact self-heating.

Here we focus on the activation of ion implanted silicon donors by rapid thermal annealing of AlGO grown by metalorganic chemical vapor deposition on a bulk GO substrate by varying the implant concentration, anneal duration, and anneal temperature. Films were ion implanted with silicon concentrations of 5×10^{18} cm^{-3}, 3×10^{19} cm^{-3}, and 1×10^{20} cm^{-3} approximating box profiles ~60 nm deep into the ~100 nm thick AlGO films. Anneals were performed from 900 to 1140 °C with varying nominal durations from 6 to 600 seconds. Standard Ti/Au contacts were used with a short ohmic anneal for 60 seconds at 470 °C.

Linear transmission line measurements (LTLMs) indicate that ohmic contact was achievable at all implantation doses tested, with the broadest anneal process latitude available at the highest silicon concentration of 1×10^{20} cm^{-3}. At this concentration, the specific contact resistance was at or below 10^{-3} ohm-cm^2 for most anneal conditions and achieving a minimum measured value of 5×10^{-5} Ω-cm^2 for a 6 second anneal at 1100 °C, however, the minimum sheet resistance was measured for anneals near 1000 °C for 6-60 seconds at ~3 kΩ/sq. At 3×10^{19} cm^{-3} Si concentration, optimal annealing conditions again centered around 1000 °C for 6-60 seconds achieving sheet resistances of 5-10 kΩ/sq with specific contact resistances of ~3×10^{-2} Ω·cm^2. At the lowest silicon concentration of 5×10^{18} cm^{-3}, longer and lower temperature anneals were favored at 900 °C 1-10 minutes or 1000 °C for 1 minute achieving optimal performance at 900 °C for 1 minute at 10-20 kΩ/sq and specific on resistance of 2×10^{-3} Ω·cm^2.

Hall effect on samples annealed at 1000 °C for 1 minute showed mobilities of ~22 cm^2/V·s with approximately 3% of implanted species actively generating carriers, while annealing for a shorter duration of 6 seconds shows an improved mobility of 30-35 cm^2/V·s and 4-7% of implanted species generating carriers. This preference of shorter anneals agrees with LTLMs indicating degradation for long duration or higher temperatures at the same duration showing that overannealing can have a significant impact. This effect could be the consequence of excessive diffusion, coalescence into inactive aggregates, or other effects, but is as of yet unknown in cause.

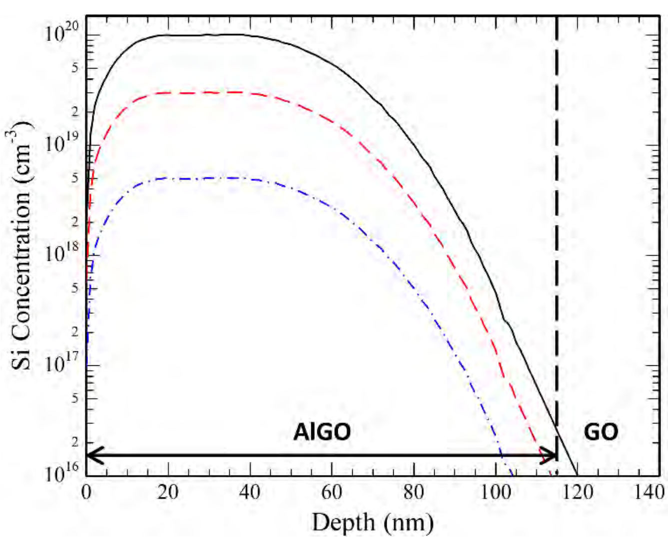

Figure 1: Simulated as-implanted silicon density profile within the AlGO on log scale. Profile indicates <0.05% of peak concentration at the UID GO interface at ~115nm.

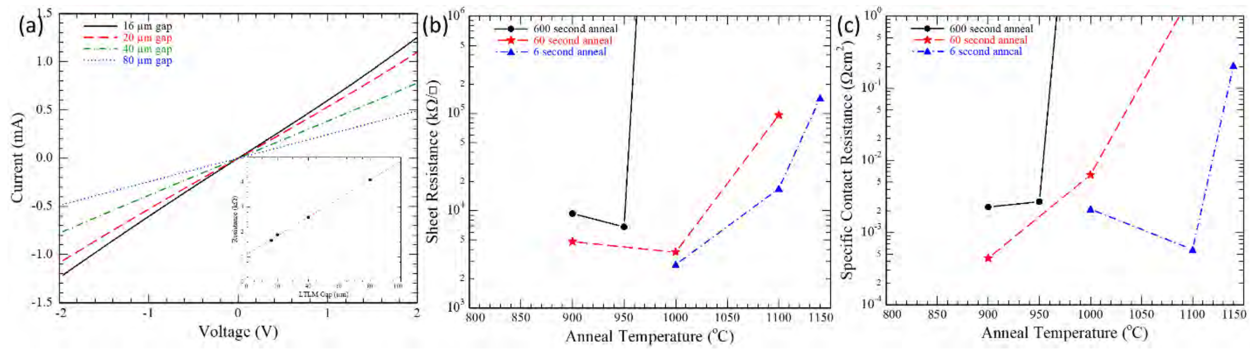

Figure 2: LTLM data for 1x10^{20} cm^{-3} implanted samples. (a) Individual I-V traces after a 60 second, 1000°C anneal spanning 16 to 80 micron lengths, (inset) TLM resistance versus gap length, (b) resultant TLM film sheet resistivity, and (c) specific contact resistance as a function of anneal duration and temperature.

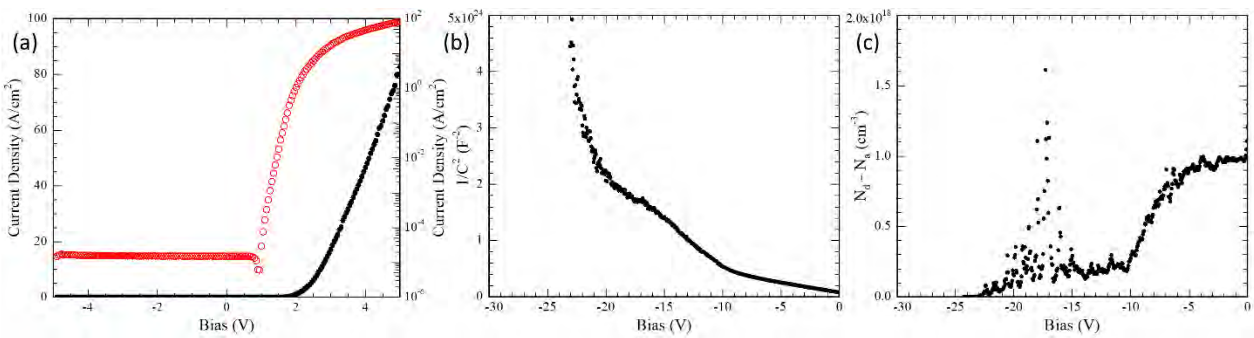

Figure 3: (a) linear and log scale low voltage Schottky (Ni/Au) diode IV trace, (b) plot of 1/C^2 versus diode bias, and (c) resultant implied carrier density.

7. Gallium Oxide Junction Barrier Schottky (JBS) Rectifiers with 1kV Operation

Over the last year, our group has made significant advancements towards the design and fabrication of a gallium oxide (Ga_2O_3) nickel oxide (NiO) junction barrier Schottky (JBS) diode. Our learning to date have resulted in exploration of multiple areas that comprise a hetero JBS diode including the fabrication, heterojunction formation, and contacts. Further understanding of these areas is key to improving the device performance and reliability.

Self-Aligned Fabrication Process:
At the conclusion of FY22, it was determined that a self-aligned lithography process was necessary for the fabrication of a hetero JBS diode. High power plasma etchants and aggressive chemicals are commonly used when fabricating nonplanar Ga2O3 devices, meaning a robust lithography mask is required. Our group has conceptualized and reduced to practice a novel self-aligned process for Ga2O3 processing that is capable of withstanding high temperatures and aggressive chemical treatments. The first demonstration of this process yielded features sizes down to 1 µm in width. The mask design allows for a wide processing window where the layers are specifically chosen for the desired temperature and chemical treatments. For example, if phosphoric acid is desired for post etch clean up, an oxide interlayer must be placed in between the silicon lift-off layer and the hard mask. If hydrochloric acid is preferred, no oxide interlayer is needed. A provisional patent was filled during FY22 and the reduction to practice and filing of the disclosure was completed in June 2023. While this process is extremely beneficial to the Ga2O3 research community, the

application to other semiconductor heterostructures was detailed in the disclosure further highlighting the versatility of our process.

Platinum oxide Schottky and Ohmic contacts:

A key aspect of the JBS diode is the metal contacts. Proper operation of a JBS diode requires that a single metal contact satisfy both types of electrical contacts, Schottky to the n- (Ga2O3) and Ohmic to the p+ (NiO). Ga2O3 Schottky contacts have received much attention in the literature with metals such as Ni, Pt, and metallic oxides such as PtOx. However, the Ohmic contact to NiO has received little to no attention outside of Ni. For the most recent batch of JBS diodes that our group has processed, sputtered PtOx was used for the anode metal. We have demonstrated for the first time an Ohmic contact to NiO using PtOx as well as benefits that extend beyond the traditional Ni contact. JBS diodes with PtOx anode metals currently show a reduction in leakage current of nearly four orders of magnitude compared to JBS diodes with Ni anode metal. When comparing the breakdown voltage, PtOx shows an improvement of almost 200 V beyond the performance of the Ni anode. In parallel to the JBS diode testing, the PtOx NiO Ohmic contact is being characterized alongside Ni and Pt. To date, PtOx is showing a reduction in specific contact resistance to NiO. The motivation for exploring the NiO Ohmic contact has two driving factors. The first is for the improvement of our current devices and to address a void in the literature. The second factor can be found in past SiC research. The demonstration of a SiC merged PiN Schottky diode with robust surge-current capability was only realized after improvements to the p+ semiconductor were achieved. A Ga2O3 NiO MPS diode has not been realized due to the lack of p-type conductivity in Ga2O3. Current and future work on the Ohmic contacts to NiO in the Ga2O3 JBS diode serve to explore the possibility of such a device.

Atomic Gallium Flux Etching:

An alternative method to etching Ga2O3 has been recently demonstrated without the use of high powered plasma or the need for etch damage removal. This removes a large number of issues and challenges faced when etching with traditional high powered plasmas. We have successfully etched Ga2O3 with a Ga flux for the subsequent deposition of NiO into the etch regions. We have demonstrated the first JBS diode using Ga flux etching and are currently performing electrical characterization for a publication on the matter. The Ga flux etched JBS diodes did not utilize the above mentioned self-aligned fabrication process. Ga flux etching occurs at high temperatures between 700-1000°C. At the time of fabricating the Ga flux etched diodes, the self-aligned process could not withstand such high temperatures. Since then, the lift-off layer of the mask has been replaced with poly-silicon and can be used at such conditions unlike amorphous silicon. A future round of fabrication is planned utilizing both the Ga flux etching and self-aligned lithography process.

Reliability Testing:

High voltage reliability and stress testing has been performed on the Ga flux etched diodes. JBS diodes were stressed at 800 V for a total time of 2000 seconds without failing. Preliminary data is showing that the Schottky portion of the device is not impacted by the high voltage testing, evidenced by repeatable and unchanging device turn-on characteristics. Such results mean that there is minimal to no sidewall trapping occurring between the etched sidewall of the Ga2O3 and sputtered NiO filling the etched region. This type of reliability testing has not yet been reported in Ga2O3 devices.

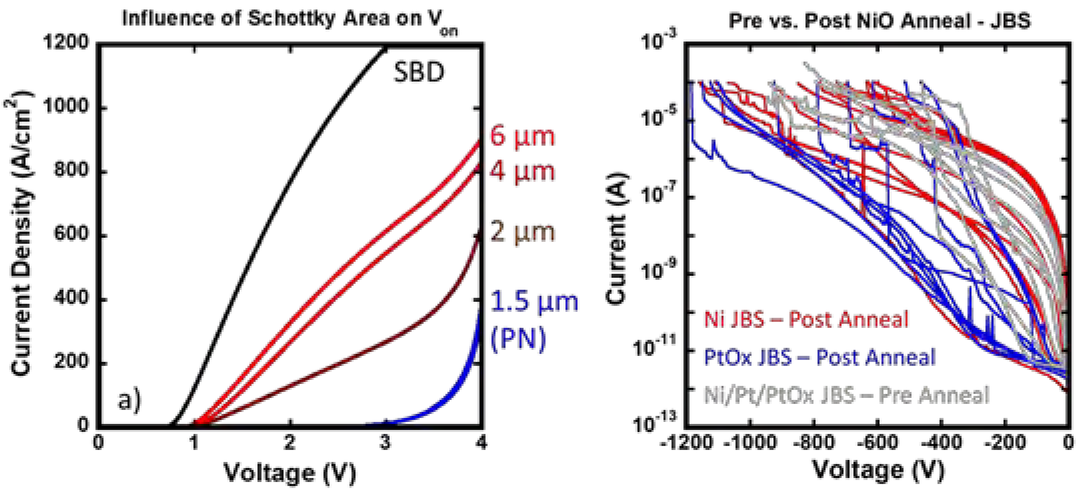

Figure 1. Forward (left) and reverse (right) bias operation of Ga2O3 JBS diodes with NiO heterojunction, damage-free Ga flux etched trenches, and three different anodes (Ni, PtOx, or Ni/Pt/PtOx).

8. Assessment of channel temperature in β-$(Al_xGa_{1-x})_2O_3/Ga_2O_3$ heterostructure field-effect transistors using visible wavelength thermoreflectance thermal imaging

The temperature rise in the channel of a β-$(Al_{0.21}Ga_{0.79})_2O_3/Ga_2O_3$ heterostructure field effect transistor (HFET) was mapped using thermoreflectance imaging at 470 nm. First, the thermoreflectance response of the HFET channel was measured using a monochromator revealing a maximum of the reflectance change around 470-480 nm. Thermoreflectance calibrations were then performed at 470 nm (peak of the reflectance change) and yielded an average thermoreflectance coefficient of $1.06 \pm 0.07\times10^4$ K^{-1}. Subsequent measurements of the device (power densities of 0.15-1.47 W/mm, gate-source voltage of 0 V) enabled extraction of a device-level thermal resistance of 51 mm·K/W in the channel at the drain-side of the gate. High-resolution, in-situ scanning thermal microscopy measurements of the channel temperature rise show good agreement with and further support the thermoreflectance measurements. Finally, the thermal profile across the entire device length (metal electrodes and semiconductor channel) was simultaneously measured using thermoreflectance imaging at 470 nm, and the peak temperature rise was measured in the channel at the drain-side of the gate electrode. This work demonstrates direct, rapid 2D mapping measurement capabilities of the ultrawide bandgap semiconductor channel of $(Al_xGa_{1-x})_2O_3/Ga_2O_3$ transistors without sample contamination (e.g., Ti nanoparticles), long acquisition times, or sophisticated thermometry such as developing novel deep-UV compatible thermoreflectance systems.

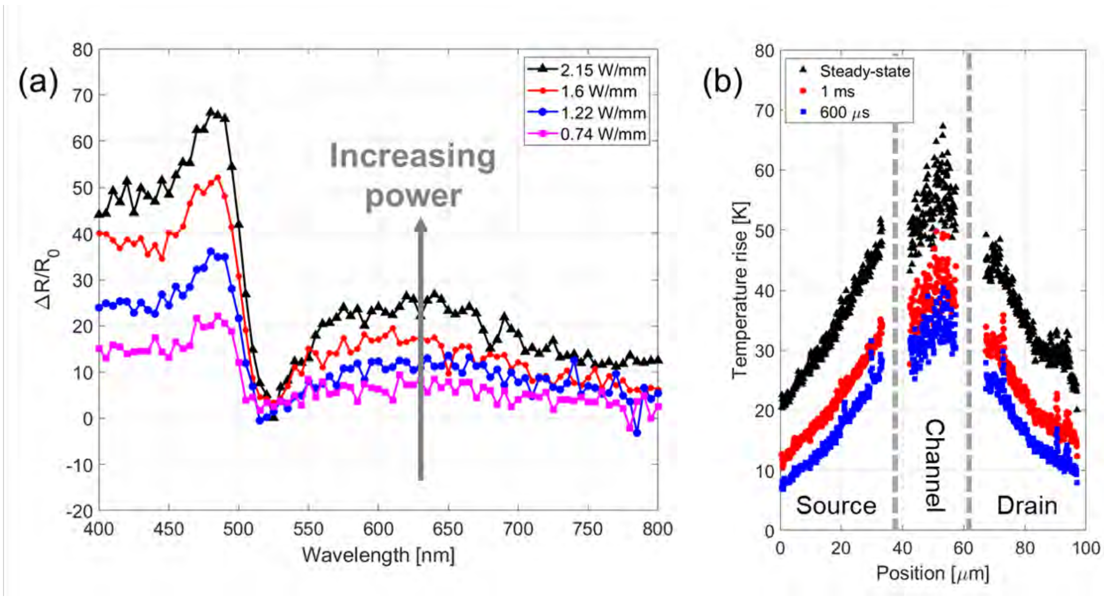

Figure 1. (a) Thermoreflectance spectra showing relative change in reflectivity of an β-$(Al_{0.21}Ga_{0.79})_2O_3/Ga_2O_3$ HFET at various power densities (V_{GS} = 4 V). (b) Temperature rise across the length of an β-$(Al_{0.21}Ga_{0.79})_2O_3/Ga_2O_3$ TLM structure at the same bias condition (P = 200 mW, V_{DS} = 27.5 V) with different electrical pulse widths.

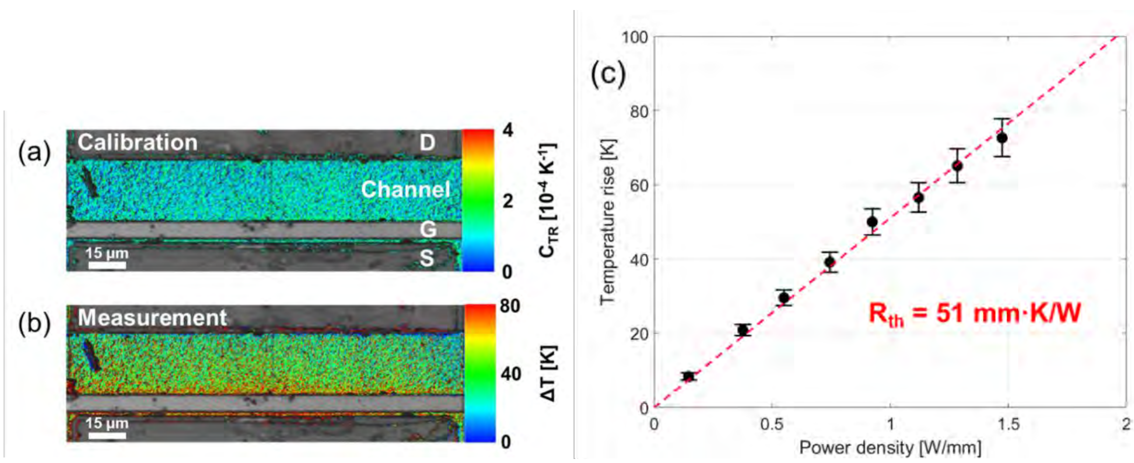

Figure 2. (a) An exemplary calibration map of an HFET (λ = 470 nm). D, G, and S correspond to drain, gate, and source, respectively. (b) An exemplary thermal map of the HFET operating at a power density of 1.47 W/mm (V_{GS} = 0 V). (c) Peak temperature rise as a function of power density (V_{GS} = 0 V). The dashed line is a linear fit to the data, indicating the thermal resistance (51 mm·K/W). The error bars represent the uncertainty due to the thermoreflectance coefficient, C_{TR}, which is calculated as two standard deviations of the mean C_{TR}.

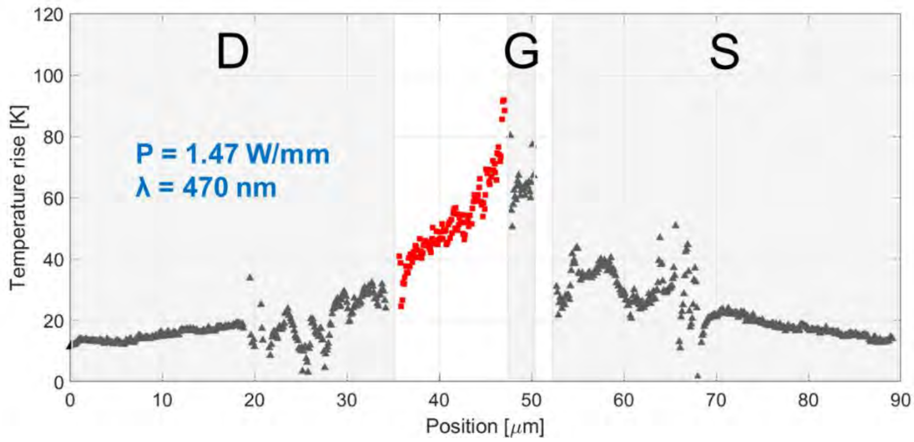

Figure 3. Temperature rise across the length of an HFET when operating at a power density of 1.47 W/mm (V_{GS} = 0 V). The temperature distribution was extracted at the centerline of the device width from both the metal electrodes (triangles) and semiconductor channel (squares). A probing wavelength of 470 nm was used for both the metal electrodes and semiconductor channel. D, G, and S stand for drain, gate, and source, respectively.

9. Progress towards cold ion-splitting of (010) β-Ga_2O_3 using implanted Helium

A crucial engineering challenge to developing high-performing β-Ga_2O_3 power devices is incorporating thermal management solutions to combat counter the low thermal conductivity of the material. One proposed thermal management solution includes wafer thinning and bonding the Ga_2O_3 substrate to a high thermally conductive material (e.g. SiC or Diamond). Two methods for achieving thin films of Ga_2O_3 for bonding includes chemical-mechanical polishing [1], which can be wasteful, and mechanical exfoliation, which is limited to the natural cleavage planes of β-Ga_2O_3, (100) and (001) [2], [3]. Other techniques such as spalling and remote epitaxy have been proposed as well. The SmartCut™ technique, described as the light atom (helium or hydrogen) ion implantation with subsequent annealing is a well-understood method of tuning the thickness of exfoliated thin films of Si. Liao, et al., demonstrated this exfoliation technique on β-Ga_2O_3 showing after 500°C anneals, blisters are formed in the He-implanted region of the (010) β-Ga_2O_3 [4]. This technique has also been demonstrated on other orientations of β-Ga_2O_3 (i.e. (001) and (-201)) with successful bonding to 4H-SiC substrates [5]–[7]. Cold ion-splitting, which has been demonstrated with Si, lowers the necessary annealing temperature after the He^+ or H_2 ion implantation and relies on a mechanical force causing the exfoliation rather than a thermally induced delamination [8], [9]. Here, we will report our progress on expanding on these techniques to ultimately achieve cold-ion splitting of (010) β-Ga_2O_3.

UID (010) β-Ga_2O_3 substrates from NCT were implanted with He+ ions at an energy of 160 keV and a dose of 5×10^{16} cm^{-2} with a resulting implant depth of ~600 nm following reference [4]. A BCl_3 plasma (800 W ICP, 60W RIE, 5 mTorr, 40 sccm) was used to etch ~1 μm of the β-Ga_2O_3 creating mesas for device-level exfoliation future micro-transfer printing testing [10]. A PECVD SiO_2 mask was used for the etch and the remaining SiO_2 was left on top of the mesas during annealing, which took place on a calibrated hotplate. Blanket-implant samples without the SiO_2 were also annealed and used for X-ray Diffraction (XRD) measurements. Liao, et al., showed that strain in the lattice due to the implanted He ions could be observed in oscillations in the symmetric (020) ω:2θ XRD scans. After annealing and visible blistering of the implanted He layer these oscillations were no longer seen in the XRD scans due to the relaxation of the latttice [4]. With the blanket He-implanted (010) β-Ga_2O_3 samples, symmetric (020) ω:2θ XRD scans were measured after anneals with increasing temperatures. Figure 1 shows that after annealing at 500ºC for 1 hour, oscillations are no longer observed in the XRD scan, but in Fig. 2 (left image) no blisters are visible in the Normarski microscope image of the sample. After 5 total hours of annealing at 500ºC, blisters are observed in the microscope image (fig. 2 middle) and full blistering of the sample is shown in fig. 2 (right) after an additional 1 hour covered in Al foil at 500ºC. Atomic force microscope (AFM) images were performed on the sample after the first notice of blistering (after 500ºC for 5 hours). The AFM image of the center of the sample (Fig. 3 center), where there are no visible blisters, does possibly indicate the formation of He bubbles forming within the implanted region when compared to AFM image of the visibly blistered surface (left) and of an implanted sample without annealing (right). With additional annealing experiments, we plan to optimize this approach to achieve minimial blistering and transferring of thin (010) β-Ga_2O_3 mesas.

[1] Y. Song et al., ACS Appl Mater Interfaces, vol. 13, no. 34, pp. 40817–40829, Sep. 2021.
[2] J. Montes et al., Appl Phys Lett, vol. 114, no. 16, Apr. 2019.
[3] Y. Zhang, Q. Su, J. Zhu, S. Koirala, S. J. Koester, and X. Wang, Appl Phys Lett, vol. 116, no. 20, May 2020.
[4] M. E. Liao et al, ECS Journal of Solid State Science and Technology, vol. 8, no. 11, pp. P673–P676, 2019.
[5] M. E. Liao et al, Journal of Vacuum Science & Technology A, vol. 41, no. 6, Dec. 2023.
[6] M. E. Liao et al., ECS Trans, vol. 112, no. 3, pp. 269–278, Sep. 2023.
[7] Z. Cheng et al., ACS Appl Mater Interfaces, vol. 12, no. 40, pp. 44943–44951, Oct. 2020.
[8] K. Henttinen, I. Suni, and S. S. Lau, Appl Phys Lett, vol. 76, no. 17, p. 2370, 2000.
[9] K. Henttinen et al., Nuclear Instruments and Methods in Physics Research B, vol. 190, pp. 761–766, 2002.
[10] B. P. Downey et al., IEEE Transactions on Electron Devices , vol. 70, no. 6, pp. 2994–3000, Jun. 2023.

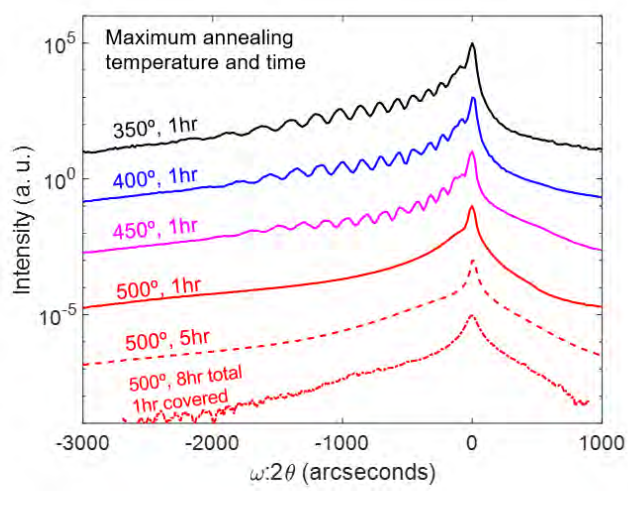

Fig 1. ω:2θ X-ray Diffraction (XRD) scans of the annealed, He-implanted (010) β-Ga_2O_3 substrate. The fringes in the scans correspond to the strain in the lattice due to the He-implant. Up to 450ºC, the strain is still visible. At 500ºC for 1 hour, the fringes go away, but blistering is not observed on the surface of the sample. Blistering was first observed after 5 hours of annealing at 500 ºC.

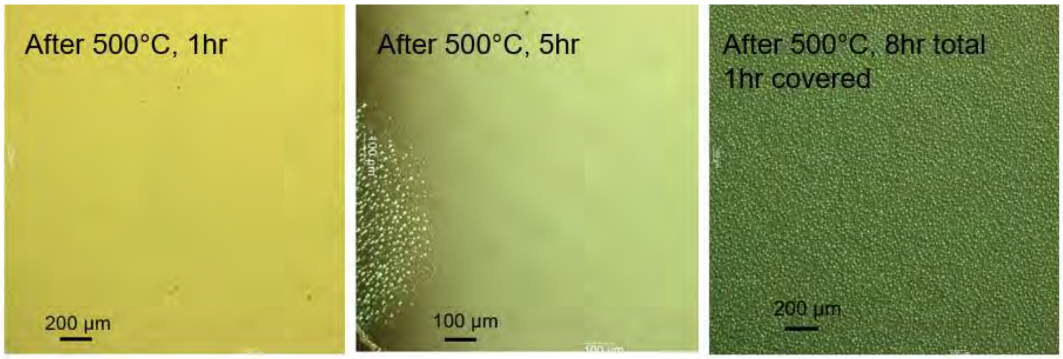

Fig. 2. Nomarski microscope images of the sample after annealing at 500 ºC, (from left to right) after 1 hour, after 5 hours when blistering is observed, and after 8 total hours of annealing (1 hour sample covered by Al foil) where the sample is fully blistered.

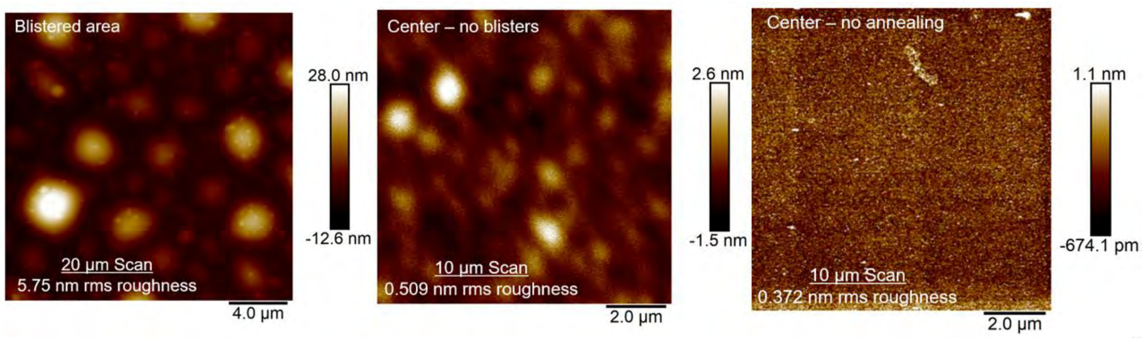

Fig. 3. Left and middle atomic force microscope (AFM) images are taken from the same sample (after 500 ºC for 5 hours) showing the visibly blistered area (left) and the center of the sample with no visible (by microscopy) blisters (middle). The middle image does show the formation of bubbles under the surface. The right AFM image is taken from an implanted sample with no high temperature annealing showing a smooth surface and no He bubble formation.

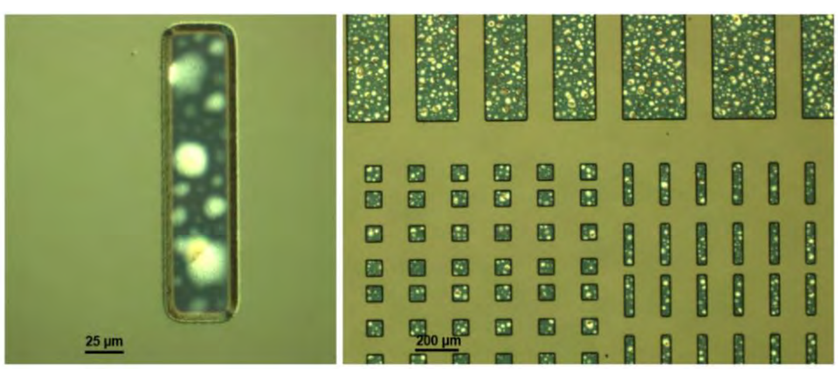

Fig. 4. Nomarski microscope images of the blistered etched mesas after annealing for 12 hours at 200 ºC and then 1 hour at 500 ºC covered.

10. Vertical β-Ga_2O_3 Schottky barrier diodes with in situ Nitrogen co-doped epitaxial layer

The high critical field of β-Ga_2O_3, estimated to be about 6-8 MV/cm, has motivated significant research into vertical power switching devices based on this semiconductor. In any vertical power device, the electric field profile in reverse bias is determined by the doping density of the drift layer. It is preferable that this doping density is low for high breakdown voltage; however, low-doped drift layers must be of appropriate thickness in order to obtain reasonable on state resistance. In β-Ga_2O_3, the halide vapor phase epitaxy (HVPE) method has been demonstrated to yield high quality, low-doped (10^{15}-10^{16} cm^{-3}) electron concentration via Silicon doping. While p-type doping has shown to be challenging in β-Ga_2O_3, deep acceptor dopants, especially Nitrogen, have been useful in forming highly resistive β-Ga_2O_3 films, either through ion implantation[1] or in-situ co-doped epitaxy [2]–[4]. In this work, we experimented with additional thin layer of Nitrogen co-doped HVPE β-Ga_2O_3 as this approach may be beneficial in improving the reverse-bias characteristics of vertical β-Ga_2O_3 devices.

Using 2-inch (001) β-Ga_2O_3 Sn-doped substrates, a 10 µm thick UID β-Ga_2O_3 was grown using halide vapor phase epitaxy (HVPE) with a carrier concentration (N_d-N_a) of ~1×10^{16} cm^{-3} measured by electrochemical capacitance-voltage (ECV) technique. The samples were then polished before HVPE was used again to grow the N co-doped β-Ga_2O_3 layer. The resulting N co-doped epilayer thicknesses for the two samples discussed here are ~200 nm (sample A) and ~490 nm (sample B). The thin N co-doped epilayers were not polished via chemical mechanical polishing (CMP) after the second HVPE growth step; this resulted in the facets shown in the atomic forced microscope image shown in Fig. 2. The backside Ohmic contact was formed by a blanket electron beam (e-beam) evaporation of Ti/Au (20/200nm) metal stack. Top-side circular contacts (500 µm diameter) were formed by e-beam evaporation of Ti/Au (20/200nm) using a 500 µm diameter shadow mask on half of the sample area. The samples were then annealed at 470 ºC in N_2 for 1 minute. On the other half of each sample, Schottky anodes were deposited with the same shadow mask and with an e-beam evaporation of Ni/Au (20/200 nm). The cross-sectional schematics of both samples are shown in Fig. 1. Current density-voltage (*J-V*) characteristics of the vertical Schottky diodes are shown in Fig. 3. Both samples exhibited a low reverse leakage current of <10^{-7} A/cm^2 up to a reverse bias of -20 V. The thinner N co-doped epilayer in sample A resulted in a $10^3\times$ higher forward current compared to sample B. The *J-V* characteristics of a referenced HVPE β-Ga_2O_3 Schottky diode is also shown in Fig. 3; while the reference diode shows higher forward current due to the absence of the N co-doped epilayer, higher reverse leakage is also observed. Breakdown testing of these samples will be performed with properly field terminated diodes. The leakage current in the N co-doped epilayer was also investigated by measuring neighboring Ti/Au anodes (Fig. 4). Low leakage was observed in the thicker N co-doped epilayer sample, while the 200 nm N co-doped epilayer was not able to block current in this lateral measurement. The inset of Fig. 4 shows that non-linear ohmic contacts were made to the N co-doped β-Ga_2O_3 layer. More analysis will be performed to determine if the leakage is due to the thickness or possible defects in the N co-doped epilayer. The N concentration will be determined by secondary ion mass spectroscopy (SIMS). The net doping concentration (N_D-N_A) in the N co-doped epilayers will be estimated from low-frequency capacitance-voltage measurements of the fabricated Schottky diodes. In Fig. 5, X-ray diffraction (XRD) ω scans of the (001) symmetric reflection for both samples show high crystal quality of the epilayers.

[1] M. H. Wong *et al.*, *Appl Phys Lett*, vol. 113, no. 10, Sep. 2018. [2] T. Kamimura, Y. Nakata, M. H. Wong, and M. Higashiwaki, *IEEE Electron Device Letters*, vol. 40, no. 7, pp. 1064–1067, Jul. 2019. [3] D. Wakimoto, C. H. Lin, Q. T. Thieu, H. Miyamoto, K. Sasaki, and A. Kuramata, *Applied Physics Express*, vol. 16, no. 3, Mar. 2023. [4] M. J. Tadjer *et al.*, *Appl Phys Lett*, vol. 113, no. 19, Nov. 2018.

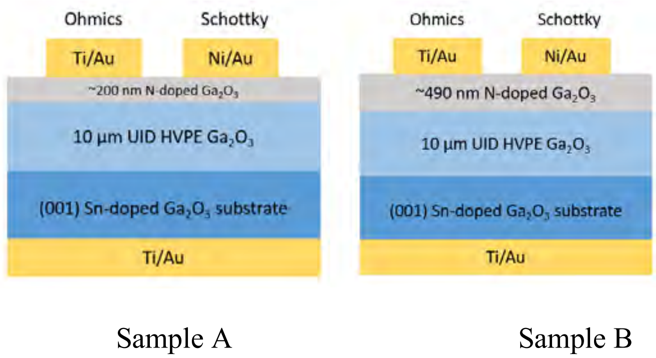

Fig. 1. Cross-sectional schematics of the HVPE Ga_2O_3 stacks with Ti/Au backside contact and Ti/Au (ohmic) and Ni/Au (Schottky) contacts formed with a shadow mask.

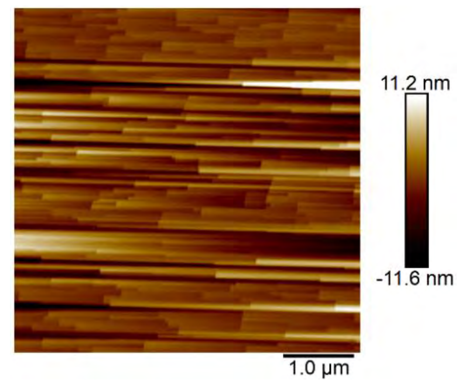

Fig. 2. Atomic force microscopy (AFM) image of the N co-doped epilayer Ga_2O_3 surface. No chemical mechanical polishing was performed on the surface to maintain the N co-doped layer thickness. RMS roughness was measured to be 3.03 nm.

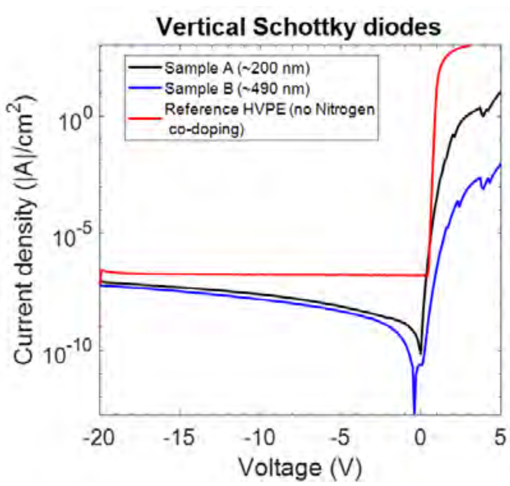

Fig. 3. *J-V* of vertical Schottky diodes for both samples. Sample A with the thinner N co-doped layer showed 3 orders of magnitude higher forward current, and both samples showed similar reverse current of < 10^{-7} A/cm^2. A reference HVPE vertical Schottky diode is shown in red. Much higher forward current is observed due to the lack of N co-doping, but reverse current of the reference diode is also higher.

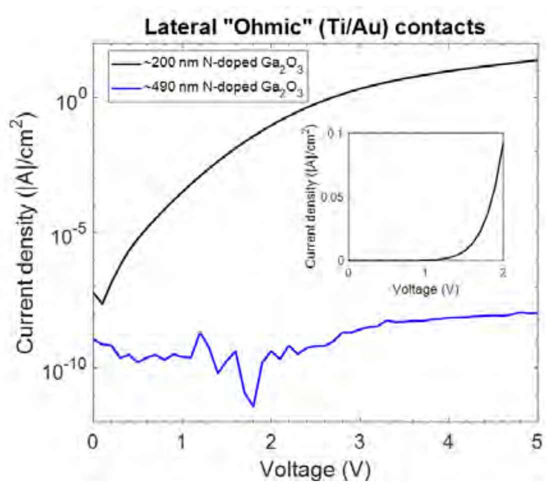

Fig. 4. *J-V* of lateral “ohmic’ to “ohmic” contact measurements. The inset shows the linear *J-V* of sample A. While the Ti/Au did not form a true ohmic contact to the N co-doped Ga_2O_3, current is able to flow either through the thin N co-doped layer or through the UID epi-layer. Sample B saw minimal current conduction through the lateral “ohmics” due to the thicker N co-doped layer.

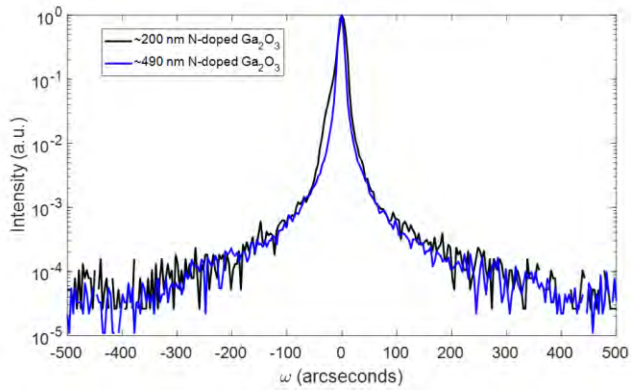

Fig. 5. ω X-ray diffraction scans of (001) symmetric reflection peak for Sample A and B. Full width half maximum was ~12.6 and 10 arcseconds for sample A and B, respectively.

11. Method for Eliminating Thermal Expansion Anisotropy in β-Ga_2O_3

Due to its low-symmetry monoclinic crystal structure, various properties of β-Ga_2O_3 exhibit a high degree of anisotropy. In the context of materials integration processing, anisotropy in the coefficients of thermal expansion (CTE) can introduce thermal-strain challenges. Our previous work measured the CTE of β-Ga_2O_3 and calculated thermal strain of various β-Ga_2O_3 heterostructures [1]. For all heterostructure combinations with (100), (010), (001), or $(\bar{2}01)$ β-Ga_2O_3, the magnitude of thermal strain due to CTE differences varies along different in-plane directions. Furthermore, some heterostructure combinations resulted in simultaneous tensile and compressive thermal strain.

Amidst the complexity of its crystal structure, we discovered a unique high-index plane in β-Ga_2O_3 that exhibits isotropic in-plane CTE. The surface normal of this orientation is parallel to the [13 31 13] direction and has an isotropic in-plane CTE of ~6.55 × 10^{-6} K^{-1}. If integrated with an isotropic material (e.g., Si, diamond, c-plane GaN/AlN/SiC), the resulting thermal strain would be uniform and of the same type (either tensile or compressive only). For example, if (010) β-Ga_2O_3 where bonded to (0001) AlN at room temperature then brought up to 600 °C for subsequent β-Ga_2O_3 homoepitaxy [2], the thermal strain would vary from -1400 ppm (compressive) to +700 ppm (tensile). In contrast, the thermal strain of this unique isotropic β-Ga_2O_3 plane on (0001) AlN under the same conditions would be uniformly -1400 ppm. Optimizations of various heterostructures and orientations of β-Ga_2O_3 that minimize the integrated thermal strain will be discussed, which will cover solutions involving the best theoretical orientations of β-Ga_2O_3 and solutions restricted by commercially available orientations. The methodology of finding the isotropic plane will be focused on thermal expansion and β-Ga_2O_3, but we demonstrate that our method applies to any second-rank tensor material property [3,4] as well as any crystalline material including the lowest-symmetry triclinic crystal structure.

References:
[1] M. E. Liao, et al., APL Mater., 7, 022517 (2019).
[2] Y. Song, et al., ACS Appl. Mater. Interfaces, 15, 7137 (2023).
[3] P. Jiang, et al., Appl. Phys. Lett., 113, 232105 (2018).
[4] C. Sturm, et al., APL Mater., 3, 106106 (2015).

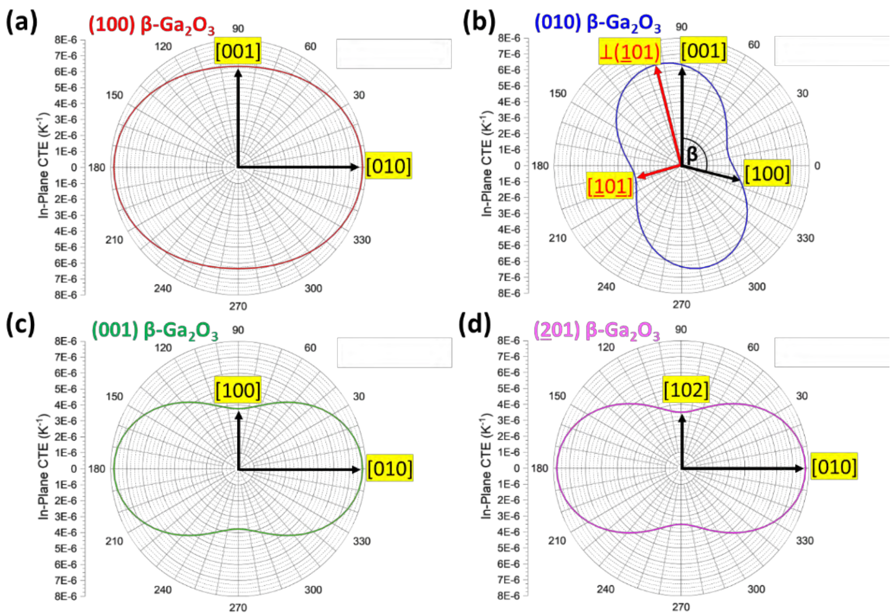

Fig. 1 In-plane coefficients of thermal expansion (CTE) profiles for commercially available β-Ga_2O_3 substrates: (a) (100), (b) (010), (c) (001), and (d) ($\bar{2}01$). The CTE variation ranges from ~20% for (001) to ~50% for (010).

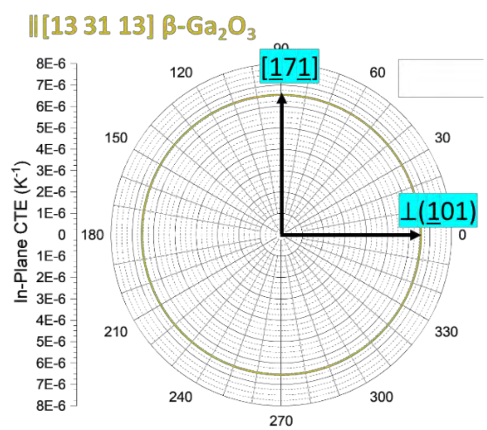

Fig. 2 In-plane CTE profile for the unique high-index isotropic plane whose surface normal is parallel to the [13 31 13] lattice direction. The CTE is ~6.55 × 10^{-6} K^{-1} for all in-plane directions.

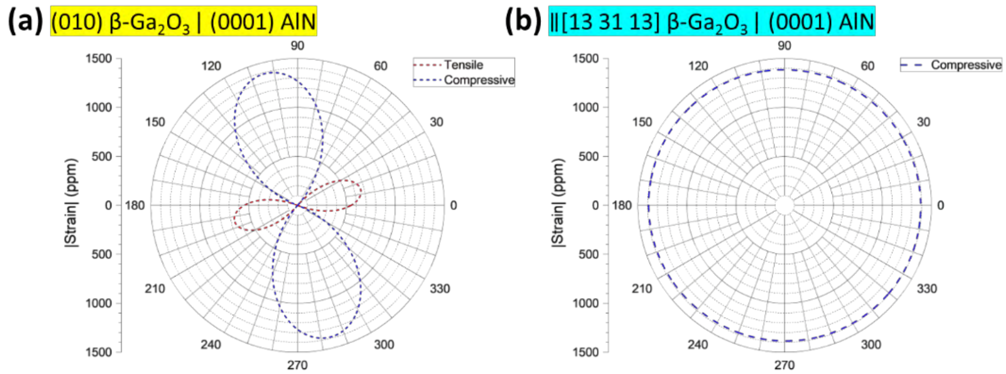

Fig. 3 Thermal strain profile from 20 °C to 600 °C for (a) (010) β-Ga_2O_3 and (b) isotropic β-Ga_2O_3 both integrated with (0001) AlN (e.g., annealing after room-temperature wafer bonding). Red indicates tensile strain while blue indicates compressive strain.

3. Findings and Conclusions

A number of fundamental studies in Ga_2O_3 were carried out addressing challenges for Ga_2O_3 based electronics. For MOCVD Ga_2O_3 homoepitaxy on EFG substrates provided by Novel Crystal Technology, we have detailed for the first time extended defects in thick epilayers and also the effect of buffer thickness on electrical and thermal performance of thin UID MOCVD epilayers. In thin heteroepitaxial AlGaO, we have detailed critical thickness limitations governed by crystal fracture theory (Griffith criterion), and also demonstrated HFET devices capped with diamond based on this technology. We have further shown a novel sub-gap wavelength transient thermoreflectance approach for noninvasive thermal mapping due to a detectable enhancement in reflectivity near 480 nm in these structures. The low thermal conductivity of Ga_2O_3 is a challenge particularly for lateral devices which must be mitigated via high thermal conductivity material integration, such as diamond. Furthermore, thermal conductivity anisotropy complicates integration with any isotropic high thermal conductivity materials. NRL has carried out comprehensive calculations and identified a high index plane along which any second tensor quantity, including thermal conductivity, is uniform. Experimental verification is pending using Novel Crystal Technology twin-free EFG crystal. Another approach via wafer bonding to Silicon Carbide has been studied using a direct bonding technique and a novel cold-split technique is under additional research using patterned He-implanted samples from Novel Crystal. We have developed a self-aligned JBS diode process integrating p-type NiO and further demonstrated 1 kV JBS diodes.

4. Plans and Upcoming Events

In CY2024, the remaining deliverables from the program will be delivered to NRL, and any pending conference presentations and journal publications will be disseminated upon competing the publication clearance process.

5. Transitions and Impacts

The current and prior NICOPs with Novel Crystal Technology have supported internal research at NRL in the field of Ga_2O_3 for several years now. The prior NICOP has impacted almost every research publication on Ga2O3 at NRL in the 2016-2024 period, and we expect research under the present NICOP to elevate Ga_2O_3 technology to TRL 4 where transition opportunities can be identified.

6. Collaborations

Agency/Org	Performer	Project Name	Purpose of Research/ Collaboration
ONR	Capt. Lynn Petersen	Homoepitaxial Ga_2O_3 Structures for Power Device Applications	Program Co-sponsor
ONR Global	Richard Yamada	Homoepitaxial Ga_2O_3 Structures for Power Device Applications	Program Co-sponsor
ARL	Aivars Lelis, Tim Leong	Homoepitaxial Ga_2O_3 Structures for Power Device Applications	Program Co-sponsor (year 3 only)

7. Personnel

Principal investigator: Akito Kuramata
Business Contact: +81-4-2900-0072, kuramata@novelcrystal.co.jp
Novel Crystal Technology, Inc., 2-3-1 Hirosedai, Sayama, Saitama, 350-1328, Japan
Team Members: Kohei Sasaki

8. Students

Not applicable.

9. Technology Transfer

Not applicable.

10. Products, Publications, Patents, License Agreements, etc.

Publications resulting from this project:

<u>Archival Publications</u>

a. Experimental determination of critical thickness limitations of (010) β-$(Al_xGa_{1-x})_2O_3$ heteroepitaxial films
b. Applied Physics Letters
c. James Spencer Lundh, Kenny Huynh, Michael Liao, William Olsen, Kaicheng Pan, Kohei Sasaki, Keita Konishi, Hannah N Masten, Jennifer K Hite, Michael A Mastro, Nadeemullah A Mahadik, Mark Goorsky, Akito Kuramata, Karl D Hobart, Travis J Anderson, Marko J Tadjer
d. Gallium oxide, aluminum gallium oxide, heteroepitaxy, critical thickness
e. Distribution Statement A: Approved for public release. Distribution unlimited.
f. Published
g. DOI
h. 10.1063/5.0174682
i. 27 November 2023

j. Volume 123
k. n/a
l. First Page Number 222204
m. American Institute of Physics: https://doi.org/10.1063/5.0174682
n. Acknowledgement of Federal Support? Yes
o. Peer Reviewed? Yes

a. Assessment of channel temperature in β-(Al_xGa_{1-x})$_2O_3$/Ga_2O_3 heterostructure field-effect transistors using visible wavelength thermoreflectance thermal imaging
b. Applied Physics Letters
c. James Spencer Lundh, Georges Pavlidis, Kohei Sasaki, Andrea Centrone, Joseph A. Spencer, Hannah N. Masten, Marc Currie, Alan G. Jacobs, Keita Konishi, Akito Kuramata, Karl D. Hobart, Travis J. Anderson, Marko J. Tadjer
d. Gallium oxide, aluminum gallium oxide, thermoreflectance
e. Distribution Statement A: Approved for public release. Distribution unlimited.
f. Published
g. DOI
h. 10.1063/5.0177609
i. 31 January 2024
j. Volume 124
k. n/a
l. First Page Number 054103
m. American Institute of Physics: https://doi.org/10.1063/5.0177609
n. Acknowledgement of Federal Support? Yes
o. Peer Reviewed? Yes

11. Point of Contact in Navy

None

ONR Industry contracts

Implementation of tunable dielectric and multiferroic materials for high power microwave applications

Grant No. N00014-22-1-2694

Annual Report for Fiscal Year 2023

Period of Performance: 1 October 2022 to 30 September 2023

Prepared by:
Dr. Somnath Sengupta, Principal Investigator
Powerhouse Consulting Group
Tel: (443) 820-7798
Email: somnath@powerhouseconsultinggroup.com

This work was sponsored by the Office of Naval Research (ONR), under contract number N00014-22-1-2694. The views and conclusions contained herein are those of the authors only and should not be interpreted as representing those of ONR, the U.S. Navy or the U.S. Government.

Grant or Contract Number: N00014-22-1-2694
Date Prepared: January 31, 2024
Project Title: Implementation of tunable dielectric and multiferroic materials for high power microwave applications
Annual Summary Report: FY23 execution period, 1 October 2022 to 30 September 2023
Principle Investigator: Somnath Sengupta, 443 820 7798; somnath@powerhouseconsultinggroup.com; Powerhouse Consulting Group; Small Business

Section I: Project Summary

1. Overview of Project

Based on our accomplishments in the previous phase of demonstrating the scalability of the tunable dielectric materials developed by Powerhouse, this annual report describes the objective for the current phase of the work performed in the period of 1 October 2022 to 30 September 2023. The current contract completion date is March 31, 2024.

The **goals** of the current phase of work include (a) development and testing of tunable delay lines from the novel dielectric materials assessed and scaled in the previous phases and (b) evaluate multiferroic materials for implementation into an electromagnetic delay line.

For the first goal the approach includes the two-tone high RF incident power testing to determine the intermodulation products and thermal effect, pulsed modulated high-power testing of tunable dielectric materials, and then fabrication and measurement of delay designed from the materials tested for high RF power handling. The testing of the delay lines was to be performed by Naval Research Laboratory. The **key technology advancement/payoff** for this part of the work is to develop a capability with the ability to fine-tune delays that allows the creation of different waveforms on target due to pre-designed constructive and destructive interference, including allowing electronic beam steering for UWB arrays.; *all at high incident RF peak power*. To our knowledge, such tunable delay lines at high RF power have not been demonstrated for high power microwave (HPM) applications.

For the second goal the approach includes the synthesis and characterization of multiferroic materials, design and fabrication of delay line, and delay measurements. two-tone high RF incident power testing to determine the intermodulation products and thermal effect, pulsed modulated high-power testing of tunable dielectric materials, and then fabrication and measurement of delay designed from the materials tested for high RF power handling. The measurements of these delay lines were to be performed by NSWCDD. The **key technology advancement /payoff** part of this work is to develop the flexible capability to tune either the magnetic or the dielectric part of the material while providing the system to evaluate which method is optimal for their implementation and increase power handling capability over traditional ferromagnetic-based delay lines. To our knowledge, this capability currently does not exist for HPM applications, and can benefit many current ONR programs.

2. Activities and Accomplishments

For Task 1.

Figure 1 shows the results of the high pulsed power measurements. The sample was subjected to two different levels pulsed power and no damage was observed. Furthermore, the waveform integrity (output to input) was maintained during these measurements (**Figure 2**).

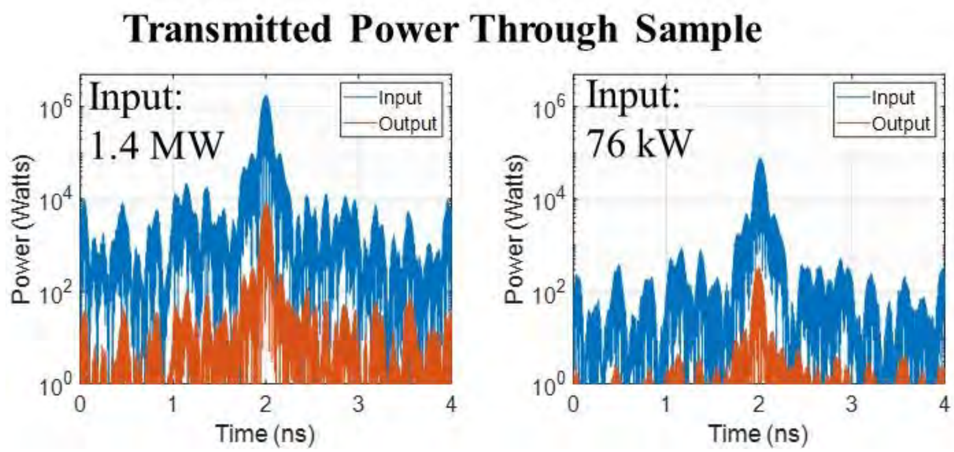

Figure 1. Sample has no damage or break down from the MW input power

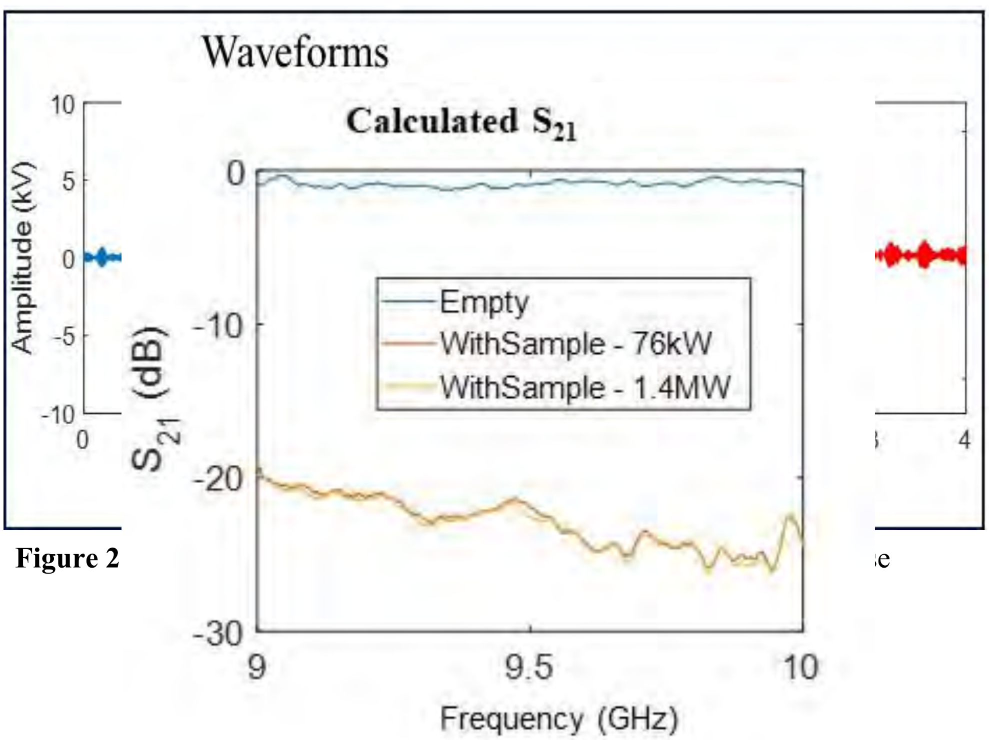

Figure 2

Figure 3. The S_{21} parameter values show that the material's intrinsic properties are not altered by higher power levels

The calculated S_{21} parameter for both power levels (**Figure 3**) were the same showing that the transmission of the pulse through the material was not different for a kW or a MW level thus providing a design advantage for high power delay lines. Previous low power S_{21} measurements show that our simulations at higher powers are reliable.

As for the fabrication of the delay lines, **Figure 4** shows the quarter wave impedance matched simulation for a wave guide delay line in X band. The full wave simulator of the CST Microwave Studio was used for this work. A previous work on antenna development was utilized for material parameter inputs.[10] The excitation frequency was in X band. A dielectric constant of 100 with matching sections at 30s and 3s, the simulation showed low absorption across the entire band and low dispersion in the signal.

It must be emphasized that the S parameter magnitudes will be impacted by the material loss at X band. The nominal material loss at X band is about 0.02. Previous work with these materials (Reference 1) has shown that the insertion loss for the antennas was about 2 to 2.5 dB at X bands.

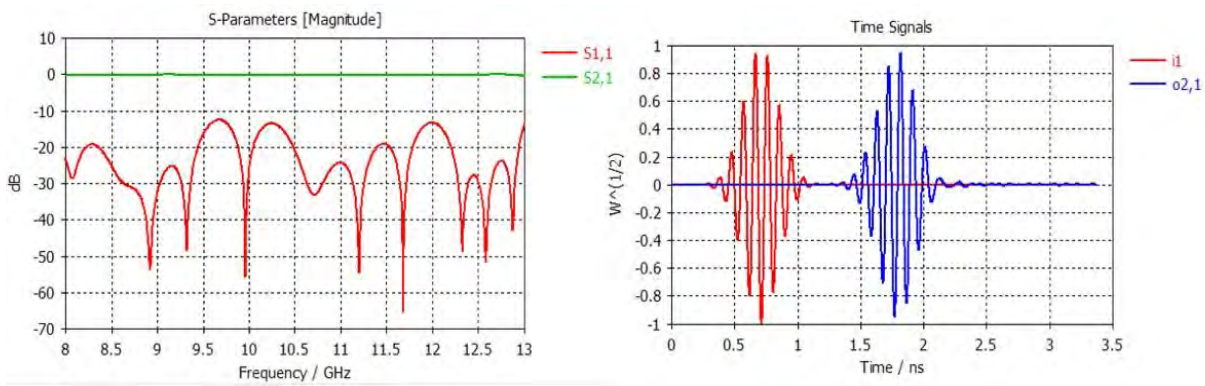

Figure 4. Our full wave simulation with the dielectric material properties showed low absorption and low dispersion across the full X band

A simulation was also performed for the group delay performance of the design (**Figure 5**). The simulation showed that the delay decreases with the lesser dielectric constant of the material; *in other words, once can electrically tune the dielectric material to reduce its dielectric constant to alter the overall delay thereby creating a continuously tunable delay line for high power RF applications.*

---

[10] Rao, Jaganmohan BL, Dharmesh P. Patel, and Vladimir Krichevsky. "Voltage-controlled ferroelectric lens phased arrays." *IEEE Transactions on Antennas and Propagation* 47.3 (1999): 458-468.

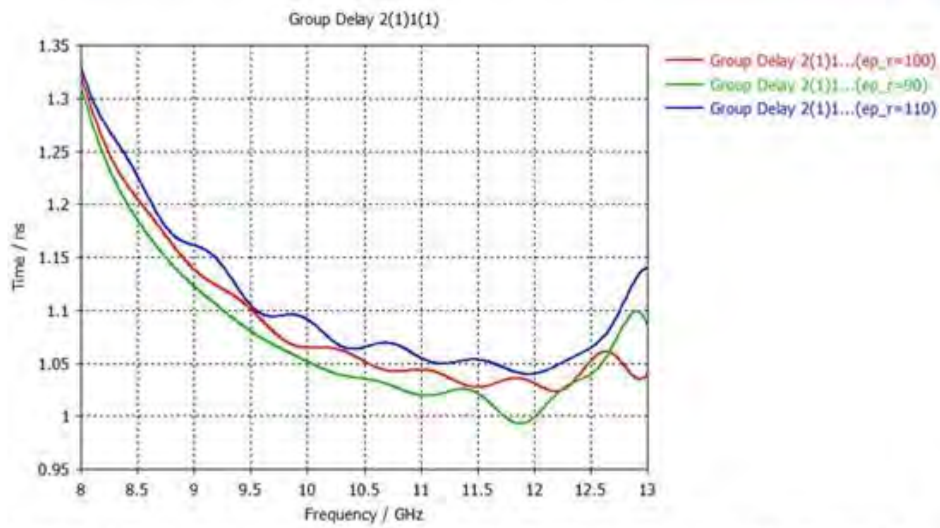

Figure 5. Group delay can be continuously changed with change in dielectric constant by applying a DC voltage on the material

Powerhouse has delivered multiple pieces of their materials and their matching sections for NRL to assemble and test a waveguide delay line. The work continues at NRL. Meanwhile Powerhouse has measured a coaxial delay line and are in the midst of measuring the delay as an alternate path for delay line demonstration. The results of both sets of delay lines will be presented in the next annual report.

As for the Task 2 regarding multiferroics, our accomplishments include:

The activities and accomplishments for this task include the synthesis of a number of multiferroic materials, working with Professor Garner at Purdue and Professor Wetz at UT to collect data collaboratively an provide NSWCDD with data for their decisions.

The synthesis of the toroid of multiferroic materials and its machining process were developed at Powerhouse and then the knowledge was shared with the UT group graduate students. The multiferroics consisted of barium strontium titanate (BST; the dielectric part) and ferrites like Barium Hexaferrite ($BaFe_2O_{19}$), Magnesium Ferrite ($MgFe_2O_4$), and yttrium iron oxide ($Y_3Fe_5O_{12}$; YIG)). The results of their Xray diffraction and other material properties have been discussed in earlier reports. One important task was to establish some sense of repeatability of sample fabrication. As such, Powerhouse and Dr. Wetz's team collected data on YIG samples fabricated over the past 4+ months to determine how close they are in their dielectric (**Figure 6**) and magnetic measurements (**Figure 7**). From the data of Figure 7, we learned that repeatability of the multiferroic materials may not be an overall issue if we identify the correct sintering temperatures to attain the material properties. These materials have been supplied to NSWCDD along with the multiferroic samples of BST/$BaFe_2O_{19}$. The important premise of our multiferroic work is the presence of a magnetoelectric coupling coefficient without which we will require an electrical and a magnetic impulse to control the material which will make it use more driving power. The Magnesium Ferrite material based multiferroic was not pursued because it did not show measurable response of the coupling coefficient even after poling the material. As for the BST/BaFe samples, the sample showed a measurable magnetoelectric (ME) coupling (**Figure 8**). The ME response for this one was measurable across a wide frequency range and shows about a 0.72% change in capacitance as well.

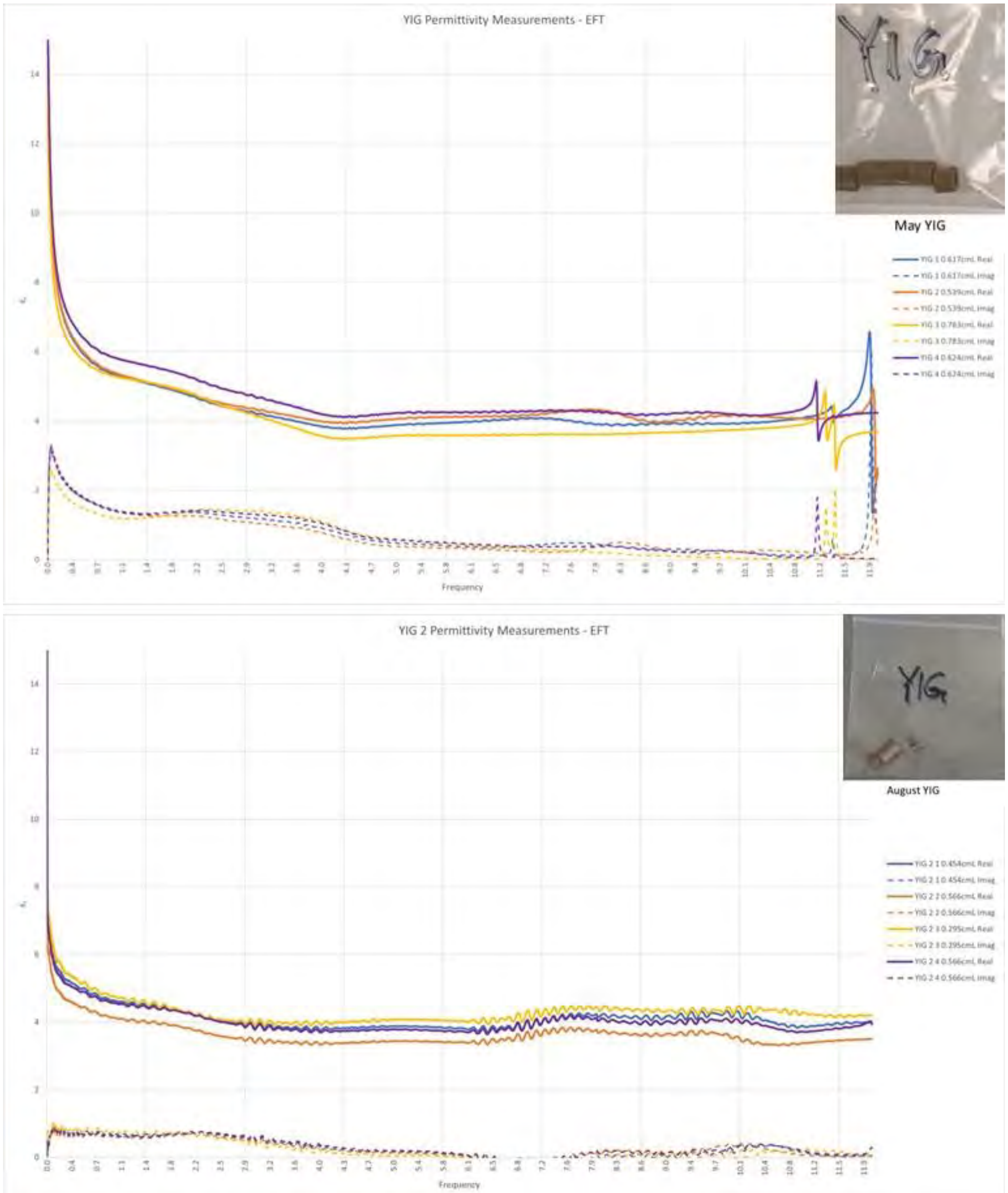

Figure 6. When redrawn in the same y-axis scales, the real part of epsilon seems to match; the May sample sintered at a lower temperature) seems be more lossy; the x-axis is frequency

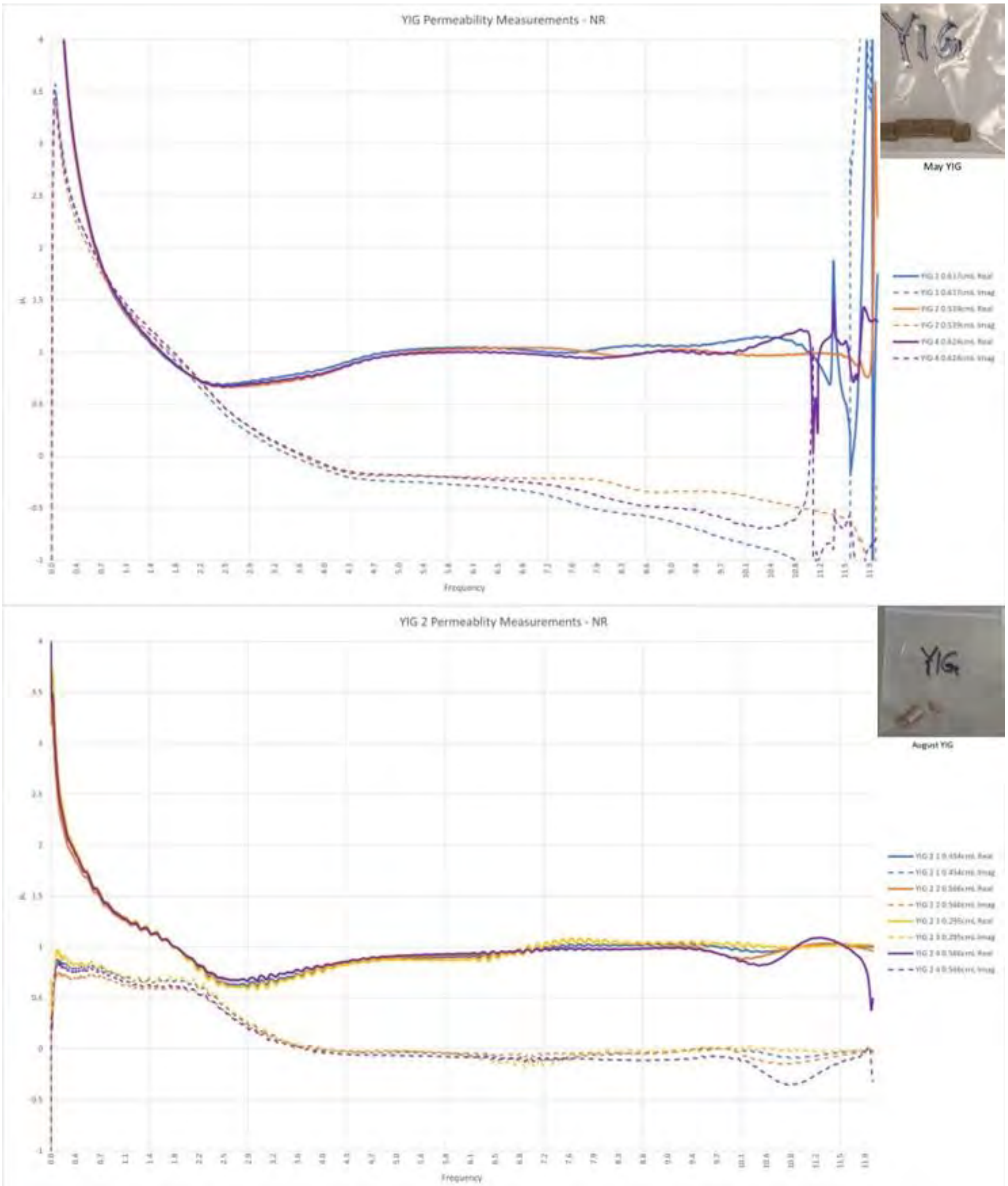

Figure 7. When redrawn in the same y-axis scales, the real part of permeability seems to match; the May sample (sintered at a lower temperature) seems be more lossy though. The x-axis is frequency

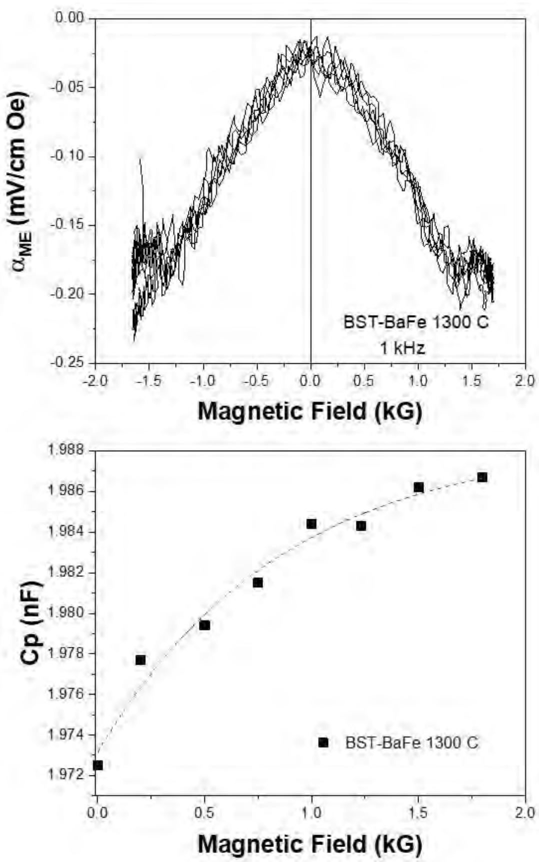

Figure 8. BST/BaFe samples showed measurable magnetoelectric response

3. Findings and Conclusions

With regards to the dielectric material-based work, all aspects of the work in the period of reporting have shown that we will build and demonstrate a tunable delay line that will provide a ***significantly enhanced*** capability of signal generation for the pulse generator. As for the multiferroic work, we have demonstrated that we can synthesize materials whose electrical and magnetic properties can both be controlled by applying voltage and current. This leads to the design of devices where wave propagation can be controlled through electrical and magnetic path delays.

4. Plans and Upcoming Events

- Complete the measurement of delay and its tunability @ NRL
- Complete the design of delay lines using multiferroics @ NSWCDD

Recommendations for Future Work: Since we have demonstrated coaxial delay for the dielectric materials, we would suggest that we proceed to fabricate multiple coaxial delay lines from our tunable materials and implement them with a pulse generator to demonstrate waveform generation. Meanwhile we would have completed the testing of the multiferroics which can then lead us to dovetail those materials into the coaxial design for pulse generator demonstration too.

5. Transitions and Impacts

Please see write up for future work above. It is related directly to transitioning the capability for an application for the Navy.

6. Collaborations

Powerhouse has collaborated with government laboratories at all levels- from material characterization to determining system applications. The following is a summary of the interactions:

1. NRL High Power Microwave Section, Code 5745 (Drikas). The Code 5745 HPM team will be submitting a proposal to ONR for evaluating Powerhouse's tunable dielectric materials for tunable delay line applications for wideband pulse generation

2. NRL Advanced Materials Section, Code 6127 (Laskoski). Powerhouse performs the RF material characterization in collaboration with Dr. Laskoski's team. The thick film capability is also being developed in collaboration with Dr. Laskoski.

3. NSWCDD E13, HPM Technology Development Branch (Fairbanks). Dr. Fairbanks will utilize the magnetodielectric tunable materials for his applications in delay lines if we are awarded a follow-on contract.

7. Personnel

Principal investigator: Somnath Sengupta
Business Contact: Somnath Sengupta

8. Students

This program was utilized to train adults with autism on sustainable high technology laboratory skills. It is our hope that we will continue to develop cutting edge science and technology for the Navy while impacting employment for this underrepresented group.

9. Technology Transfer

Not Applicable

10. Products, Publications, Patents, License Agreements, etc.

Publications resulting from this project:
Not Applicable.

11. Point of Contact in Navy

Dr. Tim Andreadis; Code 5745; Naval Research Laboratory. Last Contact: January, 2024
Dr. Zachary Drikas; Code 5745; Naval Research Laboratory. Last Contact: January, 2024.
Dr. Andrew Fairbanks; Naval Surface Warfare Center - Dahlgren Division. Last Contact: January, 2024
Dr. Matthew Laskoski, Code 6127; Naval Research Laboratory. Last Contact: January, 2024.

ONR Grants new starts

Grant or Contract Number: N00014-23-1-2801
Project Title: Enhanced free recovery for Kilohertz operation of spark gaps.
Period of Performance: 1 August 2023 to 30 September 2023
Principle Investigator: Jane Lehr
Organization: University of New Mexico

Project Summary

Major Goals & Objectives: High power radiofrequency (HPRF) systems capable of operating at a high pulse repetition rate (PRR) have operational advantages including depositing more energy on targets even with moving platforms. Tesla transformer-based modulators are of interest because of their compact size and the potential of using folded energy lines for further reductions in size and weight. Their full potential is not yet realized because of the PRR limitations imposed by the spark gap on the Tesla's secondary. The goal is to repetitively operate spark gaps in a static pressure environment by investigating the enhancements to free dielectric recovery.

Accomplishments: The study of free dielectric recovery will be accomplished with two testbeds. One is a 50 kVDC single switch testbed, designed for flexibility which will enable quick screening of parameters. It is designed to operate with a single power supply and measure the recovery times corresponding to a 1 kHz PRR. The operation of the power supply requires a fairly low capacitance under these constraints. This first testbed is being fabricated. The other testbed is a Tesla transformer based one. This requires a high capacitance on the primary side and produces a high voltage on a much lower capacitance on the secondary side and is capable of both recovery time measurements and high PRR operation. While it is thought that the dielectric recovery time corresponds directly to the PRR, this has not been observed in realized systems. It is interesting to note that the charge time of the secondary is several microseconds at minimum. This means the time is essentially DC and should correspond directly to that of the single switch testbed. Auxiliary items such as digital pressure monitors have been constructed. High pressure spark gaps have been ordered from ASR and a high voltage switch will be borrowed for the Tesla transformer.

A detailed literature review has shown first a great variety of demonstrated PRR performance and that heat has long been suspected as a culprit in dielectric recovery. Heat is related to dielectric recovery through its relationship with the gas density. Interestingly, as repetitive pulse power became relevant for mission-oriented applications, the role of heat was forgotten and gas flow through the switch showed moderate PRRs. There are some thumb rules which are highly relevant: namely the high PRR capability with increasing pressure and small gaps. Several studies across a wide range of parameters indicate that dielectric recovery is largely independent of both gap length and transferred energy. This curious result has implications for the correlation between dielectric recovery and demonstrations of PRR which are impossible to evaluate from literature. An analysis was performed by first separating the breakdown processes into phases for modeling. The small effect of gap length is explained by the final breakdown phase. The energy deposited in the channel was estimated using the resistive time constant. This is the portion of the breakdown where the impedance of the switch decreases sufficiently to allow energy to flow. This expression increases sublinearly with the gas density and decreases superlinearly with electrical breakdown field. Since both gas density and electrical breakdown field vary with pressure, it is possible to look at channel expansion as the balance of the constrictive force of pressure with the expansive one of electric field. As the breakdown field for air is known, an expression was developed to look at the energy absorbed by the spark channel as a function of pressure. The result shows that less energy is absorbed in the spark channel with increased gas pressure, resulting in less heat and higher PRRs. This is a well-known observation. The mass density of hydrogen is much less than air so that higher PRRs are expected and may have little to do with the high speed of sound.

Supercritical fluids have interesting properties such as ultrahigh breakdown voltages and increase thermal conductivity. The properties of relevant switching gases are collected into a matrix for evaluation. Many gases have reasonable critical points in temperature and pressure.

A study on electrode profiles has begun to examine the variations with gap distance. A profile that enhances the surface area of the switch has been found which will distribute the arc over the surface to increase predictability and reduce erosion.

Grant or Contract Number: N00014-23-1-2305
Project Title: Novel HPM source topologies for high power microwave and millimeter wave generation
Period of Performance: 1 April 2023 to 30 September 2023
Principle Investigator: Jacob Stephens
Organization: Texas Tech University

Project Summary

Texas Tech began working on Grant # N00014-23-1-2305 on April 1, 2023. The primary objective of this research effort is to develop novel split-cavity oscillator designs that would enable the realization of a simplified HPM platform, requiring little to no external magnetic field, and minimal flat-top voltage requirements from the pulsed power driver. Simultaneously, this system should be able to generate 100s of MW of output power in the higher frequency ranges, beginning at X-band and exploring scaling into K-band and higher frequency. We are still in the first year of this effort and are thus far our progress is consistent with the timeline and schedule detailed in the original proposal. Our key successes thus far include 1) development of a simple pulse forming network (PFN) topology that will allow for a PFN-Marx generator system for testing the devices, 2) development of a space-charge wave model of device operation, and 3) development of a particle-in-cell (PIC) model of our SCO devices.

With regard to the PFN-Marx development, we have experimentally characterized various PFN topologies and based on this experimental study developed a complete design of our planned PFN-Marx system. Experimentally, we have designed a scaled version of this system, which is currently being fabricated. We anticipate completing characterization of the scaled model in the next two months, with the full fabrication to be completed by April 1.

Optimization of our SCO design via PIC simulation is ongoing. At present, we have achieved ~300 MW output power (in simulation), which included the output mode converter and window. We are currently developing a complete CAD model of this system and expect to begin fabrication soon. Consistent with the originally proposed timeline, we expect to conduct first tests this Spring.

Grant or Contract Number: N00014-23-1-2306, N00014-23-1-2282
Project Title: Elucidating Plasma Formation Near Dielectric Interfaces in High Power Microwave Systems
Period of Performance: 1 April 2023 to 30 September 2023
Principle Investigator: Thomas C. Underwood
Organization: University of Texas at Austin

Executive Summary: The first year of this project has focused on designing, characterizing, and fabricating diagnostics to probe plasma generation near dielectric interfaces in HPM systems. Efforts have been broken down into two independent thrusts, (1) to develop a microwave resonant cavity to simulate HPM breakdown near dielectrics and (2) to develop and test diagnostics to infer when and how plasmas form (including predicting their formation before microwave reflection occurs).

For thrust (1), we have configurated a microwave resonant cavity that can drive resonances, amplify field strengths locally (up to Q ~ 1000), and form plasmas close to surfaces. This reactor has been configured and we are awaiting delivery. We extended our design to include optically accessible test sections to probe the formation of plasmas near materials as well as circulators to protect our microwave amplifier from being damaged as power is reflected.

For thrust (2), we have developed and tested a hybrid THz-TDS architecture that can combine our single-shot

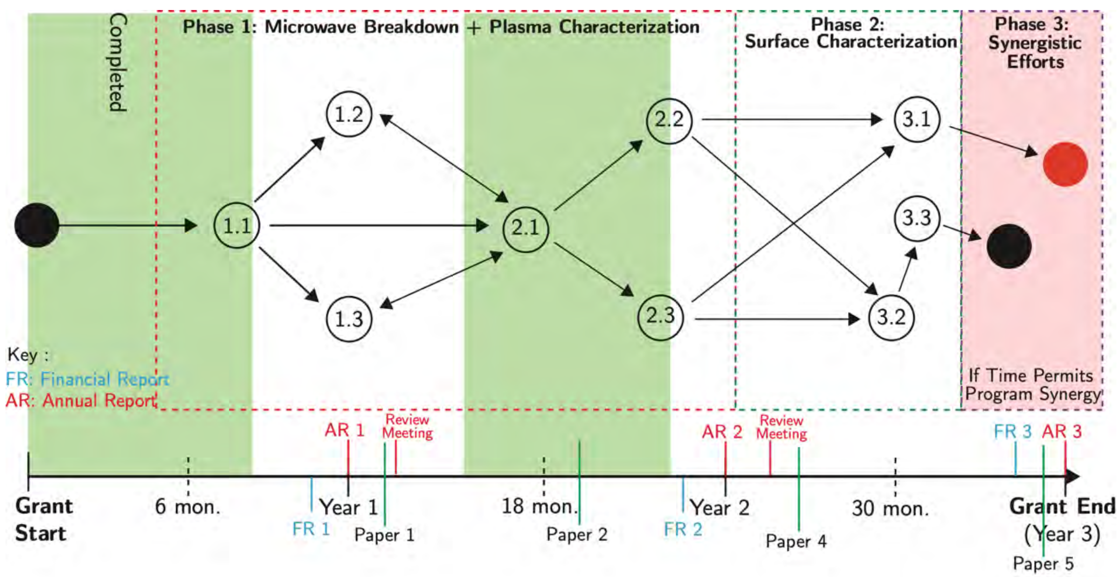

Figure 12. Project flowchart depicting deliverables and a breakdown of tasks. Efforts over the past month have focused on continued developing and validating plasma diagnostics related to THz spectroscopy (Task 2.1) as well as the design of the microwave cavity as equipment is procured, delivered, and installed. This fall will then focus on progressing in the generation of plasmas near dielectric surfaces in a resonant cavity (Task 1).

detection efforts with a delay-line approach. This setup has been used to validate the amplitude and phase of THz transmission in the time-domain (with time resolutions down to ~ 300 fs and repetition rates up to 500 kHz) and will ensure accurate quantification of plasma properties in HPM environments. We also developed a detection scheme using the single-shot approach that combines balanced and phase-resolved measurements to increase SNR, decrease the detection limits of plasma environments, and extend the

operation of the diagnostic to infer gaseous spectra near dielectric surfaces. Other diagnostic improvements include redesigning the optical layout to utilize phase-locked measurements in a single-shot scheme. Finally, we have used this diagnostic to measure RF plasma properties, including the density of free electrons, index of refraction, and some absorptive gas characteristics. Highlights of our progress include:

- Designed and configured a resonant cavity configuration to enable the circulation of amplified microwaves after plasms are generated. This will serve as a test bed to develop mechanistic understanding of HPM breakdown near surfaces.
- Developed a hybrid delay-line and single-shot THz-TDS scheme to validate measurement approaches.
- Extracted the amplitude and phase response of transmitted THz.
- Measured plasma properties using single-shot THz-TDS.
- Developed and validated a lock-in approach to single-shot THz-TDS to improve SNR and simulated plasma density and gaseous absorption spectra.
- Identified detection limits of plasma properties with this measurement approach in HPM environments.
- Improved THz signal strength and signal modulation depth of the single-shot approach.

Grant or Contract Number: N0001423WX00811
Project Title: Advanced Solid State Device Design, Development, and Demonstration (AS2D4) for Pulsed Power Applications
Period of Performance: 1 Dec 2022 to 30 September 2023
Principle Investigator and Organization: Andrew D. Koehler (U.S. Naval Research Laboratory) and Dr. Michael R. Hontz (Naval Surface Warfare Center Philadelphia)

Project Summary

The AS2D4 program this year demonstrated significant progress in developing a computer simulation-guided fabrication process for drift strep recovery diodes (DSRDs) and demonstrating a highly manufacturable, high performance DSRD fabrication process at the Defense Microelectronics Activity (DMEA). Key DSRD fabrication process modules developed include: 1) Al ion implantation dose and energy, 2) long duration, high temperature drive-in annealing temperature and time, 3) protective annealing capping layers, 4) N+/P+ contact injector layer ion implantation and annealing conditions, 5) cleaning processes, 6) DSRD stacking by Al-Ge wafer-scale eutectic bonding and pick-and-place die-level bonding, 7) singulation by saw, laser microjet, and plasma dicing, 8) assembly using copper stand-offs and epoxy resin. Spreading resistance profilometry validated the accuracy of TCAD process simulation to model deep PN junction formation and confirms the highly uniform PN junction depth and profile across wafer and wafer-to-wafer. TCAD device simulations model the operation of the DSRD, which input to a TCAD to SPICE (T2S) simulation link, provides toolbox for simulating DSRD performance in SPICE circuits. Pulse forming testing was performed to calibrate the TCAD device, T2S link, and SPICE circuit models. A demonstration of a 16-stacked DSRD providing a 12 kV pulse amplitude with a < 3 ns full-width half maximum (FWHM), providing a gain of ~9, demonstrates a high-performance device fabrication process, guided by the computational simulation. The progress toward establishing reproducible and manufacturable devices achieved under the AS2D4 program can enable further investigation into reliability and operational lifetime of DSRDs, which will be performed under ROLE of DSRDs in FY24.

Grant or Contract Number: N0001423WX02070_B
Project Title: Automated Diode Opening Switch Evaluation (ADOSE)
Period of Performance: April 19, 2023 to March 31, 2024
Principle Investigator: Shawn Higgins, 760-939-1047, shawn.o.higgins.civ@us.navy.mil
Organization: Naval Air Warfare Center Weapons Division (NAWCWD), China Lake, CA

Project Summary

In this applied research project China Lake Naval Air Warfare Center Weapons Division (NAWCWD) high power microwave (HPM) team's newly developed fast opening switch evaluation circuit was utilized for the performance characterization of over one hundred (100) Drift Step Recovery Diodes (DSRDs) comprised of sixteen (16) models from twelve (12) manufacturers, and averaging seven (7) similar DSRD tested per model. The study evaluated the individual performance of each DSRD with forward current pumping times between 40 ns and 150 ns and reverse current pumping times between 25 ns and 80 ns. The amplitude of the pumping current was varied between 10 amps and 500 amps for forward pumping current and 20 amps and 600 amps for reverse pumping current. A study was conducted with similar parameters to the single diode characterization to determine the additive effect of matched and mismatched recovery times of opening switches in an array configuration: series and parallel stacked. A newly developed evaluation circuit for the characterization of Fast Ionizing Dynistor (FID) closing switches in an impact ionization mode was utilized for the characterization of thirty (30) commercial off the shelf (COTS) thyristors comprised of six (6) models from four (4) manufacturers, and averaging five (5) similar devices tested per model. Performance data of the COTS thyristors were cataloged with respect to the closing time of the current. Through the characterization of the opening switch performance per pumping times and current, mismatched opening switch recovery times in an array configuration, and COTS dynistor closing response to high voltage rise rates, the results of this project will aid in the development of future solid-sate high-voltage impulse and Marx generators for HPM applications.

Grant or Contract Number: N00014-19-C-1008
Project Title: DREAM2
Period of Performance: 7 April, 2023 to 30 September, 2023
Principle Investigator: Walter Clover, walter.clover@verusresearch.net
Organization: Verus Research

Project Summary

The focus of the Directed Radio-frequency Energy Assessment Model Generation 2 (DREAM2) modeling and simulation (M&S) effort was to develop an initial simulation framework to model electronic target response to incident High-Power Radio-Frequency (HPRF) energy, to allow optimization of the front-door in-band high-frequency engagement problem. For this current version, a fixed system model was used following our baseline use case of a scanning radar. DREAM2 predicts multiple classes of effects by modeling system functionality in a signal processing simulation, representing non-linear component effects using measured poly-harmonic distortion (PHD) data for susceptible components. The system model was implemented in MATLAB Simulink, and the PHD data is pre-processed into neural network data-fitting models to represent component response in the simulation. A separate GUI runs the simulation so that end-users need not have Simulink installed. This development expands the effects modeling paradigm by

enhancing the assessment of system-level responses beyond upset/damage effects to include degraded performance or alternate functional effects.

ONR SBIR/STTR contracts

Contract Number: N68335-23-C-0489, SBIR Phase I
Project Title: HPM Broadband Tapered Transmitter Line Solid State Amplifier
Period of Performance: 17 July 2023 to 16 Jan 2024
Principle Investigator: David Cope, 781-275-9444, cope@divtecs.com
Organization: Diversified Technologies, Inc.

Project Summary

Diversified Technologies, Inc. (DTI) developed a high power density, wideband solid-state tapered transmission line combining topology for RF amplification. The technique is a simple, efficient, compact, and broadband means to couple the outputs of multiple RF transistors into a single, high power density amplifier that can be adapted to meet a variety of Navy power and frequency requirements. The technique is general in applicability and valid over a wide range of power and frequencies from L-band to X-band. DTI designed 2-D and 3-D tapered conical transmission lines to combine the output power from commercially-available transistors into a single multi-kilowatt wideband output. 2-D and 3-D tapered transmission lines and critical components with integral heat sinks were fabricated and measurements showed expected excellent performance. A 20:1 output transformation was demonstrated with high power obtained from a dual GaN HEMT S-band device. This device could yield tens of kilowatts of RF output in a small volume for a very high power density. The tapered transmission line combiner achieves all specified parameters, in particular high power and wide bandwidth.

Contract Number: N68335-23-C-0010, SBIR Phase II
Project Title: Improved Marx Pulse Generator for HPM Systems
Period of Performance: 9 March 2023 to 17 March 2025
Principle Investigator: Sam Dickerson, sdickerson@sara.com, 719-302-3117
Organization: Scientific Applications & Research Associates, Inc.

Project Summary

SARA is working to contribute to the next wave of US sourced high-power microwave (HPM) systems by developing an innovative, solid-state, semiconductor opening switch (SOS) based pulse generator. The pulse generator is made up of an SOS driver and the opening switch. The driver system adequately pumps the opening switch diodes enabling generation of very high peak power, fast risetime pulses. The driver system consists of a solid-state Marx generator, saturating transformer, and pumping capacitor.

The solid-state Marx generator, functioning as the primary energy store for the system, utilizes state-of-the-art high voltage silicon carbide (SiC) MOSFETs for switching. The advanced switching characteristics of SiC devices enable the SOS arrays to be efficiently operated using just a single magnetic switching component: the saturating transformer. Currently, the Phase II base effort is in progress, focusing on the fabrication, assembly, characterization, and demonstration of the solid-state Marx generator. This stage commenced with an experimental evaluation of candidate 3.3 & 6.5 kV SiC MOSFETs. After evaluating various options, the team selected the most suitable switching device for this application. The detailed design process for the Marx generator system is now underway. This includes developing a custom high voltage/high power semiconductor module, as well as integrating the module into a Marx generator stage and the overall Marx generator system. In the next phase, Phase II Option, the effort will focus on designing a full-scale gigawatt (GW) class pulse generator based on SOS technology. Following this design phase, the pulse generator will be assembled using the latest US-sourced SOS diodes. Full scale demonstrations will show the pulse generator's capability to generate pulses over 300 kV with risetimes under 10 nanoseconds at pulse repetition frequencies surpassing 300 Hz.

Contract Number: N68335-19-C-0255, SBIR Phase II
Project Title: Miniaturization of High Average Power, High Peak Power, Wide Bandwidth Antennas and DSRDs
Period of Performance: 3 Jul 2019 to 22 Jun 2023
Principle Investigator: Michael Abdalla, 505-830-3000, mda@asrcorporation.com
Organization: ASR Corporation

Project Summary

The overall goal of the effort was to develop thermally stable electrically small antennas (ESAs) that can be driven with drift step-recovery diode (DSRD) based sources to yield fully functioning, robust, and compact high-power microwave sources that can be operated at high pulse repetition rate (PRR). These DSRD based sources were developed to meet the requirements of interest to end users by driving antennas that are appropriate for the ultimate application. The ESA antenna effort has resulted in the development of a true ESA array and a moderate bandwidth array.

The primary DSRD fabrication processes addressed here include dopant and heterostructure optimization of tried-and-true silicon construction. Decreased rise time and increased reverse current density ratings, made possible by improved junction structures and packaging, enables higher current and lower internal impedance operation. Silicon is the material of choice, as it provides a sustainable commercial path and can perform at the required metrics. New DSRD fabrication process flows have been identified, developed and implemented. The focus is on leveraging gas-phase epitaxy, as well as traditional diffused-junction diode manufacturing. New wet processing methods for beveling and passivating DSRD devices have been developed to increase voltage-holdoff, reliability and pulser lifetime; while increasing die-to-die consistency issues seen in prior work. Potential advantages of the new DSRD process flow over traditional methods have been analyzed and described in two patent applications and three presentations at conferences. Pulsed power from DSRD circuits designed by the Missouri Institute for Defense & Energy has been demonstrated.

The primary area of research focus in Phase II antenna development was to investigate strategies to incorporate focusing into the antennas to reduce overall source volume. True electrically small antennas (ESA) have been considered. Due to fundamental bandwidth limitations for true ESA designs, alternate compact antennas have been considered. The ESA work was transitioned to bi-conical resonators and comparable ultra-wide-band and high-power radiating structures. These radiating structures included TEM horns, bi-cones, quarter-wave oscillators and continued advances in high efficiency wideband resonant radiators. These antennas are larger, with higher radiating efficiency, however, the wider bandwidth makes these more applicable to wideband HPM applications.

Contract Number: N68335-19-C-0445, SBIR Phase II
Project Title: Navy-Electronic Battle Damage Indicator (eBDI) Tool for Non-Kinetic High-Power Radio-Frequency (RF) Engagements
Period of Performance: 10 April 2023 to 15 Jan 2024
Principal Investigator: Donald Voss, 505-255-4201, donv@vosssci.com
Organization/Contractor: Voss Scientific, LLC

Project Summary

The ability to reliably detect faults in single components and subsystems during automated High Power Radio Frequency (HPRF) laboratory testing has the potential to greatly enhance susceptibility characterization and improve HPRF source effectiveness. In prior Phase II work, Voss Scientific demonstrated an electronic Battle Damage Indicator (eBDI), termed ADAM (Autonomous Damage Assessment Module). Tested in multiple laboratory and field demonstrations at a TRL-7 level, ADAM successfully provided immediate feedback regarding the status of multiple target systems. In ongoing 'Option' work, the ability to rapidly assess target responses is being combined with the previously developed Autonomous Susceptibility Test Apparatus (ASTA), to enable automated laboratory testing of a broad range of components and subsystems. By rapidly scanning over a multi-variable source parameter space, ASTA has been shown to lead to the discovery of highly beneficial source waveform parameters, i.e. reducing the power required or increasing the potential range for an existing capability. In this option work, the ASTA-X extends this integrated capability to the x-band frequency range. At this point we have designed, built, tested, and characterized a highly efficient, dual solid state x-band amplifier that is being integrated into the legacy ASTA for Navy-specific direct-injection testing purposes. Control and diagnostic software is also being developed specific to the direct injection methodology. Ongoing work is being coordinated with local Air Force staff so that it complements broader test program efforts. ASTA-X testing will commence in Spring 2024.

Contract Number: N68335-23-C-0491, SBIR Phase I
Project Title: Broadband Amplifier Source with Innovative LRU-based Integration using Solid-state for Kilowatt-outputs (BASILISK)
Period of Performance: 17 July 2023 to 16 Jan 2024
Principal Investigator: Johana Yan, 858-480-1628, johana@maxentric.com
Organization/Contractor: MaXentric Technologies LLC

Project Summary

The Navy is seeking innovative, high power kilowatt solid-state amplifier solutions for replacing TWTAs. In response, MaXentric proposes a **B**roadband **A**mplifier **S**ource with **I**nnovative **L**RU-based **I**ntegration using **S**olid-state for **K**ilowatt-outputs (*BASILISK*).

The *BASILISK* design consists of wideband combiners covering multi-octave frequency ranges, arranged symmetrically. At the submodule level, GaN devices can deliver a few hundred watts of output power. The LRU structure allows the submodules to be replaceable, reducing the long-term maintenance cost. As a result, *BASILISK* is capable of handling kW power levels while excelling in wideband performance.

During Phase I, MaXentric developed the *BASILISK* system architecture, determined the GaN Technology node optimal for these specifications, designed and analyzed 4 LRU submodule configurations, designed a kW wideband power combiner, and performed thermal analysis to provide a comprehensive trade-space analysis of the available implementation options based on state-of-the-art technology available today. The trade-space analysis was determined based on 4 different configurations to maximize different parameter objectives, namely:

- LRU1-based *BASILISK* a Minimum cost COTS-based solution
- LRU2-based *BASILISK* a Maximum output power COTS-based solution
- LRU3a-based *BASILISK* a Maximum tunable bandwidth solution
- LRU3b-based *BASILISK* a Maximum duty cycle supported solution

Contract Number: N68335-22-C-0642, SBIR Phase II
Project Title: Next-Gen Solid-State Power Module for High Power Microwave Drivers
Period of Performance: 29 Aug 2022 to 29 Aug 2024
Principle Investigator: Jacob Young, 719-302-3117 x8638, jyoung@sara.com
Organization: Scientific Applications & Research Assoc., Inc.

Project Summary

High power microwave (HPM) sources have conventionally been driven by gas-switched pulsed power generators due to high voltage, high current, and fast rise-time requirements. However, these traditional technologies impose significant limitations on advancements in HPM technology due to low repetition rate, short lifetime, limited waveshaping capabilities, and difficulty of synchronization. Recent advancements in solid state device technology, including wide bandgap semiconductors such as silicon carbide (SiC), have opened the door for development of a next generation of pulsed power drivers capable of overcoming these limitations, with rep-rates in the 10's to 100's of kHz, million-shot lifetime, arbitrary waveform capability, and sub-ns jitter. Further, optimization of solid-state device characteristics and packaging techniques tailored towards pulsed power applications can result in smaller, lighter, and more efficient systems than can currently be achieved with commercially available devices. A solid-state alternative to traditional HPM drivers was developed during Phase I leveraging SARA's ability to evaluate, test, and package state-of-the-art (SotA) silicon carbide die into large pulsed power systems. Further, characterization of SotA semiconductor devices demonstrated exceptional rise time performance and peak current handling capabilities. In addition, SARA has developed custom gate drive technology allowing these devices to switch with ultra-fast rise times that is at least twice as fast compared to any commercially available gate driver. Building upon these development efforts, the modulator design is undergoing refinement in preparation for experimental demonstration during Phase II.

Contract Number: N68335-21-C-0435, SBIR Phase II
Project Title: Solid-state, Sub-nanosecond Pulse Sharpener for Generating High Power Impulses
Period of Performance: 1 August 2023 to 31 January 2024 (6 month NCE)
Principle Investigator: Dr. Jason Sanders, 310-212-3030, jason@transientplasmasystems.com
Organization: Transient Plasma Systems, Inc.

Project Summary

The Office of Naval Research issued this SBIR topic to fund the development of a solid-state closing switch capable of producing high power ultra-wideband (UWB) electrical pulses. This effort has researched the fabrication of Semiconductor Avalanche Shaping (SAS) device structures in both Si and

SiC, with Si being viewed as the conservative approach for achieving the threshold specifications of this topic. SiC material properties suggest it is likely well suited for impact-ionization avalanche switching inherent to SAS, which does not rely on long minority carrier lifetime for practical implementation in the same way that other wideband opening switches, such as Drift Step Recovery Diodes (DSRDs), do. Devices have been designed and simulated during Phase I. In Phase II solid-state devices capable of switching kW-MW power pulses with risetimes faster than 300 ps at high pulse repetition rate are in development. Both Si and SiC parts were fabricated in 2023 and tested using a testbed developed by TPS for characterizing switching performance and durability. Si parts, which are expected to provide nearest-term capability for NAVY requirements, fabricated at TPS facilities are currently producing multi-kV pulses with risetimes that are hundreds of picoseconds. Initial durability testing, measured in shots fired, has also been promising, with no failures recorded to date. This effort will continue in 2024, funded by a Phase II Option, with emphasis on maturing the fabrication processes to produce parts that can be provided to NAVY stakeholders to test for their UWB applications.

Contract Number: N68335-23-C-0492
Project Title: High Power Microwave (HPM) Solid State Amplifier Topologies
Period of Performance: 17 July 2023 to 17 January 2024
Principle Investigator: Dr. Todd Nichols, todd.nichols@vadumin.com
Organization: Vadum

Project Summary

The objective of this work is to develop a radio frequency (RF) Solid State Power Amplifier (SSPA) topology specific to high power microwave (HPM) applications for use either as a stand-alone source or in an array, capable of generating a variety of waveforms while exploring the trade-off between power and bandwidth. Maximizing radiated RF power demands trade space optimization at the antenna, circuit, and die levels. The physics of thermal transport and electric field breakdown, and the mathematics of impedance matching, are the ultimate limiters of the available radiated power from a given HPM system.

The Vadum approach is to reduce system losses beyond what is normally achieved when forcing both PA and antenna to an improper impedance. Bridging unnecessarily large impedance transformation ratios needlessly increases losses and limits bandwidth (by increasing Q).

Key results to date are:

- Co-designing the die, circuit and the antenna element/aperture to minimize impedance transformation ratio reduces losses and increases bandwidth. The potential to reduce system loss is ~1.5dB which directly translates into increased output power
- Optimizing the semiconductor die and thermal system expands the breadth of waveforms the SSPA accommodates
- An array spreads a given amount of RF power across a series of smaller radiators, reducing the probability of electric field breakdown failure and enabling electronic beamsteering.

Vadum has shown that SSPA performance for HPM systems can be improved over the current state of the art. Further analysis and testing are needed to validate these findings and position the technical approach for deployment within the Navy and other customers.

Contract Number: N68335-23-C-0490
Project Title: Advanced 150V GaN Solid State Power Amplifier Topologies for High Power Microwave Applications
Period of Performance: 17 July 2023 to 17 January 2024
Principle Investigator: Dr. Tom Kole, tkole@integratech.com
Organization: Integra

Project Summary

Next generation high power microwave (HPM) applications require dramatically higher performance SSPAs (5kW, 1GHz bandwidth, cutoff frequency f_c 2GHz, 70% efficiency, up to 50% duty cycle) which are constrained by current commercial semiconductor technology.

Integra pioneered and introduced the industry's first high voltage (HV) RF GaN in 2020 after a decade of development. In 2022 Integra extended its HV GaN patent portfolio with its novel Gen4 transistor structure that dramatically reduces intrinsic transistor resistance, leading to a substantial breakthrough in transistor power and efficiency. Leveraging its 150V GaN/SiC process with its novel transistor structure, Integra achieved measured power density of 29W/mm, another industry first at 350% higher than commercial GaN. This breakthrough power density is the key to achieving the 5kW SSPA target specification.

In Phase I, Integra designed and ran compact models augmented with data supplied by Integra's own IRAD to simulate four 150V GaN/SiC based SSPA topologies, each focused on overcoming specific physical constraints (e.g., thermal, bandwidth...). Additionally, Integra identified energy loss mechanisms inside the transistor which could improve SSPA efficiency by 10%, and evaluated a new diamond composite transistor package which enables a 300% Rth improvement compared to today's commercially available packages.

Integra's Phase I investigation identified Topology 4, the Integrated Feedback SSPA, combining Integra's 150V GaN/SiC, the diamond composite package, and mitigated energy loss mechanisms, as the solution to achieve the full 5kW target specification. Integra also recommends Topology 3, Integra's Gen4 150V GaN/SiC as ideally suited for 5kW SSPA requirements with duty cycles of less than 10%. In addition to HPM applications, these 150V GaN/SiC SSPA topologies can address Industrial, Scientific, and Medical markets.

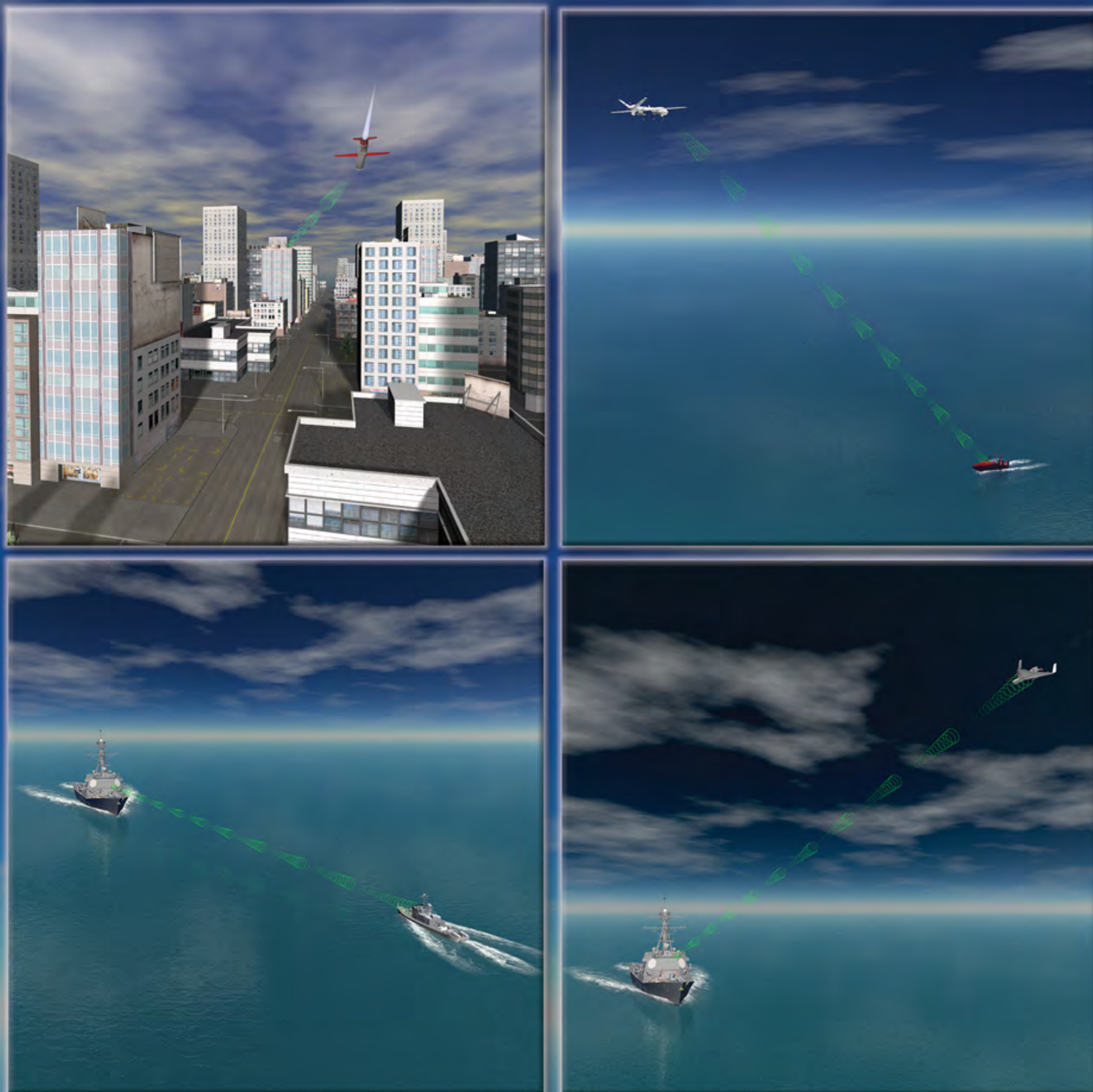

Office of Naval Research
875 N. Randolph Street
Arlington, VA 22203-1995
www.onr.navy.mil